ABSTRACT

Title of Document: ENERGETIC BIOCIDAL MATERIALS AND SPORE NEUTRALIZATION

Wenbo Zhou, Doctor of Philosophy, 2015

Directed By: Professor Michael R. Zachariah, Department of Chemical and Biomolecular Engineering and Department of Chemistry and Biochemistry

The objective of this dissertation is to explore a more accurate and versatile approach to investigating the neutralization of spores suffered from ultrafast heating and biocide based stresses, and further to explore and understand novel methods to supply ultrafast heating and biocides through nanostructured energetic materials

A surface heating method was developed to apply accurate (± 25 ˚C), high heating rate thermal energy (200 - 800 ˚C, ~10^3 - ~10^5 ˚C/s). Uniform attachment of bacterial spores was achieved electrophoretically onto fine wires in liquids, which could be quantitatively detached into suspension for spore enumeration. The spore inactivation

increased with temperature and heating rate, and fit a sigmoid response. The neutralization mechanisms of peak temperature and heating rate were correlated to the DNA damage at ~10^4 ˚C/s, and to the coat rupture by ultrafast vapor pressurization inside spores at ~10^5 ˚C/s. Humidity was found to have a synergistic effect of rapid heating and chlorine gas to neutralization efficiency. The primary neutralization mechanism of Cl_2 and rapid heat is proposed to be chlorine reacting with the spore surface.

The stress-kill correlation above provides guidance to explore new biocidal thermites, and to probe mechanisms. Results show that nano-Al/$K_2S_2O_8$ released more gas at a lower temperature and generated a higher maximum pressure than the other nano-Al/oxysalts. Given that this thermite formulation generates the similar amount of SO_2 as O_2, it can be considered as a potential candidate for use in energetic biocidal applications. The reaction mechanisms of persulfate and other oxysalts containing thermites can be divided into two groups, with the reactive thermites (e.g. Al/$K_2S_2O_8$) that generate ~10× higher of pressure and ~10× shorter of burn time ignited via a solid-gas Al/O_2 reaction, while the less reactive thermites (e.g. Al/K_2SO_4) following a condensed phase Al/O reaction mechanism. These different ignition mechanisms were further re-evaluated by investigating the roles of free and bound oxygen. A constant critical reaction rate for ignition was found which is independent to ignition temperature, heating rate and free vs. bound oxygen.

ENERGETIC BIOCIDAL MATERIALS AND SPORE NEUTRALIZATION

By

Wenbo Zhou

Dissertation submitted to the Faculty of the Graduate School of the
University of Maryland, College Park, in partial fulfillment
of the requirements for the degree of
Doctor of Philosophy
2015

Advisory Committee:
Professor Michael R. Zachariah, Committee Chair
Professor Sheryl H. Ehrman
Professor Srinivasa R. Raghavan
Professor Vincent T. Lee
Professor Bryan W. Eichhorn, Dean's Representative

Dedication

To

My parents

Zhanggeng Zhou and Mingzhen Wang,

And my wife

Ya Zhang.

Thank you for your unlimited love and support.

Acknowledgements

I would like to express my sincere appreciation and gratitude to my advisor, Dr. Michael R. Zachariah, for the patient guidance and mentorship he provided to me, throughout my entire PhD study in the Department of Chemical & Biomolecular Engineering at UMD. Dr. Zachariah's intellectual insights, experiences and professionalism have inspired me deeply. He not only taught me a variety of R&D methodologies, but also nurtured my scientific temper, both of which will be valuable assets throughout my life. Dr. Zachariah also cares about my future career in the industry field. He continuously provides me good suggestions. I still remember in our last routine research discussion, he again recommended me to update my knowledge of the recent progress on high temperature corrosion by salt ions that will be very useful for the semiconductor field I will engage in.

I would also like to thank Dr. Vincent T. Lee from the Department of Cell Biology & Molecular Genetics, for his assistantship in the characterization of bacterial spores. His meticulous scientific thinking, optimistic altutitude, and industrious work impressed me a lot, and particularly helped me to overcome the toughest issue on finding a reliable and convenient way to characterize the viability reduction of spores. I still remember he emailed me one day that he would be in his lab helping me count spores. It was during the week of Christmas Day. I am truly fortunate to have had the opportunity to work with him, and really feel that our extensive collaborations deserve more achievements than what we have now.

I am indebted to my other committee members, Dr. Sheryl H. Ehrman and Dr. Srinivasa R. Raghavan, for their friendly guidance and thoughtprovoking suggestions

that each of them offered to me over the years. The weekly department seminars hosted by Dr. Ehrman, as well as the course of *Nanobiotechnology* taught by Dr. Raghavan, also opened my horizon and raised my research interst. In a similar vein, I am grateful for Dr. Bryan W. Eichhorn for having agreed to serve on my committee as Dean's Representative. Special thanks go to Mr. Tim Maugel in the Laboratory for Biological Ultrastruture, and Mr. Sz-Chian Liou in AIMLab at Maryland Nanocenter, for their sustained assistance of electronic microscopy. The help from Dr. Peter Setlow from University of Connecticut is also appreciated.

I must also recognize all previous and current members in Zachariah's group. It is thankful to Jeff DeLisio, Guoqiang Jian, Garth Egan, Lu Liu, Xizheng Wang, Philip Guerieri, D-H. Tsai, and previous and current visiting graduate students Haiyang Wang, Xiangyu Li, Xiuli Hu and Chuan Huang, for our collaborative work in the published and submitted papers. Particularly, Mr. Jeff DeLisio is greatly appreciated for his help in conducting TOF-MS tests and in the language editing for papers. I am also grateful to Ms. Mona W. Orr and Ms. Sarah K. Watt from Dr. Lee's group, for their collaborative work in experiments and papers.

Finally, I'd be remiss if I didn't acknowledge the innumerable sacrifices made by my wife, Ya in U.S., and my parents far away in China. Without their encouragement and love, I can not imagine that I have bridged my research topics from polymeric biomaterials (when I was in the Master study in China), to energetic materials here, and I can hardly hold the invariable faith on finishing my PhD.

Thank you !

Wenbo Zhou

Table of Contents

List of Tables

List of Figures

Chapter 1: Introduction

1.1. Why is the study of bacterial spore neutralization important?

Recent threats of bio-terrorism highlight the need for preemptive neutralization of biological agent munitions, stockpiles and production facilities. Unfortunately current capabilities in the U.S. military are limited to conventional warheads, which rely on a "thermal kill" mechanism. While effective on chemical agents, these warheads may not be sufficient to neutralize biological agents, in particular those strains that form hardy bacterial spores. In the civilian field, for example, in an industrial or a hospital environment, bacterial spores carried bio-aerosols are easily generated from waste management facilities, posing a high risk to the public health. Currently there is no effective way to devastate the airborne spores in a large scale. Facing the ever-increasing danger from the epidemic bacterial spores (e.g. *Bacillus anthracis* leading to Anthrax), systematic understanding of the spore structure and its resistance mechanisms is required, followed by extensive exploration of effective spore neutralization approaches.

1.2. Bacterial spores: multilayered structure

Bacterial spores belong to a cell type that are formed in a sporulation process and are liberated from their mother bacterial cells in response to the changes in the environment [1-3]. Typically, this occurs when the level of external nutrients is reduced. Once the nutrients become available, spores will germinate to bacteria. In order to sustain a very long period without nutrients (even millions of years [4]),

bacterial spores have evolved to be metabolically dormant. This is reflected by several characteristics including containing very little ATP, showing no detectable metabolism and enzyme activity, and low levels of water within the spore core [2]. The extreme resilience of spores can be attributed to its multilayered structure. From the outside and proceeding inward there are several constituent layers include the exosporium, coat, outer membrane, cortex, germ cell wall, inner membrane and core (Fig. 1.1) [2,3]. The exosporium is the outermost layer of some bacterial spores, such as *Bacillus anthracis*. Some other species such as *Bacillus subtilis* do not have this layer. The spore coat sits below the exosporium, and comprises a series of sub-layers. There have been many reviews introducing the structure and molecular compositions for this layer [5-8]. In brief, the coat is mainly made of more than 70 different proteins typically for *Bacillus subtilis* spores, which are cross-linked and serve as an initial hurdle to many oxidizing agents (e.g. hydrogen peroxide, ozone, chlorine dioxide and hypochlorite). Below the coat lies the outer spore membrane, which is needed for spore formation, but less important for the spore resistance to heat and chemicals [9]. Between the coat and the core exists the cortex which is composed of peptidoglycan in a low level of cross-linking, and has been identified to be probably responsible for maintaining the spore core dehydration. The next layer is the inner membrane which is believed to be correlated with the low spore permeability of some small molecules. The mechanism of resistance lies in the immobile liquid molecules inside this layer that confer its remarkable impermeability. The innermost compartment is the spore core which stores the genomes and most of the spore's enzymes [2]. The core is commonly remained in a dehydrated state, which is thought

to contribute to the low metabolism level and the DNA protection mechanisms. The core also contains high levels of dipicolinic acid (DPA) complexed with Ca cations, which protect the DNA backbones. Other resistance mechanisms include the existence of a type of small acid-soluble proteins (SASPs) that directly shield the DNA strand from chemical attack, as well as the DNA repair system during the spore outgrowth. To conclude, the strong resistance of bacterial spores is due to the cumulative effects of both structural and biochemical properties.

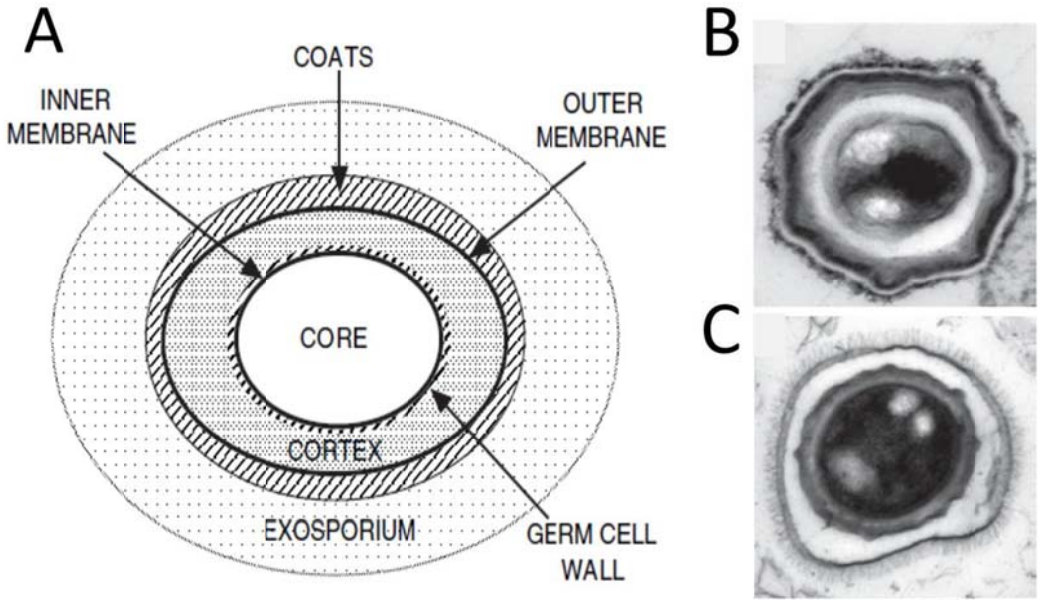

Figure 1.1. (A) Multilayered structure of bacterial spores. Each layer is labeled and not drawn to scale [2]. (B) Thin section TEM image of a Bacillus subtilis spore [5]. (C) Thin section TEM of a Bacillus anthracis spore [5].

1.3. Bacterial spores: resistance to heat and chemicals

The spore resistance mechanisms against heat and chemicals are summarized in Table 1.1 [2]. The commonly adopted heating method for spore inactivation is by suspending spores in a high-temperature aqueous environment. In this case, many factors contribute to the wet heat resistance, such as the low core water content, the

SASPs, and the DPA and Ca complex. However, the mechanism of spore killing was demonstrated to be not due to the DNA damage. Recent studies have revealed that the wet heat treatment seemed to kill spores by denaturing one or more key proteins [10,11], probably some metabolic enzymes [12]. Alternatively, α/β-type SASPs play the predominant role for the dry heat resistance (Table 1). The α/β-type SASPs can stabilize the DNA backbonds from breakdown by heat damage. Accordingly, the spore killing mechanism by dry wet is due to the loss of DNA protection by SASPs. Another important factor to the dry heat resistance is the DNA repair system that rectifies the gene mutations during the spore outgrowth.

Table 1.1. Mechanisms of spore resistance to and killing by heat and chemicals [2].

Treatment	Factors in spore resistance	Mechanism of spore killing
Wet heat	Low core water, SASPs, core mineralization, DPA	Protein damage
Dry heat	SASPs, DNA repair	DNA damage
Chemicals	Coats, inner membrane impermeability, SASPs, DNA repair	DNA damage, inner membrane damage

The spore's resistance to chemicals can be classified into two types. For some genotoxic chemicals such as formaldehyde and nitrous acid, spore neutralization is from DNA damage since the survival spores after the treatment of these chemicals were found to have accumulated mutations [13,14]. For other chemicals such as oxidizing agents, the spore neutralization is due to some type of damage to spores' external layers, mainly the inner membrane. The experimental evidence is that when the treated spores germinated, the compromised membrane ruptures leading to the spore death [15]. In addition, the spore coat only plays a minor role in spore

resistance to oxidizing agents, and serves as a detoxifier for these chemicals before they enter the inner structures [16].

1.4. More efficient spore inactivation approaches

In the fight again food starvation, spores have evolved a variety of mechanisms to protect themselves from damage, which include modern disinfection/sterilization procedures. One of the major focuses in previous studies of defining spore neutralization is to use hydrothermal energy (<120 ˚C) in the absence of pressure or in the combination of heat and pressure with inactivation timescale in the order of minutes [2,17]. The time scales of these methods do not allow for rapid inactivation of large quantities of spores. To further improve the killing efficacy, heat schemes with a high peak temperature have started to raise interest as one of the next generation spore inactivation strategies. Aerosol based techniques are being developed to study rapid inactivation of airborne bacterial spores by rapid heating (>200 ˚C within a timescale of a second) [18-24]. Gate et al used an aerosol shock tube and subjected the airborne spores to 200 – 700 ˚C under 2 – 7 atm [18,19]. Results show that spores lost the ability to form colonies when heated to the peak temperature of 230 ˚C, while appreciable breakdown of the spore's morphology was found at the temperatures above 480 ˚C (Fig. 1.2A). An analogous approach of spore inactivation by dry heat has been tested using a controlled axially heated air flow (Fig. 1.2B). After exposure to air temperatures ranging from ~150 ˚C to > 1000 ˚C, the viability reduction was found to be 4 logs when the peak temperature reached 320 ˚C [20]. Further genome analysis concluded that the heat-induced damage was due to the

increased DNA mutational frequency [22]. Although these methods are capable of neutralize spores, an accurate and quantitative relationship of time-temperature-kill for spores is not available due to the variability in temperature distribution and the resident exposure time of these heating schemes. Nevertheless, a precise time-temperature-kill relationship is needed for predicting and ensuring a successful outcome of large-scale neutralization events. In order to improve the accuracy of measurements of the temperature history on spores, an alternative approach has been developed by heating spores deposited on surfaces that allows the accurate measurement of the transient temperature. Hofmann et al employed a pulsed UV-laser light to rapidly heat *Bacillus* spores deposited on a laser aBsorbing matrix (Fig. 1.2C) [25]. Results show that laser fluences below 20 mJ/cm^2 enabled to change the spore morphology and induce the release of endogenous DNA indicative of spore inactivation. Another group from Air Force Institute of Technology rapidly heated *Bacillus anthracis* spores by a thermal tip using atomic force microscopy (Fig. 1.2D) [26,27]. A typical 2 logs spore viability reduction was achieved when heating spores to ~430 ˚C within 0.1 s. These two surface-based heating approaches provide accurate temperature measurement for spores, though the heat zone is limited by the instrumentation and it required further improvement for scaling up.

As another important way to inactivate bacterial spores, biocidal chemicals can presumably synergize the above rapid heating approaches. A primary study by the same group for the work in Fig. 1.2B investigated the spore viability exposed to iodine vapor containing hot air flows [28]. Compared with hot air flows, the iodine containing flows increased the spore inactivation by 2 orders of magnitude.

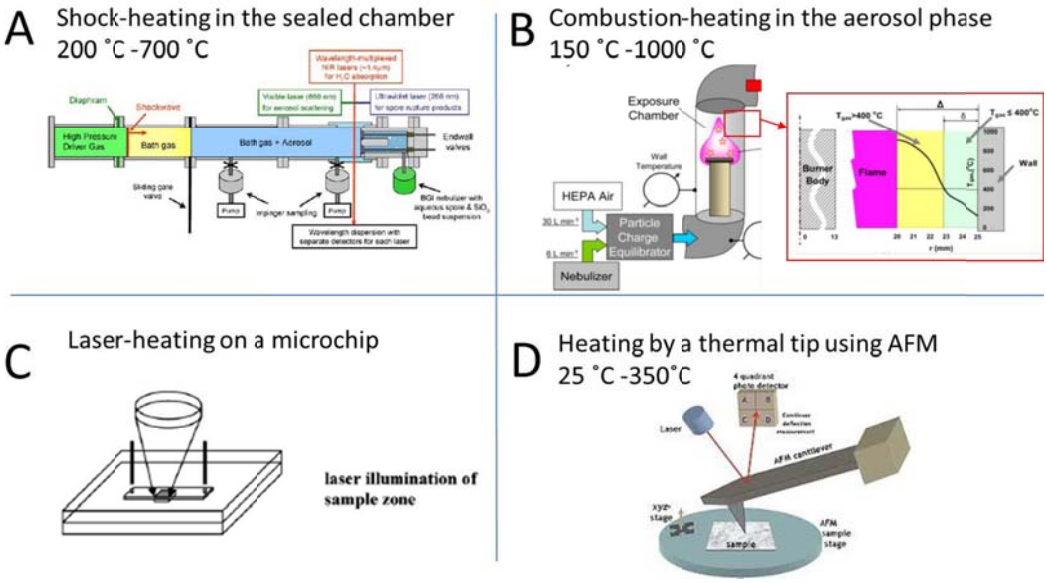

Figure 1.2. Four high-temperature short-time heating approaches for bacterial spores. (A) Spores heating in the shock chamber [18]. (B) Spore heating in the hot air flow [20]. (C) Spore heateing by a UV laser [25]. (D) Spore heating by a thermal tip using AFM [27].

1.5. Energetic materials

One of the promising approaches to generate substantial heat in a short time is energetic materials (EMs). Energetic materials are defined as a class of reactive materials containing both fuels and oxidizers, which feature an extremely high exothermicity, intensive light emission, and shock generation by the self-sustained reaction (Fig. 1.3) [29-32]. Based on their formulations, conventional energetic materials can be classified as homogeneous and heterogeneous (composite) materials according to whether the fuel and oxidizer constituents are chemically or physically linked (Fig. 1.3) [29]. Most homogeneous EMs have their both constituents contained into one molecule, such as Dynamite (nitroglycerine) and TNT. Heterogeneous EMs are composites involving separated fuel and oxidizer. A typical example for

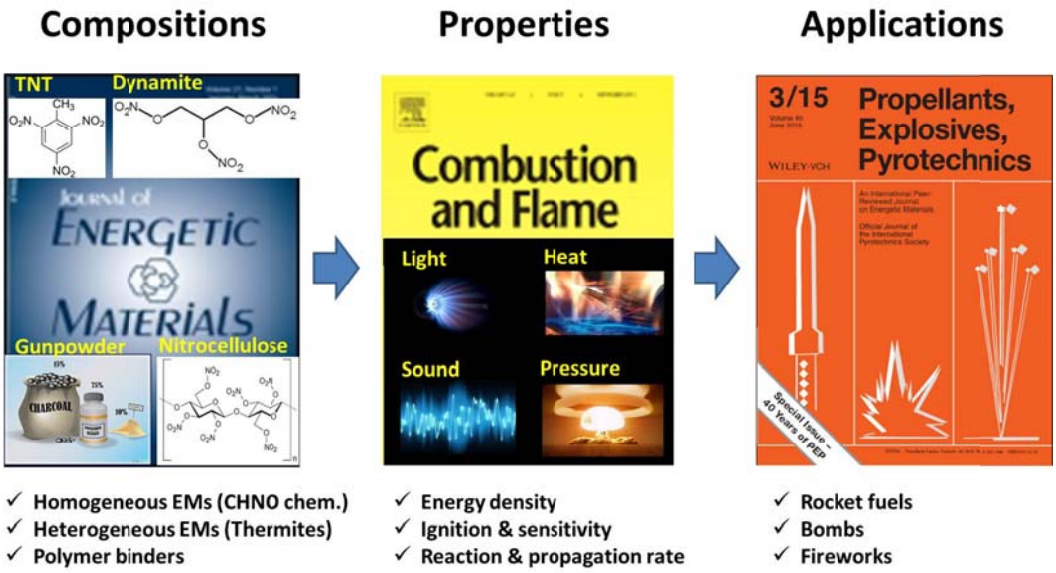

Figure 1.3. Compositions, properties and applications of conventional energetic materials. The cover images of three important journals in the field of energetic materials are taken to demonstrate the different research aspects. On the cover image of *Journal of Energetic Materials*, four different representative EMs are presented. On the cover image of *Combustion and Flame*, Four energy types of energy release from the reaction of EMs are presented.

heterogeneous EM is the gunpowder that contains potassium nitrate as the oxidizer, and carbon and sulfur as the fuels (Fig. 1.3) [33]. Traditional EMs are widely used as propellants, explosives, and pyrotechnics. Propellants and pyrotechnics generate their energy via relatively slow deflagration processes that last for several seconds (combustion), whereas explosives release energy in fast detonation processes (microsecond) [29]. Basically, homogeneous EMs belong to explosives that are relatively sensitive and difficult to manipulate. Due to their capability of generating high pressure products and intensive shock waves, they are exclusively used in fields that require destructive forces. Distinctively, heterogeneous EMs are mostly used as propellants and pyrolants that are more favorable to generate high temperature flames

upon combustion, thus are more relevant to my focus of finding an premier heat source.

Research emphasis on heterogeneous EMs in modern times starts from a type of energetic formulations named thermites, which are comprised of a reactive metal as the fuel, and a metal oxide as the oxidizer. The typical thermite reaction undergoes as follows:

$$A + BO \rightarrow B + AO + \Delta H \quad (1.1)$$

where A is a reactive metal, B is a less reactive metal, ΔH is the heat of reaction. The characteristic of thermites is that they have much higher energy densities and greater stability than common organic explosives (Fig. 1.4A), thus offering the promise in the military, space exploit, and civilian use [32]. The most widely adopted metal is aluminum due to its abundance and competitive reactivity when compared with other metals (Fig. 1.4B) [31]. Al is also a relatively safer metal due to the formation of a thin oxide layer at the outer surface that prevents Al powder from spontaneous combustion. Because of these advantages, Al has long been used as a metallic doping particle in composite explosives and propellants for improving the reaction heat, as well as decreasing the sensitivity to external stresses. Compared with Al, boron shows a higher energy density both on a mass and volume bases (Fig. 1.4B). However, its high ignition temperature is a drawback to application [32]. Scheafer and Nicolich showed that the addition of boron decreased the impulse of a cast-cured explosive by half, as well as elongated the ignition delay [34]. These results indicate that due to the poor kinetic characteristics of boron, it could act as an inert diluent to the energetic materials, and its full potential cannot be harnessed.

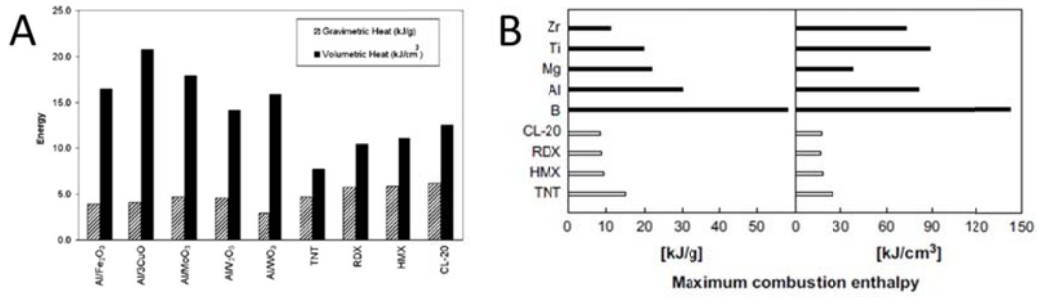

Figure 1.4. (A) volumetric (black bar) and gravimetric (pattern filled bar) density of energy for some thermites and conventional organic explosives [32]. (B) Maximum combustion enthalpies for some reactive metal fuels and some monomolecular energetic compounds [31].

Up to now, many transient metal oxides and main group metal oxides have been investigated as oxidizers in thermite formulations. Table 1.2 summarizes the thermo-physical properties of thermites as reported by Fischer et al [35]. Among these formulations, MnO_2 and MoO_3 present the compatibly high adiabatic flame temperatures as CuO, SnO_2 and WO_3, and relatively higher heat of reaction than the others (Table 1.2). Dreizin et al reported that the activation energy of Al/MoO_3 was the lowest of the thermites, indicating that Al/MoO_3 also shows the highest reaction rate [31]. In addition, the Al/MnO_2 reaction possesses the largest gas generation (Table 1.2), indicating that it is a better gas generator.

A new type of nanothermites involves oxysalts as oxidizers instead of conventional metal oxides. The most widely used oxysalts in pyrotechnics and propellants are nitrates [36-38] and (per)chlorates [39-42], due to their lower decomposition temperatures and higher gas generation than metal oxides. The advantages of oxysalts in thermite performance stem from the higher atomic oxygen content they possess (Table 1.3) [43]. In addition, Nonmetal-oxygen bonds (Cl-O, I-O, etc.) in peroxy salts typically have lower dissociation energies, than metal-oxygen bonds (Cu-O, Fe-O, Bi-O, etc.) in metal oxides (Table 1.3), suggesting a higher oxygen mobility in peroxy

Table 1.2. Thermo-physical properties of some thermite reactions [35].

Constituents	Adiabatic reaction T (K)		Gas production (mole/100g)	Heat of reaction	
	w/o phase change	w/ phase change		-kJ/g	-kJ/cm^3
$2Al+Bi_2O_3$	3995	3253	0.4731	2.1	15.3
$8Al+3Co_3O_4$	3938	3201	0.2196	4.3	20.0
$2Al+Cr_2O_3$	2789	2327	0	2.6	10.9
2Al+3CuO	5718	2843	0.5400	4.1	20.8
$2Al+Fe_2O_3$	4382	3135	0.1404	4.0	16.5
$4Al+3MnO_2$	4829	2918	0.8136	4.8	19.5
$2Al+MoO_3$	5574	3253	0.2425	4.7	17.9
2Al+3NiO	3968	3187	0.0108	3.5	18.0
Al+PbO	3968	2327	0.4146	1.4	11.4
$4Al+3SnO_2$	5019	2876	0.2928	2.9	15.4
$4Al+3TiO_2$	1955	1752	0	1.5	5.5
$10Al+3V_2O_5$	3953	3273	0.0699	4.6	14.2
$2Al+WO_3$	5544	3253	0.1434	2.9	15.9

salts that can lead to decomposition and oxygen release at lower temperatures [43]. However, the widely used peroxy salt, $KClO_4$, is hygroscopic and has environmental issues, due to the presence of chlorine. These issues have limited its application in many traditional pyrotechnic formulations. A recent study demonstrated that KIO_4, alternatively, has lower toxicity and hygroscopicity making it ideal for applications in illumination and gas generation [44]. Compared with metal oxides, the thermo-physical properties for oxysalts is still relatively unclear.

Table 1.3. List of bond energies of M-O in peroxy salts (M=Cl, Br, I, Mn, Cr, S) as well as oxygen contents in peroxy salts and relevant aluminum-based, stoichiometrically mixed thermite composites [43].

Thermite[a]	BDE (kJ/mol)[b]	Oxygen content in salt (%)	Oxygen content in thermite (%)
3CuO+2Al	287 (Cu-O)[1]	20	16
Fe_2O_3+2Al	407 (Fe-O)[1]	30	22
Bi_2O_3+2Al	337 (Bi-O)[1]	10	9
$3Ag_2O$+2Al	221 (Ag-O)[1]	7	6
$3I_2O_5$+10Al	184 (I-O)[2]	24	19
$3KIO_4$+8Al	184 (I-O)[2]	28	21
$3KBrO_4$+8Al	235 (Br-O)[2]	35	25
$3KClO_4$+8Al	269 (Cl-O)[2]	46	30
$3KMnO_4$+8Al	406 (Mn-O)[2]	41	28
$3K_2Cr_2O_7$+14Al	423 (Cr-O)[2]	38	27
3K2S2O_8+16Al	142 (O-O)[3]	47	31
$3K_2SO_4$+8Al	365 (S-O)[3]	37	26

Note:

[a] Fuels and oxidizers mixed in a stoichiometric ratio that presumably all the oxygens in oxidizers were converted into alumina in the product.

[b] Bond dissociation energy (BDE) data were based on measurement of the standard dissociation enthalpies of M-O diatomic species at 25 ˚C by either spectroscopic or thermochemical methods. BDE data of Cr-O was calculated at -273 ˚C.

When one evaluates the reactivity for a specific thermite formulation, the energy density is not the unique criterion. Another essential criterion is the reaction kinetics, such as the combustion rate, pressurization rate and propagation speed. While the energy density of thermites is more correlated to the chemical nature, the reaction kinetics can be influenced by many factors. Similar to the energy density, different thermite formulations have different reaction rates. For instance, although the reaction heat for Al/CuO and Al/Fe_2O_3 is similar (Table 1.2), Al/CuO is usually considered as a fast-reaction thermite while Al/Fe_2O_3 is relatively a slow-reaction thermite. A more significant and tunable factor for the reaction kinetics is the size of particles. Additive

micrometer-sized Al can significantly increase the energy release for the propellants and explosives; however, the burn rate was found not to accelerate much because the oxidation process for microscale Al particles are much slower than organic CHNO explosives [31]. Recently, the rapid development of nanotechnology has made the synthesis of nanoscale Al possible, which has been suggested as a potential substitute for conventional microscale Al powders due to the significant improvement in oxidation kinetics and the decrease in ignition temperature (Fig. 1.5B and 1.5C) [30]. In a thermite system, decreasing the dimensions of both fuel and oxidizer particles to nanoscale (nanothermite) also correlates to the increment reactivity, including faster pressurization and temperature rise rate, while remaining the total heat of reaction as high as that for microscale thermite. In 1995, Aumann et al firstly reported the production of Al/MoO_3 nanothermites by ultrasonic mixing [45]. Their results show that the nanothermites can burn 10^3 times faster than the corresponding macroscale thermites. The combustion propagation speed was also measured as ~1000 m/s when the nanoparticle size drops to ~40 nm. In comparison, the propagation speed for microscale thermite is only 10 mm/s [46]. Similarly, Bhattacharya et al evaluated the some other nanothermites and found that the propagation speeds for nanoscale Al/CuO and Al/Bi_2O_3 are ~450 m/s and 150 m/s respectively, both of which are much faster than the corresponding microscale thermites [47]. Unlike the heat of reaction, there is still no agreement for the standard combustion/propagation speed for different nanothermties. One reason for this lack of knowledge is the fact that particles of different nano-sizes or different geometrical shapes were used by different research

groups, and even particles with the same morphology may have distinct size distributions.

As mentioned before, decrease in the length scale for energetic materials to nanometers enables to improve the reaction kinetics by orders of magnitude. This is mainly due to the significant increase in surface areas for energetic materials, which leads to a shorter diffusion time for both fuel and oxidizer reactants, as well as an enlarged reaction interface (Fig. 1.5A) [30]. For thermite formulations, dropping down to nanoscale means a better combustion performance such as faster energy release rate (e.g. faster pressurization rate and optical light emission rate), and faster reaction propagation rate. Other important endeavors in this research direction

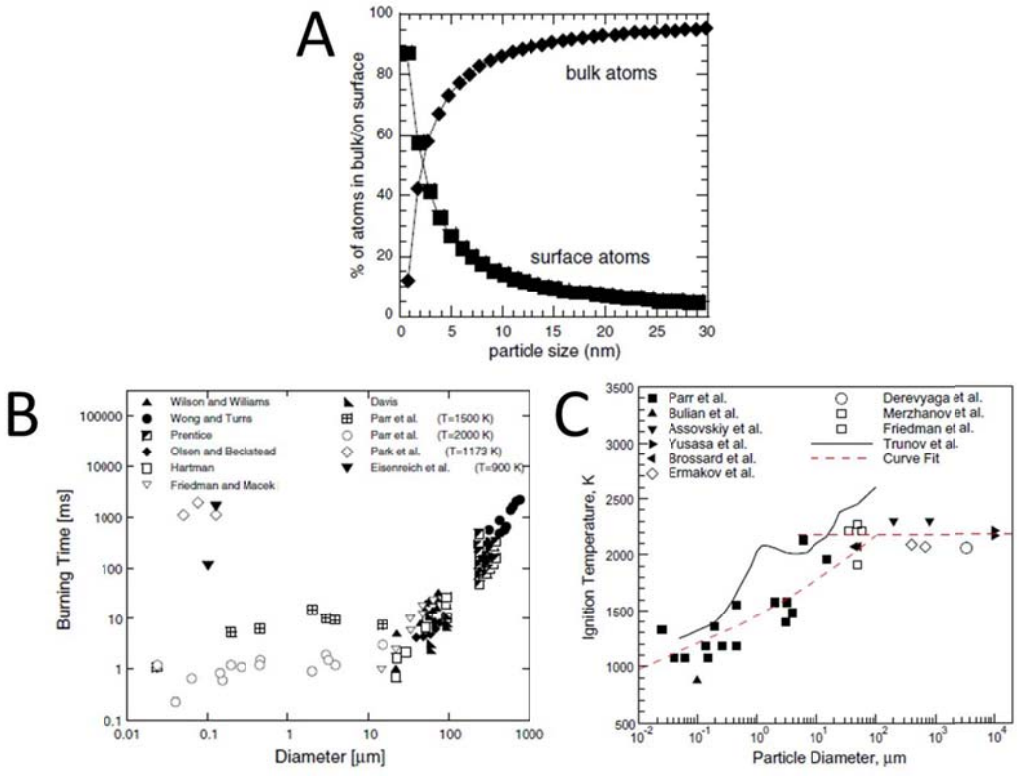

Figure 1.5. (A) Surface to bulk atomic ratio for iron nanoparticles [30]. (B) Relationship between the particle burning times and the particle diameter [30]. (C) Relationship between the particle ignition temperatures and the particle diameter [30].

include producing various nanostructures for reactants, typically for oxidizers, in order to further increase the reaction interface. Due to the limitation of manufacturing techniques, decreasing the size of fuel/oxidizer nanoparticles becomes harder when going below 50 nm. Alternatively, evident progress has been seen to generate other nanostructures with high surface-to-volume ratios. Researchers at Lawrence Livermore National Lab introduced the sol-gel chemistry to synthesize porous nanoscale EMs [48,49]. Metal oxide xerogels were produced by solvent removal of the precursor colloid solution (sol), featuring a collapsed gel structure. Alternatively, aerogels were prepared by superciritical drying that remains the open pores inside the sol, leading to highly porous metal oxide structure. A following approach by Prakash et al produced a novel core-shell nanostructure based on a two-temperature aerosol spray pyrolysis procedure [50]. In detail, the inner $KMnO_4$ particle from the desiccation of the first aerosol was coated with a thin layer of Fe_2O_3 from the second aerosol, leading to core-shell oxidizer nanoparticles with tunable oxidation capability and better environmental stability. A distinct route to the above hydrothermal chemistry is to deposit alternative multilayers of fuel and oxidizer in vacuum by chemical vapor deposition or reactive magnetrom sputtering [51,52]. The major advantage of this technique is that it can ideally manipulate the thickness of each layer with nanometer scale and conformal uniformity, thus enable to maximize the contact area. A modified strategy to the deposition route is to create a nanoarray of core-shell structure by a template sacrifice technique [53-55]. Fuel or oxidizer nanorods after embedded onto the substrate were deposited with the counterpart

component, leading to either fuel core/oxidizer shell or fuel shell/oxidizer core nanostructure. All the above approaches successfully resulted in nanothermite structures that show greatly enhanced combustion performance, though there is a high cost for preparing the layered nanostructures, and risk concerns for the hydrothermal methods in adversely causing the oxidation or hydrolysis of metal fuels.

Apart from the pursuit of higher surface-to-volume ratios, another important research direction is to improve the intimacy of fuel and oxidizer formulations.

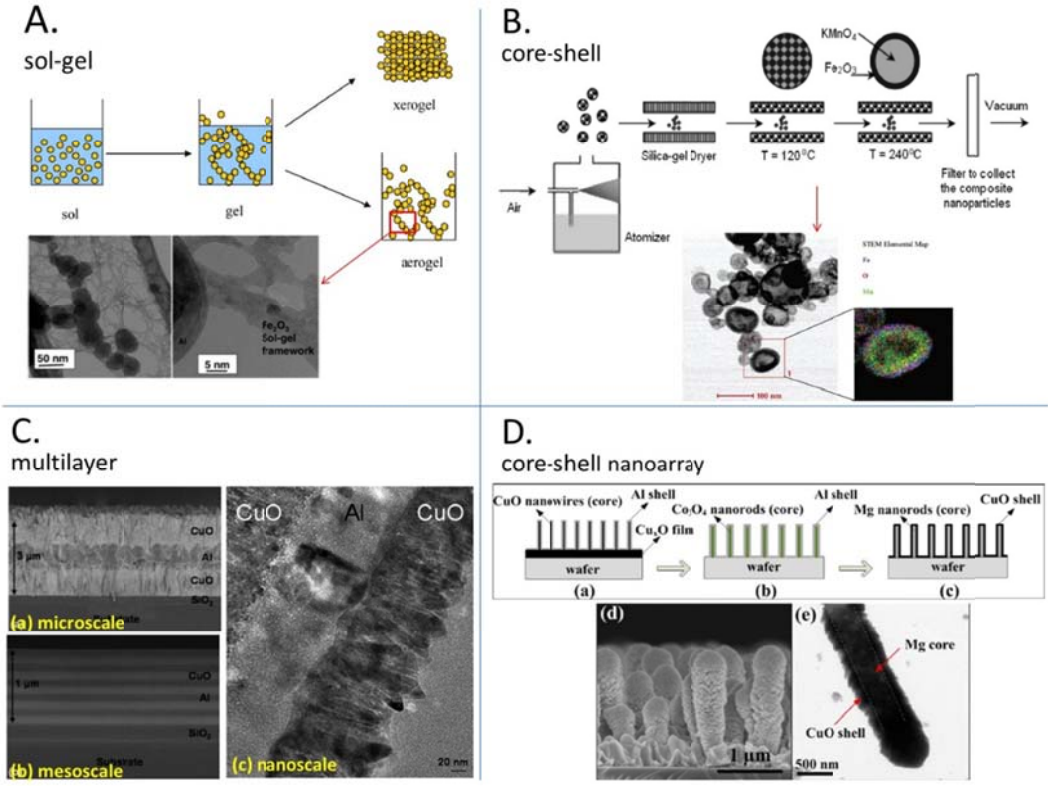

Figure 1.6. (A) Schematic diagram of sol-gel methodology and TEM images of Al/Fe_2O_3 nanothermites prepared by sol-gel process [48,49]. (B) Schematic showing the aerosol spray drying system for the synthesis of core-shell nanocomposite oxidizer [50]. TEM image and STEM elemental mapping demonstrate the nano-$KMnO_4$ coated with Fe_2O_3. (C) Cross-sectional EM images of CuO/Al multilayers in the dimensions of (a) micrometer scale, (b) mesoscale, and (c) nanometer scale [51]. (D) Schematic diagrams (a-c) of three design concepts of core-shell nanoarrays. Cross-sectional SEM (d) and TEM (e) images of the core-shell nanostructures [43-45].

Common preparation method of thermites by simply mixing the fuel and oxidizer powders in liquid can only lead to a packing density of ~10-20% for the final desiccated mixture, indicating that there is a large space gap between particles. In addition, it is difficult to obtain a homogeneous distribution of fuel and oxidizer nanoparticles by physical sonication. To overcome these limitations, various methods have been assessed. The first approach is to directly improve the physical powder mixing by high-energy ball milling [56]. This mechanical approach is able to not only homogenize the distribution of fuel and oxidizer, but also decrease the size of particles to the nanoscale. A more ideal route is to modify the particle surface either physically or chemically in order to improve the particle intimacy of fuel and oxidizer. Kim and Zachariah created a self-assembly structure of nano-Al/Fe_2O_3 composite, which is controlled by the electrostatic forces between charged aerosol particles [57]. Alternatively, the assembled composite can be prepared by surface modification of biological molecules. Rossi's group has recently reported an assembling way by modifying the surfaces of Al and CuO nanoparticles with complementary DNA strands [58]. The hybridization of these DNA chains caused the self-assembly of nanoparticles. A similar method was reported by Slocik et al who investigated the protein cages as biological surface modifiers [59]. The results show that the effective ferritin components inside the nano oxidizers loaded protein cages enabled the assembling of n-Al. The methods above are based on surface modification, which are relatively complex and difficult to scale up. Alternatively, it is more convenient and scalable to assemble nanoparticles by incorporation into polymer matrix via a physical route. This method is especially valuable from a scale-up manufacturing

point of view, since it is tunable in the viscosity and nanoparticle loading for castable propellant mixtures [60,61]. Different with the conventional particle filling approaches such as the doctor blade casting, the electro-hydrodynamically driven approach is more controllable in the dimension and packing density of the products. The basic mechanism is by electrifying a mixed suspension of nanoparticles and

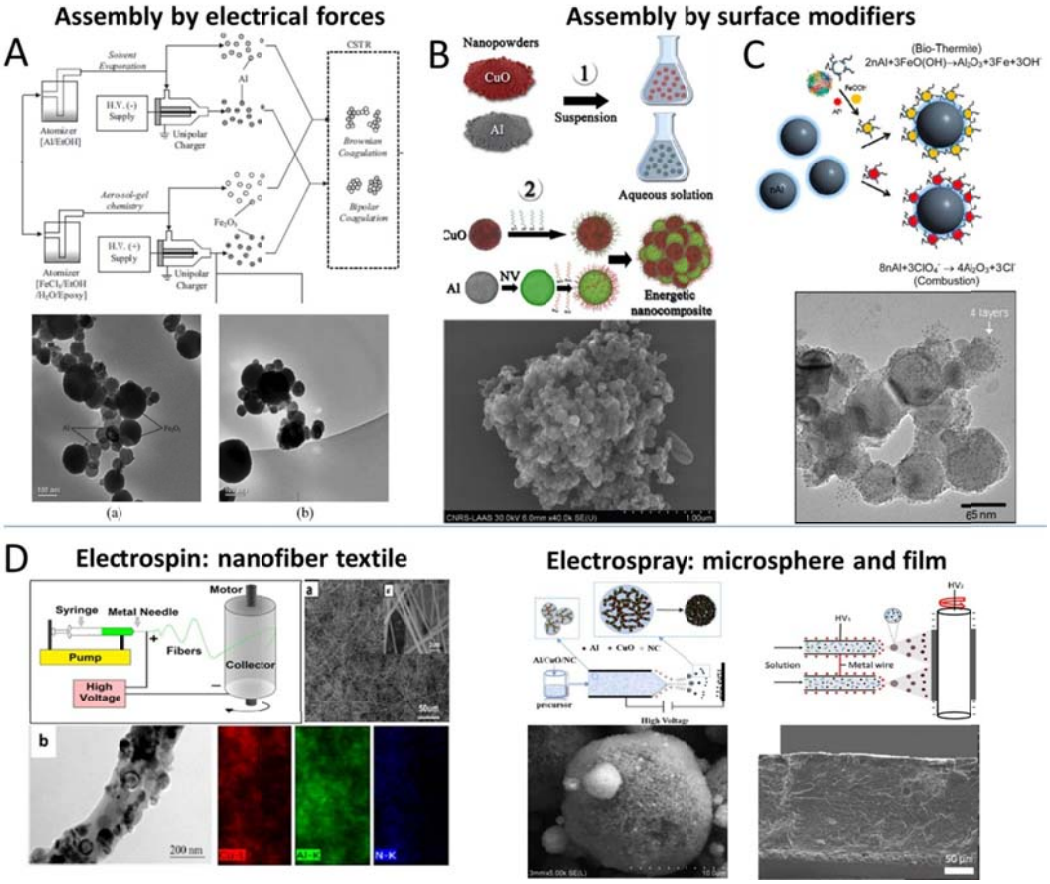

Figure 1.7. (A) Schematic of two paralleled, oppositely charged aerosol generation systems and the process of generating electrical force driven nanoparticle self-assembly [57]. TEM images show Al/Fe_2O_3 nanothermites by random assembly (a) and electrostatic assembly (b). (B) Schematic of the different steps for the DNA-directed assembly of the Al/CuO nanothermites. SEM image shows the DNA-directed Al/CuO nanothermite assembly [58]. (C) Schematic of the assembling process of Al nanoparticles with cationized ferritin loaded with either Fe_2O_3 or NH_4ClO_4 [59]. TEM image shows the n-Al coated by two-layer ferritin. (D) Schematics of eletrospin and electrospray procedures to make nanofiber textiles, Al/CuO nanothermite microspheres and films [63-68]. SEM images of these different structures are shown.

polymer binders inside a pressure driven tube, and injecting it in the form of thin microthread away from the charged meniscus of the tube exit (developed into a cone shape called Taylor cone) [62]. Prior to depositing on an oppositely charged substrate, the microthread remains (electrospin) or fragments into a spray of highly charged droplets (electrospray) depending on several variables such as the applied voltages, the distance between jet exit and substrate, as well as the concentration of nanoparticles. Yan et al [63] and Li et al [64] electrospun NC nanofibers of n-Al based thermite composites into textiles, which show enhanced burning rates. Wang et al electrosprayed NC gelled n-Al or mixed n-Al/CuO microspheres that offer the advantages of better mixing of nanoparticles and significantly improved combustion performance [65,66]. Alternatively, Huang et al [67] and Li et al [68] prepared nanothermites incorporated polymer films by electrospray deposition, which yield a high mass loading of nanothermites, and a strong mechanical flexibility. An additional advantage for the polymer matrix based strategy is its larger material incorporation capability, which is especially favorable for my concerns of involving biocidal functions to the nanothermites. We will discuss this point in the next section.

1.6. Biocidal energetic materials

Using energetic materials in the biocidal applications is notnew. In fact, ancient alchemists discovered that the power of gunpowder is not limited to its destructive effect [33]. Gunpowder was taken as a valuable medicinal herb in ancient China. The great medical work “Compendium of Materia Medica” reported that the components in gunpowder (probably sulfur) had a therapeutic effect for bacterial contamination,

skin infection, and plague [69]. However, the main function of energetic materials as an intensive heat source has seldom been recognized for the thermal sterilization purposes, probably due to its believed overwhelming effect in the field of common medical care, especially towards the human body. The development of energetic materials studies aiming at utilizing these materials as biocidal agents remain stagnant until the recent emergence of ever-increasing bioterrorism concerns. As previously mentioned bacterial spores are resilient to external stresses [1-3]. Facing the need for extreme sterilization methods opens up the potential of energetic materials. Lee et al reported a 10^7 CFU/cm^2 reduction in viable bacteria by combustion of a spray-coated mixture of nanoaluminum [70]. In order to improve the neutralization efficiency, other groups also fabricated dual-functional energetic formulations by incorporating biocidal elements such as iodine into the formulation. A proof-of-concept investigation was conducted by Mulamba et al by using hot iodine gas to interact with bacterial spores [71]. Their results concluded that the biocidal gas and heat (630 K) synergized the spore neutralization by 80% in tens of milliseconds, while thermal treatment alone required ~1300 K for the same inactivation. The first iodine-containing energetic formulation is M-I_2 (M is active metal) composites studied by Zhang et al using mechanical alloying [72-74]. They found that through this technique they could achieve metastable mixtures on the atomic scale, and adding more than 10 wt% iodine retained the high combustion enthalpy of Al. Upon ignition (eq 1.2), this M-I_2 composites increased the spore inactivation by 2 orders of magnitude more than non-halogenated thermites. The possible limitation of this design lies in its uncertain thermal stability (iodine physically bound) and not maximized exothermicity (due to

micro size of Al through milling). Another strategy is to find a thermite system that contains halogen elements in the oxidizer formulation. Examples are iodine pentoxide (I_2O_5) [75-80] and silver oxide (Ag_2O) [81,82] which once reacted with active metal fuels such as Al, can reach high temperature combustion meanwhile generating biocidal agents I_2 and Ag respectively (eqs 1.3 and 1.4). Comparably, Al/I_2O_5 possesses much higher heat of reaction (9.1 kJ/g) and flame temperature (8680 K w/o phase change) than Al/Ag_2O (1.0 kJ/g and 4941 K) and all the other Al/metal oxide nanothermites (Table 1.2). I_2O_5 also features a lower decomposition temperature (~660 K) than most of the metal oxides [83], thus correlating to a higher thermite reactivity (flame speed = 2000 m/s) [75]. The major demerit of I_2O_5 is that it is sensitive to humidity and can readily react with water in the ambient air. To decrease the adverse water aBsorption, Feng at al used a two temperature aerosol approach to coat the aerosolized I_2O_5 particles with a shell of less hygroscopic oxidizer such as Fe_2O_3 [79]. The results show that by controlling the thickness of Fe_2O_3 shell, the combustion performance was largely enhanced. Recently, a more complex oxidizer $AgIO_3$ was evaluated which contains both iodine and silver elements [84]. It was found that this compound outperformed normal metal oxides in gas release pressure due to its enhanced oxygen content. Unfortunately, the decomposed iodine tends to form compounds with Ag (eq. 1.5), thus decreasing the biocidal property of this oxidizer. Other similar formulations ($Mg(ClO_4)_2$, $NaClO_4$, KIO_4, etc) have also been tested, yet no major release of halogen gas was found though superior oxygen release and thermal output were reported [39-42,44]. In all, these chemically halogenated energetic materials are more stable than the M-I_2 composites while maintaining or

even enhancing their combustion behavior. However, they can load less wt% of halogens than the M-I_2 composites. The biocidal efficiency of these novel biocidal nanothermites has not been evaluated.

$$M \bullet I_2 = M + I_2 \tag{1.2}$$

$$10Al + 3I_2O_5 = 5Al_2O_3 + 3I_2 \tag{1.3}$$

$$2Al + 3Ag_2O = Al_2O_3 + 6Ag \tag{1.4}$$

$$2Al + AgIO_3 = Al_2O_3 + AgI \tag{1.5}$$

$$4Al + 3CaSO_4 = 2Al_2O_3 + 3Ca + 3SO_2 \tag{1.6}$$

Compared with halogens that are usually considered as biocides for spores, sulfur is widely used as a pesticide [85] and some sulfur-containing species such as sulfur dioxide (SO_2) [86] and sulfuryl fluoride (SO_2F_2) [87] have effective bactericidal and fungicidal properties. Sulfur-containing nanoparticles were able to kill 5 log bacterial spores after 30 mins of contact without heating, demonstrating sulfur's strong sporicidal capability [88]. Recent studies attempted to test the thermite performance of sulfate salts which have been employed as a pyrotechnic time delay composition [89]. Comet et al reported that metal sulfates (e.g. $CaSO_4$) containing nanothermites have outstandingly high heat of reaction (4-6 kJ/g) comparable with conventional metal oxide based nanothermites (Table 1.2), as well as high propagation speed (200-840 m/s) [90]. In addition, sulphur dioxide is liberated during the thermite reactions (eq. 1.6) [89], indicating that this type of thermite formulations poses the promise of the coupled thermal-biocidal gas synergistic sterilization effect. The sporicidal capability of sulfur has not been compared to traditional biocides such as Ag and I_2

despite the large natural abundance of sulphur [91]. Therefore, incorporating sulfur into nanothermite formulations, demonstrates potential for an effective biocidal energetic material.

1.7. Thermite reaction mechanism

We have indicated in the preceding sections that the reactivity of thermites can be tremendously enhanced by decreasing the length scales of both fuel and oxidizer constituents, as well as by improving their intimacy of contact. This is based on the idea that the reaction is controlled by the interfacial reaction between condensed phase fuel and oxygen ions, and decreasing the particle dimensions and shortening the distance between fuel and oxidizer yield the increased surface area and the decreased diffusion length, respectively. These changes will then lead to the increased reaction rate. The same tendency is effective for the initial stage of the thermite reaction process which is usually taken as ignition. It has been experimentally confirmed that as the particle size decreased, the ignition temperature and minimum ignition energy of thermites decreased [92-94]. Compared with the overall combustion, the initial ignition features a much slower reaction rate yet a faster transient nature, as well as a higher sensitivity to external stimuli, such as pressure, heat, friction, etc [94,95]. These features make it more difficult to study and manipulate than the overall combustion. In addition, ignition is further complicated for nanoscale aluminium by the thin (~2-5 nm) native oxide shell, alumina (Al_2O_3), that acts as a passivation layer at low temperatures [96,97].In order for ignition to occur, the predominant ignition mechanism indicates that a threshold must be

surpassed where the mutual transfer of Al and O across the Al_2O_3 shell is rapid enough to induce a sufficiently higher energy release rate relative to energy loss to the surroundings. It is expected that oxygen anions and aluminum cations migrate radially inward and outward respectively by the concentration gradients (Fig. 1.8A) [98]. In addition, the outward transport of Al cations is primarily driven by a built-in electrical field across the alumina shell, as described by the Cabrera-Mott theory [99,100], as well as by the pressure-driven outward convection due to the volumetric expansion of Al core during heating [101,102]. Given these two additional mechanisms, and that the Al cations are smaller than the oxygen anions [98], the Al flux outwards should exceed that of oxygen inwards. This diffusion bias is prevailingly evidenced by several reports showing that hollow structures are formed during the oxidation of n-Al particles [103-105]. Therefore, the reaction interface is expected to be at the outer surface of the aluminum enriched alumina shell [98,103].

In light of the origination of oxygen that involves in the ignition event, the mass diffusion based ignition mechanism above (Fig. 1.8A) can be further divided into two categories: the interfacial condensed phase, and the heterogeneous gas-condensed phase. The condensed phase ignition mechanism has been evidenced for many Al/metal oxide formulations (e.g., Al/Bi_2O_3 [106]). In these thermites, O_2 is released from oxidizers at a higher temperature than the corresponding ignition temperature, indicating that ignition is mainly triggered by the condensed phase reaction between Al and bound oxygen. In some other cases (e.g. Al/CuO [107]), oxygen release is prior too, or synchronized with ignition, suggesting that the predominant reactive oxygen that participates in the initiation reaction could be gaseous O_2. Due to the

reactive sintering of fuel and oxidizer at the initiation stage for many thermite formulations as observed from post-reaction products analysis [108,109] and in situ fast-heating electron microscopy [108,110,111], the two aforementioned ignition mechanisms may be actually coincident in a single ignition event.

There exists another important ignition mechanism that is independent on the mass diffusion across the alumina shell. This so-called melt dispersion mechanism (MDM) [102,112,113] was proposed and later experimentally justified typically for nano-Al reactions under high flame speeds and high heating rate (>10^6 K/s) conditions. In detail, the melting of Al commences before the oxide shell fracture. The volumetric increase by 6% within the alumina shell due to melting induced heightened pressures (1-2 GPa) in the Al core that further causes dynamic spallation of the shell (Fig. 1.8B). The exposed molten Al driven by the high pressure gradient evolves to small Al droplets dispersed in all directions at high velocity. Therefore, the ignition process is not limited by mass diffusion, which is distinct with the traditional mechanism for microscale particles and for nanoscale particles at slow heating rates (Fig. 1.8B).

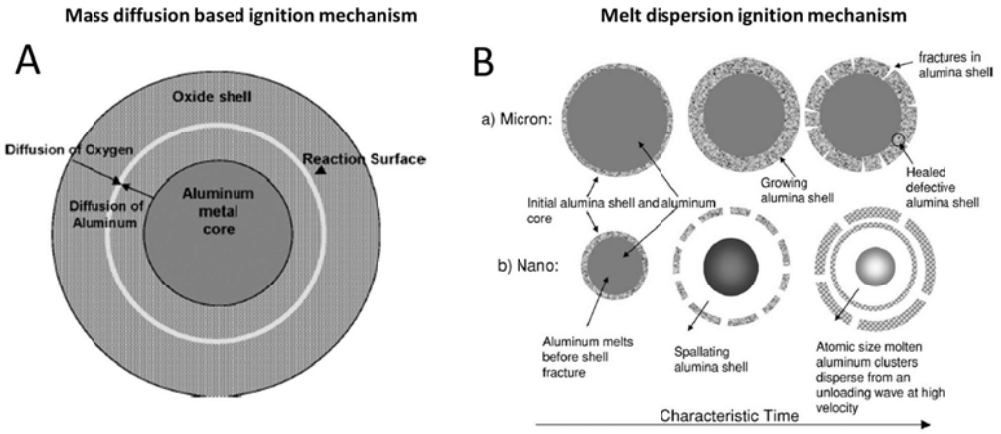

Figure 1.8. Schematics for the mass diffusion based ignition mechanism (A) [104] and the melt dispersion ignition mechanism (B) [112].

1.8. Research plan

The emergence of biocidal energetic materials opens an unprecedented broad window for the research of spore neutralization, which offers the promise of bridging the latest knowledge on spore's resistance mechanism, and the state-of-the-art techniques in materials synthesis and characterization.

In this dissertation, I attempted to probe the spore neutralization mechanisms in ultrafast heating processes and by tuning energetic biocides. Given that the surface-based heating modality is more accurate in the temperature control, I first studied the optimal deposition approach for bacterial spores. I then utilized a pulsed heating apporach to define the time-temperature-kill relationship for bacterial spores, and compared the killing efficiency with the conventional thermal and chemical approaches. The synergistic rapid heat-biocidal gas effect on the spore neutralization was evaluated in order to further explore a more efficient sterilization approach. By using the accumulated time-temperature-kill knowledge from the above studies, I continued to explore new biocidal energetic nanocomposite formulations. Finally, the reaction mechanisms of different energetic formulations were systematically studied aiming to better manipulate these novel biocidal energetic formulations for spore inactivation in the future.

Chapter 2: Quantitative Attachment and Detachment of Bacterial Spores from Fine Wires through Continuous and Pulsed DC Electrophoretic Deposition*

Overview

To achieve a platform for the later neutralization studies of bacterial spores, the surface heating method for immobilized spores was assessed instead of the aerosol borne spore heating method. I demonstrate the uniform attachment of bacterial spores electrophoretically onto fine wires in liquids and subsequently quantitatively detached back into suspension. It was found that the use of a pulsed voltage method resulted in a uniform coverage of spores and prevented visible bubble formation resulting from water electrolysis which tended to dislodge the spores from the wires. By monitoring the electrophoretically derived current, this method could also be used to quantitatively measure the surface charges on spores and the deposition rate. The method is generic and should be applicable to the deposition of any charged biological material (e.g. spores, bacteria, viruses) onto metal surfaces.

2.1. Introduction

Concerns on bioterrorism [1,2] have prompted efforts to discover, quantify and compare neutralization methods such as heat [3,4], chemical [5] and other synergistic effects [6-8]. The extreme stress-resistance of bacterial spores [9] has provided the

* The results presented in this chapter have been published in the following journal article: **W. Zhou**, S. K. Watt, D-H. Tsai, V. T. Lee*, M. R. Zachariah*. Quantitative Attachment and Detachment of Bacterial Spores from Fine Wires through Continuous and Pulsed DC Electrophoretic Deposition. ***J. Phys. Chem. B***, 2013, 117, 1738-1745.

impetus to develop quantitative studies to more precisely define various neutralization mechanisms. Previous studies in defining spore neutralization have focused on heating under 100˚C in the absence of pressure or the combination of heat and pressure with inactivation timescale in the order of minutes [10,11]. In particular, a temperature-time relationship for spore inactivation for high temperatures (100 – 1000˚C) and short times (10 ms – 10 s) is still not available. The first approach to address this problem is to initiate thermal reactions in sealed chambers in which the temperature between 200˚C and 700˚C is monitored and correlated with the number of recovered viable spores [4,12,13]. These experiments are limited by the ability to precisely manipulate the temperature and exposure time. Another approach recently employed has been to disperse spores in the aerosol phase and subject them to high temperatures between ~150˚C and >1000˚C and chemical environments [3,14]. However, there exists a temperature distribution in the aerosol flow in these studies, which causes decrease in the precision of the temperature-viability relationship. A third approach is to immobilize spores on a surface that can be thermally varied in a precise manner. This approach can cover a larger temperature range in short time scales and allows convenient enumeration of viable spores immediately after thermal exposure [15].

The latter method is only useful if a well-defined spore population can be coated on the surface. Typically this might be accomplished in a liquid suspension either naturally [16-18] or by laboratory manipulation [19,20]. Bacteria naturally have various adhesins to promote attachment to plastic, glass and metal surfaces to form biofilms [16-18]. In the laboratory, poly-L-lysine can be coated to impart a net

positive charge on the surface to promote electrostatic interaction with the negatively charged exterior of most bacteria. However, neither mechanism can be utilized for the studies of spores as spores are biological inert and often fail to attach to poly-L-lysine coated surfaces [21]. We sought to develop an alternative approach to attach spores onto wires using physical forces.

Previously, dielectrophoresis has been utilized in the manipulation of bacterial spores [22]. In the presence of an electric field gradient, a net force is imparted on the spore due to polarization, the magnitude of which is highly dependent on the material properties of the spore (including size) [23], the characteristics of the fluid (including ionic strength and dielectric permittivity of the solvent and solute) [24] and the field gradient [25-28]. Dielectrophoresis is contrasted with electrophoresis which can take place if the cell has a net charge, and is directly proportional to the magnitude of the field [29,30]. Most reported studies however modeled spore transport in liquids as being net neutral in charge, and only considered the dielectrophoretic effect [31-33]. Actually, in aqueous dispersions the glycoproteins and polysaccharides that comprise the exosporium (i.e. outer layer) are negatively charged. These negative charges arise from deprotonation of aldehydes (-RCOH), phosphodiester (-$(RO)_2POOH$) and carboxylic acids (-RCOOH), which have been detected by the infrared spectroscopy [34] and zeta potential analysis [35].

Electrophoretic deposition (EPD) has been used in the past for a wide variety of bio-particles including bacteria [36,37], protein inclusion bodies [38] and yeast cells [39]. While the generic process of EPD of bio-particles is similar, the exact rates of attachment to the wire may be complicated by side effects including bubble formation

[40,41], surface chemistry [42,43], electrode curvature effects [44] and excretion of adhesive extracellular media [45,46]. Bubble formation appears to be a significant problem for controlled and effective EPD. Two approaches have been reported to minimize this effect. AC-EPD has been found as a powerful method to mitigate the water electrolysis under some frequency conditions [47,48]. Pulsed DC-EPD has also been shown to obtain dense bubble-free deposits at suitable pulse widths and duty cycles [49,50]. From a practical standpoint, pulsed DC-EPD is a simpler approach that is easier to implement.

Besides the electrostatic interaction forces and the bubble formation effects on attachment, other forces may also contribute to the attachment of spores to surfaces. The Lifshitz-van der Waals force between the spore surface and the electrode surface can be described by the well known Derjaguin-Landau-Verwey-Overbeek (DLVO) theory [51]. The image force which arises due to induced dipole effect between the charged spore and the surface can also influence deposition and has been detected by the atomic force microscopy [52]. While the Lifshitz-van der Waals force, the image force and the electrostatic force all have an inverse square distance relationship, for the problem under consideration here it has been shown that the dominant effect can be attributed to the electrostatic force [53].

In this study, I will investigate electrophoretic attachment of uniform layers of spores to fine wires, and demonstrate reversible detachment. We demonstrate that by applying a pulsed direct current (DC), I can quantify incremental spore attachment with time by measuring the electrical current to the wire electrode. The advantages of this charging mode will be shown over the continuous charging mode. By using the

measured current which can be directly related to the spore flux to the surface, I am further able to validate a transport model and use the model to directly determine the average spore surface charge and spore deposition efficiency. This methodology developed here is to my knowledge the first demonstration of direct quantitative attachment and detachment of spores from fine wires.

2.2. Experimental approach to spore attachment and detachment

2.2.1. Spore deposition cell

The spore deposition cell is shown schematically in Fig. 2.1. It is composed of four compartments: an outer PTFE tubular shell with sealed base, a stainless steel cylinder as the outer electrode, a central wire as the deposition surface and inner electrode, and two PTFE plates to center the wire. The stainless steel outer electrode has an inner diameter of 16 mm and a height of 20 mm. For the wire central deposition electrode I use 76.2 μm platinum (Pt) (Omega Engineering, Inc.), since it is very stable in aqueous systems and will not be oxidized. The spore strain adopted in these studies is *Bacillus subtilis* (*Bs*) spores ATCC#6051 (see the optical microscopic image in Fig. 2.2), which were sporulated by growth in Difco Sporulation Medium (DSM) at 30˚C for 48 h. A 250 ml DSM was prepared which included 2 g Bacto nutrient broth, 2.5 ml 10% KCl, 0.375 ml 1M NaOH and 2.5 ml 1.2% $MgSO_4 \cdot 7H_2O$. The initial spore number concentration was regulated to be 8×10^9 CFU/mL.

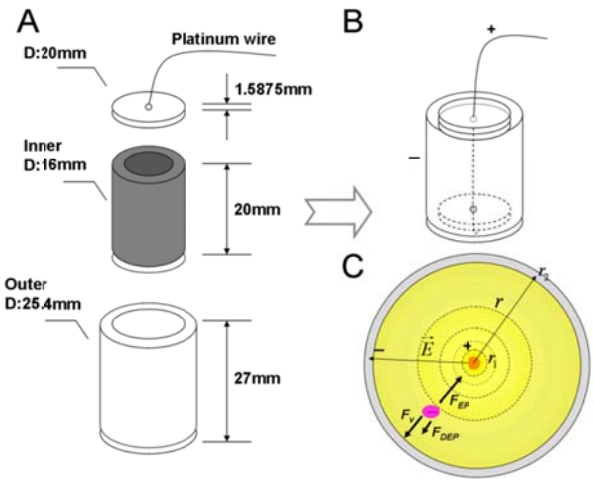

Figure 2.1. (A) Components of the spore deposition cell which includes an outer protection cylindrical shell, an inner stainless steel tube, two PTFE center-pierced plates and the central wire. (B) Assembled cell in spore coating process, with the wire as the anode and the stainless steel tube as the cathode. Part C shows the electric field distribution between two electrodes and the forces that the negatively charged spores experience in the liquid phase.

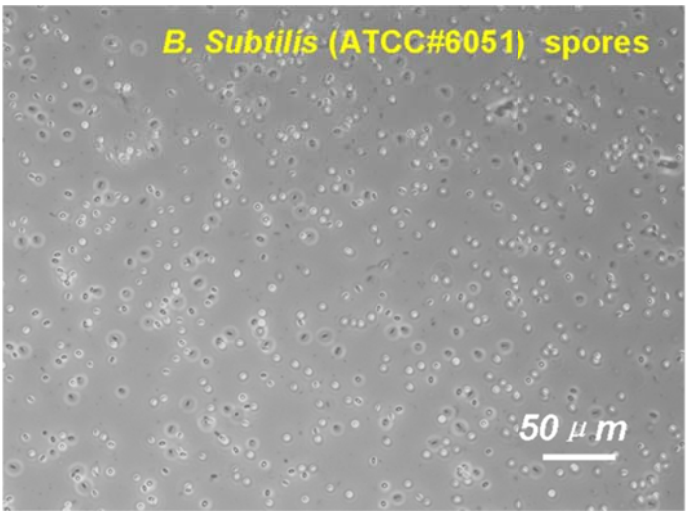

Figure 2.2. Optical microscopic image of *Bs* spores ATCC#6051.

The power supply and current detection were performed with a 6430 sub-femtoamp remote sourcemeter from Keithley. Ultrasonication employed a Branson Model 5510 ultrasonic cleaner. Optical microscopic images were taken by Zeiss AxioObserver microscrope using a 40X objective with phase contrast illumination.

Scanning electronic microscopic (SEM) images were taken of spores on wires fixed with 2% glutaldehyde, dehydrated through a series of alcohol and sputter coated with gold/palladium alloy. Images were captured with a Hitachi S4700 FESEM in the Laboratory of Biological Ultrastructure at the University of Maryland. To validate my spore charging measurement approach I employed a zeta-potential analyses from Zetasizer Nano ZS (Malvern Instruments, UK) equipped with a 633 nm laser and a palladium dip cell module. 500 μL of sample suspension was mixed with 250 μL, 10 mM ammonium acetate aqueous solution prior to the measurement.

2.2.2. Spore attachment in continuous and pulsed DC charging modes

The fine wire was stabilized inside the spore deposition cell vertically, and the spore suspension was added into the cell to immerse the wire up to a depth of 1 cm. The central wire was connected with the positive pole of the power supply, and the outer stainless steel cylinder was connected to the negative pole. A variety of EPD measurements were performed with varying voltages and on-times, and real-time current data were stored. Comparably, fine wires with different compositions and diameters were tested to find an optimal one. In the pulsed DC charging mode, a series of pulsed on-times and off-times were controlled to differentiate from the continuous charging mode, and optimal pulsed charging condition for *Bs* spores ATCC#6051 was found.

2.2.3. Optical microscopic and SEM analyses

Wires coated with spores were observed under the optical microscopy over glass slides and also by naked eye. For the SEM analyses, samples were firstly fixed in 2% glutaraldehyde in buffer for 1 h at room temperature. Excess glutaraldehyde was removed in buffer by three washes of 10 min each. The samples were post fixed with 1-2% osmium tetroxide in the above buffer for at least 30 min, and then with double distilled water. After a series of dehydration processes in ethanol, the samples were treated with critical point drying with liquid carbon dioxide. Finally, samples were mounted to stuBs and coated with gold/palladium alloy.

2.2.4. Spore detachment

A very important aspect of this work was to develop the methodology to detach spores from the wire. To accomplish this, the wire loaded with spores was placed in a clean cell with distilled water and the wire oppositely biased to be the cathode. Simultaneously, the cell was immersed into an ultrasonic bath. The separate effects of opposite biasing and ultrasonication were compared. The detached spores were harvested for spore plate counting as will be shown later. The treated wire was inspected by optical microscopic and SEM analyses to find if all the attached spores were removed from the surface.

2.2.5. Spore plate counting assay

Spores detached from wires were counted by enumerating colony forming units (CFU) by plating serial dilutions on LB agar plates. Counting was repeated for four times and an averaged value was reported.

2.3. Spore transport model

The use of the cylindrical deposition cell geometry enabled quantitative modeling since the electric field is well described as:

$$\left|\vec{E}\right| = \frac{\Delta U}{r \ln \frac{r_2}{r_1}} \tag{2.1}$$

where ΔU is the voltage difference between two electrodes, r is the radical distance from the center, r_1 and r_2 are the diameters of the inner (wire) and outer cylindrical electrodes. In my design, r_1 = 0.0381 mm and r_2 = 8 mm (Fig. 2.1). It is well known that spores when introduced into an aqueous media will acquire a net charge [34,35] and thus can be manipulated with an electric field. The electrophoretic force (F_{EP}) on a spore with q charges in an applied electric field is:

$$F_{EP} = qE \tag{2.2}$$

The presence of the field will also induce polarization within the spore, which if the field is spatially invariant will impart no net force on the spore. However in the presence of an electric field gradient the spore will also experience a net dielectrophoretic force (F_{DEP}) [22]:

$$F_{DEP} = 2\pi\varepsilon_m R^3 \,\mathrm{Re}(f)\nabla E^2 \tag{2.3}$$

where ε_m is the permittivity of the surrounding water (7.1×10^{-10} F/m) at room temperature, R is the radius of the spore, *Re(f)* is the real part of the Clausius-Mossotti factor. In a DC field, this factor is directly related to the conductance of both the spore surface and the media [22]:

$$\mathrm{Re}(f) = \frac{\sigma_p - \sigma_m}{\sigma_p + 2\sigma_m} \tag{2.4}$$

Herein, σ_p and σ_m stand for the conductivities of spores and media, respectively. At room temperature, σ_p is 10^{-7} S/m (as the cell membrane [54]) and σ_m is 5.5×10^{-6} S/m. Hence *Re(f)* is a negative value which implies that the direction of F_{DEP} is opposite to the direction of F_{EP}, as in Fig. 2.1C. Meanwhile, the retarding force (F_v) is caused by the viscous drag and can be evaluated with Stoke's law:

$$F_v = -6\eta\pi R u \tag{2.5}$$

where η is the viscosity of water (1.002×10^{-3} Pa·s) at room temperature and u is the velocity of spores. It should be noted that the *Bs* spores are not strictly spherical, thus R in both eqs 2.3 and 2.5 is an effective radius (a spherical spore with this effective radius is defined to have the same volume as a real spore). From previous reports of spore volumes [55], the effective R value for *Bs* spores is 0.336 μm. The spore motion can then be directly evaluated in a force balance:

$$\Delta F = m_s \frac{d^2 r}{dt^2} = F_{DEP} + F_{EP} + F_v \tag{2.6}$$

Since the inertia term is relatively small (i.e. the spore response time to any voltage perturbation is fast relative to the transit time), I can assume steady state ($\Delta F = 0$). The resulting governing equation becomes:

$$\frac{dr}{dt} = \frac{A}{r} + \frac{B}{r^3} \tag{2.7}$$

where $A = \Delta U \cdot q/(0.101R)$, $B = 8.26\times10^{-9}(\Delta U)^2R^2$.

The above eq. 2.7 describes the spore velocity at any radial location in the cell between two cylindrical electrodes and so that can be directly related to the experimental current data since it is the motion of spores that contributes to the current formation. The time for spores with an initial distance $r + \Delta r$ away from the center to move a differential distance of Δr is from eq 2.7:

$$\Delta t = \frac{r^2 - (r+\Delta r)^2}{2A} + \frac{B}{2A^2}\ln\frac{A^2(r+\Delta r)^2 + AB}{A^2r^2 + AB} \tag{2.8}$$

In this time interval, the total charge quantity passing through this differential distance Δr is:

$$\Delta Q = q'C\Delta V = q'C\pi l[(r+\Delta r)^2 - r^2] \tag{2.9}$$

where C is the spore number concentration in the cell, l is the immersed depth of Pt wire inside the liquid (0.01m), and V is the differential volume element around the wire. It should be noted that the charge q' is the effective overall charge after being shielded by counter ions in the vicinity of the spore surface (i.e. the diffuse double layer). The importance of this is that the mobility of a spore is influenced by the thickness of the double layer that is dragged along with the spore. The current can be expressed as:

$$I = \lim_{\Delta t\to 0}\left|\frac{\Delta Q}{\Delta t}\right| = \frac{2q'\pi Cl(Ar^2 + B)}{r^2} \tag{2.10}$$

Then, substituting for A and B above, the initial current (I_o) observed can be expressed as:

$$I_o = \frac{0.622C\Delta U}{R} q'q + 3.58\times10^{-7} C\Delta U^2 R^2 q' \quad (2.11)$$

Eq 2.11 is a simplified illustration of the current corresponding to the spore deposition rate, but which does not include possible effects due to particle-particle and particle-electrode interactions. Near the electrode, the spore transport may be complicated by electrohydrodynamic flows as well as electroosmotic flows due to the electric forces on charges from the electrode polarization layer and the equilibrium diffuse double layer near the spore [56,57]. However, since eq 2.11 describes the initial current when t = 0, the influence of those flows can be neglected. In the remainder of this chapter, I analyze my experimental results in the context of the model resulting in eq 2.11.

2.4. Results and discussion

2.4.1. Spore attachment in the continuous DC mode

To exemplify the spore attachment in the continuous DC mode, a biased voltage of 20 V and a spore number concentration of 8×10^9 CFU/mL were adopted. The EPD condition employed were chosen on the basis of prior work that showed that bacterial spores can withstand DC electric fields as high as 1500 V/cm and still maintain viability [31]. Before I proceeded with direct measurement of the current in evaluating spore deposition, I evaluated the temporal variation of current for pure water and the spore suspension in Fig. 2.3. We found that steady state could be achieved on the order of 100 sec, and that the measured current due to charge migration in the spore containing suspension was about an order of magnitude larger

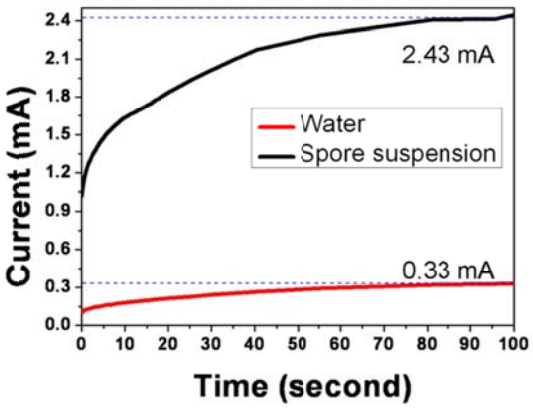

Figure 2.3. Current changes of spore suspension and pure water with time in the continuous DC-EPD mode at 20 V. Spore number concentration = 8×10^9 CFU/ml. The high plateau values are 2.43 mA and 0.33 mA, respectively.

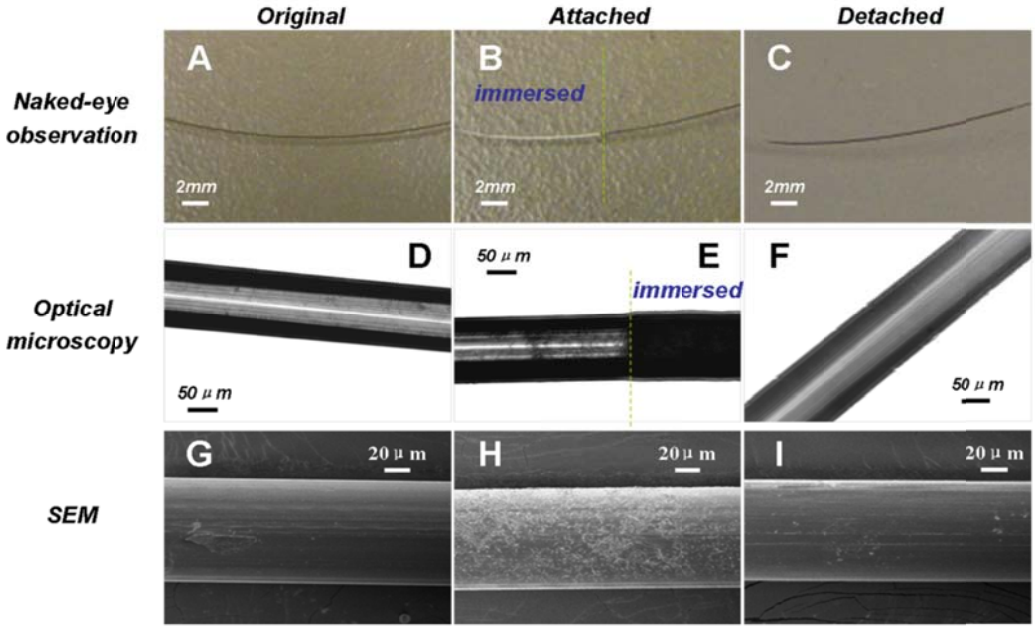

Figure 2.4. Parts A-C show Pt wires before coating, after coating and after detaching. Parts D-F show optical microscopic images of Pt wires before coating, after coating and after detaching. In both parts B and E, the immersed parts of the wire inside the spore suspension were marked. Parts G-I show SEM images of Pt wires before coating, after coating and after detaching. The charging condition for spore attachment is 20 s at 20 V. The spore detaching condition is 10-15 min at reversed 60 V, combined with the ultrasonication.

than that contributed to by pure water. This allows me to ignore the influence of the solvent in subsequent current measurements during EPD. Images of spore attachment are shown in Fig. 2.4 for a deposition time of 20 s. The visual images (Figs. 2.4A and 2.4B) show that after DC biasing, an obvious white spore coating appeared in the immersed portion of the wire. Further optical microscopic images (Figs. 2.4D and 2.4E) reflect the spore deposition in that region (the dark region represented the coverage of spores). SEM images (Figs. 2.4G and 2.4H) show an evenly distributed and dense coating on the wire and more directly demonstrated the attachment of spores. The enlarged SEM images in Figs. 2.5A and 2.5B also exhibit the structures of attached *Bs* spores on surfaces.

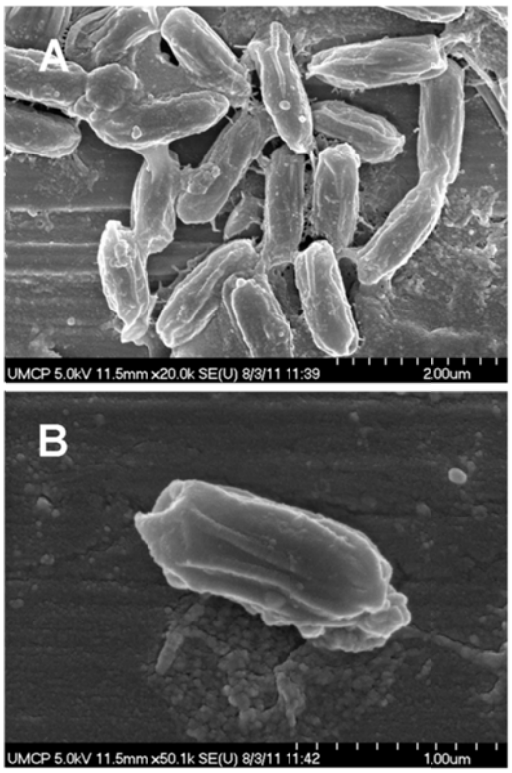

Figure 2.5. SEM images of *Bs* spores ATCC#6051 attached on Pt wires.

Nominally we should expect that increasing the charging time would cause increases in spore deposition to the surface. However such a relationship was not linear especially after a relatively long time, and when a higher voltage was applied (Fig. 2.6). In those cases, the current-time curves show fluctuations which could be correlated to the generation of visible gas bubbles formed from water electrolysis [58] (Fig. 2.7C). As a result, spore deposits became highly uneven along the wire surface, and subsequently were detached from the wire at high voltages, or long charging times (Figs. 2.7A and 2.7B). This prompted me to evaluate a pulsed deposition mode that will be described later.

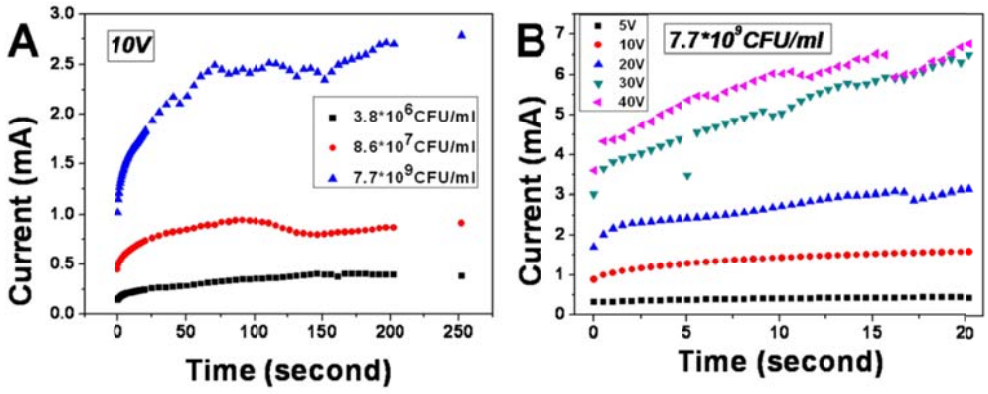

Figure 2.6. (A) Current-time relationships for spore suspensions with different concentrations. The voltage difference was 10 V. (B) Current-time relationships at different voltage differences in a short time range. The concentration of the *Bs* spore suspension was 8×10^9 CFU/ml. The immersed length of wire into the liquid was 1 cm.

2.4.2. Spore detachment

To properly evaluate my eventual exposure studies (heat, chemicals), an efficient and quantitative method to detach the spores is necessary so that standard assays can be employed. We found that either reversed biasing the wire at -60 V for 5 min or ultrasonicating for 30min allowed partial detachment of spores from the wire (Fig.

2.8). While some reports indicate that ultrasonication is known to harm spores [59,60] and repeated electric pulse cycling can also induce spore inactivation [61,62], I operated at much shorter ultrasonication time and bias voltage which are ~ 100x less than those studies. Similarly pH changes which occur during deposition (Fig. 2.9A) were evaluated for viability by exposing spores to a range of pH (5-10) (Fig. 2.9B) and were found to have no effect. We found that the combination of reverse bias and ultrsonication would detach the spores completely.

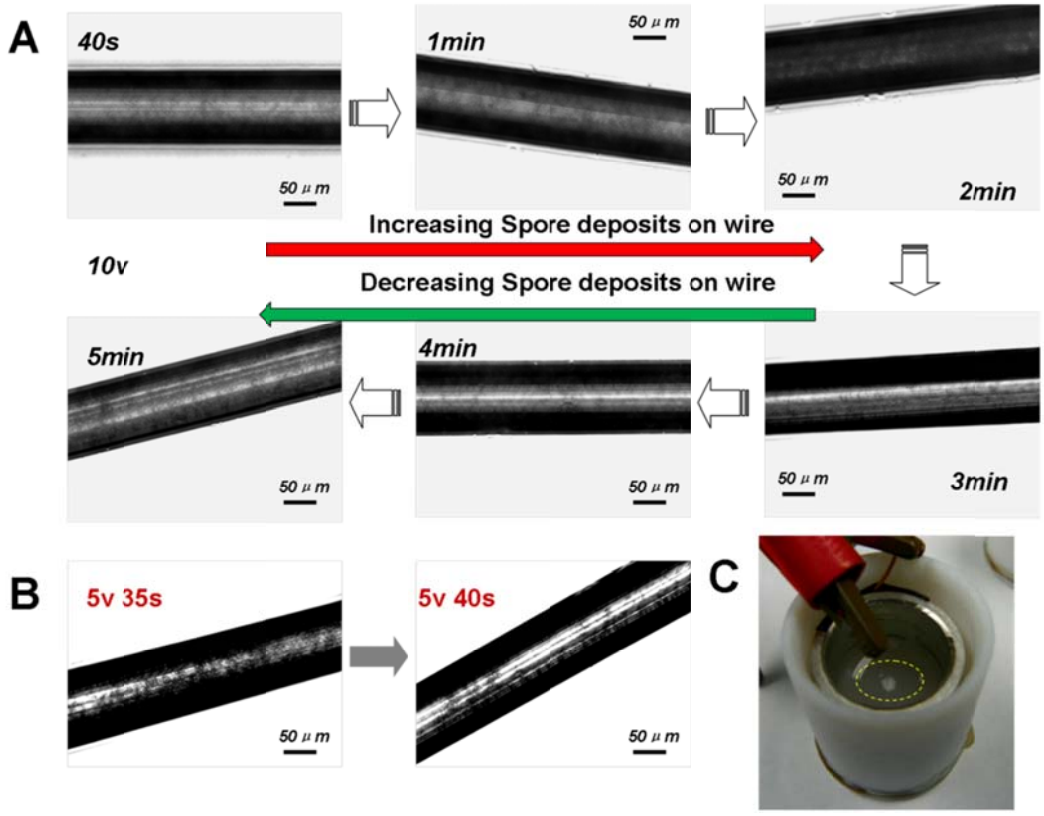

Figure 2.7. (A) Time-series of optical microscopic images of spores coated wires from 40 s to 5 min are shown. The DC charging potential difference is 10 V. Spore deposits reached the maximum at 2 min and then suddenly dropped after 3 min. (B) Optical images are shown when the charging times are 35 s and 40 s respectively, at 5 V. An obvious decrease of spore deposits on wire can be seen within 5 s. (C) Picture of spore deposition cell with bubbles forming near the central Pt wire in the dotted circle.

The photographic, optical microscopic and SEM images shown in Figs. 2.4C, 2.4F and 2.4I respectively demonstrate that all the *Bs* spores were removed from the surface after reversed biasing for 10-15 min at -60 V in an ultrasonic bath. Once the spores on the surface were removed into liquid, they could be enumerated by the plate counting method to determine the number of spores deposited on the wire. It should be noted that the reverse-bias charging time and voltage here are larger than those for spore attachment, which presumably accounts for the force required to overcome the binding energy between the spore and wire surface. Together these results indicate that the combination of reversed biasing and ultrasonication is an effective means to completely remove spores deposited on the surface.

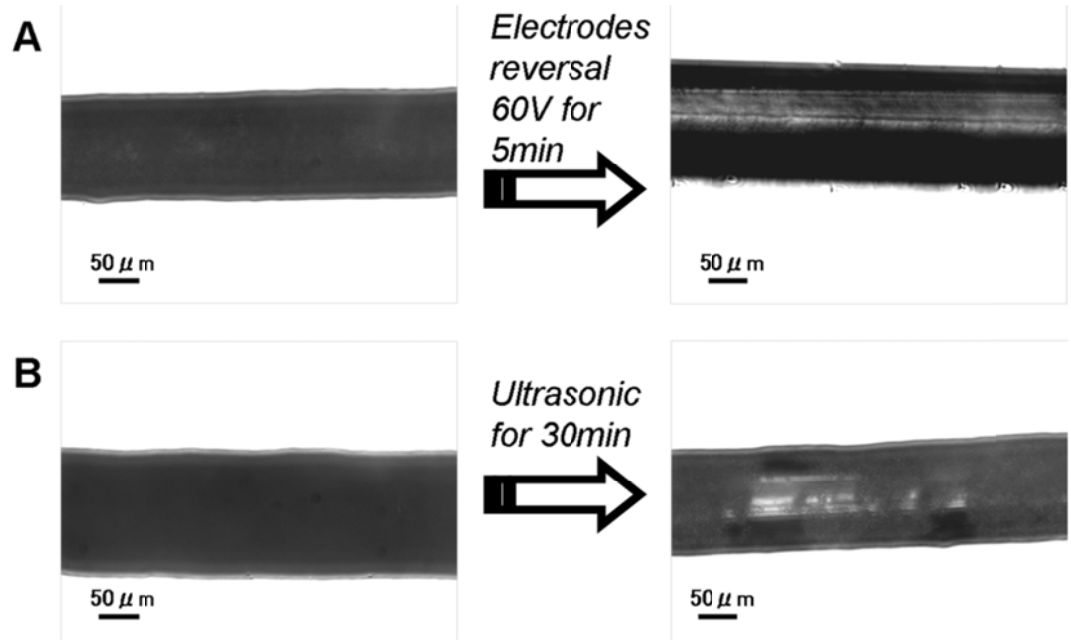

Figure 2.8. (A) Optical micrographs show the reversal charging effect towards the spore detachment efficiency. The reversal charging lasted for 5 min at -60 V. (B) Optical micrographs show the effect of ultrasonication on the spore detachment efficiency. The ultrasonication lasted for 30min. In both cases, the *Bs* spore coating was achieved by continuous DC biasing for 20 s at 20 V.

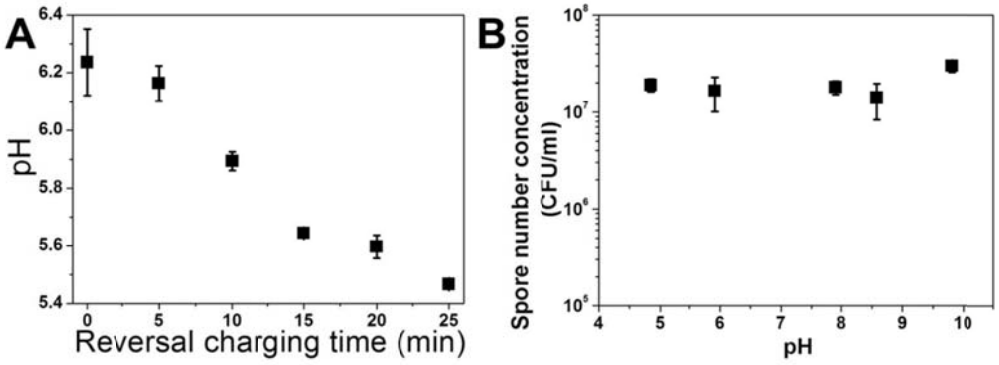

Figure 2.9. (A) pH change of the liquid with time during reverse bias accompanied by ultrasonication. Data were measured for three times, which are reflected by the error bars. (B) Spore viabilities in different suspensions with the pH range of 4.85 to 9.81. The initial number concentration of spores was 3.2×10^7 CFU/mL. The viability was reflected in the spore plate counting test by the number of spores that could germinate in the culture medium. The spores were kept in different pH suspensions overnight before the spore plate counting.

2.4.3. Spore attachment in the pulsed DC mode

The fluctuation in the deposition current observed (Fig. 2.6) coincided with visible bubble formation (Fig. 2.7C). To mitigate this effect I shifted my efforts to a pulsed DC mode, based on results of Besra et al [50] who showed that using a pulsed voltage strategy, an extension of an application used to deposit metal films, could lead to a minimization of bubble formation, and conformal deposits of small particles. We have adopted this strategy in order to generate a uniform and densely packed spore coating, by applying multiple electric pulses instead of a continuous DC bias. We have found that this leads to reproducible spore deposits by enabling consistent current measurements. In Fig. 2.10, the measured temporal currents during deposition of *Bs* spores (ATCC#6051) at a voltage of 5 V are shown, with an on-time of 30 s followed by an off-time of 30 s. Over eight cycles of this experiment, the measured current was consistent between cycles, which implies that the ionic strength of the

liquid was stable. The SEM images (Fig. 2.11) reflect the increase of *Bs* spore attachment on the surface with the pulse number. After charging for 2 pulses, only partial coverage was achieved, however these deposits were uniform. A monolayer of *Bs* spores could be formed after 4 pulses, and multiple layers of spores were found after 7 pulses. Optical microscopic images (Fig. 2.12) also show that the *Bs* spore deposits increased as the pulses accumulated. After enumerating all the spores detached from the surface, a linear relationship between the spore deposits and applied pulse number was found (Fig. 2.13A).

To estimate the packing density of spores on wire, I assume the spores formed a hexagonal packing pattern (Fig. 2.14A) which is also seen from my optical microscopic images (Fig. 2.14B). The volume for *Bs* spores (ATCC#6051) was documented as 0.16 μm^3 [55]. As a result, the 'effective' radii of these spores on the

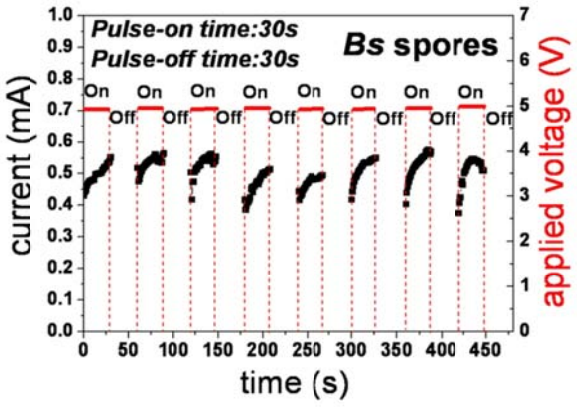

Figure 2.10. Current-time relationship in the pulsed DC charging mode for *Bs* spores (ATCC#6051). Both the charging time and the pulse-off time were 30 s, and the applied on-time voltage was 5 V. In my design, *Bs* spores were deposited to the surface for up to eight cycles.

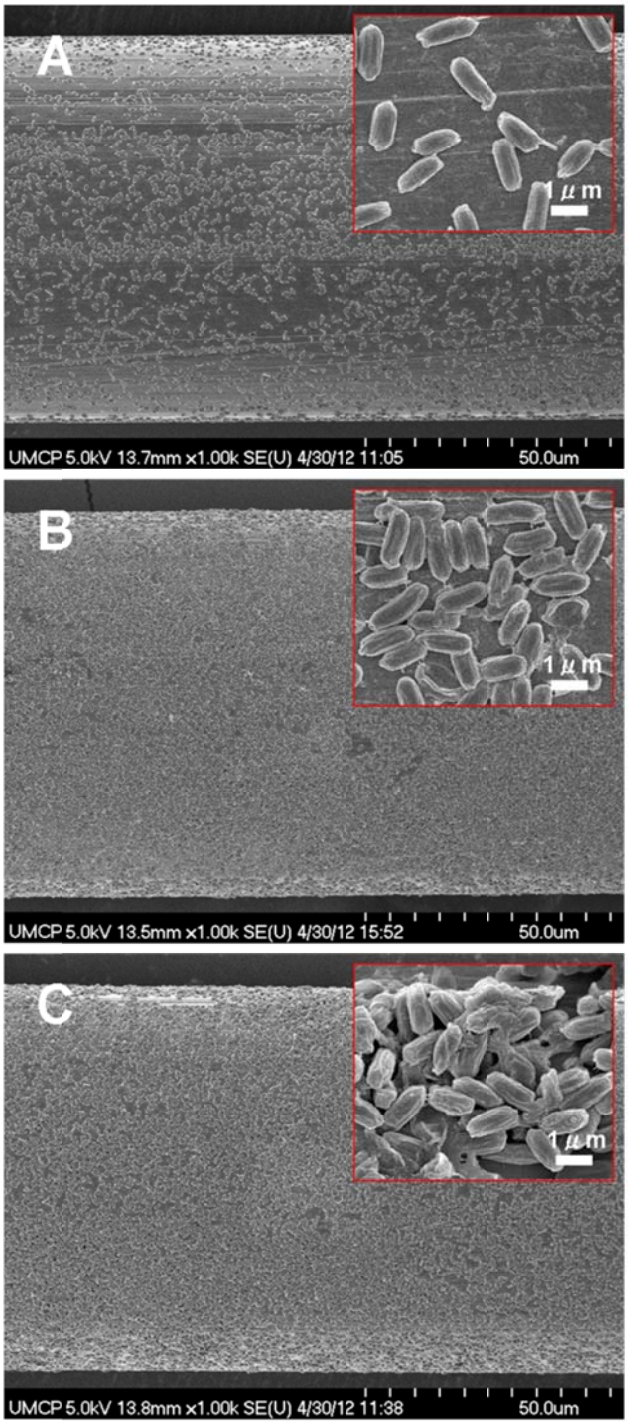

Figure 2.11. SEM images of *Bs* spore coating (ATCC#6051) on Pt wires after different biased DC pulses. A, B and C show the cases after 2, 4 and 7 pulses, respectively. Each DC pulse is set to last 30 s and stop for another 30 s before the next pulse. The enlarged SEM images are inserted which exhibit the different spore deposition densities on the surfaces.

surface are 3.36×10^{-7} m, and the area of the unit cell ($\sqrt{3}R^2$) (Fig. 2.14A) is 1.96×10^{-13} m^2. Since the total surface area, $2\pi r_1 l = 7.62\times10^{-7}$ m^2 (r_1 is the radius of Pt (=0.0381mm) wire and l is the immersed length of the wire (=1 cm)), the spore dose of one monolayer for ATCC#6051 spores and the spore number density can be calculated to be 6.1×10^{6} and 8×10^{12} m^{-2}, respectively. As are reflected in Fig. 2.13A, these are the spore deposits achieved after 4 biased pulses (on-time 30 s and off-time 30 s each).

It should be noted that in this pulsed DC-EPD process up to eight cycles, the pH value of the spore suspension did not vary much (Fig. 2.15) which had no effect on the deposition rate and spore viability.

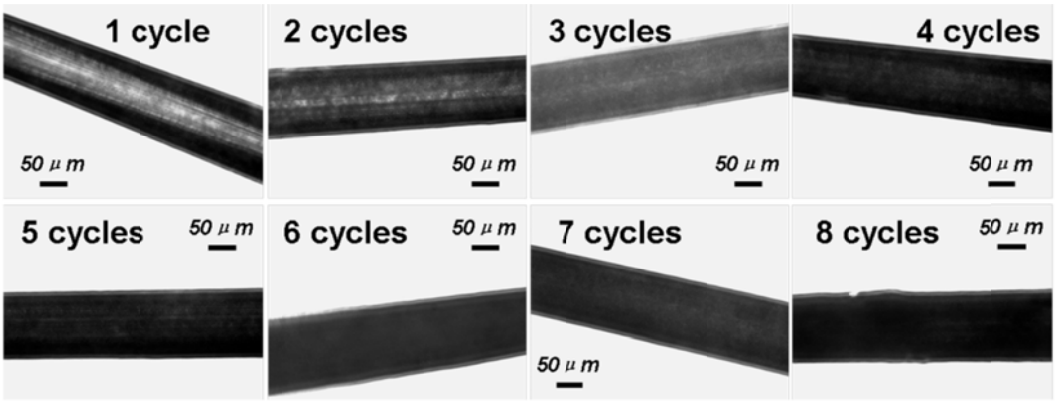

Figure 2.12. The optical microscopic images of Pt wires with *Bs* spores (ATCC#6051) coated are shown after different pulses. Both the pulse-on time and pulse-off time are 30 s.

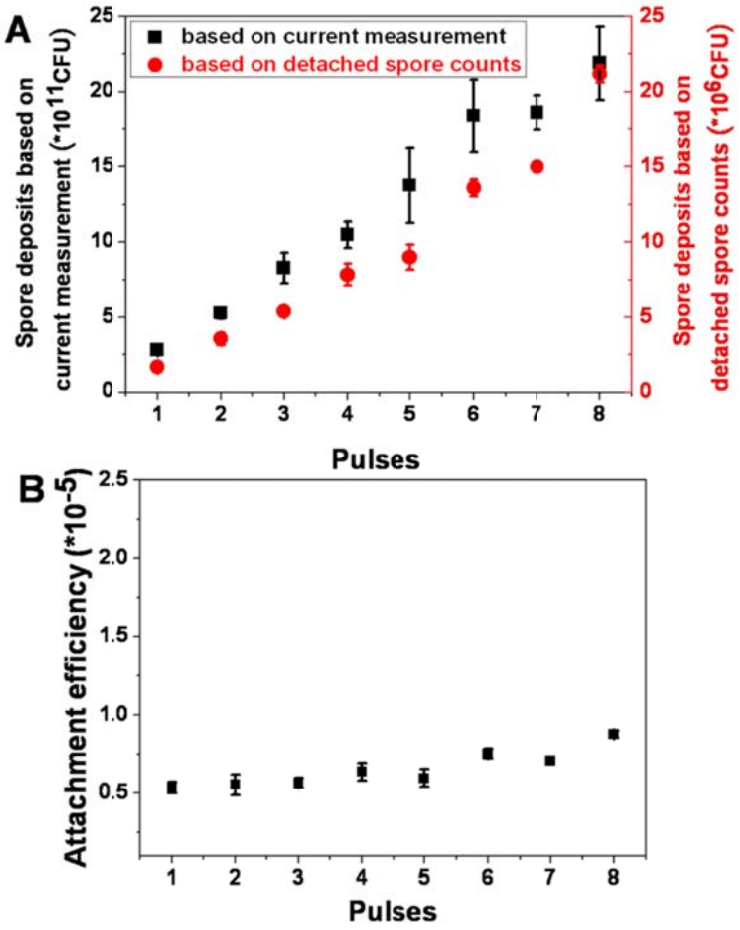

Figure 2.13. (A) *Bs* spore deposits (ATCC#6051) on the Pt wire after different pulses. The black points are for the spore deposits obtained from the current-time measurement, while the red points are from spore deposits counted from the detached spores. (B) Relationship between spore attachment efficiency and number of pulses for *Bs* spores. The spore attachment efficiency was calculated by the ratio of measured spore deposits (from the detached spore counting), over the idealized spore deposits (from the current-time data). Data were measured for four times, which are reflected in the error bars.

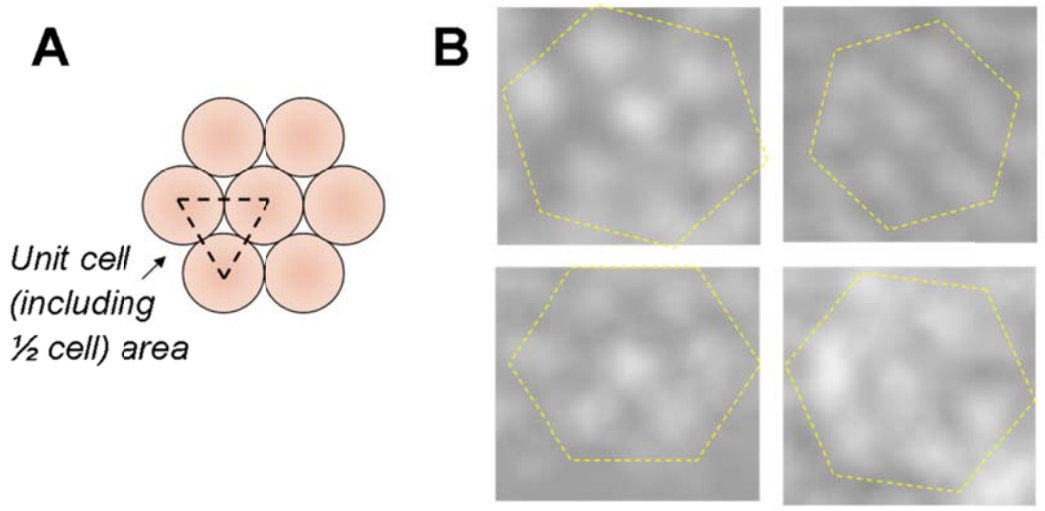

Figure 2.14. (A). Densest spore packing mode on the surface. The triangle drawn includes 1/2 spore on average and its occupying area can be calculated as $\sqrt{3}R^2$ in which R is the radius of the spore. (B) Optical microscopic images show observed packing mode of spores on the surface, as marked by dotted yellow hexagons.

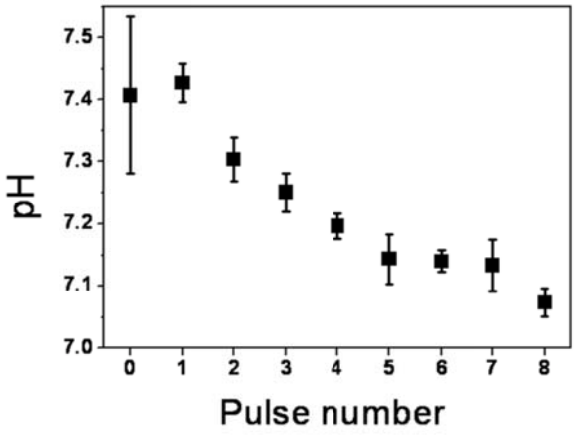

Figure 2.15. pH change in the spore suspension after different pulse numbers in the pulsed DC-EPD mode. Data were measured for three times, which are reflected by the error bars. The initial number concentration of spores was 8×10^9 CFU/ml.

2.4.4. Calculations of the spore surface charge and deposition efficiency

In principle a measurement of the current is also a measure of spore transport to the wire (but not necessarily stick to), if one knows the average charge on a spore. From eq 2.11, the average charge on a spore can be measured by a prior knowledge of the

spore concentration in the suspension and the initial current. A series of initial current of the spore suspensions were collected under different applied potentials and spore concentrations, which were further subtracted from the initial current of a solution without spores and defined as the effective initial current of spores (I_o) and tabulated in Table 2.1. The corresponding surface charge (q) per spore is evaluated from eq 2.11.

Table 2.1. Surface charges and numbers of charges for *B. subtilis* spores (ATCC#6051).

Concentration (CFU/ml)	Voltage (V)	Current (mA)	Surface charge (C)	Number of charges
3.77×10^{6}	5	0.0002±0.0002	$(5.36\pm5.36)\times10^{-14}$	$(3.35\pm3.35)\times10^{5}$
8.59×10^{7}	5	0.0031±0.0008	$(6.20\pm0.81)\times10^{-14}$	$(3.88\pm0.51)\times10^{5}$
7.67×10^{9}	5	0.1635±0.0006	$(4.81\pm0.01)\times10^{-14}$	$(3.00\pm0.01)\times10^{5}$
	10	0.4459±0.0311	$(5.61\pm0.20)\times10^{-14}$	$(3.51\pm0.12)\times10^{5}$
	20	0.8509±0.1080	$(5.47\pm0.35)\times10^{-14}$	$(3.42\pm0.22)\times10^{5}$
	30	1.4584±0.2005	$(5.85\pm0.40)\times10^{-14}$	$(3.65\pm0.25)\times10^{5}$
	40	1.7991±0.2294	$(5.63\pm0.36)\times10^{-14}$	$(3.52\pm0.23)\times10^{5}$
1.53×10^{10}	5	0.1774±0.0008	$(3.55\pm0.01)\times10^{-14}$	$(2.22\pm0.00)\times10^{5}$
	10	0.5162±0.0179	$(4.28\pm0.07)\times10^{-14}$	$(2.67\pm0.05)\times10^{5}$
	20	1.1606±0.0450	$(4.53\pm0.09)\times10^{-14}$	$(2.83\pm0.05)\times10^{5}$
	30	1.4610±0.1474	$(4.15\pm0.21)\times10^{-14}$	$(2.59\pm0.13)\times10^{5}$
	50	3.1724±0.2643	$(4.74\pm0.20)\times10^{-14}$	$(2.96\pm0.12)\times10^{5}$

Note: the average value of surface charge is 5.01×10^{-14}C, and the average number of charges on the spore surface is 3.13×10^{5}.

However, I still need a relationship between q and q' to determine the fraction of the current associated with the diffuse double layer (Fig. 2.16). One approach is to find the electrical potential at the shear plane (i.e the outer radius of solution ions that are carried along with the spore). The Helmholtz-Smoluchowski equation describes the relationship between the shear plane potential (ζ) and the mobility of spores (μ) [63]:

$$\mu = \frac{\varepsilon_m}{\eta}\zeta \tag{2.12}$$

By equating the friction force (eq 2.5) to the electrophoretic force (eq 2.2) and also omitting the dielectrophoretic force (eq 2.3) (note: it has been found that the dielectrophoretic force is much smaller than the electrophoretic force), I can obtain:

$$\zeta = \frac{q}{6\pi\varepsilon_m R} \tag{2.13}$$

In the spherical coordinates the potential as a function of radial distance from the shear plane can be evaluated, from the simplified Poisson-Boltzmann equation [63]:

$$\zeta = \frac{q}{4\pi\varepsilon_m R_\zeta}\exp(-\kappa R_\zeta) \tag{2.14}$$

where R_ζ is the radius of the shear plane, and κ is the inverse Debye length (1.0384×10^{-6} m^{-1}) in water at room temperature. By combining eq 13 and eq 14, I obtain $R_\zeta = 0.35\times10^{-6}$ m, and thus slightly larger than the radius of one *Bs* spore (0.336×10^{-6} m). The quantity of charges between R and R_ζ can be calculated:

$$q - q' = -\int_R^{R_\zeta} \rho^* \bullet 4\pi r^2 dr \tag{2.15}$$

where ρ^* is the charge density in the diffuse layer which can be expressed from the Poisson equation [63]:

$$\rho^* = (-q)\frac{\kappa^2}{4\pi r}\exp(-\kappa r) \tag{2.16}$$

Finally, the spore surface charge can be found:

$$q = \frac{q'}{0.9964} \tag{2.17}$$

Eq 2.17 implies that the contribution of charges between the spore surface and the shear layer is negligible. Evaluation of eq 2.11 gives a value of $q = 5.01\times10^{-14}$ C. Accordingly, the average number of negative charges on the spore surface is 3.13×10^{5} (Table 2.1). The result above is based on the assumption that the surface charge (or zeta potential) of spores in suspension does not vary during deposition, which is essentially what I observed experimentally (Fig. 2.17).

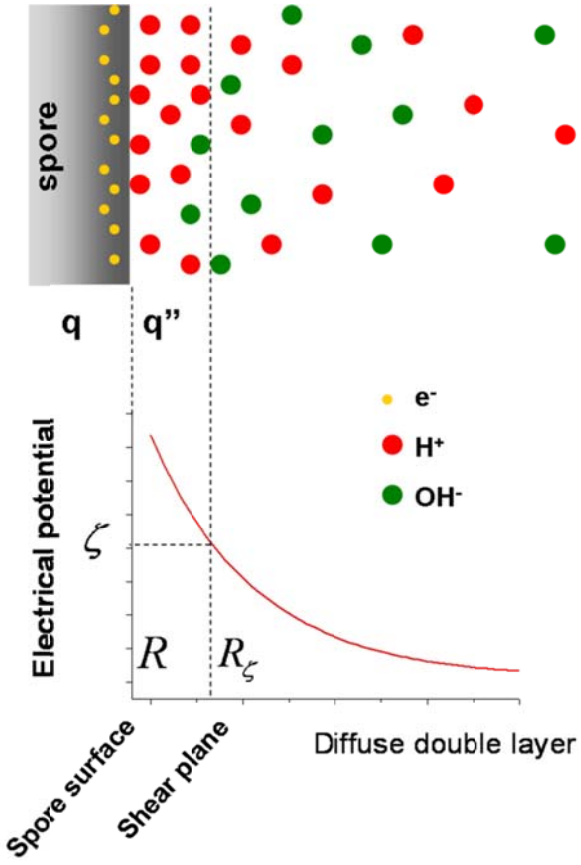

Figure 2.16. Distributions of positive and negative charges at the spore surface and in the diffuse double layer. The corresponding electrical potential decays along the radial direction from the surface of spore. The spore surface charge is q while the counter-ion charge between the spore surface and the shear plane is q''.

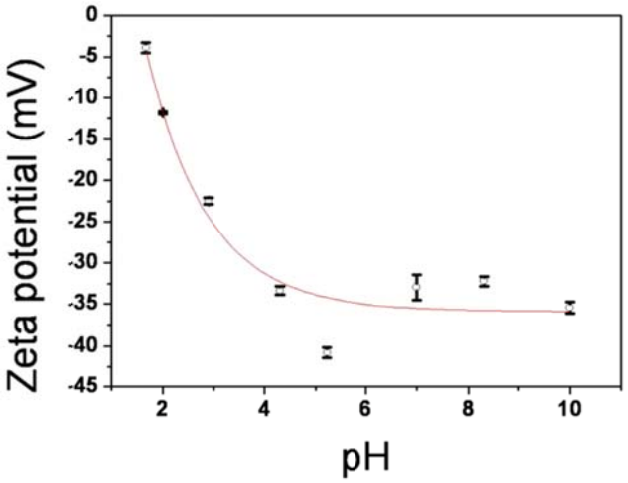

Figure 2.17. Zeta potential change with pH in a spore suspension with the spore number concentration of 3.2×10^7 CFU/mL. 500 μL of sample suspension was mixed with 250 μL, 10 mM ammonium acetate aqueous solution prior to the measurement.

The most commonly used method to detect the surface charges of particles is through a measurement of the zeta-potential [64]. The zeta-potential measured for *Bs* spores yielded values of -33mV, which accordingly gave a surface charge density of 0.0384 C/m^2. Based on the enlarged SEM images (Fig. 2.5), it is reasonable to assume the spore as a prolate ellipsoid with a semi-length axis *c* and a semi-width axis *a*, from which the spore surface area can be estimated. It has been reported that for *Bs* spores, c = 0.535 μm and a = 0.24 μm [55]. Together with the charge density data, the surface charges on the spores can be determined and are listed in Table 2.2. The table shows that the charge values obtained from my method and the zeta-potential assay are quite similar. Alternatively, Douglas [65] detected the surface charges of *Bs* spores through a mobility test in liquid (Table 2.2). These results suggest that my approach gives results that are consistent with other reported results, with the added benefit of being considerable simpler in terms of the sophistication of

the instrumentation needed, and for my purposes the in-situ nature of the measurement.

With a known shielded charge *q'*, the net charge accumulation from my current measurement can be directly used to estimate the deposition rate. Accordingly, the deposited spore dose, $N_{current}$ on the wire could be determined as (Fig. 2.10):

$$N_{current} = \int_0^t dN_{current} = \frac{1}{q'} \int_0^t I(t)dt \tag{2.18}$$

In my pulsed DC-EPD model, the relationship between spore deposits based on the current measurement and pulses is shown in Fig. 2.13A. $N_{current}$ for just one pulse is in the range of 10^{11} spores, which implies the formation of multiple spore layers. However, one densely packed monolayer of *Bs* spores (6.1×10^6) actually required 4 pulses. This leads to a somewhat surprising result that the deposition efficiency is only ~ 10^{-6} (Fig. 2.13B). Thus it appears that many spores apparently make it to the surface and become dislodged, possibly due to non-visible gas generation at the electrode [66]. In spite of this low efficiency, the measured deposited spore amount is proportional to the calculated deposits based on the current (Fig. 2.13B), consistent with the results of Hamaker [67,68]. Based on this model together with the verification from experiments, my result demonstrates that one is able to in reasonable short deposition time create a near conformal monolayer of spores and subsequently detach them.

2.5. Conclusion

I show in this chapter the ability to controllably deposit spores electrophoretically to fine wires using a pulsed voltage method which prevents electrolysis. Attached

spores can be totally removed by a combination of reversing the electrical polarity and ultrasonicating the wire. I am also able to use this method to quantitatively measure the surface charge on spores and the deposition rate. The method is generic and should be applicable to the deposition of any biological material (e.g. spores, bacteria, viruses) onto metallic surfaces.

Chapter 3: Inactivation of Bacterial Spores Subjected to Sub-Second Thermal Stress*

Overview

Rapid heat pulse is the primary method for neutralizing large quantities of spores. Characterizing heat inactivation on a millisecond time scale has been limited by the ability to apply ultrafast, uniform heating to spores. Using my system for immobilization of spores on metal surfaces (as I presented in Chapter 1), bacterial spores were subjected to high temperatures (200 ˚C to 800 ˚C) and heating rates (~10^3 ˚C/s to ~10^5 ˚C/s). Spore inactivation increased with temperature and fit a sigmoid response. I observed the critical peak temperature (T_c) which caused a 2-fold reduction in spore viability was 382 ˚C and 199 ˚C for heating rates of ~10^4 ˚C/s and ~10^5 ˚C/s, respectively. Repetitive heating to the same peak temperature had little effect on viability. In contrast, stepwise heating to elevated peak temperatures inactivated spores in a manner similar to a single pulse heating to the same peak temperature. These results indicate that the maximum temperature rather than the overall heating time is primarily responsible for spore neutralization at ~10^4 ˚C/s heating rate. The mechanism of spore inactivation was further investigated at two heating rates (~10^4 ˚C/s and ~10^5 ˚C/s). Viability reduction was mainly due to DNA damage at the heating rate of ~10^4 ˚C/s as mutant strains defective for *sspA sspB* and *recA* were more sensitive to heat than the wide-type strains. At the higher heating rate (~10^5 ˚C/s), spore inactivation was correlated with physical damage from ultrafast

* The results presented in this chapter have been published in the following journal article: **W. Zhou**, M. W. Orr, G. Jian, S. K. Watt, V. T. Lee*, M.R. Zachariah*. Inactivation of Bacterial Spores Subjected to Sub-Second Thermal Stress. ***Chem. Eng. J.***, 2015, 279, 578-588.

vapor pressurization inside spores. This new approach of pulse heating generates a temperature, time, and kill relationship for *Bacillus* spores at sub-second timescales.

3.1. Introduction

Bacterial spores are a dormant cell type that are highly resistant to heat, moisture, pressurization, radiation and biocidal stresses [1-3]. Concerns regarding bio-terrorism [4] and possibly other public health risks [5,6] require the urgent development of methods for large scale inactivation of bacterial spores. The use of thermal destruction is a straightforward and convenient approach that has been investigated for the inactivation of spores in the liquid phase [7-16]. Conventional thermal inactivation methods require time periods up to minutes or even hours and are limited by a maximum temperature of 150 ˚C [8-10,11,13]. Maintaining these temperatures for the required time periods is unfeasible for large quantities of spores. Thus, stand-off neutralization methods which can sustain higher temperatures (>200 ˚C) for short periods of time (sub-seconds) are being considered, and these new temperature-time-kill histories of spore inactivation require evaluation. Aerosol methods have recently been employed to evaluate thermal and chemical kills of spores at extreme heating conditions [17-25]. These approaches have the advantage of isotropic and rapid heat transfer to individual spores, as well as controllable shorter heating times (milliseconds to seconds) and higher heating temperatures (>200 ˚C) [17-25]. However, there existed a temperature distribution within a population of spores in these studies, which allows for calculating the average resident time and temperature of the entire spore population, but not for individual spores. These studies evaluated

the effect of peak temperature on spore viability. However, the effects of heating and cooling rates on spore inactivation were not discussed.

Precise measurements of heating rate and heating history can be achieved by an alternative method that heats spores immobilized on metal supports. Previous studies have shown that organic or inorganic nano/microparticles deposited on metal surfaces could be heated to a wide range of surface temperature (from ~100 ˚C to ~1800 ˚C) at a rate as high as ~10^6 ˚C/s [26-31]. In those studies, the heating time could be controlled with millisecond precision and the heating rate could be accurately tuned from ~10^3 ˚C/s to ~10^6 ˚C/s, allowing the application of uniform temperature to a deposited particle layer up to 5 μm thick [29] which exceeds the dimensions of a monolayer of bacterial spores. This approach allows accurate application of a uniform high temperature over millisecond time scales for individual spores, which will aid in determining the temperature-time-kill relationship of spores at high temperatures and sub-second timescales.

The mechanism of spore inactivation has been primarily studied in conventional heating schemes. Major mechanisms of spore inactivation occurred through damage to DNA and proteins [3]. Evidence supporting killing by DNA damage includes several studies that found mutants depleted in the *sspA sspB* genes (coding for α/β-type small, acid-soluble proteins (SASP)) and *recA* genes (coding for RecA) were sensitized to mutagenesis and inactivation under dry heating schemes [32-36]. In the dormant spores, SASP bind genomic DNA [32,33] to prevent depurination and strand breakage thereby confer resistance to dry heat and ultraviolet irradiation [34,35]. RecA participates in recombination repair to remove DNA lesions caused by dry heat

[36]. In contrast, denaturation of some key proteins such as metabolic enzymes was found as the mechanism of spore killing in wet heat [8,37]. However, the specific proteins to which denaturation induces spore inactivation have not been identified [38]. A second mechanism of inactivation is through permeabilization of the spore membrane, cortex and coat (encoded by genes like *cotE*), as supported by several lines of evidence [3,39-44]. Damage to spore compartments after heating has been shown with compartment-specific staining techniques [45,46]. While the spore coat was identified as the primary barrier to oxidizing agents (hydrogen peroxide, hypochlorite, ozone, etc.) [47-49], the spore cortex plays a major role in maintaining spore resistance to heat [3,39]. Failure of the cortex structure leads to spore inactivation by two mechanisms. The first is the release of dipicolinic acid (DPA) associated with DNA damage during dry heating [40,41] and protein denaturation during wet heating [38]. The second is through rehydration of the spore protoplast [39,42]. Rehydration of the core will induce a concomitant reduction in spore heat resistance by disrupting SASP-DNA interaction and permitting protein denaturation [43,44]. Through these studies, the temperature-time-kill relationships for spores from several species have been characterized under conventional heating schemes [8-11,13]. However, the exact mechanism of spore inactivation during rapid heating, which is closer to conditions seen under combustion, is poorly understood. Recent studies of bacterial spores heated in hot air show that high-temperature gas induced severe damage to the spore core [50], and the extent of inactivation was attributed to the DNA damage [22].

In this work, I present the effect of fast heating pulses (~10^4 ˚C/s and ~10^5 ˚C/s) on surface-immobilized spores as a complimentary approach to the aerosol studies. The heating scheme possesses the advantages of precise measurement of heating time and rates, as well as uniform temporal temperature for individual spores. Using this heating scheme, I determined the effect of peak heating temperature and heat rate by assessing spore viability and morphology. The heating histories of spores were also investigated through repetitive exposures as a possible factor influencing spore inactivation. To investigate the mechanism of killing, spores carrying *sspA sspB*, *recA* or *cotE* mutations were tested to determine whether known mechanisms of spore inactivation contribute to spore viability in my heating scheme. Using these results, I propose a model for the thermal destruction of bacterial spores in the heating rates of ~10^4 ˚C/s and ~10^5 ˚C/s.

3.2. Material and methods

3.2.1. Spore attachment on platinum wires

Bacillus subtilis (*Bs*) (ATCC#6051) were sporulated in Difco Sporulation Medium (DSM) at 30 ˚C for 48 h. The 250 ml of DSM included 2 g Bacto nutrient broth, 2.5 ml 10% KCl, 0.375 ml 1 M NaOH and 2.5 ml 1.2% $MgSO_4 \cdot 7H_2O$. The spore concentration was enumerated by plating to be 8×10^9 colony-forming units per milliliter (CFU/mL). The purity of spores was found more than 99%. For analysis of mechanism of killing, four isogenic *Bs* spore strains, namely, a wild-type strain (PS533) [36], a Δ*cotE* mutant strain lacking coat (PS3328) [48], a Δ*sspA* Δ*sspB* mutant strain lacking DNA protection mechanism (PS578) [32], and a Δ*recA* mutant

strain lacking DNA repair mechanism (PS2318b) [36] were generously provided by Dr. Peter Setlow (University of Connecticut). A platinum (Pt) wire with a diameter of 76.8 μm (Omega Engineering, Inc.) was used to immobilize spores. An in-house spore deposition cell was manufactured for coating the wire with Bs spores electrophoretically (Fig. 2.1). By controlling the biased deposition voltage, pulse frequency, and charging time (from a 6340 sub-femtoamp remote sourcemeter, Keithley), a uniform monolayer of spores in the central region of the wire (~1 cm) could be obtained (Fig. 3.1A). The detailed information of the spore deposition cell and charging conditions can be found in Chapter 2 [51].

3.2.2. Wire heating test

To subject spores to a defined thermal history, the spore coated Pt wire was connected to an in-house built power source, working as a temperature jump probe (Fig. 3.2). A pulse signal was generated to trigger the power supply prior to the heating of wire in air. The applied voltage (supplied from a 6291A DC power supply, HP) and the measured current (by a current probe AM503, Tektronix) were simultaneously recorded via an oscilloscope (LT344, LeCroy). The transient temperature on the wire during the heating period was measured based on the standard dynamic electric resistance temperature relationship (Callendar-Van Dusen equation) [52], in which the resistance measured from the applied voltage and the current was in a quadratic relationship with the transient temperature (see Section 3.2.3 below). The maximum temperature (~200 ˚C to ~800 ˚C) and the heating rate

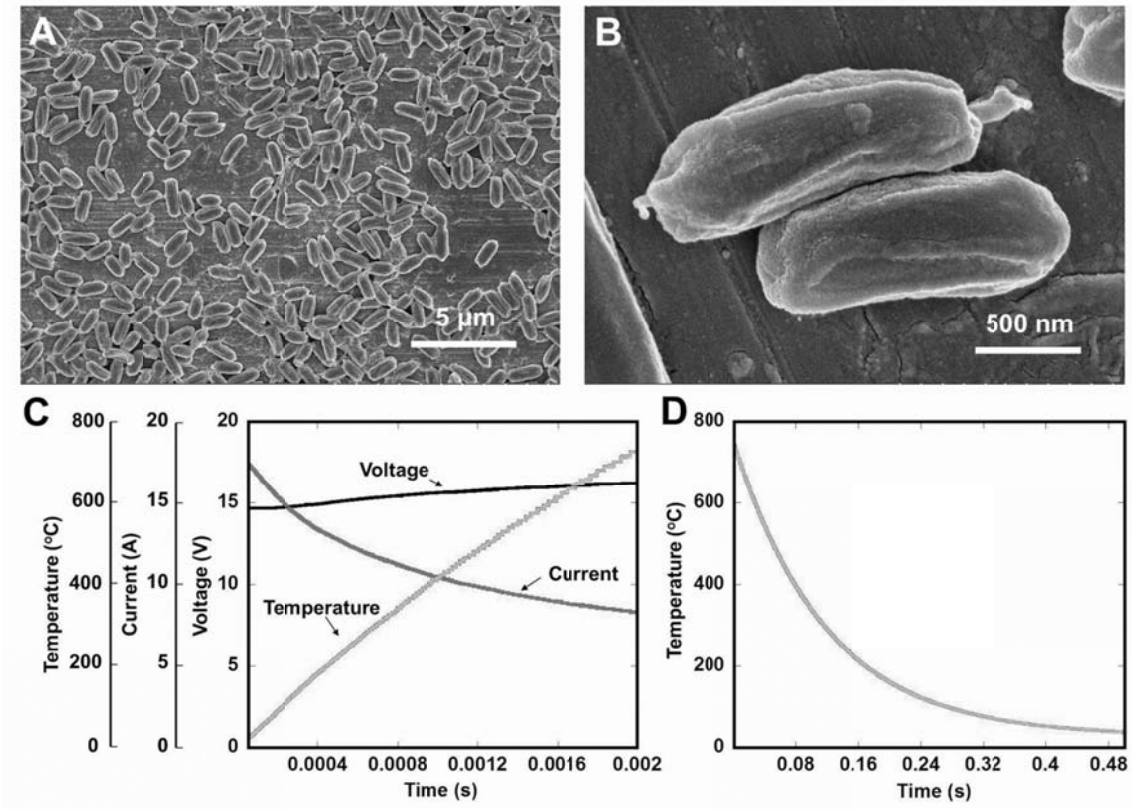

Figure 3.1. (A) Electrophoretically deposited monolayer of Bs spores on the Pt wire as imaged by SEM. (B) High magnification SEM image of two immobilized spores. (C) Example of voltage, current and temperature temporal traces on the Pt wire surface in a 2 ms pulse test. The maximal temperature is ~740 ˚C in this case. (D) Surface temperature of the wire after cessation of the heating pulse.

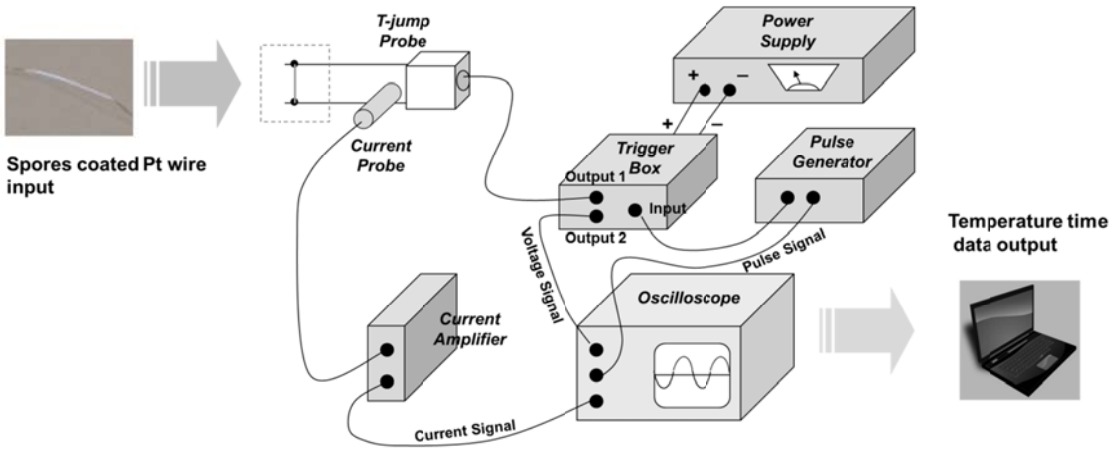

Figure 3.2. Schematic of wire heating and temperature measurement.

(~10^3 ˚C/s to ~10^5 ˚C/s) can be precisely controlled by varying the applied voltage and the pulse time (2 ms to 50 ms). The corresponding profile of the wire in the cooled region was calculated according to an energy balance equation which was dominated by the heat conduction. The detailed content of the mathematical modeling can be found in Section 3.2.4 below. The spore-coated Pt wire was replaced after each heating test, and the heated wires were processed for SEM imaging and determination of CFUs.

For wire heating tests in different pressures, two home-built chambers were used. The first chamber was connected to a vacuum pump for spore heating experiments under pressures as low as ~10^{-5} Pa, while the second chamber was connected to a high-pressure air source for experiments under pressures up to 4×10^5 Pa.

3.2.3. Temperature time model in the heating process

When pulsed with electricity at a certain voltage, the Pt wire is joule heated during the pulse-on time. The on-going wire temperature (T) can be measured as a function of transient wire resistance (R) using the Callendar-Van Dusen equation which is a standard way of measuring temperature based on material resistance temperature relationship, and has been already used to define International Temperature Scale of 1990 (ITS-90) [52] :

$$\frac{R}{R_o} = 1 + \alpha T + \beta T^2 \tag{3.1}$$

where α = 3.91×10^{-3}, β = -5.78×10^{-7}, and R_o is the wire resistance at 0 ˚C. From the temporal pulse voltage (U) and resulting current (I), the total resistance (R_{tot}) in the

electrical circuit can be calculated. By measuring the other resistance (R^*) in the circuit except the Pt wire portion, the resistance of the Pt wire (R) can be obtained:

$$R = R_{tot} - R^* = \frac{U}{I} - R^* \tag{3.2}$$

By combining the above two equations, the transient temperature on the wire can be measured as:

$$T = \frac{\alpha + \sqrt{\alpha^2 - 4\beta(1 - (U/I - R^*)/R_o)}}{-2\beta} \tag{3.3}$$

3.2.4. Temperature time model in the cooling process

Once the pulse is ceased, heat will dissipate from the Pt wire to the ambient air. Since the wire is placed in relatively still air, any heat convection by air flow is negligible in my system. Besides, the heat conduction flux is much larger than the heat radiation flux due to a high convection heat transfer coefficient (h) on Pt wire [53]. Thus the energy balance for the Pt wire can be expressed as:

$$\rho V C_p \frac{dT}{dt} = -Ah(T_{surface} - T_{air}) \tag{3.4}$$

where ρ is the density of Pt (2.15×10^4 kg/m^3) [54], V is the volume of Pt wire, C_p is the mass based heat capacity of Pt (130 J/kg·˚C) [54], A is the outer surface area of Pt wire, and $T_{surface}$ and T_{air} are the wire surface temperature and surrounding air temperature (27 ˚C), respectively. For the heat conduction term in eq. 3.4, because of the much smaller cross-section areas of the Pt wire than the surface area, any lateral heat flux is also without consideration.

To solve for $T_{surface}$, the above equation should be adjusted because of the existence of two variables T and $T_{surface}$. The right side of this equation can be changed to an expression of heat conduction inside the wire. The transient energy balance inside a cylindrical volume element (a region between radii r and $r + \Delta r$) is evaluated by equating the sum of conductive heat flows in and out of this volume. So that eq 3.4 can be transformed to:

$$\frac{\partial T}{\partial t} = \frac{k}{\rho C_p}\frac{1}{r}\frac{\partial}{\partial r}(r\frac{\partial T}{\partial r}) \tag{3.5}$$

where k is the thermal conductivity of Pt wire (71.4 W/m·˚C) [53]. We assume that the initial temperature (T_o) is uniformly distributed across r, and there is no energy absorption or generation on the wire surface. Finally, an analytical solution is approximately achieved by the first term of an infinite series of Bessel functions and the Heisler charts [55]:

$$\frac{T_{surface} - T_{air}}{T_0 - T_{air}} = \exp(-\frac{2ht}{\rho C_p r_w}) \tag{3.6}$$

where r_w is the radius of wire (38.4 μm). Since T_{air} = 27 ˚C, the surface temperature can be further simplified as:

$$T_{surface} = 27 + (T_0 - 27)\exp(-1.86\times10^{-2} ht) \tag{3.7}$$

The next step is to find h. We estimate this value by the optical images of the heated Pt wire in my wire test. A bare Pt wire was heated up to ~1082 ˚C by a 3 ms pulse and then kept still in the air to dissipate heat energy. Snapshots of the wire were taken continuously by a high speed camera (Phantom V12.1). As shown in Fig. 3.3, the onset of brightness on the wire occurred after 1.6 ms during the heating process, which corresponds to a surface temperature of ~695 ˚C. After the peak temperature

was reached at 3 ms, the cooling time for the loss of brightness on wire was 54 ms, during which $T_{surface}$ dropped from ~1082 ˚C to ~695 ˚C. Based on this set of data, h can be estimated as:

$$h = \frac{-\ln\left[(695-27)/(1082-27)\right]}{1.866\times10^{-2}\times0.054} = 4.55\times10^{2} \tag{3.8}$$

Finally, $T_{surface}$ can be expressed as:

$$T_{surface} = 27 + (T_0 - 27)\exp(-8.46t) \tag{3.9}$$

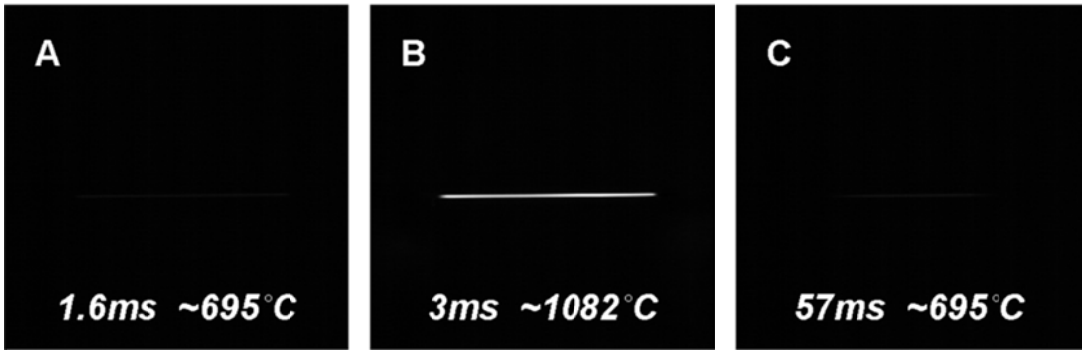

Figure 3.3. Typical snapshots of the Pt wire in the dark background during the heating (A, B) and cooling (C) processes.

3.2.5. Determination of colony forming units

The number of viable spores that survived various heating conditions was enumerated by determining CFUs. Wires coated with heated or unheated spores were completely submerged in 1 ml of Lysogeny Broth (LB) media (10 g tryptone, 5 g yeast extract and 5 g NaCl per liter) and placed on a shaker at the 37 ˚C for three hours to allow for the germination and detachment of viable spores from the wire surface. After incubation, samples were serially diluted and plated on LB agar plates to determine viable CFUs. Each test included at least six replicates. The relationship of the recovered counts with time is shown in Fig. 3.4. Previous SEM images of

unheated wires in Chapter 2 (Fig. 2.11) showed that ~10^6 spores were coated onto the platinum wires [51]. The three hours incubation time resulted in CFU counts that reflect the 10^6 spores on the wire.

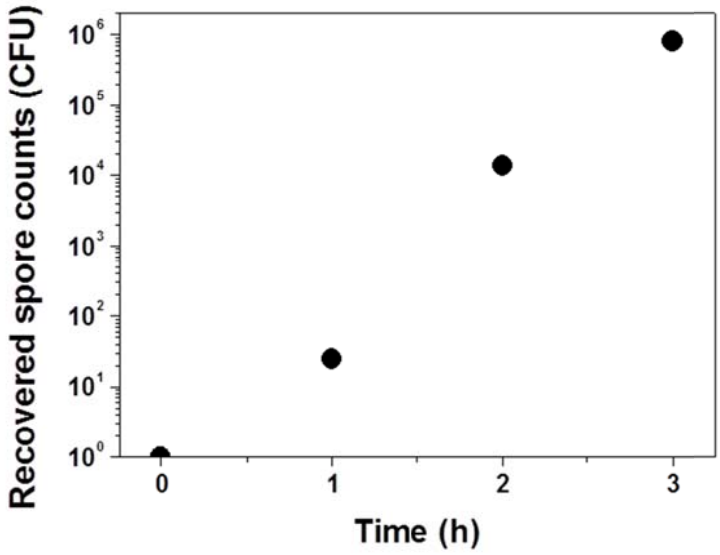

Figure 3.4. CFU counts of spores recovered at different times from the incubation medium submerged with the spores coated wire. At 3 h, the recovered counts are consistent with the original counts on wire.

The validity of this spore counting protocol was also evaluated by *in situ* phase contrast microscopy (Zeiss LSM 710, Germany) to monitor the germination of spores from wires. I found that *Bs* spores took 1 h before transition from phase bright to phase dark, and 2 h to completely detach from wires. Additional experiments were performed on wire heated to temperatures >600 ˚C, a temperature that sterilizes *Bs* spores (see Section 3.3.2 below). Prolonged incubation of these heated wires for 24 h in LB at 37˚C failed to yield any growth.

3.2.6. Spore morphological characterization

The heated wires were first mounted to stubs and then sputtered with gold/palladium alloy prior to the SEM using Hitachi S-4700. The dimensions of the spores were assessed by two parameters measured from SEM images, namely the aspect ratio (length divided by width) and the projected area (surface area inside the contour line of the cell body) of spores on the Pt surface. Statistical analyses are based on a spore population of >50.

3.2.7. Estimation of vapor pressurization inside spores

The vapor pressure and temperature relationship was calculated by a simple closed model assuming the spore allows for heat but not mass transfer. Empirical thermodynamics data of superheated vapor and steam were used to plot the standard curve of pressure rise with temperature.

In detail, the vaporization of water contained in spores, typically inside the spore core which is protected by the crosslinked cortex layer, should result in a pressure rise if the water vapor cannot escape fast enough. In the case of a heating rate of ~10^5 ˚C/s, to a peak temperature of 400 ˚C, I observe surface rounding of the spore cortex layer (see Section 3.3.3). If I make an assumption that the water vapor is contained within the spore core and cortex until rupture, and that all liquid water can be vaporized prior to reaching a liquid-vapor steady state due to a high heating event, I can estimate the *dynamic* pressure within the spore structure. The volume under the spore cortex layer was estimated from the SEM images (see Section 3.3.3), providing a rough estimate of the available volume (V) for the gas:

$$V = 0.034 \mu m^3 \tag{3.10}$$

Given that *Bs* spore core contains ~30% water by mass, and its density (ρ) is ~1.3 g/cm^3 [56], the molar amount of water *n* can be calculated. Based on the previous assumption that all water is vaporized at the temperatures of my interest (240 ˚C - 400 ˚C), ideal gas law is employed to estimate the *dynamic* pressure built-up during the time scales of my heat pulses (2-50 ms):

$$P = \frac{nRT}{V} \tag{3.11}$$

where *P* is the pressure inside spores, *R* is the gas constant (=8.31 J mol^{-1} ˚C^{-1}), and *T* is the temperature. The result is presented in Fig. 3.5. It should be noted that, since I did not consider the vapor release by diffusion across the spore cortex, this equation reports the maximum internal pressure under the spore cortex layer.

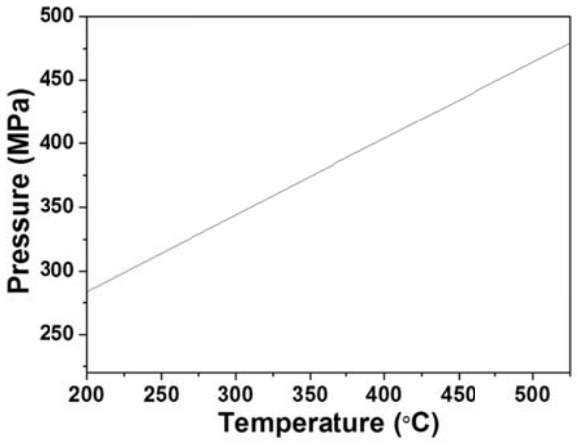

Figure 3.5. The estimated *dynamic* vapor pressures inside *Bs* spores at different temperatures. Due to the rapid temperature increase, the volumetric expansion from water vaporization is very rapid and all liquid water is assumed to be vaporized. In this regard, ideal gas law is adopted to estimate the pressure built-up inside spores.

3.3. Results

3.3.1. Temperature profiles of the Pt wire surface

Precise definition of the temperature-time-kill relationship for *Bs* spores in sub-second time scales requires accurate and fast measurement of the spore temperature. Joule heating triggered by a strong electrical pulse enables me to quickly and accurately measure the transient temperature in a sub-second heating process. My temperature-time measurement shows that the transient temperature on the wire surface during heating followed a closely linear ascending trace (Fig. 3.1C), while temperature-time calculation based on radial heat transfer estimates a slow exponential decaying trace when the pulse was turned off (Fig. 3.1D). The temperature of the ascending trace was measured from the time dependent variations of the applied voltage and current (see eq. 3.3). By tuning the pulse time (2 ms to 50 ms) and applied voltage, different maximum temperatures (200 ˚C to 800 ˚C) and

Table 3.1. Calculated cooling times required for spores with different initial peak temperatures to drop to 40 ˚C.

T_o (˚C)	t (ms)
200	306
300	360
400	397
500	425
600	448
700	467
800	483

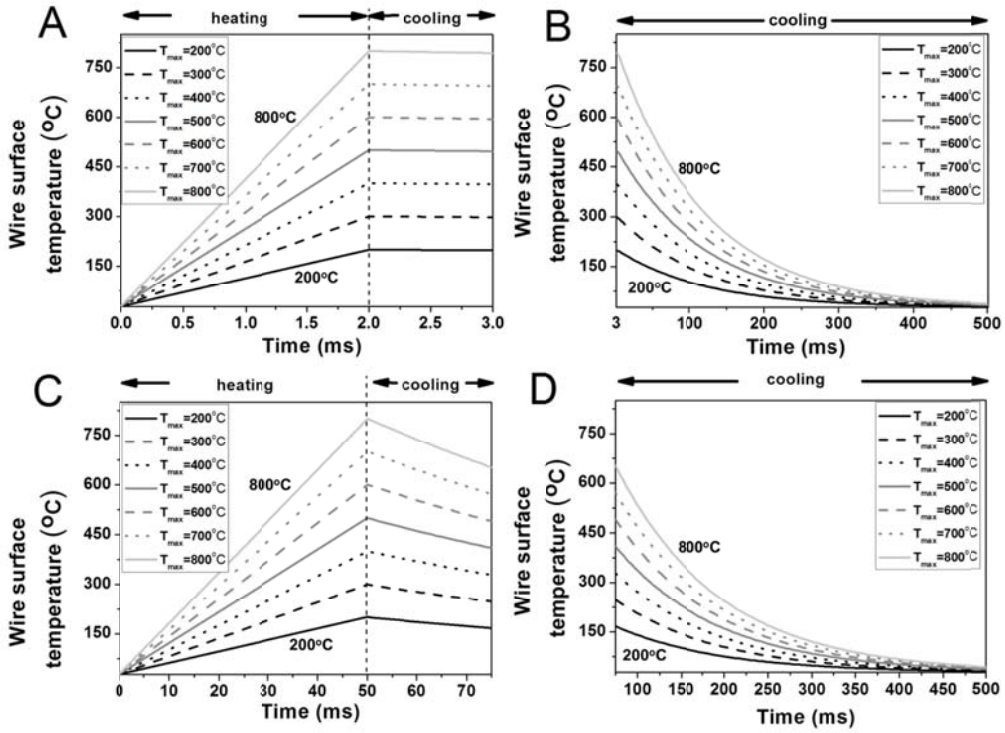

Figure 3.6. (A-D) exhibit simulated Pt wire temperatures during the heating and cooling processes. The applied electric pulse times are 2 ms (A, B) and 50ms (C, D), respectively.

heating rates (~10^3 ˚C/s to ~10^5 ˚C/s) could be obtained (Fig. 3.6). The temperature decaying trace was calculated from a radial heat transfer model by assuming that most heat loss occurred by conduction from the cylindrical wire surface (see details in Section 3.2.4). The surface temperature dropped exponentially after the voltage was turned off and returned to 40 ˚C after ~300 ms to ~500 ms (Table 3.1). While these cooling times are longer than the heating pulse times (2 ms to 50 ms), they are much shorter than the times employed in previous protocols [12,14].

3.3.2. Spore viability heated to fixed peak temperatures at two ramp rates

We assessed the effect of fast heating on the viability of Bs spores. When exposed to 50 ms fast heating pulse, spores reached peak temperatures between 200 ˚C to 800

˚C which represents heat rates of 4×10^3 to 2×10^4 ˚C/s. Peak temperatures below 350 ˚C had minimal effect in the spore viability (Fig. 3.7). Once the temperature reached over 350 ˚C, the viability of spores decreased sharply by ~5 logs from 350 ˚C to 600 ˚C. Further increases in the peak temperature to ~700 ˚C reduced spore viability by 6 logs. These results indicate that 400 ˚C was the maximum peak temperature that the spores could resist in the 50 ms heating scheme.

When exposed to a 2 ms ultrafast heating pulse, spores reached peak temperatures between 200 ˚C to 800 ˚C, however, the heat rates were higher (1×10^5 to 4×10^5 ˚C/s). The spores were inactivated at a lower peak temperature (180 ˚C) and a reduction of 5 logs was achieved at 400 ˚C compared with 600 ˚C in 50 ms pulse heating. Finally, a complete viability reduction of 6 logs was reached at temperatures over 500 ˚C. These results indicate the time-temperature-kill relationships at different heating rates show

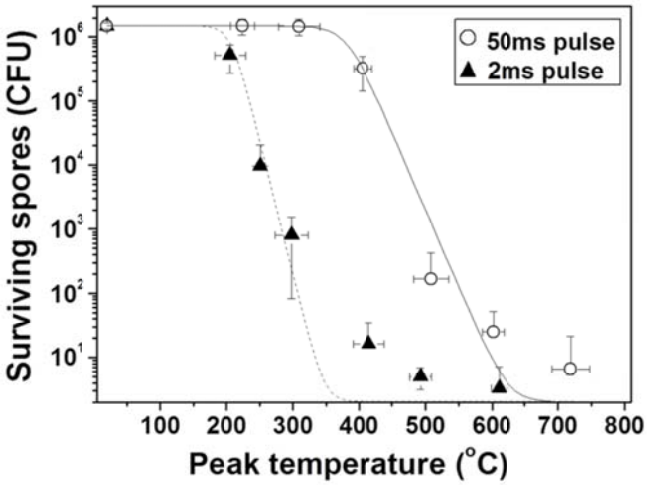

Figure 3.7. Survival curves of *Bs* spores versus peak temperature for 2 ms and 50 ms heat pulses. Each experimental point represents the average of at least 6 replicates, and the standard deviations both in the measured spore viabilities and peak temperatures are indicated.

similar sigmoidal response. However, the faster heating rate of ~10^5 ˚C/s potentiates spore inactivation and effectively reduces the peak temperature required for 6-log spore neutralization when compared to the heating rate of ~10^4 ˚C/s.

The viability data above were fitted with a standard sigmoid model used in traditional low rate heating experiments [57] as follows:

$$S = \frac{1}{1+\exp(k(T-T_c))} \tag{3.12}$$

where S is the survival ratio of spores (CFU_{final} / $CFU_{initial}$), T is the peak temperature in a heating event, T_c is the critical peak temperature at which the spore viability is reduced by half, and k is the heat resistance parameter (larger k means spore viability is more temperature sensitive). In this study, the initial number of spores on the wire was measured as ~1.5×10^6 CFU. The fitted values of T_c and k are listed in Table 3.2. I found that the k value of the curve representing the spore destruction at the higher heating rates (~10^5 ˚C/s) was larger than that of the lower heating rates (~10^4 ˚C/s) (Table 3.2). In addition, T_c at the heating rates of ~10^5 ˚C/s was lower than that at the heating rates of ~10^4 ˚C/s. Together, these results indicate that ultrafast heating rates (~10^5 ˚C/s) potentiate spore inactivation.

Table 3.2. Fitting results for the variables in eq 3.12.

Heating conditions	k (˚C^{-1})	T_c (˚C)
2 ms heating pulse (~10^5 ˚C/s)	0.096	199
50 ms heating pulse (~10^4 ˚C/s)	0.056	382

3.3.3. Spore morphology after heating to defined peak temperatures at two ramp rates

We assessed the morphological features of spores after heating. The unheated spores had characteristic longitudinal ridges along their surfaces (Fig. 3.1B). At the heating rates of ~10^4 ˚C/s, after fast heating to a peak temperature of up to 300 ˚C, the aspect ratio and the projected area remained constant (Fig. 3.8A and Table 3.3). Fast heating to 410 ˚C caused spores to shrink (projected area on surface decreased by 48% to 0.43 μm^2) (Fig. 3.8B). When heated to 570 ˚C (Fig. 3.8C), the spores were rounded (aspect ratio decreased by 37% to 1.56) without additional reduction in spore size (projected area decreased by 46% to 0.44 μm^2). The spore surface lost its integrity after fast heating to 780 ˚C (Fig. 3.8D). These results indicate that the severity of morphological change under the fast-heating and high temperature conditions correlates with spore viability at the heating rates of ~10^4 ˚C/s (Figs. 3.7 and 3.8). We also investigated the morphology of spores exposed to faster heating (2 ms pulses, ~10^5 ˚C/s). When heated to temperatures below 300 ˚C, the aspect ratio and surface area remained unchanged even though there was a large reduction in spore viability (Figs. 3.7 and 3.9B). At peak temperatures of 300 ˚C and above, pin holes and fissures were observed (Figs. 3.9C and 3.10). When heated to 410 ˚C, the aspect ratio decreased by 21% to 1.98 and the projected area decreased by 38% to 0.52 μm^2 (Fig. 3.9D). At a peak temperature of 520 ˚C, the aspect ratio further decreased by 53% to1.16 and the projected area reduced by 56% to 0.36 μm^2 (Fig. 3.9E). By comparing spores exposed to the same peak temperature at two different heating rates, spores

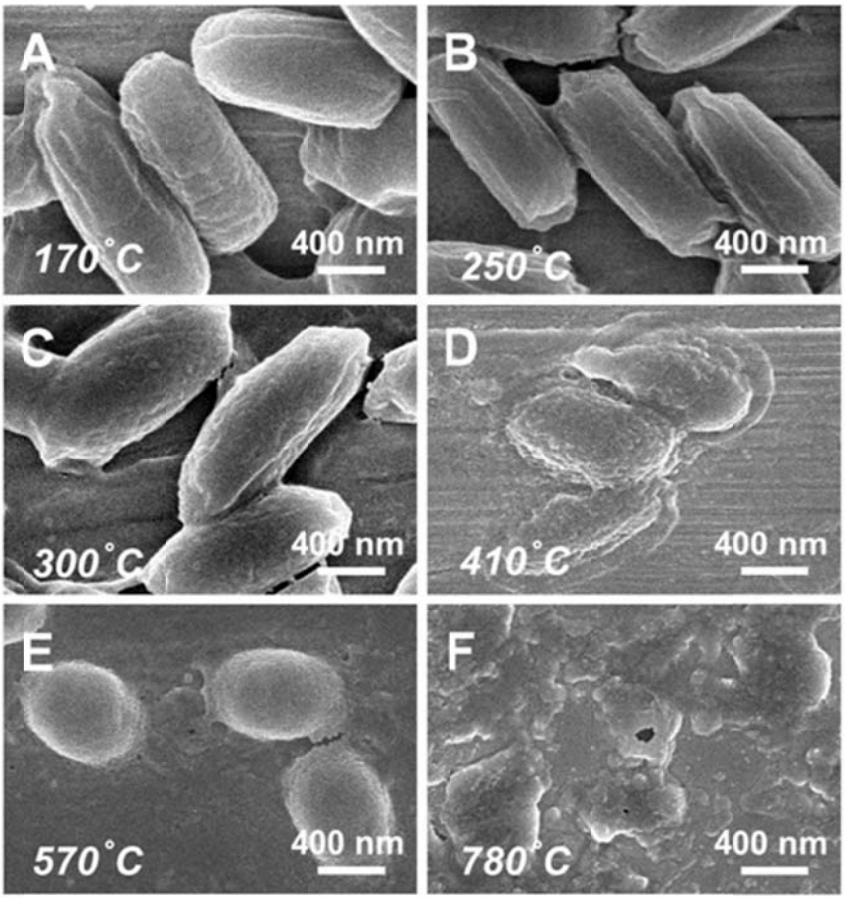

Figure 3.8. SEM images of surface attached *Bs* spores after heat treatment triggered by a 50 ms pulse (~10^4 ˚C/s). Each image shows a representative morphological change of over 50 spores. The maximum temperatures exerted on spores are indicated (A-F).

exposed to the faster heating rate (~10^5 ˚C/s) have minor morphological changes despite increased inactivation (Table 3.3, Figs. 3.8 and 3.9). These results indicate that the spore killing mechanisms in two heating rates are different.

Table 3.3. Changes to spore physical dimensions after 2 ms and 50 ms pulse heating to different temperatures, with related viability loss.

Heating conditions	Length (μm)[a]	Width (μm)[a]	Aspect ratio	Projected area (μm^2)[b]	Viability (CFU)
Unheated	1.54 ± 0.17	0.62 ± 0.05	2.49 ± 0.37	0.82 ± 0.09	1.5×10^6
2 ms pulse, heat to 200 ˚C	1.47 ± 0.17	0.62 ± 0.02	2.38 ± 0.28	0.82 ± 0.10	7.8×10^5
2 ms pulse, heat to 240 ˚C	1.40 ± 0.14	0.61 ± 0.03	2.32 ± 0.31	0.82 ± 0.07	1.7×10^4
2 ms pulse, heat to 300 ˚C	1.49 ± 0.14	0.60 ± 0.04	2.43 ± 0.25	0.84 ± 0.11	5.7×10^1
2 ms pulse, heat to 410 ˚C	1.11 ± 0.11	0.56 ± 0.05	1.98 ± 0.21	0.52 ± 0.05	2.0×10^1
2 ms pulse, heat to 520 ˚C	0.69 ± 0.05	0.60 ± 0.07	1.16 ± 0.15	0.36 ± 0.04	0
50 ms pulse, heat to 170 ˚C	1.45 ± 0.13	0.59 ± 0.03	2.46 ± 0.29	0.79 ± 0.09	1.5×10^6
50 ms pulse, heat to 410 ˚C	1.11 ± 0.09	0.44 ± 0.04	2.57 ± 0.30	0.43 ± 0.02	2.4×10^5
50 ms pulse, heat to 570 ˚C	0.81 ± 0.10	0.54 ± 0.05	1.56 ± 0.21	0.44 ± 0.04	4.2×10^1

Note: Data are derived from a random sample of 15 spores from totally more than 50 spores in SEM images.
[a]The length and width were measured as the longest distances along the longitudinal and transverse directions of the spore body.
[b]The projected area does not represent the spore volume, but acts as a comparable variable to evaluate changes in dimension under different heating conditions.

3.3.4. Effect of repetitive fast heat pulses (~10^4 ˚C/s) on the spore morphology and viability

My observations that faster heating rates and higher peak temperatures caused greater spore damage led me to propose a hypothesis that these two parameters have distinct effects on spores. To test this hypothesis, I devised two experiments to distinguish the effects of heating rate versus those of peak temperature. In the first experiment, I asked if repeated application of the same fast heating scheme resulted in accumulated damage to the spore (Fig. 3.11). The viability results show that spores exposed to 20 rounds of 200 ˚C in 50 ms decreased the survival rate by less than one order of magnitude, demonstrating that the viability loss in the first pulse is not

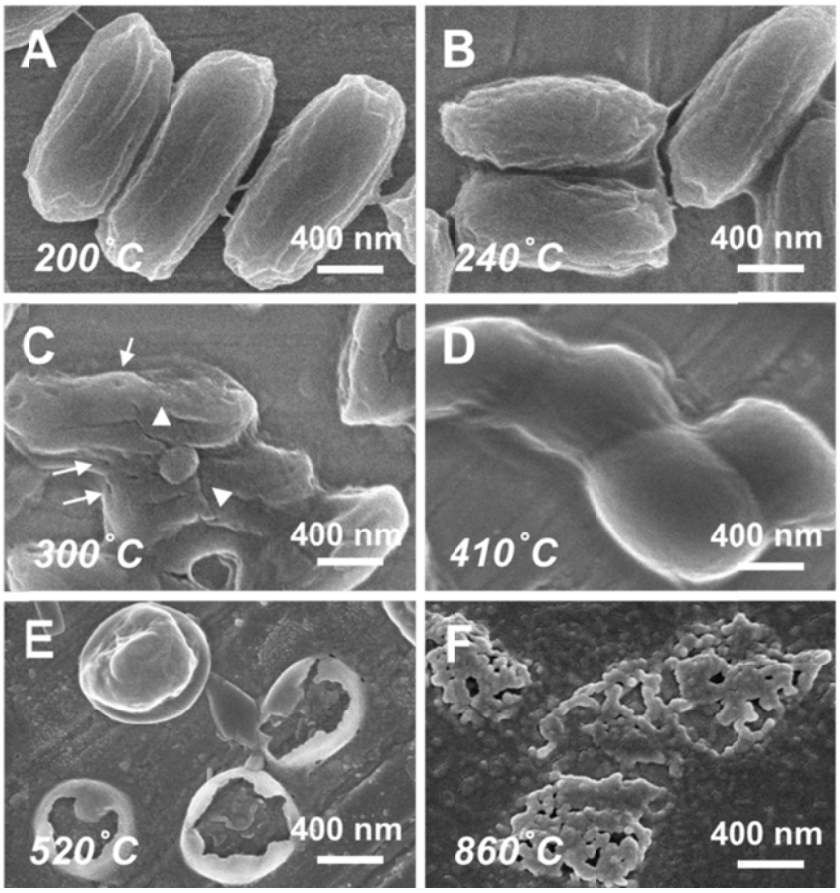

Figure 3.9. SEM images of surface attached spores after heat treatment triggered by a 2 ms pulse (~10^5 °C/s). Each image shows a representative morphological change of over 50 spores. The maximum temperatures exerted on spores are indicated (A-F). In (C), the arrows and the arrow heads indicate the location of holes and fissures on the spore surfaces, respectively.

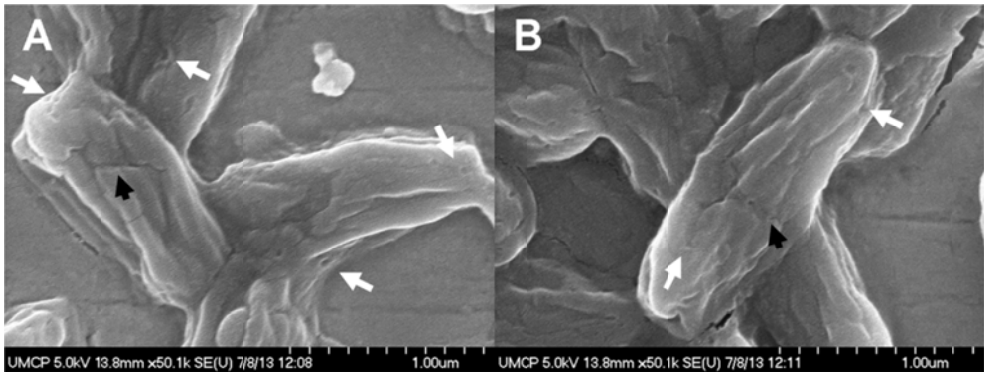

Figure 3.10. High magnification SEM images of surface attached spores after heat treatment to 300 °C triggered by a 2 ms pulse. The white arrows and the black arrows remark the formation of tiny cracks and fissures on the spore surfaces, respectively.

additive (Fig. 3.12). SEM results also confirmed that spores exposed to different heating cycles of 400 ˚C in 50 ms showed minor morphological differences or size changes (Fig. 3.12 and Table 3.4). In the second experiment, I asked if the repeated exposure of treated spores to higher peak temperatures caused additional damage to spores (Fig. 3.13). Pre-heating to 200 ˚C in 50 ms prior to pulse heating to 500 ˚C in 50 ms did not alter the viability of spores compared to just heating to 500˚C in 50 ms (Fig. 3.12A). The resulting SEM images (Fig. 3.12B - 3.12F) also show that melted and disintegrated spore structures appeared when the second and third pulse peak temperatures increased to 600 ˚C and 800 ˚C, respectively. These morphological changes could also be achieved by singular pulse heating to corresponding peak temperatures. Considering the total heating time in my experiments is less than 10 s, I propose that the heat accumulation is negligible compared with the reported heating time in traditional spore decontamination studies that was normally minutes or even

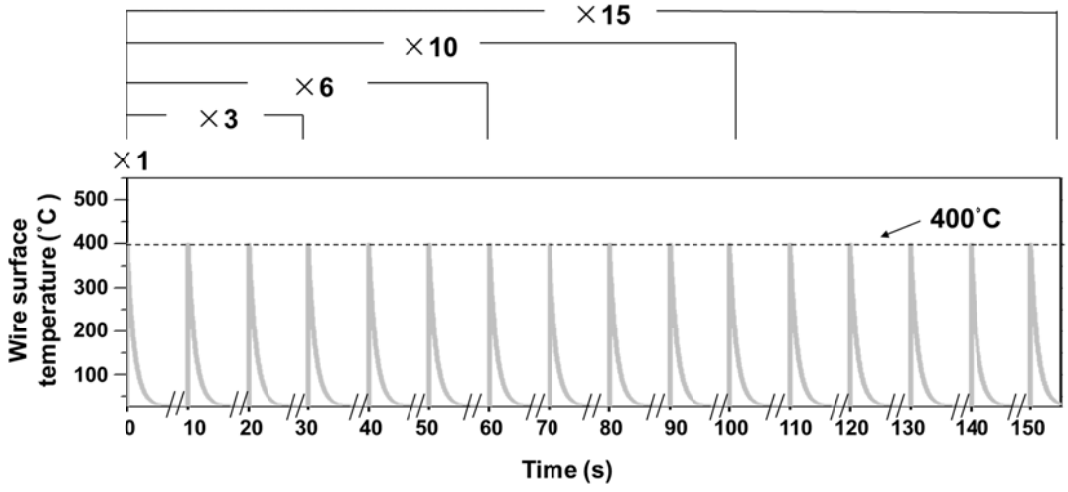

Figure 3.11. Simulated temperature temporal profiles during different repetitive pulse heating (1 to 15 times). All the heating pulses reach the same peak temperature of ~400 ˚C. The individual pulse width is 50 ms and the rest time in between is ~10 s.

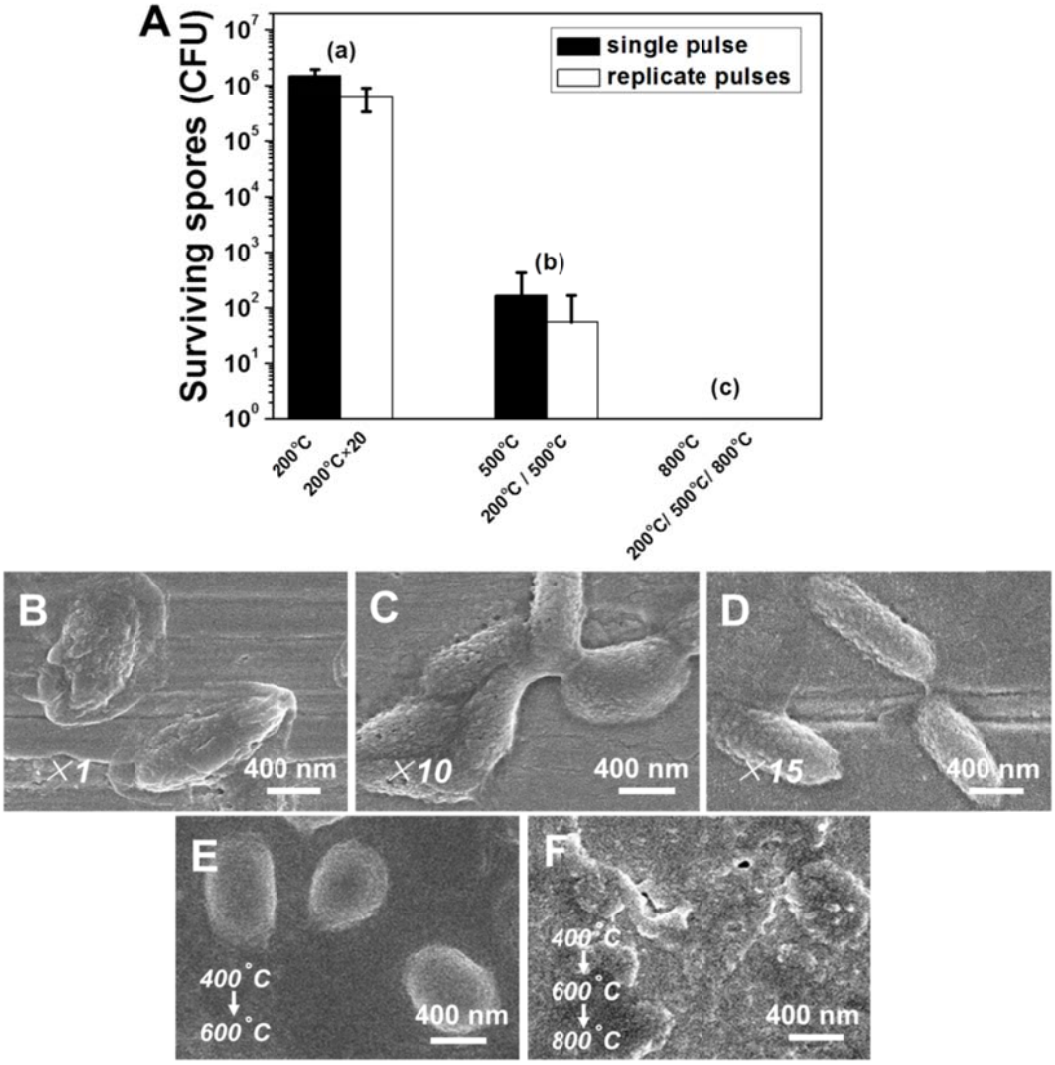

Figure 3.12. Effect of repeat heat treatment on spore viability. (A-a) CFU of spores after being heated to 200 ˚C once (black bar) or 20 times (white bar) in the 50 ms pulse heating test. (A-b) CFU of spores after being heated to 200 ˚C followed by 500 ˚C (white bar), or directly heated to 200 ˚C (black bar) in the 50 ms pulse heating test. (A-c) CFU of spores after being heated in triplicates to 200 ˚C, 500 ˚C, and 800 ˚C subsequently (white bar), or directly heated to 800 ˚C (black bar) in the 50 ms pulse heating test. Bars are not shown in (A-c) since CFU = 0. Results are an average of at least 6 replicates and standard deviation is shown. In SEM images of (B-D), the heating pulse of 50 ms was tuned to yield the maximum temperature of ~400 ˚C. Samples were heated in (B), (C) and (D) for 1, 10 and 15 times, respectively. In (E), spores were first heated to 400 ˚C followed by a second pulse which heated spores to 600 ˚C. In (F), spores were heated to 400 ˚C, 600 ˚C and 800 ˚C under serial 50 ms pulses.

hours [8-10,11,13]. These results demonstrate that maximum peak temperature, rather than repetitive heating, is the primary determinant for spore morphology and viability when exposed to fast heating rates (~10^4 ˚C/s).

Table 3.4. Changes to spore physical dimensions: the role of repetitive pulse heating. Data are derived from a random sample 50 spores in SEM images.

Heating conditions	Length(μm)	Width(μm)	Projected area(μm^2)
50 ms pulse×1, heat to 400 ˚C	1.26 ± 0.13	0.63 ± 0.11	0.67 ± 0.07
50 ms pulse×10, heat to 400 ˚C	1.20 ± 0.14	0.52 ± 0.07	0.55 ± 0.07
50 ms pulse×15, heat to 400 ˚C	1.08 ± 0.11	0.45 ± 0.05	0.50 ± 0.06
50 ms pulse×2, heat to 400 ˚C, then to 600˚C	0.80 ± 0.12	0.53 ± 0.05	0.43 ± 0.02

3.3.5. Mechanism of inactivation by fast pulse heating (~10^4 ˚C/s) through analysis of mutant spores

To understand the mechanism of spore inactivation under the fast heating scheme (~10^4 ˚C/s), I have utilized wild-type strain PS533 [58] and three mutant spore strains: 1) Strain PS3328 lacks *cotE* gene [59] which encodes a protein required for outer coat assembly [60]; 2) Strain PS578 has deletions in *sspA sspB* genes [58] which encodes SASP that bind and protect DNA in spores [3, 61]; Strain PS2318b lacks *recA* gene [36] which encodes a protein required for DNA repair. Wide-type spore strain (PS553) and PS3328 retained similar viability at 300 ˚C (Fig. 3.14). In contrast, PS2318b and PS578 mutants had significant viability reductions by 1-3 logs at peak temperatures around 300 ˚C (Fig. 3.14), indicating that the DNA-repair proteins and SASP protect the *Bs* spore against fast heating pulse. At peak temperatures >400 ˚C, wild-type and all the three mutant spores had similar viability reductions of ~4 logs (Fig. 3.14).

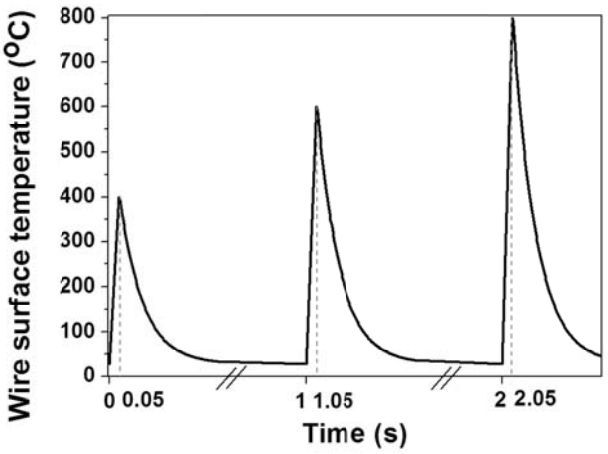

Figure 3.13. Simulated temperature temporal profiles during three different pulse heating. The serial peak temperatures these pulses triggered are 400 ˚C, 600 ˚C and 800 ˚C, respectively. All the three heating pulses have the same pulse time of 50ms and the rest time in between is ~10 s.

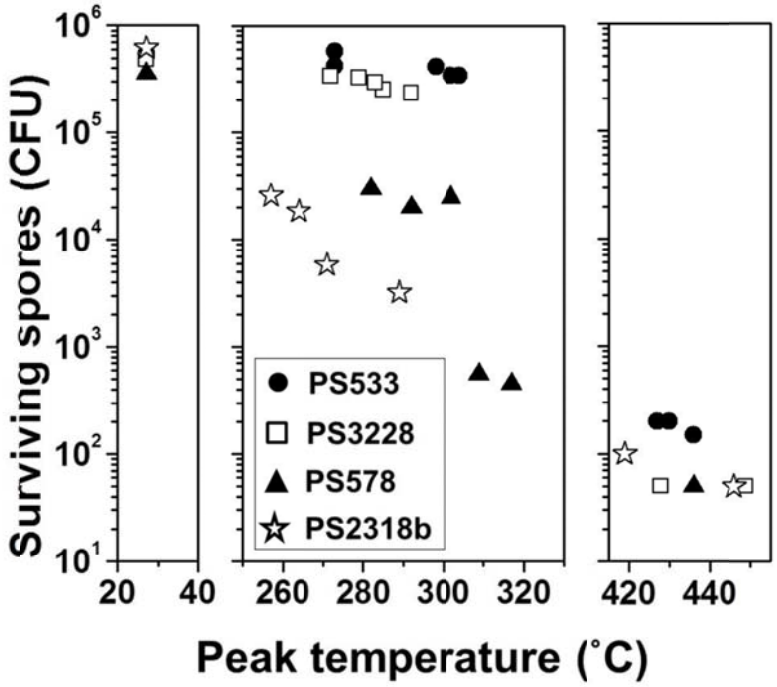

Figure 3.14. Survival counts of the wide-type strain (PS533) and three mutant strains (PS3328 (Δ*cotE*), PS578 (Δ*sspA* Δ*sspB*) and PS2318b (Δ*recA*)) of *Bs* spores at elevated peak temperatures in the 50 ms pulse heating.

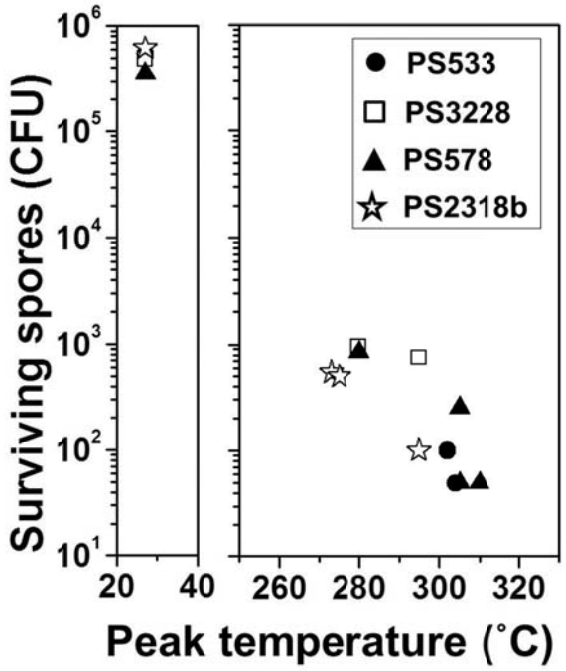

Figure 3.15. Survival counts of the wide-type strain (PS533) and three mutant strains (PS3228 (Δ*cotE*), PS578 (Δ*sspA* Δ*sspB*) and PS2318b (Δ*recA*)) of *Bs* spores at elevated peak temperatures in the 2 ms pulse heating.

Surface attached spores heated at ~10^4 ˚C/s under dry conditions had similar mechanism of killing as *Bs* spores heated in aerosols [22]. However at higher rates of ~10^5 ˚C/s, viabilities of most of mutant spores and wild-type spores were reduced similarly by ~ 4 logs at peak temperatures of as low as 300 ˚C, indicating that the spore killing mechanism at higher heating rates of ~10^5 ˚C/s is not only due to DNA damage (Fig. 3.15).

3.3.6. Heat inactivation of spores at ~10^5 ˚C/s under different external pressures

We hypothesized that ultrafast heating at rates >10^5 ˚C/s inactivate spores by increasing the internal pressure within the spore (see Discussion). We tested this

hypothesis by heating spores exposed to different external pressures. When heated at rates >10^5 ˚C/s in vacuum (1.3×10^{-5} Pa) with a peak temperature of 400 ˚C, holes formed on the spore surface indicating possible release of volatile species inside spores (Fig. 3.16). When spores were fast heated under 4 atm pressure (4.0×10^5 Pa) to 400 ˚C, bulges were observed on the surface of the spores indicating that volatile release was contained by the higher external pressure (Fig. 3.16). These results support my hypothesis that pressurization at heating rates of ~10^5 ˚C/s was associated with volatile release, thus contributing to spore inactivation.

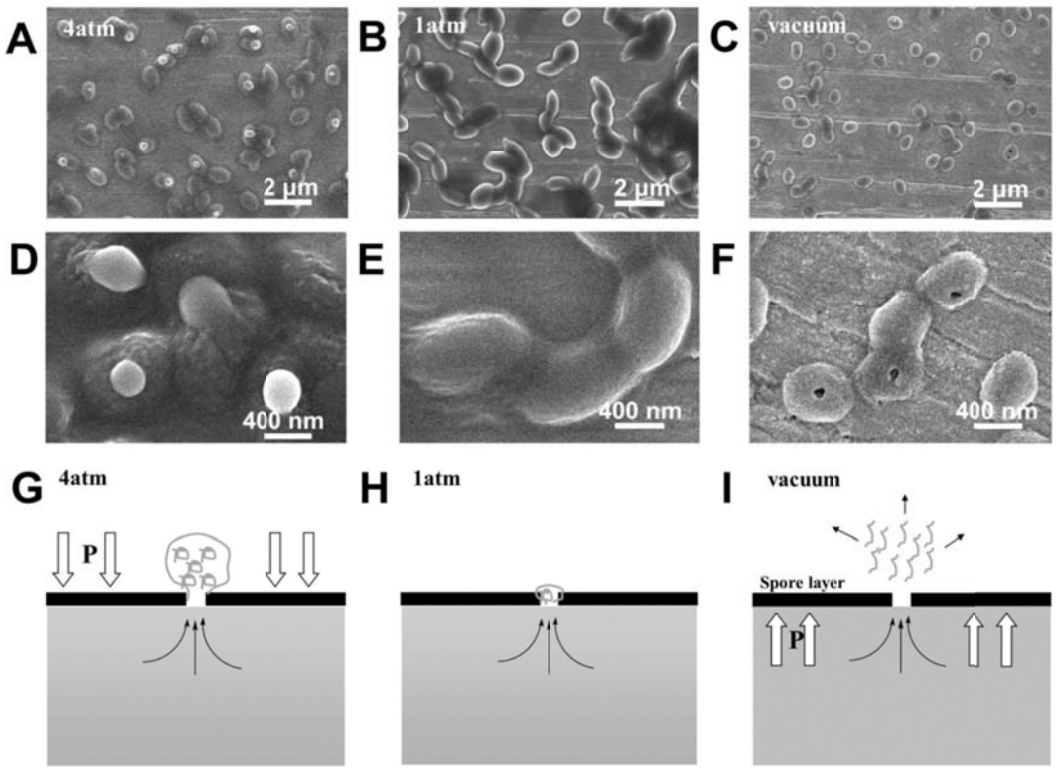

Figure 3.16. Effect of external pressure towards the morphological changes of spores heated to 400 ˚C at a heating rate of ~10^5 ˚C/s. The pressures applied to spores in image (A), (B), and (C) are 4.0×10^5 Pa, 1.0×10^5 Pa, are 1.3×10^{-5} Pa, respectively. (D), (E), and (F) are the enlarged SEM images of (A), (B), and (C), respectively. (G), (H), and (I) are schematic drawings of the effect of external pressure towards distinct spore morphologies.

3.4. Discussion

3.4.1. Temperature profiles of Bs spores on the Pt wire surface

Do *Bs* spores reach the same temperature as the Pt wire? Previous studies have revealed rapid heat transfer from the environment to the spore. Kumar et al [62] showed that the spore took ~0.1 ms to reach the surrounding temperature of ~400 ˚C. Xing et al [63] showed that the temperature could reach steady state in less than 0.5 ms. Since the spores are directly in contact with the wire (Fig. 3.1), the temperature increase of the spores will approximate the temperature increase of the wire in a 2 - 50 ms pulse heating process. I also assessed the accuracy of the temperature measurements and the distribution of heat along the length of the wire by using blackbody calibration, which showed that the wire temperature measurement fit to theoretical values precisely, especially below 1000 ˚C. Unlike the reported temperature measurements using thermocouples in the gas-phase spore inactivation studies that show a certain spatial temperature distribution [17-25], my results show a narrow temperature distribution along the entire length of the wire (see the evenly distributed temporal light intensity on wire in Fig. 3.3).

3.4.2. Spore viability heated to fixed peak temperatures under the same pulse time

There is intense interest in characterizing inactivation of *Bacillus* spores by sub-second heating pulses. Here I compare and contrast the results from thermal inactivation of spores affixed to solid surfaces to other studies. In general, sub-second heat inactivation of spores has a sigmoid temperature-kill relationship. Gates et al [18] implemented pressure shocks to rapidly increase the air temperature around

aerosolized *Bs* spores to 200 ˚C to 700 ˚C within 2-45 ms. The loss of viability occurred at ~200 ˚C, followed by decrease by 5 logs from 200 ˚C to 500 ˚C. Further reduction in viability at higher temperatures was minimal. Grinshpun et al [19, 20] exposed aerosolized *Bs* spores to hot air flow (150 ˚C to 1000 ˚C) and controlled the entire exposure time to be around 0.2 s to 1 s. Due to rapid heat transfer into aerosolized spores [62], the exact time to reach peak temperature could be much shorter. Similarly, the viability of spores started to decrease at 200 ˚C to 250 ˚C. From 250 ˚C to 370 ˚C, the viability dropped exponentially by 5 logs. Recently, Xing et al. [63] utilized a conductive heating system to rapidly heat *B. anthracis* spores placed on a gold foil in 0.1 s. They found that the viability decreased exponentially with temperature, with a reduction of 5 logs from 300 ˚C to ~700 ˚C. All these studies show clear correlations between temperature, heating time and spore inactivation efficiency. Although the temperature-kill curves from previous studies [18-20, 63] are similar to my results (Fig. 3.7), the spore inactivation mechanisms are different. Grinshpun et al [19, 20] heated aerosolized dry spores through a top-hat heating scheme and found the primary contribution to spore inactivation was the peak temperature and the heating time. Gates et al [18] killed spores in a gas dynamic heating scheme induced by mechanical shocks, in which the high pressure and top-hat temperature have synergistic effect on spore inactivation. However, the heating rate was not directly measured in these studies as an important factor. Our studies demonstrate that ~10^5 ˚C/s heating schemes can potentiate spore inactivation (Fig. 3.7).

The sigmoid nature of spore destruction kinetics is consistent with the kill curves within other time-kill models. Spores are resistant to applied heat during a short period of time, while suffered from rapid inactivation by 3-6 logs when the heating time is elongated [64]. Further increasing the heating time can induce complete inactivation of the few surviving spores [57]. Compared with these well-studied time-kill models, studies of temperature-kill relationships have been limited due to the narrow temperature range of conventional heating methods. The temperature-kill results demonstrate a similar sigmoid feature for spore inactivation. There are also three stages relative to the T_c. At temperatures well below the T_c, spores are resistant to thermal damage. At temperatures near the T_c, the spores are readily inactivated and the survival ratio drops logarithmically. At temperature well above the T_c, the remaining spores are completely inactivated.

3.4.3. Relationship of spore morphology heated to defined peak temperatures at two ramp rates

I observed two different morphological changes at the two different heating rates. When heated at ~10^4 ˚C/s rate that is similar to other heating scheme studies, I find that increasing severity of morphological change correlates with decrease in spore viability. Our results here demonstrate that when *Bs* spores heated to 400 ˚C at ~10^4 ˚C/s, a reduction of 38-42% in the projected area of spores was induced (Table 3.3). This reduction in projected area matches the ratio of areas of the spore cortex and the spore coat from previous observations made by TEM of spore thin sections [2, 65, 66]. From these TEMs, I calculated the projected areas of the intact spore with coat and

the spore that has shed the coat, and estimated the reduction in the projected area to be between 32-40% based on the removal of the coat (Table 3.5). In contrast when spores exposed to ~10^5 ˚C/s heating rate, the spore viability decreased rapidly at temperatures above 200 ˚C. However, the aspect ratio and projected area remain unchanged. The exact correlation between the mechanical changes of spores from morphological studies and the spore inactivation efficiency remains to be determined. These results suggest that spores exposed to these higher heating rates (~10^5 ˚C/s) are inactivated by a different mechanism than spores inactivated at ~10^4 ˚C/s.

Table 3.5. Reference data on the dimensions of the coat layer, cortex layer and core of *Bs* spores.

Reference	Coat thickness(μm)	Cortex thickness(μm)	Core radius(μm)	Projected area ratio
Driks, A. [65]	0.10	0.13	0.35	0.68
Nicholson,W et al. [2]	0.11	0.12	0.27	0.60
Takamatsu,H et al. [66]	0.06	0.12	0.12	0.65

Noat: The projected area ratio= (Projected area of a decoated spore) / (Projected area of an intact spore).

3.4.4. Spore inactivation at fast heating rates (~10^4 ˚C/s) through DNA damage

I determined the mechanism of heat inactivation of spores affixed on surfaces by utilizing mutant strains defective for DNA protection, DNA repair and coat assembly. I used the fast heating rate (~10^4 ˚C/s) that allows detection of increased sensitivity in mutant spores. The results show that DNA damage is a major contributor to inactivation of surface attached dry spores in the fast heat scheme, which is consistent with the mechanism for inactivation of aerosolized spores exposed to extreme dry heat [22, 50]. Spore coat is not required for heat resistance in this heating scheme which agrees with results by Setlow et al [3, 67] that demonstrated that decoated

spores had similar heat resistance to the wide-type spores. Instead, they found that the spore coat was mainly involved in resistance to some biocidal chemicals [47-49]. In agreement with the *cotE* mutant analysis, the morphological studies also show that when heated at ~10^4 ˚C/s spores with melted coats at 400 ˚C had minimal reduction in viability (Fig. 3.8B). Together, my results indicate that surface attached spores heated in my fast heating scheme (~10^4 ˚C/s) behave similar to dry spores heated in other aerosol heating schemes [17-25].

3.4.5. Spore inactivation at heating rates of ~10^5 ˚C through rapid pressurization inside spore

My results yield an interesting finding: when heated to the same peak temperature, higher heating rates of ~10^5 ˚C/s potentiate thermal inactivation of spores as compared to ~10^4 ˚C/s (see the temperature range from 250 ˚C to 450 ˚C in Fig. 3.7). What is the basis for enhanced spore inactivation by these higher heating rates? Since the peak temperature in these two heating schemes is the same, the observed enhanced killing of Bs spores must be due to the rate of heating (Fig. 3.7). We propose that this effect is due to vaporization of the internal contents of the spore, i.e. water, DPA and other volatiles. SEM images of spores heated at the ~10^4 ˚C/s revealed that the spores had minimal morphological change until >400 ˚C (Fig. 3.8 and Table 3.3). In contrast, SEM images of spores heated at ~10^5 ˚C/s formed the cracks and fissures at temperatures as low as 300 ˚C (Figs. 3.9C and 3.10). Spore viability was reduced at a lower peak temperature of 240 ˚C (Fig. 3.7) without detectable morphological change (Fig. 3.9), suggesting that transient holes may form

in the spore coat that is not detectable by SEM (Fig. 3.9B). We tested whether pressurization events are occurring on the heated spore by testing the effect of external pressure on spore morphology. Spores on a wire were heated to the same peak temperature at ~10^5 ˚C/s in three different pressures: (1) vacuum, (2) atmospheric (1 atm), and (3) four atmosphere (4 atm) pressure. Under vacuum, the spores displayed an exaggerated morphology in which large holes were formed (Figs. 3.16C and 3.16F). In contrast, SEMs of spores heated in excess external pressure showed 'balloons' on the surface of spores indicating that the external pressure contained the expansion of explosive volatiles (Figs. 3.16A and 3.16D).

Based on these observations, one possible mechanism for enhanced killing at ultrafast heating rates is the *dynamic* internal pressure generated by violent vaporization of volatiles, including water that imposes dynamic shock on spores. To estimate the *dynamic* internal pressure within spores during these heating events, I assumed that water is the primary volatile component in the cell since water comprises ~30% of the spore core mass [68]. Assuming minimal diffusive loss, and all liquid water is vigorously vaporized after 200 ˚C due to the rapid heating rates, *dynamic* pressure is a function of peak temperature [69]. Using the amount of water presented in the spore core and the volume of the spore core, the *dynamic* pressures at 240 ˚C and 400 ˚C are estimated to be 308 MPa and 404 MPa, respectively (Fig. 3.5). Based on my killing curves (Fig. 3.7) and morphological changes (Figs. 3.8 and 3.9), the maximum *dynamic* internal pressures that spores can sustain (without significant reduction of viability and failure of spore coat) are 308 MPa at a heating rate of ~10^5 ˚C/s, and 404 MPa at a heating rate of ~10^4 ˚C/s. This huge difference in the yield

stresses indicates that the assumption of minimal diffusive loss of volatiles from the spore core must be incorrect. If I assume the diffusive rate of water through the spore coat keeps constant at v (MPa/ms) during the temperature range of 240 - 400 ˚C, the real yield stress of spore coat (σ_{yield}) at both heating rates can be express as:

$$\sigma_{yield} = P_1 - vT_1 = P_2 - vT_2 \tag{3.13}$$

P_1 (308 MPa) and P_2 (404 MPa) are the maximum *dynamic* internal pressures of spores at heating rates of ~10^5 ˚C/s and ~10^4 ˚C/s, respectively. T_1 (2 ms) and T_2 (50 ms) are the pulse heating times at heating rates of ~10^5 ˚C/s and ~10^4 ˚C/s, respectively. The results are v = 2 MPa/ms and σ_{yield} = 304 MPa. Considering that the water diffusion rate (2 MPa/ms) is closer to the pressurization rate (8 MPa/ms) at ~10^4 ˚C/s, but much smaller than the pressurization rate (154 MPa/ms) at ~10^5 ˚C/s, it is easy to understand the potentiation of thermal inactivation at higher heating rates by internal pressurization. A similar explanation for spore inactivation was reported by Xing et al [63]. They found that the spore surface was ruptured after rapid heating to 300 ˚C for 10 s, suggesting the vaporized content inside spores cannot promptly diffuse out and therefore the pressure-induced mechanical stresses exceed the yield stress of spores. The authors measured the temporal modulus of spores with temperature and found the modulus to be ~ 400 MPa at 275 ˚C [70]. We should also note that the maximum hydrostatic pressures (400 – 800 MPa) employed in the industrial high-pressure sterilization approaches [71-73] are larger than my aforementioned result (304 MPa). This suggests that the dynamic yield stress of spores could be smaller than that under static pressure.

Given the approximations used in my estimates, and the fact that the tensile stress of the spore exterior layers is probably also temperature sensitive (decreases as the structure melts at high temperatures), my result indicates that spores in ultrafast-heat (~10^5 ˚C/s) and high-temperature processes are more susceptible to increased internal pressures and liable to lose both viability and morphological integrity. It should be noted that such critical heating rates may also be different for other spores, depending upon the degree of dehydration and the permeability of water in the spores.

3.5. Conclusion

Surface immobilized bacterial spores subjected to sub-second and ultrahigh heating conditions were characterized for spore inactivation and morphological changes. There are two key determinants in spore inactivation. First, maximal peak temperature greater than 700 ˚C led to 6 logs reduction in spore viability. Second, ultrafast heating of the initial pulse exceeding ~10^5 ˚C/s potentiates spore inactivation. Repetitive heating had no discernible effect on spore morphology and survival rate, implying that damage is not cumulative in sub-second heat exposures. At fast heating rates (~10^4 ˚C/s), mutant spores that lack *sspA sspB* and *recA* genes were more susceptible to inactivation, indicating that DNA damage contributes to spore inactivation at ~10^4 ˚C/s. At higher heating rates of ~10^5 ˚C/s, rapid pressurization inside spores is the major contributor to inactivation. The exact correlation between the mechanical changes of spores from morphological studies, and the spore inactivation efficiency remains to be determined. The temperature-time-kill correlation described for spores undergoing a pulse heating process (~10^3 ˚C/s to ~10^5

˚C/s) can be utilized for generating novel strategies to inactivate biological warfare threats due to bacterial spores.

Chapter 4: Synergistic Effects of Ultrafast Heating and Gaseous Chlorine on the Neutralization of Bacterial Spores*

Overview

We have seen the neutralization effect of ultrafast heat in Chapter 3. In this chapter, I continued to investigate the synergism between rapid heating (~10^4 ˚C/s to ~10^5 ˚C/s) and chlorine gas in the neutralization of *Bacillus thuringiensis* (*Bt*) spores – a close relative of *B. anthracis* (*Ba*), which is a known biowarfare agent. *Bt* spores were heated in a gas chamber with defined concentrations of Cl_2 gas and relative humidity (RH). The critical peak temperature (T_c) of spores, which corresponds to 50% reduction in viability, was decreased from 405 ˚C when heated at ~10^4 ˚C/s in air to 250 ˚C when heated at the same rate in 100 ppm Cl_2. SEM results show no obvious difference between the morphologies of spores heated in air or in Cl_2 at ~10^4 ˚C/s. These results indicate that Cl_2 gas acts in synergy with high temperatures (>300 ˚C) to neutralize Bt spores. Similarly, the T_c for *Bt* spores heated at the faster rate of ~10^5 ˚C/s was reduced from 230 ˚C when heated in air to 175˚C when heated in 100 ppm Cl_2. At ~10^5 ˚C/s, the treatment of Cl_2 did not alter spore morphology at temperatures below 300 ˚C. At temperatures above 450 ˚C with Cl_2, the spore coat detached from the underlying core. The effect of Cl_2 was further examined by changing the RH of Cl_2 gas. The results show that highly humidified Cl_2 (RH = 100%) reduced T_c by 170 ˚C and 70 ˚C at ~10^4 ˚C/s and ~10^5 ˚C/s, respectively, as compared to dry Cl_2 (RH = 0%). Energy dispersive spectrometric (EDS) results demonstrate that Cl on the spore

* The results presented in this chapter have been submitted to the following journal article: **W. Zhou**, M. W. Orr, V. T. Lee*, M. R. Zachariah*. Synergistic Effects of Ultrafast Heating and Chlorine Gas on the Inactivation of Bacterial Spores. ***Chem. Eng. Sci.***, 2015, *Submitted*.

increased with elevated peak temperature, with the majority of the Cl located in the shed spore coat. This study indicates that the major mechanism of spore neutralization by the synergism of Cl_2 and rapid heat is chlorine reacting with the spore surface.

4.1. Introduction

Bacterial spores are important since they pose a risk to public health and military biodefense [1-3]. Neutralization of spores is a significant challenge since they are much more resistant than their vegetative counterparts to a variety of external stresses such as UV irradiation, extreme pH values, chemicals, and temperature extremes [4-6]. Studies have shown that spore longevity and resilience is correlated to physical features of spores, including a tight proteinaceous spore coat that inhibits chemicals penetration, low water content in the spore core to reduce metabolism, as well as the production of proteins for DNA stabilization (e.g. α/β-type small acid soluble proteins (SASPs)) [6]. One of the primary strategies for spore neutralization is to expose them to autoclaving heat (120-150 ˚C) for minutes to hours [7-9]; however, this approach is not appropriate for the large-scale neutralization of spores. To further improve the killing efficacy, aerosol based techniques are being developed to rapidly inactivate airborne bacterial spores by rapid heating (>200 ˚C within a timescale of a second) [10-16]. At this timescale, more than 3-logs reduction in spore population can be achieved when the peak temperature ranges from 200 to 400 ˚C. An analogous approach of spore inactivation by heat has been tested using heat generated from exothermic reactions of energetic materials such as aluminum-based thermites [17].

This approach is able to produce even higher peak temperatures (> 2200 ˚C) over a shorter period (~0.1 s), and leads to a 7-log reduction of spore viability [17]. Although these methods are capable of neutralizing spores, an accurate and quantitative relationship of time-temperature-kill for spores is not available due to the variability in temperature distribution and the resident exposure time of these heating schemes. Nevertheless, a precise time-temperature-kill relationship is needed for predicting and ensuring a successful outcome of large-scale neutralization events. In order to improve the accuracy of measurements of the temperature history on spores, an alternative approach has been developed by heating spores deposited on conductive surfaces [18] that allows measurement of the transient temperature using the standard electric resistance-temperature relationships [18]. Since the transient temperature of immobilized spores can approximate that on the immobilizing surface [19], the time-temperature-kill relationship for spores can be accurately measured. Results showed that a 6-log reduction in spore counts could be achieved by rapidly heating spores to 600 ˚C within 50 ms at a heating rate of ~10^4 ˚C/s. The neutralization mechanism was likely due to DNA damage as mutants in *sspA sspB* are sensitized for killing [6]. Faster heating rates (~10^5 ˚C/s) also improved spore neutralization, which was associated with increased structural destruction of spore coat through increased pressure of vaporization [19].

In addition to heat, another commonly used disinfection procedure for spores utilizes biocidal chemicals [20]. Commonly used biocides (antibiotics, detergents, alcohol) have little effect on spore viability [21]. In contrast, strong oxidation agents, such as chlorine, iodine, sulfur, silver, and compounds containing these elements,

have demonstrated efficacy in spore inactivation [20]. Among these sporicides, Cl_2 is one of the few agents that are gaseous at room temperature. The main advantage of Cl_2 over other aqueous sporicides is that gas provides greater coverage, thus facilitating the neutralization of both airborne and surface-associated spores. Cl_2 can directly chlorinate functional groups on macromolecules in cells to damage proteins, nucleic acids and lipids [22,23]. In addition, Cl_2 can react with water to form hypochlorous acid (HOCl) and hydrogen chloride (HCl). Both compounds can also react with spores to inactivate them [24][25].

The performance of Cl_2 depends on two characteristic factors: concentration ("C") and inactivation time ("T"). The US Enivronmental Protection Agency and the water treatment industry has set the units of Cl_2 concentration in parts per million (ppm) and the inactivation time in minutes [26]. In general, the "CT" product is a constant for spores of a specific *Bacillus* strain required to achieve a defined reduction of viability [27]. Table 4.1 presents some documented "CT" results for different *Bacillus* spores [24, 26-38]. The "CT" product for a 4-log reduction in spore viability is ~3×10^4 ppm·min (~100 mg·min/l) for most of *Bacillus* spores when the Cl_2 concentration is below 3×10^3 ppm [26-30]. At much higher Cl_2 concentrations (*e.g.* 7×10^6 ppm), this "CT" value is significantly larger than ~3×10^4 ppm·min, and the minimum exposure time is 5 min [24, 31, 32]. In order to improve the neutralization efficiency at exposure times under a second, which according to the "CT" rule would require concentrations of Cl_2 >10^8 ppm (close to that of pure Cl_2 liquid). The use of these concentrations of Cl_2 would be impractical as a method to safely neutralize spores [39]. To meet the guidelines set by the U.S. Food and Drug Administration (FDA) for

food and drinking water processing (Code of Federal Regulations Title 21 Part 173/178) [40, 41], new approaches are in development to combine heat with 100 - 2000 ppm Cl_2.

Table 4.1. Chlorine concentration-exposure time-kill relationships for *Bacillus* spores in solution. All measurements were done at the room temperature.

Reference	*Bacillus* spore	Cl_2 concentration (ppm)	Exposure time (min)	Viability reduction
Brazis et al. [27]	*B. anthracis*	63-110	420	4-log
Brazis et al. [27]	*B. globigii*	50-113	1080	4-log
Rice et al. [28]	*B. anthracis*	267	120	2-log
Fair et al. [29]	*B. anthracis*	333	60	3-log
Rose et al. [26]	*B. anthracis, B. cereus, B. thuringiensis*	667	45-61	>4-log
Hosni et al. [30]	*B. globigii*	500-667	118-234	3-log
Brazis et al. [27]	*B. anthracis*	767-800	49	4-log
Brazis et al. [27]	*B. globigii*	833-867	82	4-log
Fair et al. [29]	*B. anthracis*	1000	30	3-log
Szabo et al. [31]	*B. anthracis*	3333	60	4-log
Kreske et al. [32]	*B. cereus*	6.7×10^4	5	>3.8-log
DeQueiroz et al. [24]	*B. subtilis*	8.3×10^6	5	4-log

One such potent, more environment-friendly and safer approach is to synergize the neutralization of spores by Cl_2 with heat. Xu et al. [42] studied the inactivation of *Bacillus* spores by Cl_2 (~1000 ppm) under high-temperature short-time pasteurization conditions (~80 ˚C, ~1min), and found a viability reduction of 6-logs. Further tests using a higher temperature of 120 ˚C resulted in inactivation of spores by 6-logs within 16s, whereas it took >30 mins to achieve viability reduction of 6-logs by employing either Cl_2 gas (1000 ppm) (Table 4.1) or heat (120 ˚C) [7-9]. Based on these results, higher temperatures (>200 ˚C), and diluted Cl_2 gas (< 2000 ppm) synergistically inactivated *Bacillus* spores.

In this work, I investigated the synergistic effects of ultrafast heating and Cl_2 gas on the inactivation of *Bt* spores. *Bt* spores, while closely related to *Bacillus anthracis* (*Ba*) spores that are considered as a serious bioterrorist weapon, is not pathogenic to humans. Both *Bt* and *Ba* spores were reported to have similar sensitivity to biocides [43], so I expect the results in this study can be utilized for the neutralization of *Ba* spores in the future. For these studies, *Bt* spores were electrophoretically deposited onto a fine Pt wire [19]. By tuning the heat pulse time (2 ms and 50 ms) and peak temperature (~1200 ˚C) for the Pt wire, the heating rate (~10^4 ˚C/s and ~10^5 ˚C/s) and time-resolved temperature for individual spores were measured [19]. Using this thermal approach, I evaluated the effect of 100 ppm (0.3 mg/l) Cl_2, a concentration below the FDA safety guidelines, in combination with different peak temperatures and heating rates, on the neutralization of spores. Spore viability and morphology were assessed after these treatments by determining the viable number of colony forming units (CFU) and scanning electron microscopy (SEM). To investigate the neutralization mechanism of Cl_2, spores were also heated in Cl_2 gas with different relative humidities, to see the roles of the hydrolysis products of Cl_2 (hydrogen chloride (HCl) and hypochlorous acid (HOCl)). Energy dispersive X-ray spectroscopy (EDS) was employed to determine the elemental changes of Cl and carbon (C) in spores.

4.2. Materials and methods

4.2.1. Spore attachment on platinum wires

Bt spores were sporulated in Difco Sporulation Medium (DSM) at 30 ˚C for 48 h. The 250 mL of DSM included 2 g Bacto nutrient broth, 2.5 mL 10% KCl, 0.375 mL 1 M NaOH and 2.5 mL 1.2% $MgSO_4 \cdot 7H_2O$. The spore concentration was enumerated by plating to be 8×10^9 colony-forming units per milliliter (CFU/mL). The purity of spores was found more than 99%. Bt spores were electrophoretically immobilized onto a sterilized platinum (Pt) wire with a diameter of 76.8 μm (Omega Engineering, Inc.). The electroplating experiments were conducted in an in-house spore deposition cell [44]. By controlling the biased deposition voltage, pulse frequency and overall charging time (from a 6340 sub-femtoamp remote sourcemeter, Keithley), I am able to prepare a uniform monolayer of Bt spores on the wire after 5 pulses [44]. More information of the spore deposition cell and spore coating scenarios in detail can be found in my previous studies (Chapter 2 and 3) [19, 44].

4.2.2. Wire heating test in Cl2 gas filled chamber

The spore coated wire was connected to an in-house built power source, working as a temperature jump probe (Fig. 4.1). The wire was then inserted into a gas chamber that is connected to a vacuum pump and a Cl_2 gas tank (Fig. 4.1). Prior to the pulse heating of the wire, the chamber was emptied by vacuum and replenish with the appropriate concentrations of Cl_2 gas. For evaluating the effect of relative humidity (RH) of Cl_2 gas, the chamber is also connected to a water bubbler that can supply water vapor into the chamber. RH was monitored using an attached humidity meter.

A defined thermal history for spores on wire during the heating period was measured through the dynamic electric resistance-temperature relationship for Pt (Callendar-Van Dusen equation [18]). The peak temperature (~200 ˚C to ~700 ˚C) and the heating rate (~10^4 ˚C/s to ~10^5 ˚C/s) can be precisely controlled by tuning the applied voltage and the pulse time (2 ms to 50 ms). The temperature-time profile for spores in the cooled region was calculated according to an energy balance equation which was dominated by the heat conduction. It is estimated that the cooling time scale is between ~300 ms and ~500 ms [19]. The detailed description of the transient temperature measurement on spores can be found in Chapter 3 [19].

4.2.3. Determination of colony forming units

The viable spores after various heat and Cl_2 treatments were enumerated by determining CFUs. Spore-coated wires were completely submerged in 1 mL of Lysogeny Broth (LB) media (10 g tryptone, 5 g yeast extract and 5 g NaCl per liter) and placed on a shaker at the 37 ˚C for three hours to allow for the germination and detachment of viable spores from the wire surface. After incubation, samples were serially diluted and plated on LB agar plates to count viable CFUs.

4.2.4. Characterization of morphology of spores

The surface morphology of spores with or without treatment of Cl_2 and rapid heat was investigated by SEM (Hitachi S-4700) using an accelerating voltage of 5 kV. Prior to imaging, the spore-coated wire was attached to stubs and then sputtered with gold/palladium alloy.

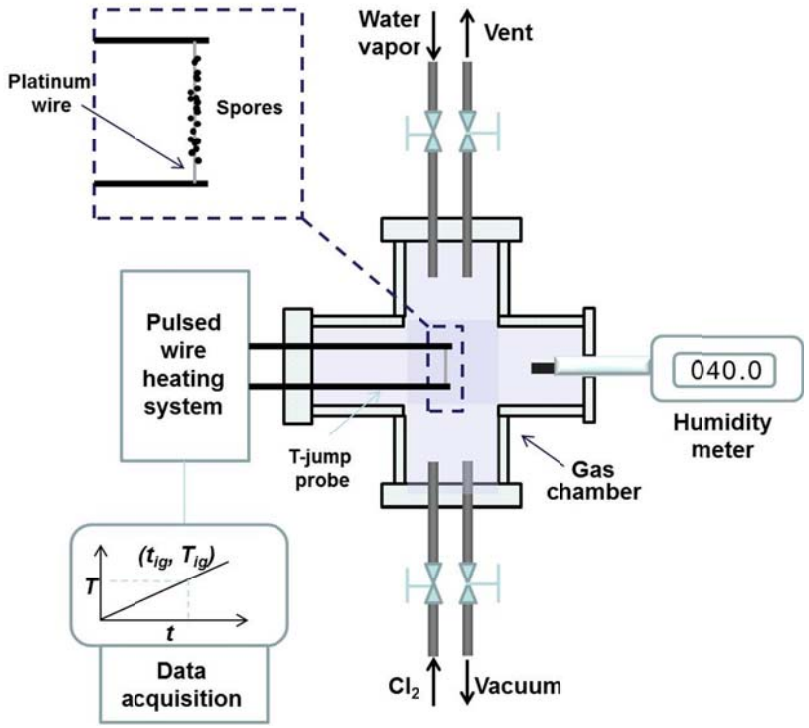

Figure 4.1. Schemetic of the T-jump probe involving one *Bt* spores coated wire, as well as the gas chamber supplemented with a humidity meter.

4.2.5. Characterization of hydrocarbon and chlorine contents inside spores

Quantitative EDS X-ray microanalysis using SEM was employed to analyze the elemental contents (carbon, chlorine and calcium) inside spores. Since calcium will not escape from spores by evaporation (boiling point at ~1500 ˚C) during the rapid heating in my temperature regimen (<700 ˚C), the detected calcium content was used as a control to measure the relative Cl and C contents. The tests were conducted in the line scan mode by detecting the elemental intensity along a line drawn across one spore. The ratio of mass fractions of Cl/Ca or C/Ca was calculated by comparing the integrated intensities of Cl/Ca or C/Ca along the line, respectively. For spores with their coats detached, a line was across either the cracked coat or the exposed core, to

analyze the distribution of elemental masses in both compartments. Statistical analyses are based on a spore population of ~10.

4.3. Results and discussion

4.3.1. Spore viability heated at two ramp rates in air and in Cl_2

The neat effect of fast heating on the viability of *Bt* spores in air was determined and the relationship between peak temperature and spore viability was plotted in Fig. 4.2. The viability data fit a sigmoidal model [45] as:

$$S = \frac{1}{1+\exp(k(T-T_c))} \tag{4.1}$$

where S is the survival ratio of spores (CFU_{final} / $CFU_{initial}$), T is the peak temperature, T_c is the critical peak temperature to induce viability reduction by half, and k is the heat resistance parameter. The fitted values of T_c and k are listed in Table 4.2. Compared to T_c (405 ˚C) at the temperature rate of ~10^4 ˚C/s, T_c at ~10^5 ˚C/s decreases to 230 ˚C. In addition, a reduction of 6-logs was achieved at the peak temperatures of 400 ˚C and 600 ˚C at ~10^5 ˚C/s and ~10^4 ˚C/s, respectively. These neutralization data for *Bt* spores resemble those for *Bs* spores in my previous studies (Chapter 3) [19], indicating that the faster heating rate of ~10^5 ˚C/s is able to effectively decrease the peak temperature required for spore neutralization when compared to the heating rate of ~10^4 ˚C/s. In addition, the k value of the neutralization curve at the higher heating rate (~10^5 ˚C/s) was larger than that at the lower heating rate (~10^4 ˚C/s), indicating that *Bt* spores are more sensitive to higher heating rates. These results show a better neutralization effect for *Bt* spores by higher heating rates and higher peak temperatures.

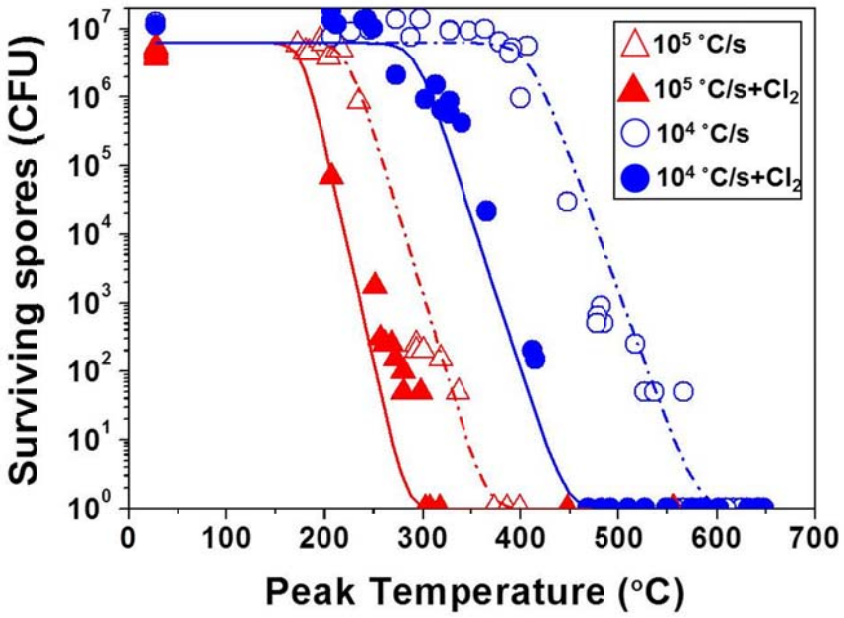

Figure 4.2. Survival curves of *Bt* spores versus peak temperature for 2 ms (10^5 °C/s) and 50 ms (10^4 °C/s) heat pulses, and with or without the presence of Cl_2 (100 ppm). The relative humidity was kept at 40%.

Table 4.2. Fitting results for the variables in eq 1.

Heating conditions	Cl_2 (+, -)	RH	k (°C^{-1})	T_c (°C)
50 ms heating pulse (~10^4 °C/s)	-	40%	0.090	407
50 ms heating pulse (~10^4 °C/s)	+	40%	0.065	252
50 ms heating pulse (~10^4 °C/s)	+	0%	0.065	352
50 ms heating pulse (~10^4 °C/s)	+	100%	0.083	180
2 ms heating pulse (~10^5 °C/s)	-	40%	0.109	232
2 ms heating pulse (~10^5 °C/s)	+	40%	0.146	176
2 ms heating pulse (~10^5 °C/s)	+	0%	0.136	247
2 ms heating pulse (~10^5 °C/s)	+	100%	0.131	177

Note: "+" represents the presence of Cl_2 during heating of spores, while "-" represents no Cl_2 during heating of spores.

The effect of Cl_2 gas and rapid heat was evaluated for their ability to synergistically neutralize *Bt* spores. The resistance of *Bt* spores to Cl_2 gas at room temperature was first assessed. After 15 minutes of exposure, spore viability was not affected when exposed to 1 ppm (0.003 mg/L) to 100 ppm (0.3 mg/L) of Cl_2 (Fig. 4.3), whereas spores were completely neutralized by 1000 ppm of Cl_2. We used 100 ppm of Cl_2 for the rest of this study since this concentration did not neutralize *Bt* spores in the absence of heat and is within the FDA guidelines (200 – 2000 ppm) [41, 42]. Heating to 250 ˚C at 10^4 ˚C/s, and 170 ˚C at 10^5 ˚C/s (Fig. 4.2) reduced spore viability. Compared to the viability results by heat treatment alone, the critical peak temperatures T_c decrease by 150 ˚C and 50 ˚C at heating rates of 10^4 ˚C/s and 10^5 ˚C/s, respectively (Table 4.1). In addition, a 6-log viability reduction was achieved at lower temperatures of 300 ˚C at 10^5 ˚C/s, and 450 ˚C at 10^4 ˚C/s. These results show a synergistic effect of rapid heat pulses and Cl_2 gas in the neutralization of *Bt* spores in both heating schemes. It should be noted that the k values for the neutralization curves of spores treated with Cl_2 and without Cl_2 are similar at the same heating rate (> 0.1 for 50 ms pulse and < 0.1 for 2 ms pulse), indicating that the temperature sensitivity of spore neutralization is primarily controlled by the heating rate instead of the addition of Cl_2.

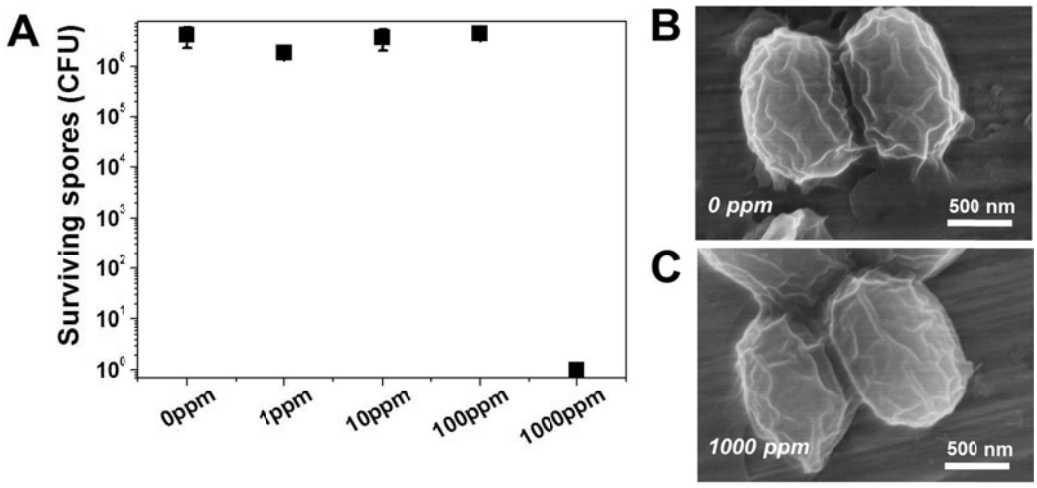

Figure 4.3. (A) The survivability of *Bt* spores exposed to Cl_2 gas with different concentrations for 15 mins in ambient air. (B) and (C) are SEM images of original *Bt* spores and *Bt* spores after treated with 1000 ppm Cl_2 for 15 mins.

4.3.2. Spore viability heated in Cl_2 gas of different RH at two ramp rates

To understand the mechanism of spore inactivation by Cl_2, different humidities were supplemented to the 100 ppm of Cl_2 in the gas chamber used for heat inactivation of *Bt* spores. The gas chamber for the results described in Section 4.3.1 has a relative humidity of ~40%, similar to that of ambient air. At ~10^4 ˚C/s, the critical peak temperature for spores heated in dry Cl_2 (0% RH) is 100 ˚C higher than that in moderately humidified Cl_2 (40% RH), whereas the critical peak temperature for spores heated in moist Cl_2 (100% RH) is 70 ˚C lower (Table 4.2). These results show that the T_c is reduced as the humidity of Cl_2 increases indicating that the synergistic effect of Cl_2 and rapid heat is potentiated by high humidity.

When the heating rate for *Bt* spores increases to ~10^5 ˚C/s, T_c increased for *Bt* spores treated with dry Cl_2 (0% RH) (Fig. 4.4B), similar to spores heated at ~10^4 ˚C/s heating rate (Fig. 4.4A). In contrast, moderately humidified Cl_2 (40% RH), and moist

Cl_2 (100% RH) resulted in similar T_c, 176 ˚C and 177 ˚C, respectively (Table 4.2). These ~10^5 ˚C/s results are distinct from those at ~10^4 ˚C/s since there is minimal change of spore neutralization when RH of Cl_2 increases from 40% to 100% (Fig. 4.4B). Thus, the synergistic effect of Cl_2 in different humidities at 10^5 ˚C/s is reduced as compared to the lower heating rates of ~10^4 ˚C/s. The reduction in the effect of humidity can be in part attributed to the reduced change in T_c (~60 ˚C) for spores heated in air and in Cl_2 at ~10^5 ˚C/s, which is much smaller than that (~160 ˚C) at ~10^4 ˚C/s (Fig. 4.2 and Table 4.2). To evaluate the heating-rate-dependent synergistic effects of Cl_2, I assessed the changes to *Bt* spore morphology and composition in response to Cl_2 and rapid heat.

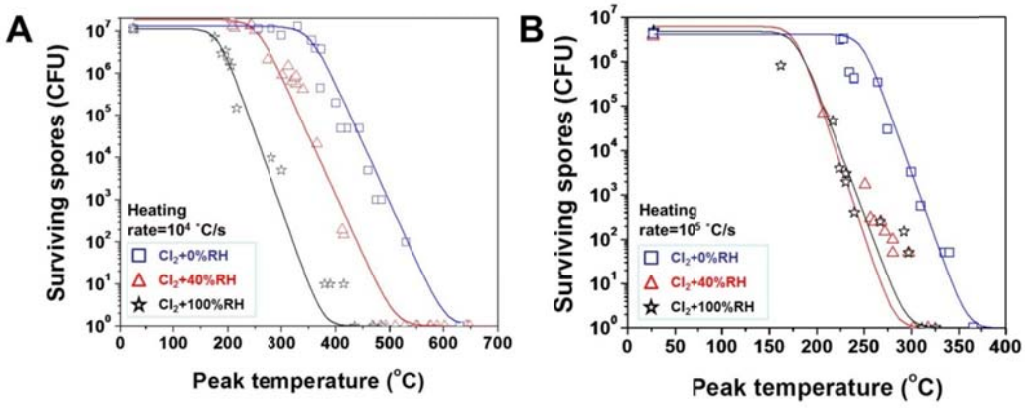

Figure 4.4. Survival curves of *Bt* spores versus peak temperature for 50 ms (10^4 ˚C/s) (A) and 2 ms (10^5 ˚C/s) (B) heat pulses. The blue, red, and black curves fit the survival of spores in response to Cl_2 and heat at 0%, 40%, and 100% relative humidities.

4.3.3. Spore morphology after treatment of rapid heat and Cl_2 gas

Cl_2 vapor in the chamber surrounds the immobilized spores and is in contact with the surface of the spores. The effect of Cl_2 and heat on *Bt* spores was assessed by scanning electron microscopy (SEM). The unheated spores had a general dimension

of 1.5 μm (longitudinal) times 1.0 μm (transversal) with wrinkly protrusions along their surfaces (Fig. 4.5A and Fig. 4.3B). In the absence of heat, treatment with Cl_2 gas up to 1000 ppm, which was sufficient to completely inactivate *Bt* spores, did not alter spore morphology (Fig. 4.3C). The relationship between spore morphology and peak temperature was investigated first for *Bt* spores exposed to the higher heating rates (~10^5 ˚C/s). The spore coat remains unaffected when heated to a peak temperature of 200 ˚C at ~10^5 ˚C/s (Fig. 4.5B). When heated to 300 ˚C at ~10^5 ˚C/s, the spore surface started to melt and the surface protrusions were reduced (Fig. 4.5C). Further increases in the peak temperature to ~400 ˚C at ~10^5 ˚C/s caused the surfaces of *Bt* spores to melt (Fig. 4.5D). At higher peak temperatures of >450 ˚C, the surface coat was completely melted and only the underlying core remained (Fig. 4.5E and 4.5F).

When 100 ppm Cl_2 was used, *Bt* spores were morphological indistinguishable from the spores treated by heat alone when the peak temperature is below ~400 ˚C (Fig. 4.5G-4.5I and Fig. 4.5A-4.5C). However, a distinct morphology emerged after ~400 ˚C when additional surface cracks were formed and the spore coat were detached from the underlying core (Fig. 4.5J-4.5K) in contrast to the spore coat melting in the absence of Cl_2. The disintegration of spore coat was further deteriorated when the humidity of Cl_2 increased to 100% at 400 ˚C (Fig. 4.6), suggesting that the effect of Cl_2 on the destruction of spore coat is associated with RH. Together these results indicate that Cl_2 acts on the surface of the spore to alter the fluidity of the spore coat.

The SEM images of *Bt* spores at a lower ramp rate of ~10^4 ˚C/s revealed similar morphological changes (Fig. 4.7A-4.7D) as that at a higher ramp rate of ~10^5 ˚C/s (Fig. 4.5A-4.5D). *Bt* spores started to melt at the peak temperature of ~300 ˚C, and

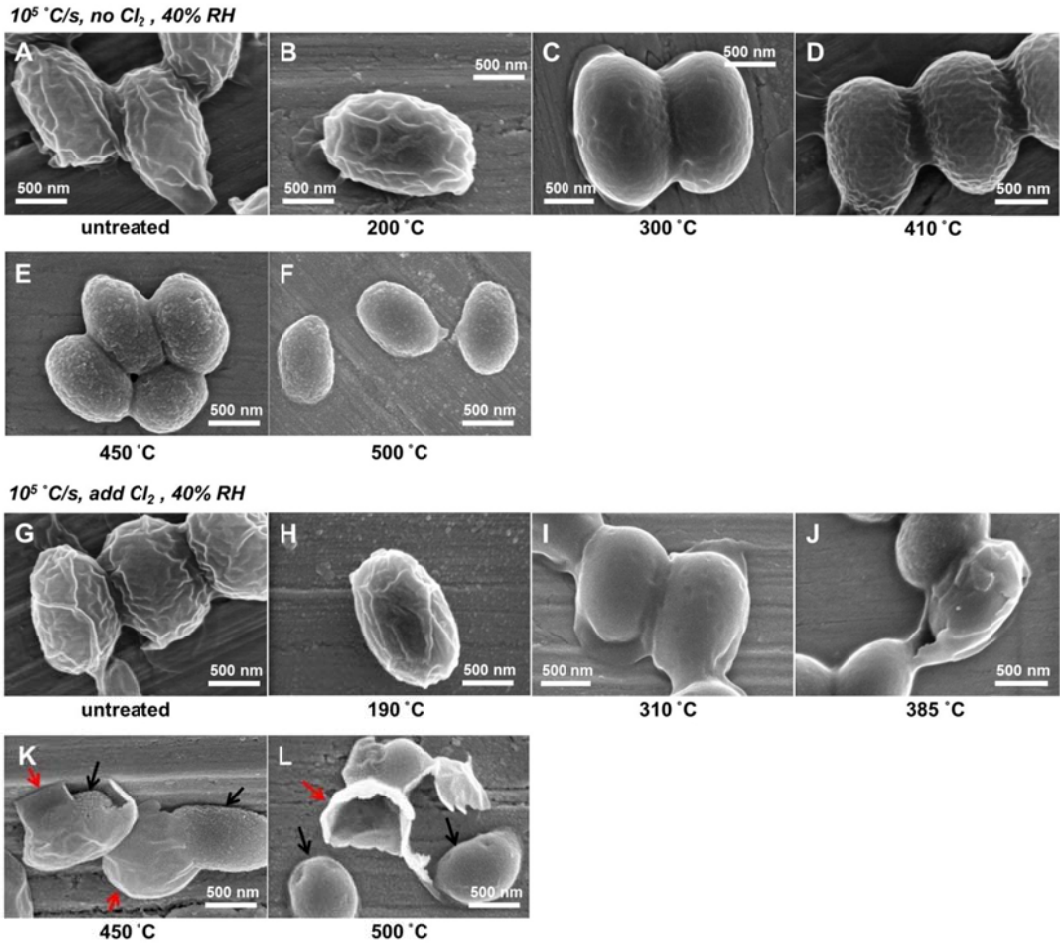

Figure 4.5. Spore morphologies when heated to different peak temperatures at 10^5 ˚C/s without (A-F) or with (G-L) the presence of Cl_2. The relative humidity was kept at 40%. The red arrows and the black arrows in image 4K and 4L designate detached spore coats and exposed spore cores, respectively.

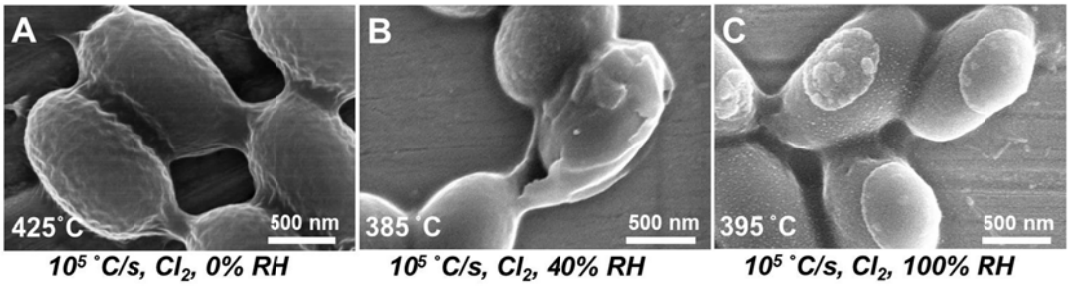

Figure 4.6. Spore morphologies when heated to ~400 ˚C at 10^5 ˚C/s in Cl_2. The relative humidities are controlled as 0% (A), 40% (B) and 100% (C), respectively.

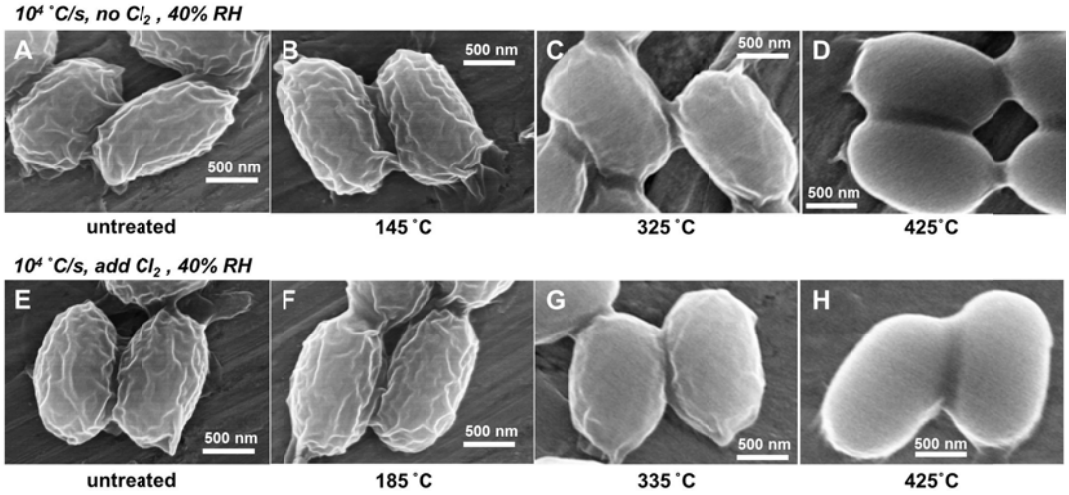

Figure 4.7. Spore morphologies when heated to different peak temperatures at 10^4 ˚C/s without (A-D) or with (E-H) the presence of Cl_2. The relative humidity is was kept at 40%.

completely melted at the peak temperature of ~400 ˚C. The addition of Cl_2 did not alter *Bt* spore morphology (Fig. 4.7E-4.7H) compared to the effect of heat alone (Fig. 4.7A-4.7D). These results indicate that the morphological changes were determined by peak temperatures at ~10^4 ˚C/s.

4.3.4. Changes in C and Cl contents inside Bt spores exposed to rapid heat and Cl_2

To evaluate the effect of Cl_2 on spores, the mass fractions of chlorine (Cl) and carbon (C) within spores treated by different heating schemes were measured using EDS. Calcium was used in these experiments as a standard since the calcium content inside spores will not change within my experimental temperature range (< 700 ˚C) (Fig. 4.8). The Cl content of the spores exposed to Cl_2 at room temperature was low indicating that Cl_2 gas does not react readily with the spores at ambient temperatures. The Cl content was increased as the peak temperature rose at ~10^4 ˚C/s, with the mass concentration of Cl for spores heated to 400 ˚C ~50 folds higher than that at room

temperature. At the higher ramp rate of ~10^5 ˚C/s, a similar trend of increased Cl content was observed for spores exposed to higher peak temperature. At each temperature, the Cl content of spores exposed to ~10^5 ˚C/s heating rate was higher than spores exposed to the ~10^4 ˚C/s heating rate (Fig. 4.8B). These results demonstrate that both heat and heating rate enhance the reaction of Cl_2 with the spores. To determine the location on the spore that is reacting with Cl_2, I took advantage of the SEM observation that the spore coat detaches from the core when heated to 500 ˚C at ~10^5 ˚C/s heating rate in the presence of Cl_2. EDS of the detached spore coat revealed that there is a Cl/Ca ratio of 0.335 as compared to 0.005 Cl/Ca ratio in the core (Fig 4.8B). The 70-fold increase in Cl concentration in the spore coat indicates that Cl_2 is reacting primarily with the surface of the spores during the rapid heating event.

Since SEM images reveal that the spores disintegrated at high temperatures, the carbon content within spores was evaluated. Spores heated either in air or in Cl_2 at ~10^4 ˚C/s did not lose carbon content (Fig. 4.8C). Given that the spore coat was not completely melted until 400 ˚C (Fig. 4.7), this result shows that the intact spore surface inhibits the release of volatile carbons. When rapidly heated at ~10^5 ˚C/s, the C content in spores decreased starting at 300 ˚C and 400 ˚C for *Bt* spores heated in Cl_2 and in air, respectively (Fig. 4.8D). The decrease in carbon content correlates with the SEM images of revealing damage to the *Bt* spores heated both in air and in Cl_2 at 400 ˚C (Fig. 4.5D and 4.5J). In addition, at 300 ˚C the remaining C content for spores heated in 100% RH Cl_2 is 40% less than that for spores heated in 0% RH Cl_2 (Fig. 4.9), indicating that the carbon release increase at a higher RH. This is consistent with

the fact that heating in the presence of Cl_2 gas at a higher RH induces more damage to the spore surface (Fig. 4.6). The carbon release occurred at peak temperatures that are higher than the corresponding T_c for *Bt* spores, indicating that release of volatile carbons is not the primary factor for spore neutralization at both temperature rates.

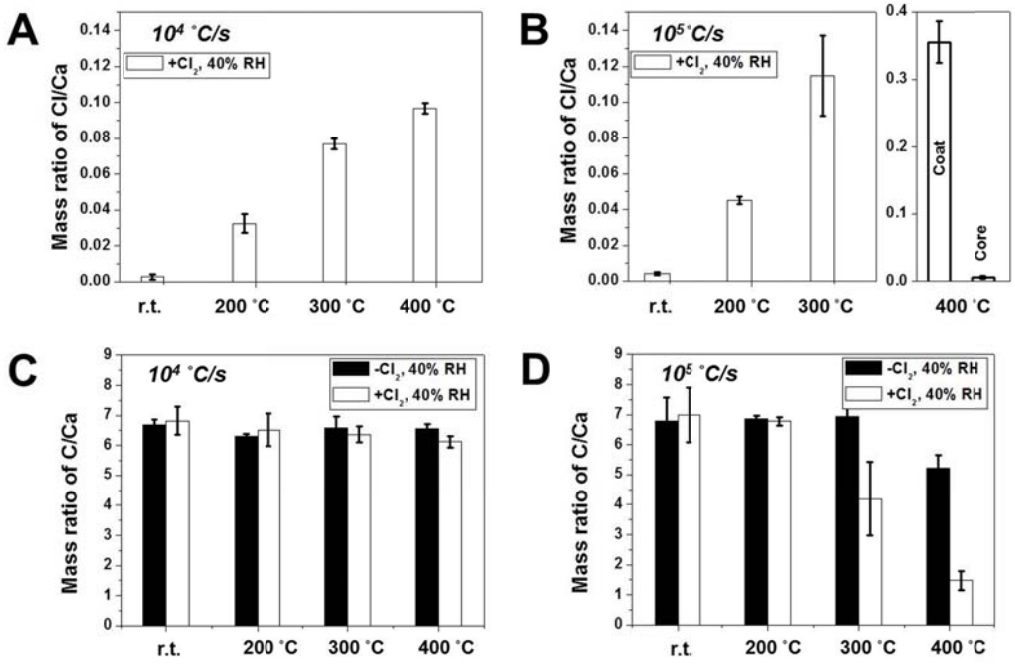

Figure 4.8. EDS (energy dispersive spectroscopic) results on the chlorine (A and B) and carbon (C and D) mass contents in spores heated at ~10^4 °C/s (A and C) and ~10^5 °C/s (B and D) rates. The right side of the graph (B) shows the relative mass contents of Cl in the coat and core of spores heated to 400 °C at 10^5 °C/s. The constant content of Ca inside spores is taken as a control and normalized to 1. Both the relative contents of Cl and C are presented as the mass ratios of Cl/Ca and C/Ca, respectively.

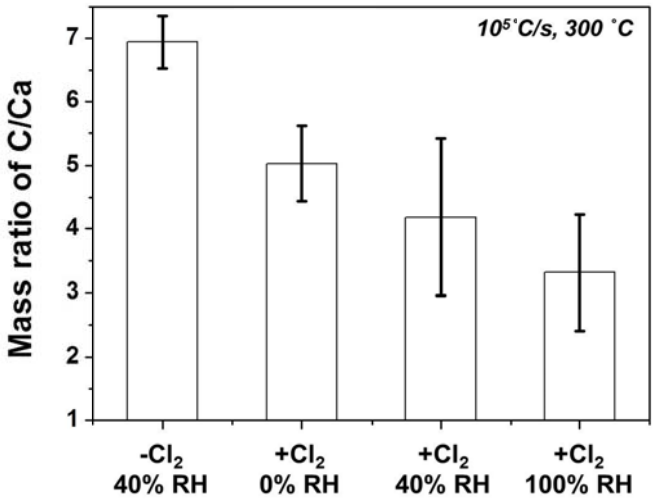

Figure 4.9. EDS results on the carbon mass contents in spores heated to 300 ˚C at ~10^5 ˚C/s. The RH was changed from 0% to 100%. The constant content of Ca inside spores is taken as a control and normalized to 1. The relative contents of C are presented as the mass ratios of C/Ca.

4.4. Discussion

4.4.1. Neutralization of Bt vs Bs spores at two heating rates without Cl_2

Our results (Fig. 4.2 and Table 4.2) show that the neutralization of *Bt* spores by rapid heat treatment alone is determined by the peak temperature and heating rate. The critical peak temperatures for *Bt* spores heated at ~10^4 ˚C/s and at ~10^5 ˚C/s are 407 ˚C and 232 ˚C, respectively (Table 4.2). Previously, I have also studied the neutralization of *Bs* spores under similar heating schemes [19]. The critical peak temperatures for *Bs* spores heated at these two ramp rates are 20 - 30 ˚C lower, indicating that *Bs* spores are more sensitive to rapid heat than *Bt* spores. SEM observations of *Bs* and *Bt* spores heated at ~10^4 ˚C/s show that spore coats melt at 410 ˚C [19] and 425 ˚C, respectively. When heated at ~10^5 ˚C/s, the coats of *Bs* spores started to generate visible fissures at a peak temperature of 300 ˚C [19]. In contrast, at

the same heating rate and temperature, there are only very small pin holes observed on the surface of *Bt* spores (Fig. 3C). Together, these results indicate that the spore coat of *Bt* is less temperature sensitive, which corresponds to the fact that *Bt* spores possess a higher T_c to rapid heat.

The previously reported neutralization mechanisms for *Bs* spores depend on the heating rate [19]. At ~10^4 ˚C/s, inactivation is likely due to the thermal damage to DNA since mutants lacking small acid-soluble proteins that protect the DNA within spore showed enhanced sensitivity to heat. At ~10^5 ˚C/s, the spore coat was compromised by elevated internal vapor pressurization from rapid heating [19]. Since neutralization of *Bt* and *Bs* was increased at the elevated ~10^5 ˚C/s heating rate, *Bt* spores likely undergo the same neutralization mechanism as *Bs* spores. This is supported by the similarity of SEM morphological changes in response to heating at ~10^4 ˚C/s. Furthermore, heating of *Bt* at ~10^5 ˚C/s to 300 ˚C caused the emergence of holes on the surface of the spores indicating that the *Bt* spores experienced a similar pressurization event as the *Bs* spores (Fig. 4.5C). Although the size of the holes on the surface of *Bt* spores are reduced in size, heating of *Bt* spores at ~10^5 ˚C/s to > 400˚C in the presence of Cl_2 led to the entire spore coat detaching from the underlying core. This phenomenon also supports the idea that internal pressure lead to rupture of the fixed spore coat. Results presented here and in earlier studies demonstrate that *Bs* and *Bt* spores undergoing rapid heat treatments can be neutralized through two different mechanisms depending on the rate of heating.

4.4.2. The interaction of Cl_2 and spores

Cl_2 synergizes with rapid heat pulses to inactivate spores at both the ~10^4 ˚C/s and ~10^5 ˚C/s heating rates (Fig. 4.2). Our results thus raise two central questions: 1) which form of Cl_2 is enhancing the synergistic killing of *Bt* spores? 2) where is this form of Cl_2 acting on the spore? The mechanism by which Cl_2 synergizes with heat pulses is not completely understood. Cl_2 gas, in addition to being a potent oxidizer, can form chemical bonds with numerous organic and non-organic molecules [23]. Our study has revealed several important findings regarding the form of Cl_2 that is enhancing synergistic killing with heat. First, increased water vapor concentrations in the chamber enhanced the potency of Cl_2 (Fig. 4.4). Cl_2 can readily react with H_2O to form HCl and HOCl [23]. Since Cl_2 synergizes with heat pulses minimally in the absence of humidity (Fig. 4.4), the compounds that actively enhance neutralization are likely HCl or HOCl rather than Cl_2 gas. Additional evidence for the higher neutralization activity of HCl/HOCl than Cl_2 is that when the peak temperature increases from 100 ˚C to 300 ˚C, the molar ratio of Cl_2/HCl decreases from ~4 to ~0.13 due to a biased reaction equilibrium from $Cl_2 + H_2O$ towards HCl + HOCl at high temperatures (according to CEA (NASA Chemical Equilibrium with Applications) calculations [46] given that the initial concentration of Cl_2 is 4.2×10^{-3} mol/m^3 with a RH of 40 %). Correspondingly, the spore viability reduced significantly as the temperature increased suggesting that HCl/HOCl is more effective in spore neutralization. HCl and HOCl have unique chemical properties. HCl is a strong acid that can act to denature proteins on the spore coat [47-49]. In contrast, HOCl can react with organic molecules leading to chlorine covalently attached to the

molecules on and in the spores [23]. But neither at room temperature appears to be efficient at neutralizing Bt spores (Fig. 4.3) suggesting that the reaction of HCl or HOCl with spores is promoted by heat. For reasons described below, I believe that HOCl is likely the active form of chlorine. Nonetheless, future studies with HCl alone, HOCl alone, or the combination of the two will provide definitive data regarding the specific form of chlorine that promotes synergistic killing with rapid heat pulses.

The target of Cl_2 inactivation on the spore is also an area of interest since this can reveal vulnerabilities of *Bacillus* spores that can be exploited in biodefense. The EDS data on Cl support the idea that the heat treatment with Cl_2 leads to an accumulation of Cl on the detached spore coat (Fig. 4.8) indicating the chlorine is interacting primarily with the surface of the spore during the heating pulse. The Cl detected in the spore coat by EDS is either deposited as Cl^- anion from deprotonated HCl or covalently attached through chemical reactions of HOCl to cellular organic molecules. There are two reasons, one chemical and one biological, that favor covalently attached chlorine through HOCl. Our observation that heat synergizes with the form of chlorine that attacks the spore suggests that HOCl rather than HCl is the active agent. This is because the electrophilic attack on biological molecules by $Cl^{\delta+}$ (partially polarized chlorine) from the HOCl molecule possesses a high reaction rate constant and is more temperature-dependent, with an increased reaction rate in a high temperature range (> 100 ˚C) [23]. In contrast, even though deprotonation of HCl occurs rapidly at room temperature, the electrophilic attack by H^+ is less dependent on temperature and more dependent on the pH value of the system. Supporting the theory that HOCl rather than HCl is responsible is the observation that spores are

quite resistant to acid stress alone [6]. The observed synergistic effect of heat pulse and Cl_2 only at elevated temperatures argues against the pH change caused by HCl, which would occur even at ambient temperature. Future studies of the synergistic effect of HOCl with rapid heat pulse would provide direct evidence to support the active compound that inactivates spores. Furthermore, future identification of the spore coat protein(s) that are covalently modified by chlorine will reveal the bacterial target(s) that confers sensitivity.

4.4.3. Synergistic neutralization mechanisms for Bt spores by rapid heat and Cl_2

There are two potential mechanisms for the observed synergistic effect in spore neutralization between rapid heat and Cl_2: 1). A chemical mechanism in which heat activates Cl_2 to become a more potent biocide or 2). A biological mechanism in which Cl_2 and heat damage different targets in the spores to enhance inactivation. Although these two potential mechanisms are not mutually exclusive, the synergistic effect of heat and Cl_2 is at least in part due to the heat pulse overcoming the activation energy of reactions between chlorine and the spore. The EDS data shows that exposure to Cl_2 alone does not increase Cl content in the spore. Only when heated does the Cl content of the spore increase, supporting the idea that heat enhances the reactivity of Cl_2. In addition to the increase in Cl_2 reactivity, the biological targets of heat and Cl_2 act on different parts of the spore. Heat pulses at ~10^4 ˚C/s damage DNA [19], whereas Cl_2 targets the spore coat. The combination of coat damage and DNA damage can act synergistically to neutralize spores. Support for this model of inactivation is that heat pulses at ~10^5 ˚C/s, which inactivates spores primarily

through physical damage of the spore coat [19], synergizes minimally with Cl_2. Thus damaging different targets within the spores, rather than the same target, enhances synergistic neutralization.

Another feature of the synergism of Cl_2 with heat pulses is that this effect occurs at peak temperatures and heating rate far below what was required to fix and detach the spore coat (Fig. 4.8). An open question is whether the effect observed at the higher peak temperature (>500˚C) and high heating rate (~10^5 ˚C/s) applies to the lower peak temperature and heating rates, which nonetheless synergize with Cl_2 to neutralize *Bt* spores. Despite the lack of visual changes of the spores as detected by SEM at peak temperatures of under 300 ˚C, the Cl content on the spore increases as detected by EDS. One interpretation of these results is that at heat pulses between 200-300 ˚C activates Cl_2 to interact with spores. Even this lower level of chlorine modification of the spore surface can negatively impact the function of the spore coat and increase spore inactivation.

4.5. Conclusion

Surface immobilized *Bt* spores subjected to the synergistic effects of ultrafast heating and biocidal chlorine gas were characterized by several observations including changes in viability, morphology, and composition. At the heating rates of ~10^4 ˚C/s, the critical peak temperatures for spore neutralization were reduced from 407 ˚C in air to 252 ˚C when exposed to 100 ppm Cl_2. At the higher heating rates of ~10^5 ˚C/s, the critical peak temperatures for spore neutralization are decreased from 232 ˚C in air to 176 ˚C when exposed to 100 ppm Cl_2. Cl_2 synergizes with rapid heat

pulse to enhance spore neutralization. Additional experiments revealed that the synergistic effect of Cl_2 and heat was increased in high humidity, whereas the synergistic effect decreased in low humidity. Cl_2 can react with water to generate HCl and HOCl, which in turn react with the spore. Despite enhancing neutralization, Cl_2 and heat pulses under 300 ˚C did not alter the morphology of the spores. However, treatment of spores at peak temperatures >450 ˚C at ~10^5 ˚C/s caused the spore coat to detach completely from the endospore. EDS results showed that Cl is present in heated spores and the majority of the chlorine is present in detached spore coat indicating that chlorine is acting on the surface of the spores. These results suggest that the spore surface damage caused by Cl_2, via HOCl and/or HCl, was found to be the major mechanism in enhanced spore neutralization by rapid heat.

Chapter 5: Persulfate Salt as an Oxidizer for Energetic Nano-thermites*

Overview

In this Chapter, I started to evaluate the heat and biocidal effects of novel energetic materials, expecting to bridging to the temperature-time-kill database I achieved in previous studies (Chapter 2 and 3). Nanoscale potassium persulfate ($K_2S_2O_8$), was evaluated as an alternative to other peroxy salts, such as periodates (KIO_4), in aluminum-fueled energetic nano-composite formulations. High speed imaging coupled with temperature jump (T-jump) ignition found the nano-Al/$K_2S_2O_8$ reaction to have an ignition temperature of 600 ˚C which is comparable to nano-Al/KIO_4 and lower than nano-Al/K_2SO_4. Results from constant-volume pressure cell experiments further show that nano-Al/$K_2S_2O_8$ releases more gas and has a longer burn time than nano-Al/KIO_4. Thermal analyses at low heating rates (10 ˚C/min) by coupled differential scanning calorimetry (DSC), thermal gravimetric analysis (TG) and mass spectrometry (MS) show that there are three main steps of thermal decomposition for nano-$K_2S_2O_8$, with initial exothermic decomposition to release O_2 at 270 ˚C, and following endothermic decomposition to release both O_2 and SO_2 at higher temperatures. The Heat of Formation of $K_2S_2O_8$ was measured to be -1844.5 kJ/mol based on the DSC results. Experiments performed at ultrafast heating rates (~10^5 ˚C/s) using temperature-jump time-of-flight (T-jump/TOF) MS show that the low O_2 generation temperature of nano-$K_2S_2O_8$ contributes to its high reactivity in nano-

* The results presented in this chapter have been published in the following journal article: **W. Zhou**, J. B. DeLisio, X. Li, L. Liu, M. R. Zachariah*. Persulfate Salt as an Oxidizer for Biocidal Energetic Nano-thermites. ***J. Mater. Chem. A***, 2015, 3, 11838–11846.

thermite compositions. An ignition mechanism involving gaseous oxygen was proposed for nano-thermite compositions containing reactive oxysalts such as nano-$K_2S_2O_8$. In contrast, a condense phase ignition mechanism was proposed for nano-thermites involving less reactive oxysalts such as nano-K_2SO_4. Given that the nano-Al/$K_2S_2O_8$ system is highly exothermic in addition to generating a considerable amount of SO_2, it may be a candidate for use in energetic biocidal applications.

1. Introduction

Energetic nano-composites, commonly referred to as nano-thermites, are studied for application in propellants, explosives and pyrotechnics due to their rapid exothermic reactions with high energy density [1-4]. For nano-aluminum (Al) fuel based energetic composites, typical oxidizers include nano-sized metal oxides (CuO [5-7], Fe_2O_3 [8-10], Bi_2O_3 [11,12], etc.), oxysalts (NH_4NO_3 [13,14], $NaNO_3$ [15], $NaClO_3$ [16], etc.), and the more oxidative peroxy salts (NH_4ClO_4 [17,18], $KClO_4$ [19,20], $NaIO_4$ [21,22], etc.). In comparison to metal oxides and oxysalts, peroxy salts possess a higher atomic oxygen content (Table 1.3), therefore they typically outperform the aforementioned oxidizers in gas generation and burn rates [20]. Nonmetal-oxygen bonds (Cl-O, I-O, etc.) in peroxy salts typically have lower dissociation energies, than metal-oxygen bonds (Cu-O, Fe-O, Bi-O, etc.) in metal oxides (Table 1.3) [23,24], suggesting a higher oxygen mobility in peroxy salts that can lead to decomposition and oxygen release at lower temperatures. However, the widely used peroxy salt, $KClO_4$, is hygroscopic and has environmental issues, due to the presence of chlorine. These issues have limited its application in many traditional

pyrotechnic formulations [20]. A recent study demonstrated that KIO_4, alternatively, has lower toxicity [26] and hygroscopicity [25] making it ideal for applications in illumination and gas generation.

The formal oxidation state of oxygen in each of the aforementioned oxidizers is -2. Exceptional metal peroxides and metal superoxides exist that have higher oxidation states of oxygen (e.g. -1 for Na_2O_2 and -0.5 for NaO_2) resulting in stronger oxidation capability. Compared with common metal oxides and peroxy salts whose oxidation capability is based on satiated bonding of oxygen with another element (metal or nonmetal), peroxy compounds with oxidation states greater than -2 feature an oxygen-oxygen bond that has much lower bond dissociation energy [27] resulting in higher oxidative strength (Fig. 5.1). More importantly, the intermediate radicals (e.g. hydroxyl radical ($OH\cdot$)) generated from decomposition of these peroxy compounds in solution are able to initiate a chain of degradation reactions involving other subsequent radicals and oxidants, imposing even higher oxidation ability than the original oxidizers that mainly follow an electron capture based oxidation mechanism [28-31]. As of now, researchers have yet to investigate oxygen-oxygen bond containing oxidizers in the nano-thermite formulations most likely due to the oxidizers being unstable solids at room temperature [32].

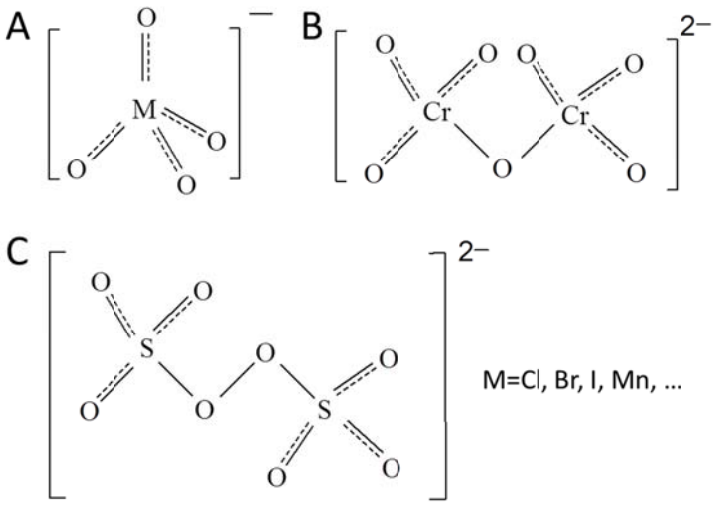

Figure 5.1. Molecular structures of three types of peroxy salt anions. (A) includes perchlorate (ClO_4^-), perbromate (BrO_4^-), periodate (IO_4^-), permanganate (MnO_4^-). (B) is dichromate ($Cr_2O_7^{2-}$). (C) is persulfate ($S_2O_8^{2-}$).

Energetic nano-thermites have been recently investigated for potential widespread neutralization of harmful microorganisms due to recent threats of bio-terrorism [33] and public health issues [34]. Bacterial spores, protected by their multiple self-defending mechanisms, are one of the most resilient and vastly distributed microorganisms [35,36]. Traditionally, two of the most studied and effective inactivation strategies include extreme heat and exposure to biocidal chemicals (e.g. iodine and silver) [36]. In order to enhance the inactivation efficiency, especially on an emergency basis, dual-function approaches that incorporates biocidals into thermite formulations, are attractive as they ideally can generate a lot of heat, and release biocidal agents upon ignition. Zhang et al [37-39] studied a mechanically mixed energetic formulation assembled via cryomilling of iodine and aluminum powders, and found the mixture to be thermally stable when the iodine content is below 30% by mass. An alternative manner to incorporate biocidal elements into

thermite formulations is through chemical bonding. Both silver oxide (Ag_2O) [40,41] and iodine oxide (I_2O_5) [42-47] have been previously investigated in thermite compositions. Both systems are competitively high in energy density when compared to other high performance metal oxides. In addition, they have exceptional, >60% w.t., generation of biocidal products (Ag and I_2) in the aluminum-fueled thermites. Another class of strong oxidizers containing biocidal elements are halogenated oxysalts/peroxysalts such as chlorates/perchlorates and iodates/periodates as mentioned before [17-22,25]. Recently, silver iodate was considered as an oxidizer in a biocidal thermite system [48]. Despite the higher activities of these halogenated (per)oxysalts, neither systems produces elemental silver or halogen as a potential biocide [17-22,25,48].

Considering the challenge of identifying new potential oxysalts capable of generating biocidal products as well as possessing high energy density, an alternative strategy of substituting the halogens in oxysalts with other biocidal elements is employed. Sulfur is widely used as a pesticide [49] and some sulfur-containing species such as sulfur dioxide (SO_2) [50] and sulfuryl fluoride (SO_2F_2) [51] have effective bactericidal and fungicidal properties. A recent report shows that sulfur-containing nanoparticles were able to kill 5 log bacterial spores after 30 mins of contact without heating, demonstrating sulfur's strong sporicidal capability [52]. The sporicidal capability of sulfur has not been compared to traditional biocides such as Ag and I_2 despite the large natural abundance of sulphur [53]. Therefore, incorporating sulfur into nano-thermite formulations, especially into peroxy

compounds with oxygen-oxygen bonds, demonstrates potential for an effective biocidal energetic material.

Persulfate, which has a symmetrical molecular structure bridging two sulfate groups with an oxygen-oxygen bond (Fig. 5.1), shows higher stability at room temperature analogous to periodate [25,29]. At elevated temperatures, persulfate anions in solution show stronger oxidation capability than permanganate anions [29] and periodate anions [54], and can trigger the oxidation of a variety of compounds [28-30]. This oxidative priority of persulfate facilitates its wide-range applications in antiseptics and remediation of contamination in nature [29-31,55-57]. Although persulfate displays strong oxidative capabilities in water, it has never been utilized in more violent solid state reactions (e.g. thermite reactions).

In this work, potassium persulfate ($K_2S_2O_8$) was chosen as a potential biocidal oxysalt due to its high oxidation state as well as rich content of sulfur. Potassium sulfate (K_2SO_4) and Potassium periodate (KIO_4) were employed as controls. These nano-sized oxysalts were prepared using a spray-drying approach. Simultaneous differential scanning calorimetry (DSC), thermal gravimetry (TG) and quadruple mass spectrometry (MS) were performed to investigate the decomposition of $K_2S_2O_8$ nanoparticles at low heating rates. In order to analyze the reaction mechanisms at high heating rates, which more accurately simulate a combustion event, temperature-jump time-of-flight (T-jump/TOF) MS was employed. A constant-volume combustion cell was used to evaluate the pressurization rise and optical emission intensity during the combustion of nano-thermites. High speed imaging of the

combustion of rapidly heated nano-thermites was also conducted to test the ignition temperatures of these thermite systems.

5.2. Experimental section

5.2.1. Preparation of nano-oxysalts and nano-thermites

$K_2S_2O_8$ powders were purchased from Fluka. K_2SO_4 and KIO_4 powders were purchased from Sigma-Aldrich. Al nanopowders were obtained from the Argonide Corporation, and have a size of 50 nm as designated by the supplier.

Nano-sized particles of the oxysalts above were prepared by aerosol spray-drying (Fig. 5.2). In detail, 0.47 g $K_2S_2O_8$ as-received powders were dissolved in 100 mL H_2O, which were then sprayed into water droplets of ~1 μm in size [20,25] by ~35 psi pressure air flow. The droplets were first passed through a diffusion dryer to remove most of the water, followed by a tube furnace at 150 ˚C for complete dehydration. Finally, the nanoparticles were collected on a Millipore membrane filter (0.4 μm). In the preparation of nano-K_2SO_4 and nano-KIO_4, 0.3 g and 0.4 g of as-received K_2SO_4 and KIO_4 powders were dissolved in 100 mL H_2O, respectively, followed by the same synthetic route as for nano-$K_2S_2O_8$ with the exception of the furnace temperature being set at 180 ˚C. The sizes of these three types of nanoparticles were measured by scanning electron microscopy (SEM, Hitachi, SU-70 FEG-SEM). The crystal structures of these nano-oxysalts were confirmed by powder X-ray diffraction (XRD) from Bruker D8 Advance using Cu Kα radiation.

Three nano-thermite compositions comprised of nano-Al and collected nano-oxysalts above were prepared by mixing these nanoparticles in hexane

stoichiometrically and sonicating for 30 mins [20,25]. The solvent was then evaporated at room temperature, and the solid nano-thermite powders were collected. It should be noted that since nano-Al contains 30% w.t. alumina (Al_2O_3) shell, the actual weight of nano-Al added was 1.4 times higher.

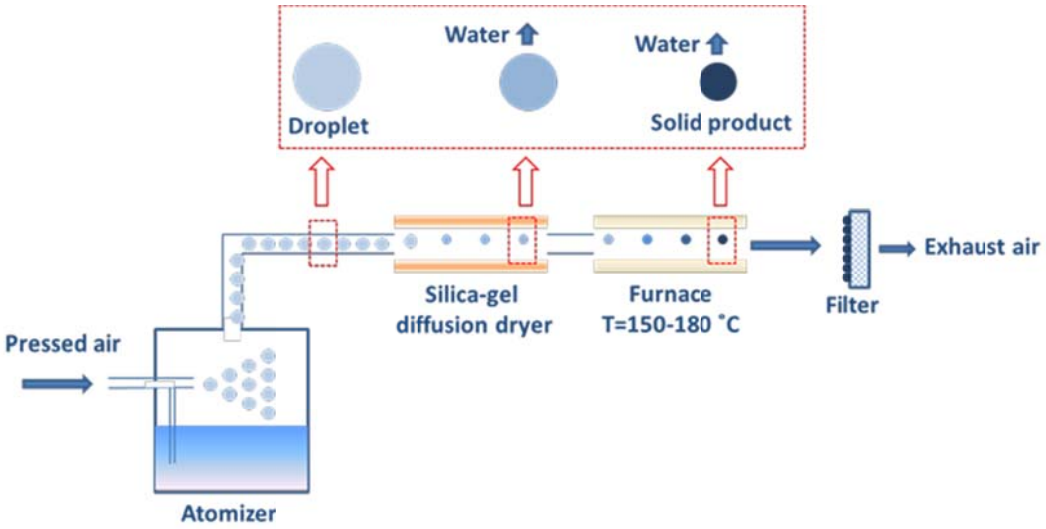

Figure 5.2. Spray-drying process of preparing nano-oxysalts.

5.2.2. Constant-volume combustion of nano-thermite reactions

A constant-volume combustion cell was used to study the pressurization and optical emission during the nano-thermite reactions. 25 mg of nano-thermite sample was loaded inside the ~13 cm^3 combustion cell in air. After ignition via a resistively heated nichrome coil resting on top of the sample, and the temporal pressure and optical emission from the nano-thermite reaction were measured by a piezoelectric pressure sensor and a photodetector, respectively. Each experiment was repeated for at least twice. More details of the experimental setup can be found in ref. 25.

5.2.3. Nano-oxysalts and nano-thermites at ultrafast heating rates

T-jump/TOF MS was employed to analyse the evolution of gaseous species during the decomposition of nano-$K_2S_2O_8$ at ultrafast heating rates of ~10^5 ˚C/s. Nano-$K_2S_2O_8$ powders were dispersed in hexane and ultrasonicated for 30 mins and then deposited onto a 76 μm Pt wire. The coated mass on wire was controlled around 50 μg [25]. The Pt wire was then inserted into the MS chamber where it is rapidly joule-heated to ~1200 ˚C by a 3 ms pulse. The current and voltage signals were recorded and the temporal temperature on wire was measured according to the Callender–Van Dusen equation. MS spectra were measured every 0.1 ms. For the detailed experimental set-up, please find in ref. 58.

In order to determine the ignition temperatures of thermite mixtures in different environments, a Vision Research Phantom v12.0 high speed camera (14.9 μs per frame) was used to monitor the combustion on the wire during heating. Ignition temperatures of nano-thermite reactions in vacuum were measured from the correlation of optical emission from high speed imaging and temporal temperature of the wire, and were further analyzed in combination with the temporal mass spectra. Ignition temperatures in air and in Ar at atmosphere pressure were also measured in a separate home-built chamber. Each experiment was repeated for 3 times.

5.2.4. Thermal decomposition of nano-oxysalts at lower heating rates

DSC, TG, and MS tests were conducted simultaneously in a SDT Q600 coupled to a DiscoveryTM quadruple mass spectrometer from TA Instruments, U.S.A. Around 2 mg of nano-$K_2S_2O_8$ was loaded into the sample crucible inside the apparatus and

heated at 10 ˚C/min in 100 L/min Ar flow up to 1400 ˚C. A heated micro-capillary (~300 ˚C) connects the SDT Q600 chamber to the MS, enabling transport of the thermally decomposed species to the MS detector. The linear relationship between the concentration of gas species *i* (C_i) and its ion intensity (I_i) detected from MS is [59]:

$$I_i = K\sigma_i C_i \quad (5.1)$$

where K is the instrumental constant and σ_i is the electron-impact ionization cross-section of species *i* (O_2, SO_2 or Ar). Ar was used as an internal standard to determine the effective instrumental response factor. At incident energy of 70 eV in the MS system, the ionization cross-sections for O_2, SO_2 and Ar are 2.4 $Å^2$, 5.0 $Å^2$, and 10.0 $Å^2$, respectively [60]. Given that I_i can be measured and C_{Ar} was known by the Ar flow rate, the concentrations of O_2 (C_{O2}) and SO_2 (C_{SO2}) can be theoretically measured through eq. 5.2:

$$C_i = \frac{I_i \sigma_{Ar} C_{Ar}}{I_{Ar} \sigma_i} \quad (5.2)$$

Finally, the net quantities of O_2 and SO_2 can be measured by integration of C_i over time.

5.3. Results and discussion

5.3.1. Analysis of prepared nano-oxysalts and nano-thermites

All of the as-received oxysalt powders are micro-sized in a wide size range. The average particle sizes are 40.7 μm, 33.7 μm and 21.9 μm for $K_2S_2O_8$, K_2SO_4 and KIO_4 powders, respectively (Figs. 5.3A, 5.4A and 5.4B). Nano-sized oxysalts were prepared by spray-drying of aqueous oxysalt solutions (Fig. 5.2). The average sizes of nano-oxysalts are 0.46 ± 0.19 μm, 0.42 ± 0.24 μm, and 0.46 ± 0.27 μm for nano-

$K_2S_2O_8$, nano-K_2SO_4, and nano-KIO_4, respectively (Figs. 5.3B, 5.4C and 5.4D). The average particle sizes above were determined by SEM images based on >100 particle counts.

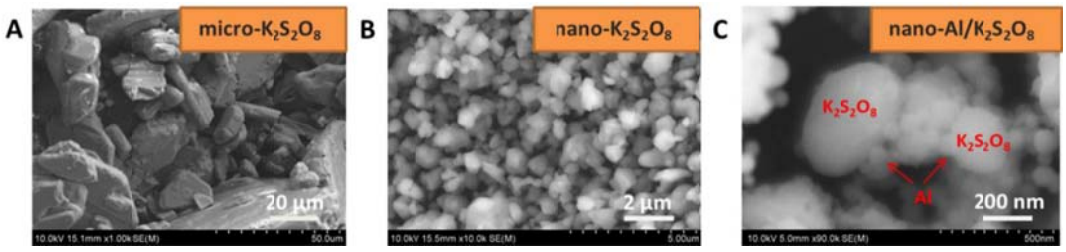

Figure 5.3. (A) SEM of as-received micro-sized $K_2S_2O_8$; (B) SEM of nano-sized $K_2S_2O_8$ prepared by spray-drying of $K_2S_2O_8$ solutions; (C) SEM of nano-thermite formulation of nano-Al and nano-$K_2S_2O_8$.

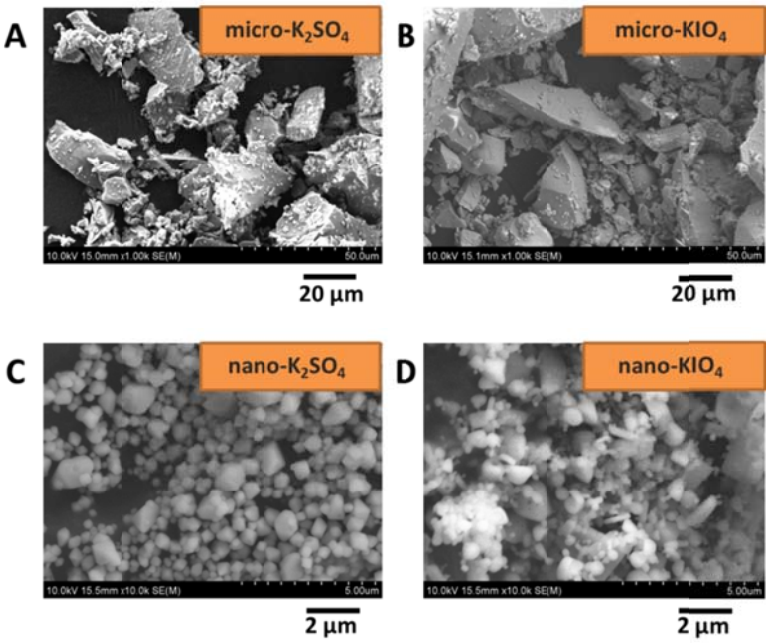

Figure 5.4. SEM images of as-received micro-sized K_2SO_4 (A) and KIO_4 (B) powders, as well as SEM images of nano-sized K_2SO_4 (C) and KIO_4 (D) prepared by spray-drying.

Nano-thermites were prepared by sonicating the mixture of nano-oxysalts and nano-Al in hexane. Although the size of the nano-K2S2O8 is 10 times larger than that

of nano-Al, there is still intimate contact as seen in the SEM image of the nano-thermite mixture (Fig. 5.3C).

5.3.2. Ignition of nano-thermites

The ignition of nano-thermites at high heating rates was characterized in the T-jump heating experiments monitored by a high-speed camera. The time-resolved light intensities were measured using the high speed videos (Fig. 5.5), and the ignition times were identified as the points where light intensities begin to rise (Fig. 5.6). These ignition times correlate to the time resolved wire temperatures to determine the ignition temperatures for the nano-thermite compositions. Fig. 5.6A shows that the nano-Al/$K_2S_2O_8$ has an ignition temperature of 595 ± 22 ˚C in Ar, which is similar to that of nano-Al/KIO_4 (600 ± 27 ˚C), but much lower than that of nano-Al/K_2SO_4 (805 ± 15 ˚C). The large temperature difference demonstrates that nano-$K_2S_2O_8$ and nano-KIO_4 are more reactive in the aluminum-fueled thermites than nano-K_2SO_4. This result also indicates that the oxygen in nano-$K_2S_2O_8$ and nano-KIO_4 were able to react with Al at temperatures where Al is still solid, while nano-K_2SO_4 reacts with the Al melt (> 660 ˚C). In open air, ignition temperatures of both nano-Al/$K_2S_2O_8$ and nano-Al/KIO_4 were around 600 ˚C (Fig. 5.6B), which are equivalent to their ignition temperatures in Ar. This alludes to the fact that although the O_2 in air may play a role in the overall reaction, it does not have an impact on the ignition process for these systems. This also indicates that nano-$K_2S_2O_8$ and nano-KIO_4 were able to provide a higher transient concentration of reactive oxygen species around the Al nanoparticles, ensuring ignition at temperatures approaching the melting point of Al where Al

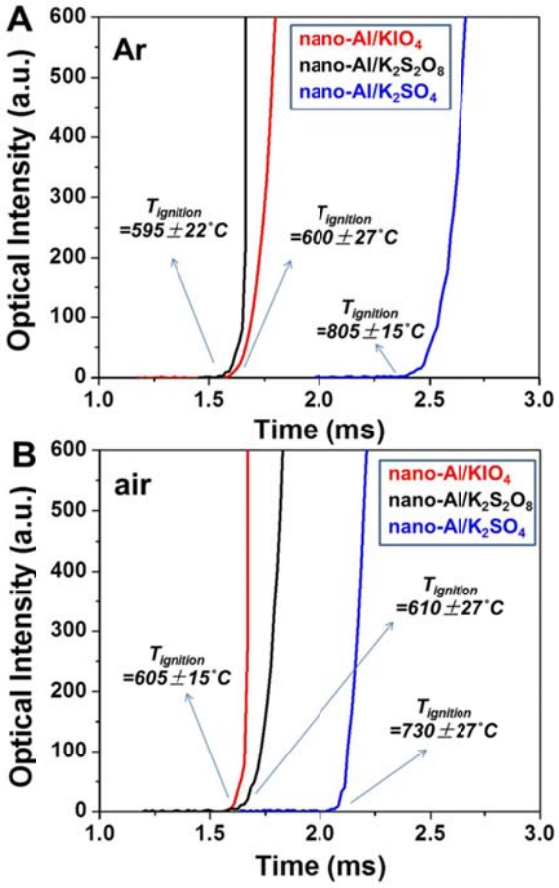

Figure 5.5. Time-resolved optical intensity profiles of nano-Al/$K_2S_2O_8$, nano-Al/KIO_4, and nano-Al/K_2SO_4 thermite reactions in Ar (A) and in air (B). Optical intensities were measured from high-speed camera videos. The ignition temperatures of thermite reactions are labelled. The heating rate is ~4×10^5 ˚C/s.

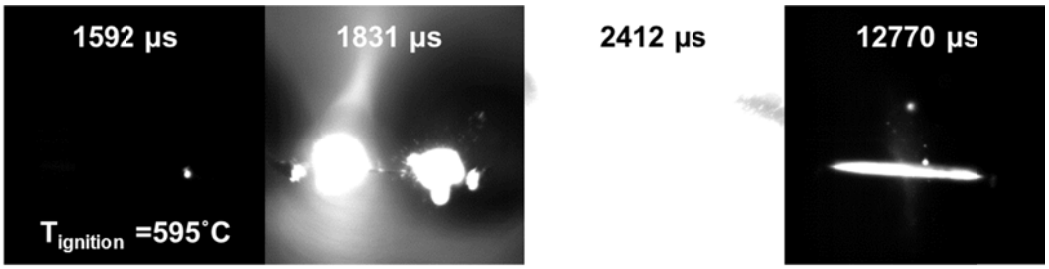

Figure 5.6. High speed imaging of the wire burning tests for nano-Al/$K_2S_2O_8$ in Ar. The pulse lasting time for each snapshot and the ignition temperatures are denoted. The heating rate is ~4×10^5 ˚C/s.

becomes highly mobile and diffuses outwards through the oxide shell. Conversely, the ignition temperature of nano-Al/K_2SO_4 (730 ± 27 ˚C) in air is lower than that in Ar (805 ± 15 ˚C), suggesting that the gaseous oxygen in air augmented the ignition by reacting with the Al melt. The reactivity of the nano-Al/$K_2S_2O_8$ and nano-Al/KIO_4 thermites in vacuum (data not shown), showed overall weak optical emission and higher ignition temperatures (~740 ˚C). At the low pressure used in these experiments (~10^{-7} Torr), gaseous oxygen if released from the oxidizer, will have little time to interact with the fuel and I should expect a delayed ignition. This suggests that for the persulfate the initiation process is not a condensed phase reaction between solid Al and bound oxygen in solid $K_2S_2O_8$, but initiated by the reaction between solid Al and gaseous O_2 released from $K_2S_2O_8$.

5.3.3. Pressurization and optical emission of nano-thermite reactions

Pressurization rate and burn time were measured using sample masses 2 orders of magnitude larger than what is required for the T-jump ignition experiments above (25 mg vs. 0.05 mg). Results from the constant-volume combustion cell tests (Fig. 5.7A) show that the pressurization rate and maximum pressure in the nano-Al/$K_2S_2O_8$ reaction are 151 ± 26 kPa/μs and 1206 ± 208 kPa, respectively, which are considerably higher than the reported pressurization rate and maximum pressure in the standard nano-thermite reaction of Al/CuO (V_p = 60 kPa/μs, P_{max} = 700 kPa) [20]. Previously, it was reported that the nano-Al/KIO_4 reaction possessed the highest measured pressurization rate per mole of Al [25]. The nano-Al/$K_2S_2O_8$ reaction convincingly demonstrates a higher pressurization rate and peak pressure exceeding

that of nano-Al/KIO_4 reaction (V_p = 91±19 kPa/μs, P_{max} = 909±185 kPa) (Fig. 5.7A). A simple explanation for the higher pressurization in the nano-Al/$K_2S_2O_8$ reaction than the other nano-Al/oxysalt reactions is its high content of oxygen per mass of thermite (31%) (Table 1.3). Nano-Al/K_2SO_4 thermite has a little smaller oxygen content (26%) when compared to the nano-Al/$K_2S_2O_8$ thermite (Table 1.3), though the difference observed in peak pressures during reaction is much larger (Fig. 5.7A). This result implies that the pressurization observed in a thermite reaction is also dependent on the available oxygen that can be released from the oxysalt.

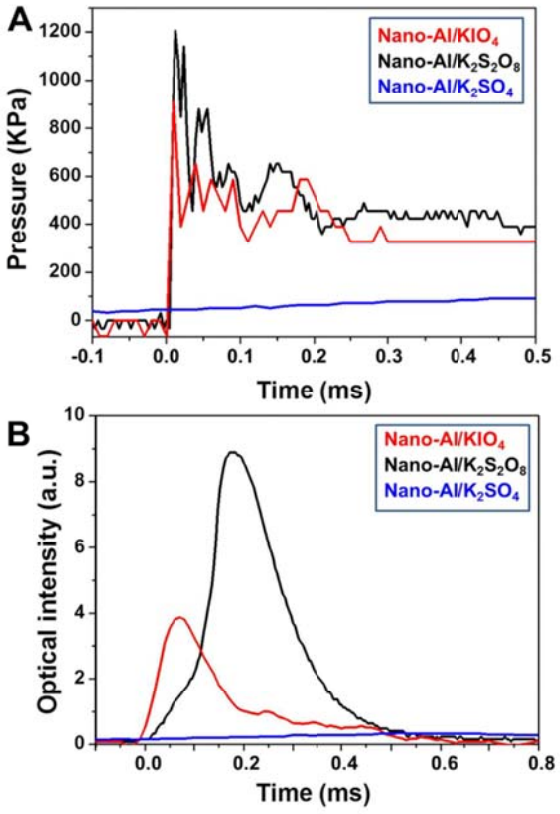

Figure 5.7. Temporal pressure (A) and optical intensity (B) in the combustion cell tests of nano-thermites including nano-Al/$K_2S_2O_8$, nano-Al/KIO_4, and nano-Al/K_2SO_4, respectively. The temporal pressure in (A) represents the pressure increase from 1atm.

The burn time of the thermite reactions, which is defined as the full width at half maximum of the optical emission peak, was detected in the combustion cell tests (Fig. 5.7B). Fig. 5.7B shows that the nano-Al/$K_2S_2O_8$ reaction has a 2-fold higher optical emission, as well as burn time, than the nano-Al/KIO_4 reaction despite the nano-Al/KIO_4 reaction showing a higher optical emission rate. This result indicates that although the nano-Al/KIO_4 thermite burns faster, the nano-Al/$K_2S_2O_8$ thermite provides more optically intensive (higher temperature), longer sustained combustion. While nano-Al/$K_2S_2O_8$ behaves superior to nano-Al/KIO_4 in this metric, both reactions show much stronger optical emission than nano-Al/K_2SO_4 (Fig. 5.7B). Furthermore the nano-Al/$K_2S_2O_8$ thermite is still one of the fastest burning species I have measured and second only to nano-Al/KIO_4. The pressurization and optical emission results for all the three thermite systems are presented in Table 5.1. In general, from both pressurization and combustion intensity, as determined by light emission, nano-$K_2S_2O_8$ is a far more effective oxidizer in the aluminum-fueled thermite.

Table 5.1. Pressurization rates (V_p), maximum pressures (P_{max}), burn times (T_{burn}), and maximum optical intensities (I_{max}) of the thermite reactions of nano-Al/$K_2S_2O_8$, nano-Al/KIO_4, and nano-Al/K_2SO_4 in the combustion cell tests. P_{max} represents the maximum pressure increase from 1 atm.

Nano-thermites	V_p (kPa/μs)	P_{max} (kPa)	T_{burn} (μs)	I_{max} (V)
nano-Al/$K_2S_2O_8$	151±26	1206±208	205±38	9.0±1.9
nano-Al/KIO_4	91±19	909±185	130±35	4.0±0.5
nano-Al/K_2SO_4	0.06±0.02	104±14	2800±400	0.3±0.1

It should be noted that the time scales of pressurization and optical emission are different. In both nano-Al/$K_2S_2O_8$ and nano-Al/KIO_4 reactions, the time required to reach peak pressure (8 - 10 μs) was about one tenth of their burn times (T_{burn} = 205 -

130 μs), suggesting that product gas is generated from the oxysalts prior to the start of ignition and combustion. Thus, the gaseous reactive oxygen species that initiate ignition of the thermite may be from the product gas. Distinctively, for the nano-Al/K_2SO_4 reaction, the burn time is comparable to the time to reach maximum pressure (> 1 ms) (Table 5.1), suggesting that gas is generated during the ignition process.

5.3.4. Thermal decomposition pathways of nano-oxysalts at low heating rates

The characterization of ignition and combustion of the three nano-thermites both in small and large reaction scales demonstrate that the thermite reactivity and energy density are strongly dependent on the oxysalt used. Thermal and mass analyses of the decomposition of oxysalts can provide the energetics of the reaction, as well as decomposition products and global pathways, which can be connected to the ignition and pressurization mechanism. At a low heating rate of 10 ˚C/min, the TG, DSC and MS profiles for nano-$K_2S_2O_8$ show several sequential mass and enthalpy changes (step a-f) (Figs. 5.8 and 5.9). The nano-$K_2S_2O_8$ was first dehydrated below 270 ˚C with a mass loss of 0.6% (Fig. 5.8A). Importantly this degree of hygroscopicity when compared with other oxysalts such as KIO_4 (17.66%, see Fig. 5.10A) is negligible. Starting from 270 ˚C, the nano-$K_2S_2O_8$ predominantly underwent three decomposition steps. The first step is the decomposition of $K_2S_2O_8$ to $K_2S_2O_7$ and O_2, which shows two mass reduction sub-steps at 270 ˚C and 310 ˚C (Fig. 5.8A), indicating bimodal oxygen release peaks (Fig. 5.8C). The measured quantity of released O_2 from MS (0.125 mg) (Fig. 5.8C) is consistent with the mass reduction of

the nano-$K_2S_2O_8$ loaded (2 mg × 5.8% = 0.116 mg) (Fig. 5.8A), confirming that O_2 is the only product gas at this stage. DSC results show that this step is highly exothermic (-288 J/g-17.1 J/g = -305.1 J/g) (Fig. 5.8B and Table 5.2, see detailed enthalpy analysis in the following Section 5.3.5). Given that most metal oxide and oxysalt decompositions are endothermic [25], the exothermicity of nano-$K_2S_2O_8$'s decomposition would presumably ensure better reactivity in a thermite composition. A similar phenomenon has been previously published for nano-KIO_4 [25], although the exothermicity is less than half of what is observed for nano-$K_2S_2O_8$ (-121 J/g, Fig. 5.10B).

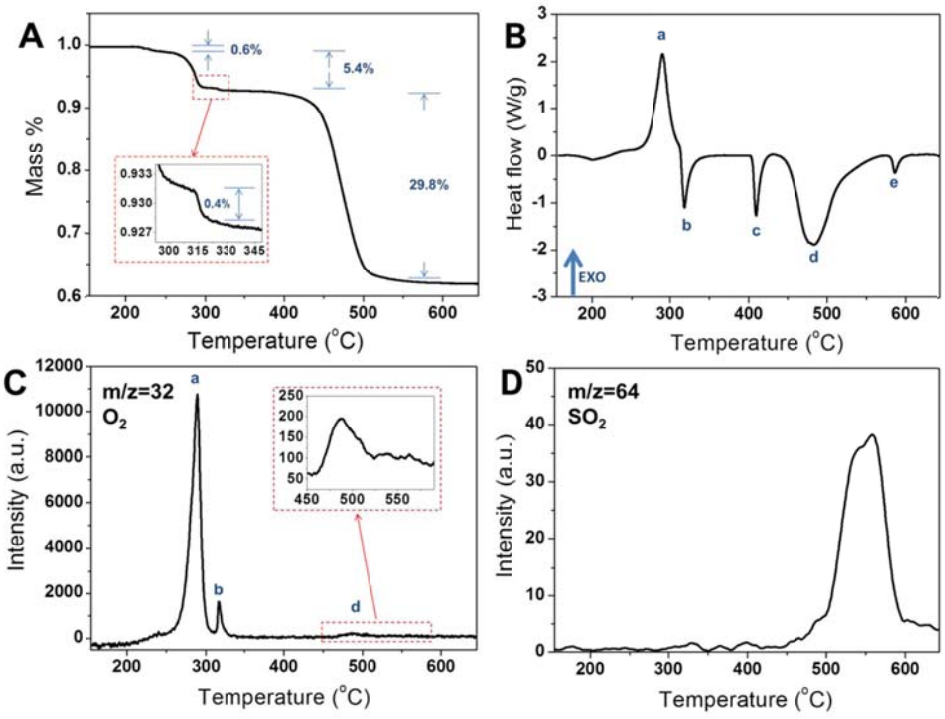

Figure 5.8. TG (A), DSC (B) and MS for O_2 (C, m/z=32) and SO_2 (D, m/z=64) profiles of $K_2S_2O_8$ in the temperature range from room temperature to 645 ˚C. The heating rate is 10 ˚C/min.

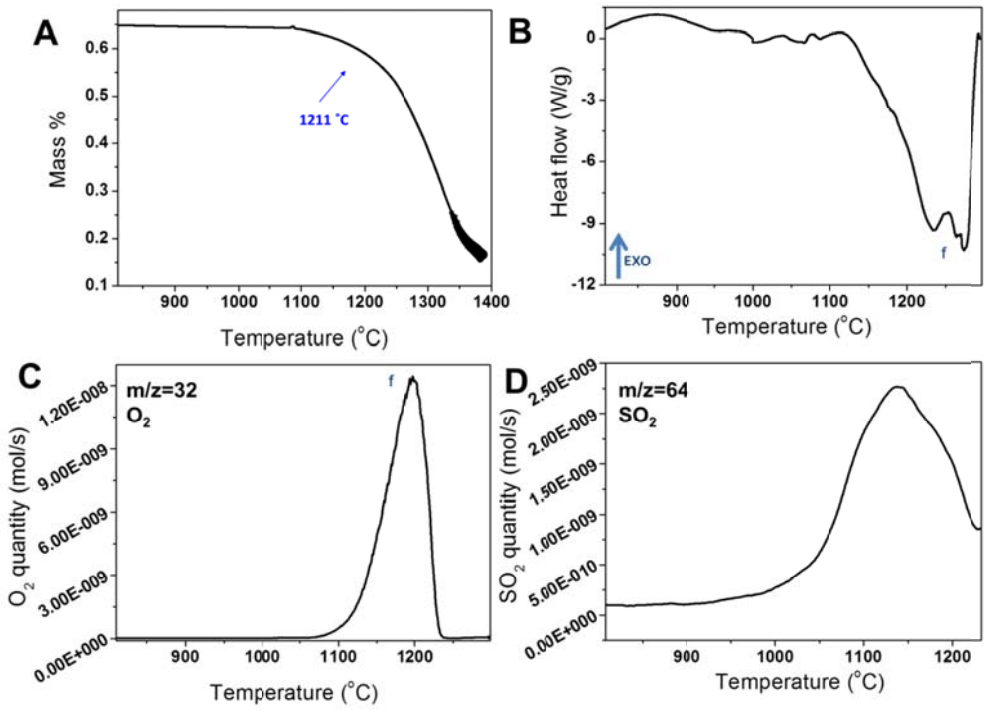

Figure 5.9. TG (A), DSC (B) and MS for O_2 (C, m/z=32) and SO_2 (D, m/z=64) profiles of nano-$K_2S_2O_8$ in the high temperature range starting from 800 ˚C.

Table 5.2. Thermal decomposition steps of nano-K2S2O8 from TG, DSC and MS tests at a heating rate of 10 ˚C/min.

Steps	T_{onset} (˚C)	Physiochemical changes	ΔH (J/g)
a	270	$K_2S_2O_8(s) = K_2S_2O_7(s) + 0.5\ O_2$ (most)	-288
b	310	$K_2S_2O_8(s) = K_2S_2O_7(s) + 0.5\ O_2$	-17.1
		$K_2S_2O_7(s) = K_2S_2O_7(s)$ (phase change)	81.3
c	405	$K_2S_2O_7(s) = K_2S_2O_7(l)$ (melting)	61.8
d	450	$K_2S_2O_7(l) = K_2SO_4(s) + 0.5\ O_2 + SO_2$	570
e	580	$K_2SO_4(s) = K_2SO_4(s)$ (phase change)	13.3
f [a]	1110	$K_2SO_4(s) = 2K + O_2 + SO_2$	5463

Note: [a] This reaction equation was implied from the MS results. The exact products are unknown.

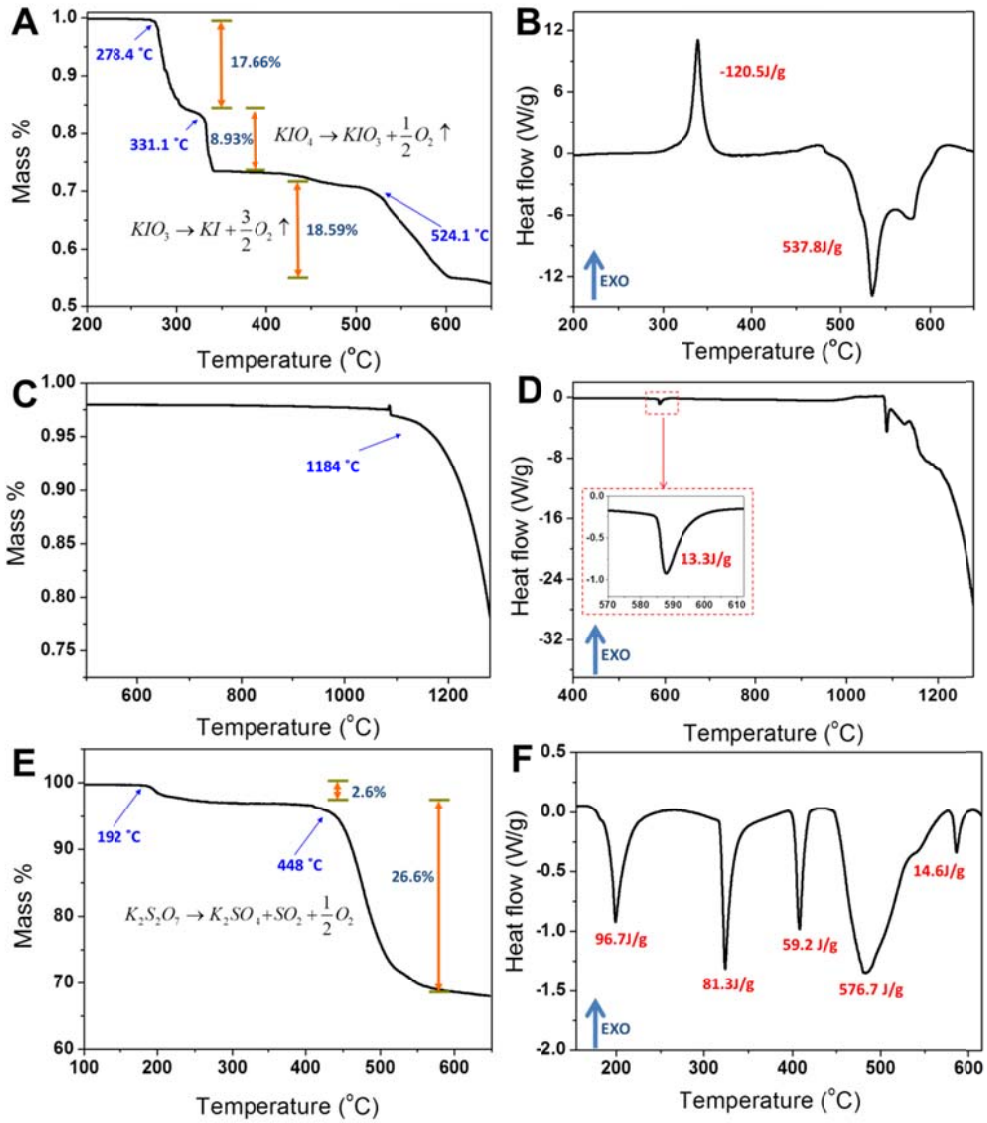

Figure 5.10. TG and DSC profiles of nano-KIO_4 (A and B), nano-K_2SO_4 (C and D), and $K_2S_2O_7$ (E and F). The heating rate is 10 ˚C/min. The initial mass reduction in $K_2S_2O_7$ pertains to a water evaporation step (2.6% mass loss) (E), with an endothermic enthalpy change of 96.7 J/g (F).

The second step is the decomposition of $K_2S_2O_7$ to K_2SO_4, SO_2, and O_2 at 440 ˚C as confirmed by TG (Fig. 5.8A) and MS (Fig. 5.8C and 5.8D) results. It should be noted that the molar quantities of O_2 and SO_2 detected in MS (Fig. 5.8C and 5.8D) are

much smaller than those quantities measured from the mass reduction in TG (Fig. 5.8A). The likely reason for the discrepancy is that SO_2, as it passes through the much cooler micro-capillary (~300 ˚C), undergoes a reaction yielding sulfuric acid. The detailed explanation of this side reaction, as well as the rationalization of high conversion of O_2 and SO_2, can be found in the following Section 5.3.6.

The final decomposition step began at ~1200 ˚C (Fig. 5.9A) and its temperature range exceeded the upper limit of the TG temperature capabilities, rendering it difficult to deduce the decomposition route. However, the emergence of both SO_2 and O_2 in MS (Fig. 5.9C and 5.9D) suggests that the reaction is from K_2SO_4 to SO_2, O_2, and K, which is also confirmed by other reports [61].

The following multi-step decomposition of nano-$K_2S_2O_8$ is proposed based on the TG/DSC/MS results as summarized in Table 5.2. XRD results further confirm the main products ($K_2S_2O_7$ and K_2SO_4) during heating of nano-$K_2S_2O_8$ (Fig. 5.11). Compared to other oxysalts such as KIO_4 and K_2SO_4, $K_2S_2O_8$ possesses the lowest oxygen release temperature at 270 ˚C (vs. 330 ˚C for KIO_4 and 1200 ˚C for K_2SO_4), as well as the highest exothermic heat of -305.1 kJ/g (vs. -120.5 kJ/g for KIO_4), thus confirming better ignition and combustion performance in thermite reaction as shown in Figs. 5.6 an 5.7. Furthermore, 4 moles of gas (including O_2 and SO_2) were generated per mole of $K_2S_2O_8$ (Table 5.2), which is a factor of 2 more than per mole of KIO_4, indicating $K_2S_2O_8$ as a better gas generator.

Given that the heat of reaction in each step was quantified (Table 5.2), as well as the standard heat of formation of solid K_2SO_4 and gaseous SO_2 (-1437.7 kJ/mol and -

296.8 kJ/mol respectively) [60], I can deduce the heat of formation of $K_2S_2O_8$ from (combing equations in step a-d):

$$K_2S_2O_8 \rightarrow K_2SO_4 + SO_2 + O_2 \quad (5.3)$$

We obtain: ΔH_f $K_2S_2O_8$ = -1844.5 kJ/mol.

The global equation (from $K_2S_2O_8$ to SO_2, O_2, and K) was not used for this calculation because of the uncertainty in final products as previously mentioned.

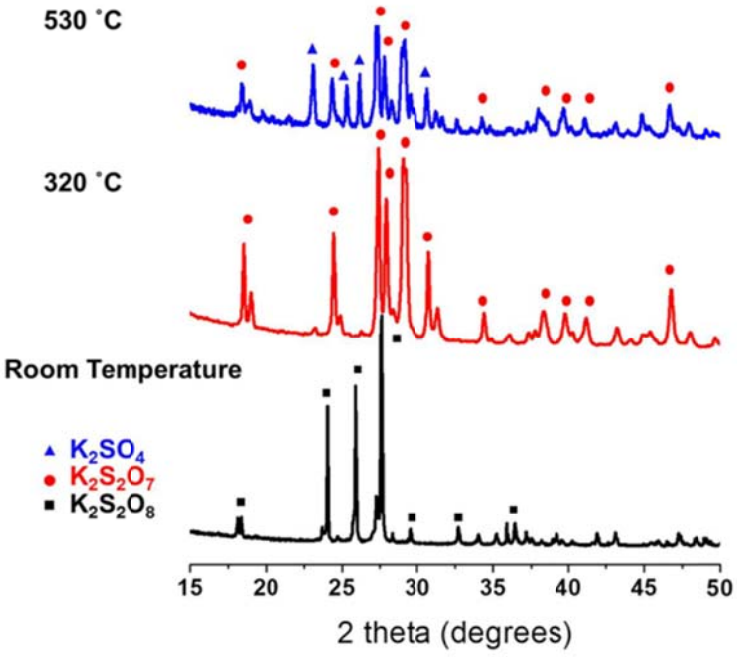

Figure 5.11. XRD profiles of prepared nano-$K_2S_2O_8$ (A) and nano-$K_2S_2O_8$ after heating to 320 ˚C (B) and 530 ˚C (C). The marks above the major peaks represent the positions of reflection corresponding to triclinic $K_2S_2O_8$ phase (JCPDS No.:32-0846), monoclinic $K_2S_2O_7$ phase (JCPDS No: 22-1239) and K_2SO_4 phase (JCPDS No: 05-0613). Some of the minor peaks in the room temperature pattern probably belong to impurities like SiO_2 from the diffusion dryer.

5.3.5. Thermal analyses of peak a and b in the DSC profile of nano-$K_2S_2O_8$

The decomposition transition from $K_2S_2O_8$ to $K_2S_2O_7$ was observed in two mass reduction sub-steps, with an initial major mass reduction of 5.4% starting at 270 ˚C

followed by a second minor mass reduction of 0.4% at 312 ˚C (Fig. 5.8A). MS results show that this two-step mass reduction is due to the generation of bimodal oxygen peaks at 270 ˚C and 310 ˚C (Fig. 5.8C). The appearance of these two subsequent sub-steps implies the possible inhomogeneity within nano-$K_2S_2O_8$, which is proposed to be due to the difference between surface and bulk of particles. While the nature of the reasons for these two steps is unclear, the mass reduction and O_2 emergence is quantitatively consistent with this transition.

DSC results further show that these two mass reduction sub-steps correspond to an initial exothermic peak *a* (T=273 ˚C) and a subsequent endothermic peak *b* (T=313 ˚C), respectively (Fig. 5.8B). Peak *a* represents the major decomposition step, yielding a heat of reaction (ΔH) of -288 J/g. In contrast, peak *b* is endothermic (ΔH=64.2 J/g). To understand this endotherm, $K_2S_2O_7$ was tested as a control, which was prepared after heating nano-$K_2S_2O_8$ to 380 ˚C as confirmed by XRD (Fig. 5.11). Fig. 5.10F shows that most of the endothermic peaks of $K_2S_2O_7$ are consistent with those of nano-$K_2S_2O_8$, except for the peak at 310 ˚C that shows a higher endothermic enthalpy change (81.3 J/g) than that of nano-$K_2S_2O_8$ at the same temperature (64.2 J/g, see Fig. 5.8B). This peak represents the phase change of $K_2S_2O_7$. Hence, the endothermic peak *b* of nano-$K_2S_2O_8$ (64.2 J/g, see Fig. 5.8B) is, in fact, a combination of an endothermic phase change peak of generated $K_2S_2O_7$ (81.3 J/g) and a small exothermic O_2 release peak of nano-$K_2S_2O_8$ (64.2 J/g-81.3 J/g = -17.1 J/g, see Table 5.2). Further combining the exotherms of the two O_2 release peaks gives the total exothermic enthalpy change of the decomposition reaction of $K_2S_2O_8$ to $K_2S_2O_7$ as -305.1 J/g (Table 5.2).

5.3.6. Side reaction of O_2 and SO_2 in the micro-capillary

In step *d*, a small oxygen signal at 455 ˚C (Fig. 5.8C) is seen in addition to SO_2 at 460 ˚C (Fig. 5.8D) suggesting that the decomposition of $K_2S_2O_7$ generates O_2, SO_2, and K_2SO_4:

$$K_2S_2O_7 \rightarrow K_2SO_4 + SO_2 + \frac{1}{2}O_2 \tag{5.4}$$

The net mole fractions of O_2 and SO_2 detected from MS in this step are 6.7×10^{-9} and 5.2×10^{-10}, respectively, which are much smaller than theoretical values (7.1×10^{-8} for O_2 and 1.4×10^{-7} for SO_2) based on the original dose of samples (Fig. 5.8A). The likely reason for the discrepancy is that SO_2, as it passes through the much cooler micro-capillary (~300 ˚C), undergoes a reaction yielding sulfuric acid:

$$SO_2 + \frac{1}{2}O_2 + H_2O \rightarrow H_2SO_4 \tag{5.5}$$

Considering that the measured intensity of background H_2O signal is around two orders of magnitude higher than that of the generated O_2 and SO_2 in the MS, it is reasonable to estimate that the molar ratio of SO_2:O_2:H_2O is 1:1:100. Using the on-line Chemical Equilibrium with Applications (CEA) code from NASA [62], the converted proportions of these reactants, after achieving the reaction equilibrium at 300 ˚C, can be obtained. The result shows that most SO_2 and O_2 were reacted and only 0.4% O_2 and 0.0003% SO_2 remained, thus supporting the proposed explanation of low intensities of O_2 and SO_2 signal in step *d*. H_2SO_4 was not apparent in the MS results. This is most likely due to H_2SO_4 adsorbing to the inner wall of micro-capillary.

At higher temperatures >1100 ˚C (step *f*), weak SO_2 and O_2 MS signals were also detected which correspond to a net mole fraction of 1.1×10^{-8} for O_2 and 4.4×10^{-9} for

SO_2, respectively. Recalculation of the chemical equilibrium in e.q 5.5 was conducted. In this case, a higher reaction temperature of 1100 ˚C and a similar molar ratio of SO_2:O_2:H_2O of 1:1:100 were employed. The result shows that 0.5% of both SO_2 and O_2 were retained, indicating that most of these gases had reacted before entering the MS.

5.3.7. Thermal decomposition of nano-oxysalts at ultrafast heating rates

To further evaluate nano-$K_2S_2O_8$ as an oxidizer in an energetic composition, high heating rate analytics that will more accurately represent timescales of a combustion event were employed. T-jump/TOF MS at a heating rate of ~4×10^5 ˚C/s was used to obtain time resolved spectra at 0.1 ms intervals that could be further analysed to determine the signal intensity over time of O_2, SO_2 and K (Fig. 5.12). Similar to the mass spectra at low heating rates (Fig. 5.8C and 5.8D), the decomposition of nano-$K_2S_2O_8$ also undergoes three major steps. The initial step has an onset temperature of 335 ˚C (Fig. 5.12A), where oxygen is generated from the decomposition of $K_2S_2O_8$ to $K_2S_2O_7$ (Table 5.2). This onset temperature is higher than that in the TG/DSC result (Fig. 5.8) due to the employment of a much higher heating rate (~10^5 ˚C/s vs. 10 ˚C/min). At a higher temperature of 435 ˚C, SO_2, in addition to a second release of O_2, was detected (Figs. 5.12A and 5.12B) representing the second step of decomposition from $K_2S_2O_7$ to K_2SO_4 (Table 5.2). The final decomposition step occurs at 710 ˚C where O, SO_2 and K were detected in the MS (Figs. 5.12A, 5.12B and 5.12C). Based on the similarity between the thermal decomposition of nano-$K_2S_2O_8$ at ultrafast heating rates and low heating rates (Table 5.2), I propose that the thermal

decomposition mechanism of nano-$K_2S_2O_8$ appears to be independent of heating rate. However, the oxygen intensity ratio of step 1 and step 2 in the ultrafast heating result (Fig. 5.12) is much lower than what is observed in the low heating result (Table 5.2), indicating that some $K_2S_2O_8$ did not decompose at the lower temperature in step 1. This could be due to the inhomogeneity of nano-$K_2S_2O_8$ (surface vs. bulk) in its first decomposition process to $K_2S_2O_7$, which also leads to the bimodal oxygen peaks as I see in the TG-MS results (Fig. 5.8A and 5.8C). The likely reason for only one initial O_2 release peak at higher heating rates (Fig. 5.12A) is that the decomposition time from $K_2S_2O_8$ to $K_2S_2O_7$ (~10^2 s, estimated from Fig. 5.8C) is much longer than the heating time in step 1 (~10^{-3} s, Fig. 5.12A), which results in incomplete decomposition of $K_2S_2O_8$ in step 1.

Decomposition of nano-K_2SO_4 (Fig. 5.13A) shows that no oxygen was detected until 840 ˚C, with the appearance of SO_2 and K at ~1000 ˚C. In contrast I found that K_2SO_4 generated from the decomposition of $K_2S_2O_8$ has a lower onset decomposition temperature at 710 ˚C (Fig. 5.12). This temperature difference suggests that the gas generation in the previous steps of $K_2S_2O_8$ decomposition facilitates the further decomposition of the K_2SO_4 product.

5.3.8. Nano-thermite reaction at ultrafast heating rates

For evaluating the thermite performance of nano-$K_2S_2O_8$ under high heating rate conditions, T-jump/TOF MS was employed to analyse the reaction between nano-$K_2S_2O_8$ and nano-Al in a stoichiometric physical mixture. Fig. 5.12 shows that both nano-thermite and thermal decomposition of nano-$K_2S_2O_8$ have an initial oxygen

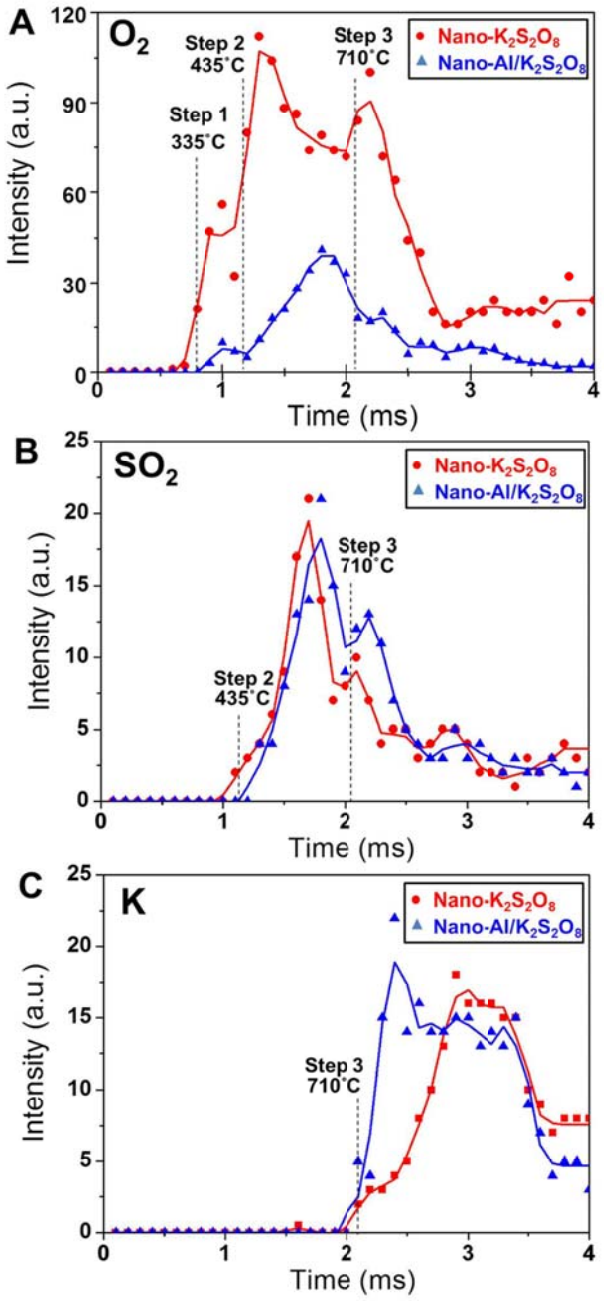

Figure 5.12. (A), (B), and (C) are TOF-MS temporal profiles of oxygen, sulfur dioxide and potassium release respectively during a 3 ms pulse heating. Measured mass intensity data at each time point are denoted as circle remarks for decomposition of nano-$K_2S_2O_8$, and triangle remarks for thermite reaction of nano-Al/$K_2S_2O_8$, respectively. The starting temperatures for select MS peaks are shown.

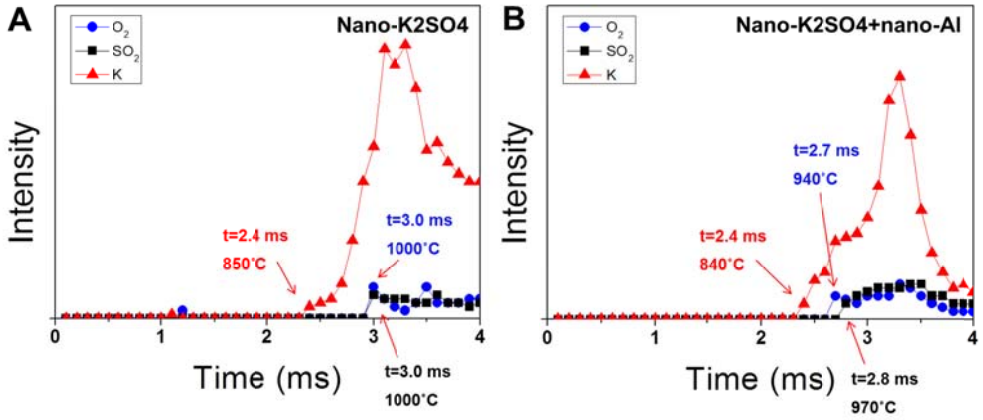

Figure 5.13. TOF-MS temporal profiles of molecular species O_2, SO_2 and K during ultrafast thermal decomposition of nano-K_2SO_4 (A) and thermite reaction involving nano-Al and nano-K_2SO_4 (B). Measured data at each time point are denoted as circle, square and triangle remarks for O_2, SO_2 and K species, respectively. The starting times and temperatures for different MS peaks are shown.

release peak at 335 ˚C. Starting from 470 ˚C, significant oxygen release was detected, though the intensity is lower than that in the decomposition of nano-$K_2S_2O_8$ (Fig. 5.12A). SO_2 was also released at this stage, with an onset temperature (435 ˚C) similar to what is observed in the pure oxidizer case (Fig. 5.12B). The similarity in SO_2 profiles implies that the produced SO_2 did not further react with Al, which was confirmed by the product analysis that showed no Al_2S_3. At higher temperature >710 ˚C at which a third decomposition step commenced for nano-$K_2S_2O_8$, K was detected with the similar intensity as that in the pure oxidizer case (Fig. 5.12C), implying that K did not participate in the reaction with Al. In this step, very little oxygen was detected in the thermite reaction (Fig. 5.12A) indicating that there was negligible intermediate product K_2SO_4 generated.

The reactive oxygen species that initiate the reaction addressed in the ignition and pressure cell tests (Figs. 5.6 and 5.7) are suggested to be gaseous species released

from $K_2S_2O_8$ decomposition as opposed to oxygen species in the solid oxysalts, or background O_2 if combusted in air. Direct evidence for this proposition is that the ignition occurs at a lower temperature when rapidly heated in argon at 1 atm as opposed to being heated at low pressures. There is a higher local concentration of reactive oxygen species near the aluminum fuel when heated at higher pressures. Thus, the thermite ignition is proposed to be initiated by the generated gaseous oxygen species reacting with solid Al at the surface of Al particle. However, nano-Al/$K_2S_2O_8$ and nano-Al/KIO_4 thermites have different oxygen release temperatures of 335 ˚C (Fig. 5.12A) and 470 ˚C [25] respectively, but they have similar ignition temperatures in Ar (600 ˚C, see Fig. 5.6). This indicates that the mobilization of Al, which increases as the melting point of Al (660 ˚C) is approached, plays a more important role in controlling ignition than the gaseous reactive oxygen generated from the decomposition of oxysalts.

In contrast, nano-Al/K_2SO_4 has higher oxygen release temperature (840 ˚C, see Fig. 5.13B) than both its ignition temperature in Ar (805 ˚C, see Fig. 5.6) and melting point of Al. Gas generation is negligible in this case (Figs. 5.7B and 5.13B), suggesting that the reaction mechanism for this type of inactive oxysalt mainly undergoes a condensed phase route resembling the case for many metal oxides [63,64].

It is important to note in the end that when compared to the decomposition of nano-KIO_4, nano-$K_2S_2O_8$ generates gaseous SO_2 thus ensuring the production of this biocidal gas during the thermite reaction (Fig. 5.12B). Bearing in minding that SO_2 is the major sulfur-containing products from thermite reaction, the amount of biocidal

SO_2 produced from the thermite reaction is estimated to be 31% by mass for nano-Al/$K_2S_2O_8$, which is higher than that for nano-Al/K_2SO_4 (26%) and nano-Al/KIO_4 (0%). Due to the high biocidal gas productivity as well as the super-reactive thermite performance, nano-$K_2S_2O_8$ can be used to formulate promising biocidal energetic nano-composites.

5.4. Conclusions

In this study, potassium persulfate was evaluated as an oxidizer in energetic aluminum-fueled nano-composite formulations for its possible biocidal deployment through the release of SO_2. The nano-Al/$K_2S_2O_8$ reaction has a low ignition temperature (600 ˚C) in Ar or air when compared to other nano-thermite compositions, and demonstrates combustion performance comparable to nano-Al/KIO_4. Constant-volume pressure cell results further show that the nano-Al/$K_2S_2O_8$ produces more gas than the nano-Al/KIO_4 and has a longer burn time indicating a more persistent combustion feature. Three major steps in the thermal decomposition for the nano-$K_2S_2O_8$ were identified including a low temperature exothermic peak corresponding to the release of oxygen at 270 ˚C, as well as the release of sulfur dioxide at 450 ˚C.

I determined that the ignition of nano-Al/$K_2S_2O_8$ is controlled by the reaction between gaseous oxygen and mobilized Al. These experimental results demonstrate that the nano-thermite formulation that consists of nano-Al/$K_2S_2O_8$ features both high exothermicity and biocidal gas generation, making it an optimal candidate for use in energetic biocidal applications.

Chapter 6: Mechanisms of Potassium Oxysalts Based Energetic Composites*

Overview

The superior performance of persulfate in thermites intrigued me to study the reaction mechansim of aluminum-based energetic materials, which poses an important guildance to the exploration, evaluation and utilization of novel biocidal nano-thermites in the future. Herein, Ignition temperature is highlighted as a simple and important parameter that pertains to both the practical aspects of thermite usage as well as a key to exploring reaction mechanisms. In this study, nine aluminum-fueled oxysalt-containing thermites including $K_2S_2O_8$, K_2SO_4, KIO_4, KIO_3, $KClO_4$, $KClO_3$, $KBrO_3$, KNO_3 and K_3PO_4, were investigated. Results from combustion cell tests show that these thermites can be divided into two groups, with the reactive thermites (*e.g.*, Al-$K_2S_2O_8$) generating ~10× higher of pressure and ~10× shorter of burn time than the less reactive thermites in the aforementioned list (*e.g.*, Al-K_2SO_4). Thermal decomposition analysis of these oxysalts at both slow and fast heating rates (0.17 K/s v.s. 10^5 K/s) demonstrates that these oxysalts have a wide range of oxygen release and melting temperatures. On the other hand, the ignition temperatures of the reactive thermites (in Ar and air) are consistent with the temperature of polymorphic phase change for alumina (close to the melting point of Al), indicating that the limiting initiation step of these thermites is the acceleration of outward diffusion flow of Al. In addition, the ignition temperatures of these reactive thermites in vacuum are

* The results presented in this chapter have been submitted in the following journal article: **W. Zhou**, J. B. DeLisio, X. Wang, M. R. Zachariah*. Reaction Mechanisms of Energetic Composites Containing Potassium Oxysalts as Oxidizers. ***Combust. Flame***, 2015, *Submitted*.

much higher than those in Ar, suggesting that ignition is based on the interaction between outwardly diffused Al, and generated gas phase O_2. In contrast, the ignition temperatures of the two less reactive thermites are insensitive to pressure. They ignite at temperatures much higher than the melting point of Al, although lower than the decomposition temperature of the corresponding oxysalts, indicating a condensed phase reaction mechanism. Finally, by employing carbon as a non-melting, non-oxide coated fuel, I found an essentially direct correlation between the oxygen release temperature and the ignition temperature.

6.1. Introduction

Since the thermite reaction was first named by Goldschmidt in 1908 [1], the concept has been currently broadened to a variety of exothermic reactions involving a metal reacting with an oxide (metal or non-metal) or an oxysalt [2-5]. Due to its extremely high energy density, the thermite system has been employed in a wide array of applications in the pyrotechnic, metallurgical, and ceramic industries [2-5], which has prompted studies to improve their utilization by tailoring their combustion and ignition behaviours [6-10]. The latter property also involves practical safety concerns related to the large-scale industrial use [11,12]. One important research direction is to improve the ignitibility of thermites, which is affected by many factors (contact area, chemical composition, hygroscopicity, etc.). The most common method is by increasing the contact area between the fuel and oxidizer, which can reduce the diffusion distance of reactive species to permit ignition at lower temperatures [13-17].

This higher degree of intimacy can be achieved by either decreasing the particle size [14-17], better mixing [13,18,19], or increasing the particle porosity [20].

For the most common aluminum-fueled thermite systems, ignition was proposed to be initiated by a solid-state reaction [21]. Subsequent reaction requires movement of reactive species towards each other, although the nature of this movement is subject to considerable debate [22-28]. However, it was previously reported that the prerequisite for ignition is the availability of molten aluminium [21,29]. Based on this speculation, ignition temperatures for a plethora of thermites should be around the melting point of aluminum. However, a recent study by Jian et al [30] shows that there can be large differences in ignition temperatures among different nano-thermite formulations involving aluminum and metal oxides. For instance, some formulations (e.g. Al-Bi_2O_3, Al-SnO_2) have ignition temperatures lower than both the melting point of aluminum, and the decomposition temperatures of oxidizers, suggesting another condensed phase reaction mechanism that is not governed by melted aluminium [31]. Similarly, Dean et al [32] examined another nano-thermite formulation (Al-NiO), which produces minimal gas upon ignition, with a much lower ignition temperature (~400 ˚C) [33] than either the melting temperature of Al or the decomposition temperature of NiO. Sullivan et al [34] implemented in situ rapid heating microscopy to monitor the nano-thermite reaction of Al-WO_3 and found a reactive sintering phenomenon [35] in which no gas was released, and the reactants deformed to maximize intimate surface contact. While several thermites appear to react via this condensed phase route [32-37], ignition temperatures of some other formulations may

exceed the decomposition temperature of metal oxides, suggesting a different reaction mechanism [30].

To date, discussions on ignition mechanism of thermites have been limited to formulations containing various metal oxides (CuO, Fe_2O_3, etc.), whereas the ignition mechanism for thermite formulations containing oxysalts (nitrates [38-40], (per)chlorates [41-44], (per)iodates [45-47], etc.) have not been explicitly studied from a mechanistic standpoint. Typically, Al-oxysalt thermites exhibit lower ignition temperatures and higher reaction rates [44,47-49], which are associated with the low oxygen release temperatures of the corresponding oxysalts. An initial exothermic decomposition of some oxysalts during heating may also contribute to the low ignition temperature [41,47]. Recently, a new formulation based on persulfates was found to be more reactive when compared to other oxysalts (see Chapter 5) [50]. The superiority of oxysalts in thermite performance can likely be attributed to the higher oxygen content, and the lower bond energy of the nonmetal-oxygen pair in oxysalts when compared to the metal-oxygen pair in metal oxides [50]. Of particular interest is whether the ignition temperature (T_{ig}) is a predictable function of the oxygen release temperature (T_{O2}), the melting temperature of aluminum ($T_{Al\text{-}melt}$), and the melting temperature of oxidizer ($T_{oxidizer\text{-}melt}$).

In this Chpater, I systematically investigated the ignition of thermites that involve Al and a variety of potassium oxysalts, in relation to the physiochemical changes of these components during heating. These studies involved using constant-volume combustion cell tests, thermal decomposition tests for oxysalts under both slow heating (10 K/min) and ultrafast heating (~10^5 K/s) conditions, and ignition tests for

both microscale and nanoscale thermites in air, in Ar and in vacuum. Nano-carbon-fueled thermites containing similar oxysalts were also used as controls to tweeze out the role of liberated oxygen.

6.2. Material and methods

6.2.1. Materials

Nano-sized aluminum was obtained from Argonide Corporation, and nano-sized carbon black was obtained from Cobot Corporation. Both materials have an average size of ~50 nm. Micro-sized potassium persulfate ($K_2S_2O_8$) powders were purchased from Fluka. All of the other micro-sized oxysalt powders, namely potassium sulfate (K_2SO_4), potassium nitrate (KNO_3) potassium chlorate ($KClO_3$), potassium perchlorate ($KClO_4$), potassium bromate ($KBrO_3$), potassium iodate (KIO_3), potassium periodate (KIO_4), and potassium phosphate (K_3PO_4) were purchased from Sigma-Aldrich. Scanning electron microscopy (SEM, Hitachi, SU-70 FEG-SEM) analysis shows that these as-received potassium oxysalts powders have a wide range of sizes from 1 μm to 100 μm.

The corresponding nine nano-sized potassium oxysalts were prepared by an aerosol spray drying process, as is shown in Fig. 6.1. In short, 0.02 mol/L water solution of oxysalt was prepared in the atomizer and sprayed into 1 μm droplets by a pressured air flow. Droplets flowed through a diffusion dryer to remove most of the water, followed by complete dehydration by a tube furnace at 150 ˚C for $K_2S_2O_8$ and at 180 ˚C for the other oxysalts. The dehydrated nanoparticles were finally collected on a Millipore membrane filter with a pore size of 0.4 μm. The average size of nine nano-

oxysalts is ~0.5 μm. Particle sizes were measured by SEM and statistically analysed from a random selection of 60 particles in SEM images.

To prepare the thermite composite, nano-fuels (Al or C) were mixed with oxysalts (microscale or nanoscale) in a stoichiometric ratio. Accounting for the alumina shell (30%) on the nano-Al, the actual weight of nano-Al added was 1.4 times higher. The mixture was then sonicated in hexane for 30 min and then the solvent was evaporated at room temperature.

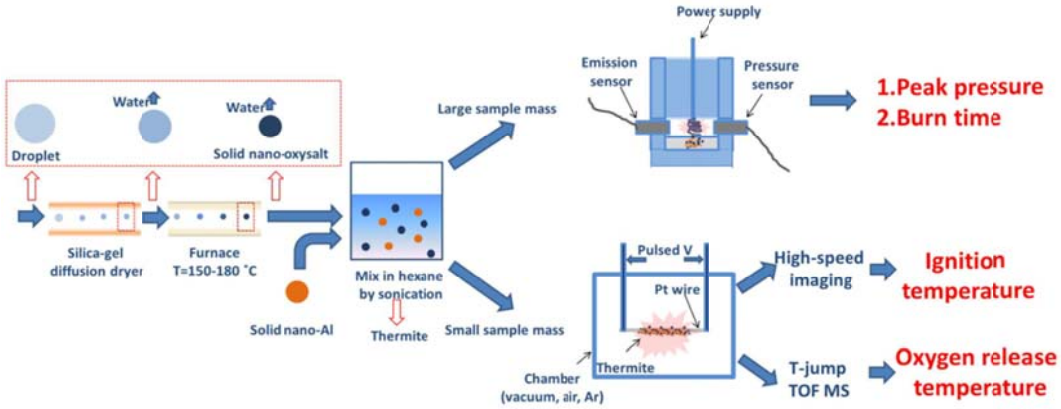

Figure 6.1. The experimental flow chart including spray drying process for sample preparation, a pressure cell for detecting pressure and optical emission from thermite reaction, and a pulsed wire heating set-up coupled with T-jump TOF-MS and high-speed camera for detecting characteristic temperatures.

6.2.2. Constant-volume combustion characterization

The analysis of nano-Al/micro-oxysalt thermite reactions was conducted in a constant-volume combustion cell (Fig. 6.1). Prior to tests, all the thermite samples were dried in vacuum for hours in order to mitigate the adverse influence of hygroscopicity. 25 mg of thermite sample was loaded inside the combustion cell that has an internal spacing of ~13 cm^3. After igniting the sample with a heated nichrome

coil, the temporal pressure and optical emission from the thermite reaction were electronically recorded.

6.2.3. TG-DSC analysis of the decomposition of oxysalts

Thermogravimetry and differential scanning calorimetry (TG-DSC) tests of microscale oxysalts were conducted simultaneously in a SDT Q600 from TA Instruments, USA. Around 2 mg of as-received oxysalt powders was loaded into the sample crucible inside the apparatus and heated at 10 K/min in 100 L/min Ar flow. The TG and DSC heat flow calibrations were conducted prior to tests. For the TG calibration, two calibration weights were used to calibrate the beam and weight correction factors. For the DSC heat flow calibration, the capacity curve of sapphire over the range of 500 - 1800 K, as well as the heat of fusion of high purity zinc metal, were analysed and compared with the standard values to generate a calibration cell constant. In the analysis of the TG-DSC results, the onset temperatures of physicochemical changes (including phase and chemical changes) are defined as the crossing points of extrapolated curves.

6.2.4. T-jump TOF-MS analysis of the decomposition of oxysalts

The decomposition of oxysalts (microscale or nanoscale) at ultrafast heating rates of 4×10^5 K/s was investigated via temperature-jump time-of-flight mass spectrometry (T-jump TOF-MS, in-house assembled). A concentrated oxysalt powder suspension in hexane was deposited onto a 76 μm Pt wire uniformly, to a thickness < 10 μm so that the temperature of the deposit is approximated by the wire temperature. The

loaded Pt wire was then inserted into the MS chamber and rapidly joule-heated to ~1400 K by a 3 ms pulse. The temporal temperature of the wire was measured from the detected current and voltage according to the Callender–Van Dusen equation [51]. TOF-MS spectra was collected every 0.1 ms. A detailed experimental description can be found in ref [52]. In the analysis of the MS results, the onset temperature of a specific species is defined based on 5% of the maximum intensity of its MS peak.

6.2.5. Ignition tests of thermite reactions

A Vision Research Phantom v12.0 high speed camera (14.9 μs per frame) was employed to determine the onset of ignition on the wire. By mapping the temporal optical emission from the high-speed imaging, and the temporal wire temperature, the ignition temperatures of thermites were identified as the points where light intensities begin to rise. These experiments were carried out in vacuum, air or Ar.

6.3. Results and discussion

6.3.1. Reactivities of oxysalts in nano-aluminum-fueled thermites

We begin with the combustion performance of the nine Al-oxysalt thermites, in the combustion cell test. Fig. 6.2 shows the maximum pressures, pressurization rates, and burn times (the full-width half-maximum of the optical emission curve) for the thermite reactions between nano-Al and micro-oxysalts. Also apparent in Fig. 6.2 is the very wide range in performance, with the maximum peak pressures for Al-$K_2S_2O_8$, Al-$KClO_3$, Al-KIO_4 and Al-$KClO_4$ being more than six times larger than those of Al-K_2SO_4 and Al-K_3PO_4 (Fig. 6.2A), indicating that the former four thermites generated

more gas during reaction. A similar result in the pressurization rate was shown for these thermite reactions, with the rates in thermites that release extensive gas (Al-$K_2S_2O_8$, Al-$KClO_3$, Al-KIO_4 and Al-$KClO_4$) more than one order of magnitude larger than the rates in less gas generating thermites (Al-K_2SO_4 and Al-K_3PO_4) (Fig. 6.2B). Not surprisingly, I also observed a general relationship of higher peak pressure or pressurization rate corresponding to a shorter burn time (Fig. 6.2C). The differences in these reaction characteristics indicate that the Al-oxysalt thermite reactivity, as is reflected from the scale of pressurization rate and burn time, is correlated to the capability of the relevant oxysalt to generate gas. Based on these results, the nine thermites can be divided into two groups: the reactive thermites (Al-$K_2S_2O_8$, Al-KIO_4, Al-KIO_3, Al-$KClO_4$, Al-$KClO_3$, Al-$KBrO_3$ and Al-KNO_3) and the less reactive thermites (Al-K_2SO_4 and Al-K_3PO_4). The combustion performance of some of these Al-oxysalt thermites was also assessed by the thermodynamic equilibrium calculation as summarized in Table 6.1. The amount of gas generation, major gas species, adiabatic flame temperature, and reaction heat were calculated using CHEETAH software for constant pressure and enthalpy. The Al and oxysalts were mixed in a stoichiometric molar ratio, without consideration of additional oxide shell on the Al particles. Table 6.1 shows that there is a correlation between gas generation and thermite reactivity. While a larger amount of gas generation (~10^3 cc/g) corresponds to a higher adiabatic flame temperature (>3700 K) and reaction heat (< -6 kJ/g) (e.g. $KClO_3$ and $KClO_4$), a poor gas generation (~10^2 cc/g) corresponds to a lower adiabatic flame temperature (<2100 K) and reaction heat (> -4 kJ/g) (e.g. K_3PO_4 and K_2SO_4). The results on the amount of gas generation are consistent with the peak

pressure from the combustion cell test (Fig. 6.2A), demonstrating that the difference in total gas volumes generated from reactive (Al-KIO_4) and less reactive (Al-K_2SO_4) thermites can be as large as 1 order of magnitude.

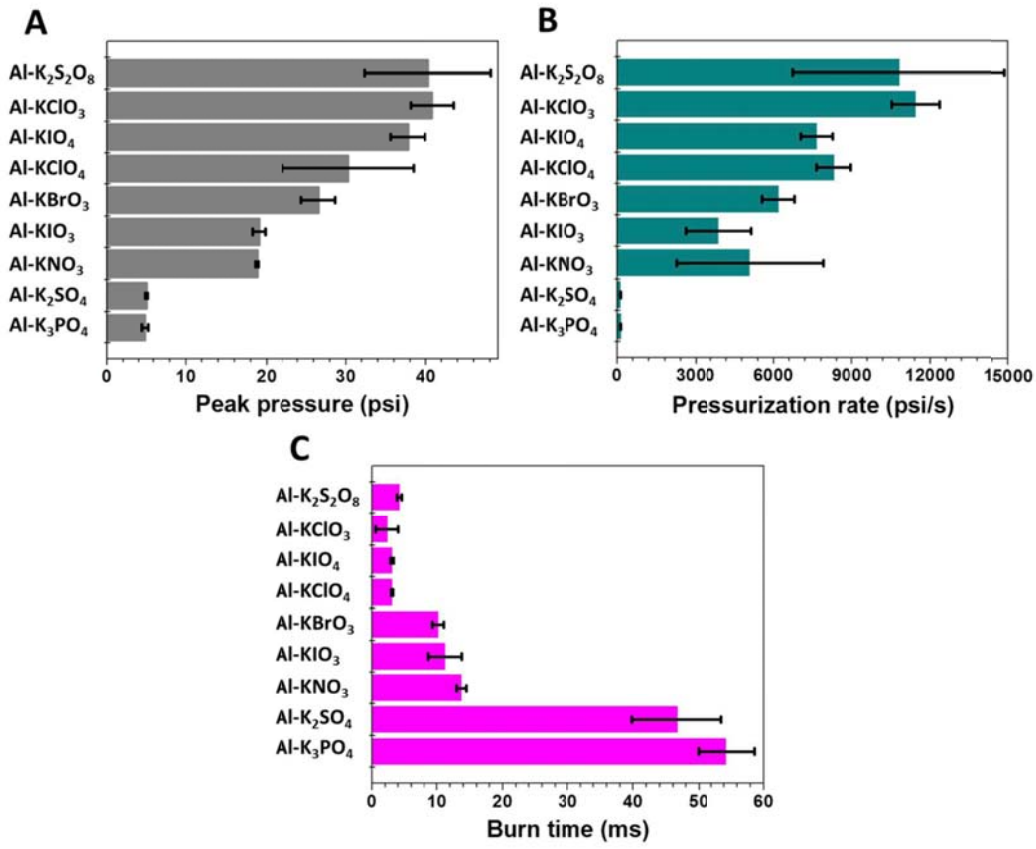

Figure 6.2. Maximum pressure (A), pressurization rate (B), and burn time (C) for thermite reactions between nano-Al and micro-oxysalts. 25 mg thermite sample was employed in each constant volume combustion cell test. Errors bars represent at least two experiments in parallel.

Table 6.1. Summary of the amount of gas generation, major gas species, adiabatic temperature and reaction heat from the Al-oxysalt thermite reactions. Thermodynamic data were calculated based on a constant enthalpy and pressure equilibrium using CHEETAH. The fuel and oxidizer were mixed in a stoichiometric ratio.

Formulations	cc gas/g [a]	Major gas products (mol%)	Adiabatic temperature (K)	Standard reaction heat (kJ/g) [b]
$Al+KNO_3$	4.0×10^3	K (49%), N_2 (24%), Al_2O_3 (25%) [c]	3732	-7.6
$Al+KClO_3$	4.1×10^3	KCl (55%) [d], Al_2O_3 (35%) [c]	3791	-9.8
$Al+KClO_4$	4.2×10^3	KCl (46%) [d], Al_2O_3 (44%) [c]	3842	-10.6
$Al+KBrO_3$	3.4×10^3	KBr (64%) [d], Al_2O_3 (34%) [c]	3789	-7.7
$Al+KIO_3$	2.5×10^3	KI (79%) [d], Al_2O_3 (20%) [c]	3686	-5.7
$Al+KIO_4$	2.9×10^3	KI (64%) [d], Al_2O_3 (35%) [c]	3796	-6.9
$Al+K_2SO_4$	4.7×10^2	K (66%), SO_2 (27%)	2040	-3.9
$Al+K_2S_2O_8$ [e]	-	-	-	-5.8
$Al+K_3PO_4$ [e]	-	-	-	-0.9

Note:
[a] cc = cubic centimeters.
[b] The standard reaction heat (kilojoules per gram of thermite) was calculated for formulations with fuel/oxide in a stoichiometric ratio in the 1atm, 298K condition.
[c] Al_2O_3 here is not molecular Al_2O_3. It involves decomposition into several gaseous products (e.g., O_2, O, AlO).
[d] KX (X=Cl, Br, I) involve gaseous KX, K, and X.
[e] The combustion temperature and gas generation for $K_2S_2O_8$ and K_3PO_4 were not found in CHEETAH.

The reaction equations were shown in the following eq. 6.1 - 6.9, and also in Fig. 6.3. The standard heat of formation for each reaction/product (Table 6.2) was used to calculate the reaction heat in Table 6.1.

$$2Al + KNO_3 = Al_2O_3 + \frac{1}{2}N_2 + K \quad [53] \tag{6.1}$$

$$2Al + KClO_3 = Al_2O_3 + KCl \tag{6.2}$$

$$\frac{8}{3}Al + KClO_4 = \frac{4}{3}Al_2O_3 + KCl \tag{6.3}$$

$$2Al + KBrO_3 = Al_2O_3 + KBr \tag{6.4}$$

$$2Al + KIO_3 = Al_2O_3 + KI \tag{6.5}$$

$$\frac{8}{3}Al + KIO_4 = \frac{4}{3}Al_2O_3 + KI \tag{6.6}$$

$$\frac{4}{3}Al + K_2SO_4 = \frac{2}{3}Al_2O_3 + 2K + SO_2 \text{ [53]} \tag{6.7}$$

$$\frac{8}{3}Al + K_2S_2O_8 = \frac{4}{3}Al_2O_3 + 2K + 2SO_2 \text{ [53]} \tag{6.8}$$

$$\frac{8}{3}Al + K_3PO_4 = \frac{4}{3}Al_2O_3 + 3K + P \text{ [53]} \tag{6.9}$$

Table 6.2. Tabulated results of standard heat of formation for reactants and products participating in the thermite reactions.

Chemicals	$\Delta_f H^o$ (kJ/mol)	Chemicals	$\Delta_f H^o$ (kJ/mol)	Chemicals	$\Delta_f H^o$ (kJ/mol)
$K_2S_2O_8$	-1845 [a]	$KBrO_3$	-360 [c]	KI	-328 [b]
K_2SO_4	-1438 [b]	KNO_3	-494 [c]	KBr	-394 [b]
KIO_4	-467 [c]	K_3PO_4	-1971 [c]	KCl	-434 [b]
KIO_3	-501 [c]	Al	0	K	0
$KClO_4$	-430 [b]	Al_2O_3	-1676 [b]	N_2 (g)	0
$KClO_3$	-389 [b]	SO_2 (g)	-297 [b]	P	0

Note:
[a] see reference [50].
[b] see reference [54].
[c] see reference [55].

6.3.2. Thermal decomposition of oxysalts at slow heating rates (10 K/min)

Since the gas generation appears to be correlated to the reactivity of oxysalt-containing thermites (Fig. 6.2), the thermal decomposition of neat microscale oxysalt powders was examined to identify the species and the temperature of gas evolution.

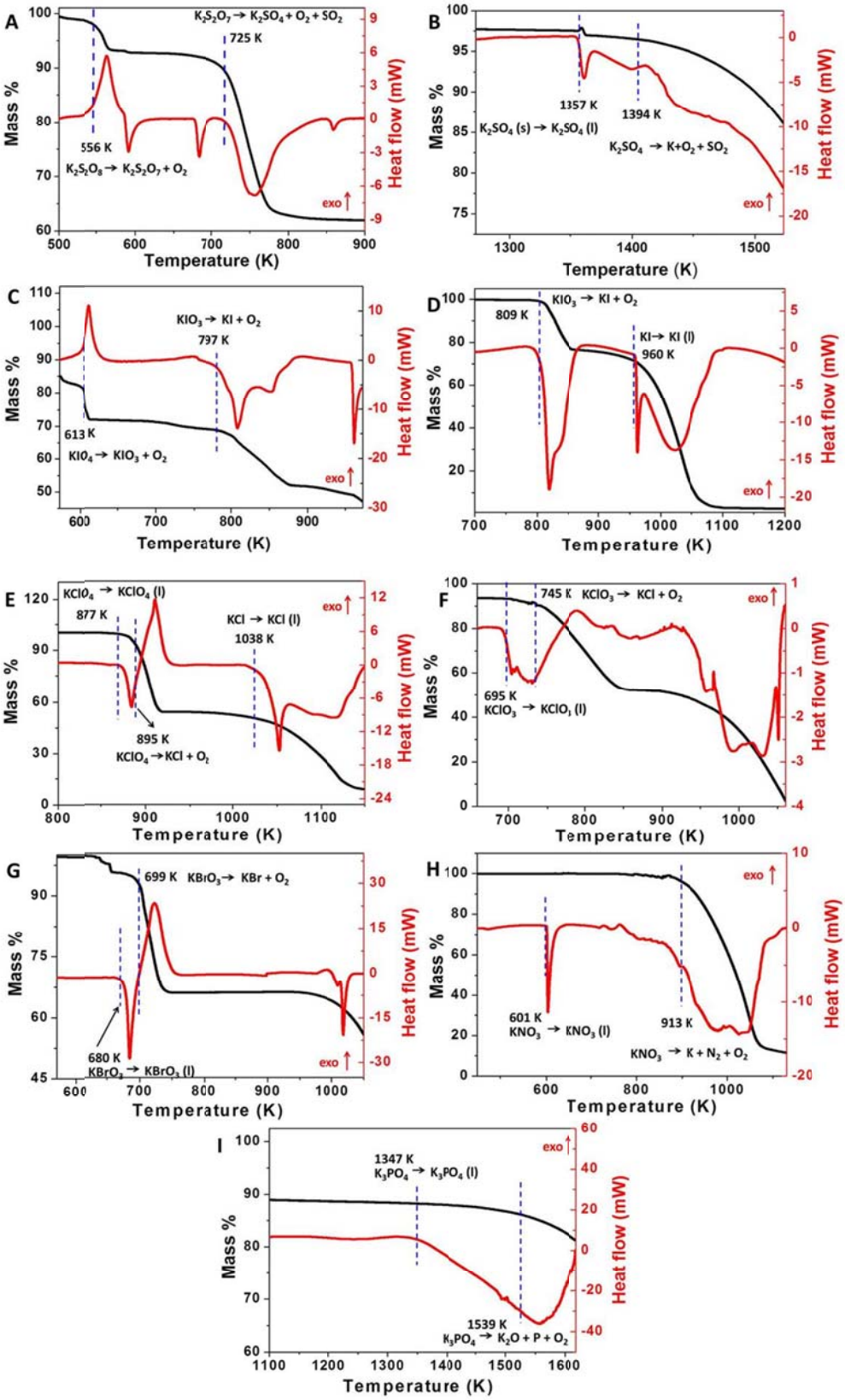
A
$K_2S_2O_7 \rightarrow K_2SO_4 + O_2 + SO_2$
725 K
556 K
$K_2S_2O_8 \rightarrow K_2S_2O_7 + O_2$
exo
Mass %
Heat flow (mW)
Temperature (K)
B
1357 K
1394 K
K_2SO_4 (s) $\rightarrow$ K_2SO_4 (l)
$K_2SO_4 \rightarrow K + O_2 + SO_2$
C
$KIO_3 \rightarrow KI + O_2$
797 K
613 K
$KIO_4 \rightarrow KIO_3 + O_2$
D
809 K
$KIO_3 \rightarrow KI + O_2$
KI $\rightarrow$ KI (l)
960 K
E
$KClO_4 \rightarrow KClO_4$ (l)
877 K
KCl $\rightarrow$ KCl (l)
1038 K
895 K
$KClO_4 \rightarrow KCl + O_2$
F
745 K
$KClO_3 \rightarrow KCl + O_2$
695 K
$KClO_3 \rightarrow KClO_3$ (l)
G
699 K
$KBrO_3 \rightarrow KBr + O_2$
680 K
$KBrO_3 \rightarrow KBrO_3$ (l)
H
601 K
$KNO_3 \rightarrow KNO_3$ (l)
913 K
$KNO_3 \rightarrow K + N_2 + O_2$
I
1347 K
$K_3PO_4 \rightarrow K_3PO_4$ (l)
1539 K
$K_3PO_4 \rightarrow K_2O + P + O_2$

Figure 6.3. TG and DSC profiles for $K_2S_2O_8$ (A), K_2SO_4 (B), KIO_4 (C), KIO_3 (D), $KClO_4$ (E), $KClO_3$ (F), $KBrO_3$ (G), KNO_3 (H), and K_3PO_4 (I). The characteristic temperatures associated with the designated reaction equations are marked by the vertical dotted lines.

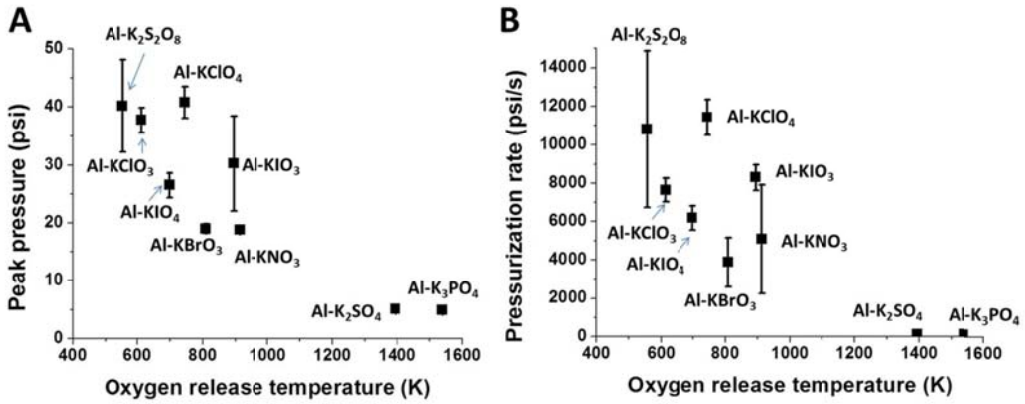

Figure 6.4. (A) Relationship between the oxygen release temperature measured from the TG-DSC tests (Table 6.3), and the peak pressure from the Al-oxysalt thermite reaction (Fig. 6.2A). (B) Relationship between the oxygen release temperature measured from the TG-DSC tests (Table 6.2), and the pressurization rate from the Al-oxysalt thermite reaction (Fig. 6.2B).

TG-DSC results (Fig. 6.3) demonstrate that these oxysalts show different onset temperatures of physicochemical changes. The primary thermal results for onset temperature, gas release, and product identification are summarized in Table 6.3. In general, all of the nine oxysalts generate O_2 at different stages, with $K_2S_2O_8$ showing the lowest O_2 generation temperature, while K_2SO_4 and K_3PO_4 release O_2 at temperatures several hundreds of Kelvin higher than the other oxysalts. In relation to the corresponding thermite reactions (Fig. 6.2A), I find that the oxysalt having a low O_2 release temperature usually corresponds to a thermite event with a high pressure and faster overall reaction (also see Fig. 6.4 for the relationships between O_2 release temperature and peak pressure (Fig. 6.4A) or pressurization rate (Fig. 6.4B)). This indicates that the oxygen release temperature is a good metric for evaluating oxysalt-containing thermites.

Table 6.3. Summary of the thermal decomposition events of oxidizers during heating (10 K/min). The onset temperature and relevant products in each event are listed. The parentheses show the melting phase change of oxidizers.

Oxidizers	T (K)	Events	Products	T (K)	Events	Products
$K_2S_2O_8$	556	Decomposition	$K_2S_2O_7$, O_2	725	Decomposition	K_2SO_4, O_2, SO_2 [a]
K_2SO_4	1357	Melting	K_2SO_4 (l)	1394	Decomposition	K, O_2, SO_2 [b]
KIO_4	613	Decomposition	KIO_3, O_2	797	Decomposition	KI, O_2 [c]
KIO_3	809	Decomposition	KI, O_2 [c]	-	-	-
$KClO_4$	877	Melting	$KClO_4$ (l)	895	Decomposition	KCl, O_2 [c]
$KClO_3$	695	Melting	$KClO_3$ (l)	745	Decomposition	KCl, O_2 [c]
$KBrO_3$	680	Melting	$KBrO_3$ (l)	699	Decomposition	KBr, O_2 [c]
KNO_3	601	Melting	KNO_3 (l)	913	Decomposition	K, O_2, NO_2 [d]
K_3PO_4	1347	Melting	K_3PO_4 (l)	1539	Decomposition	K_2O, P, O_2 [e]

Note:
[a] The final products from the decomposition of $K_2S_2O_8$ are referred to [50].
[b] The final products from the decomposition of K_2SO_4 are referred to [56].
[c] The final products from the decomposition of KIO_3, KIO_4, $KClO_3$, $KClO_4$ and $KBrO_3$ are measured from my TG-DSC results (Fig. 6.3).
[d] The final products from the decomposition of KNO_3 are referred to [57].
[e] The final products from the decomposition of K_3PO_4 are referred to [58].

It is interesting to note that many oxysalts in Table 6.3 have a melting temperature lower than the O_2 release temperature. Considering the much higher oxygen mobility in a melt, a melting event commencing prior to thermal decomposition (O_2 release) may also have a potential impact on initiating the thermite reaction.

6.3.3. Thermal decomposition of oxysalts at ultrafast heating rates (4×10^5 K/s)

In order to investigate oxygen release at heating rates that more closely represent a combustion event, T-jump TOF-MS at a heating rate of 4×10^5 K/s was employed, and the onset temperatures for corresponding generated gases were determined. As an example, the overall temporal MS intensity of molecular oxygen released from

$K_2S_2O_8$ is shown in Fig. 6.5 together with the temporal temperature trace. In comparison to the result in TG-DSC tests (10 K/min), the O_2 release temperature of microscale $K_2S_2O_8$ powders increased by only a small amount (~50 K) at ultrafast heating rates (~10^5 K/s) (Fig. 6.5). All of the other microscale oxysalts similarly release O_2 at temperatures of 30 - 100 K higher (Fig. 6.6 and Table 6.4). The MS results (Fig. 6.5) enable me to link the O_2 release temperature to the corresponding ignition temperature as will be discussed in the next section.

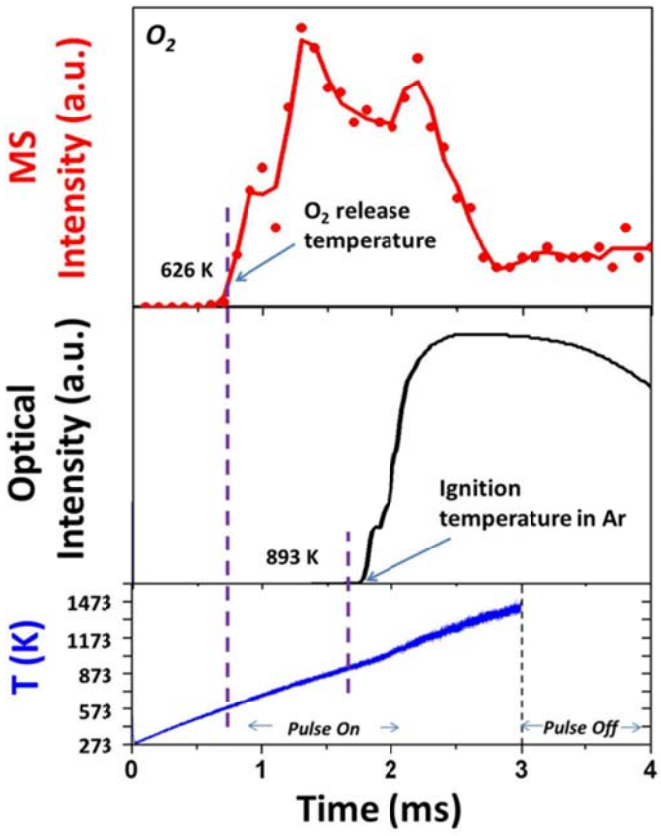

Figure 6.5. Temporal oxygen release from $K_2S_2O_8$ decomposition, and temporal optical emission from Al-$K_2S_2O_8$ reaction under ultrafast heating (4×10^5 K/s). The bottom panel shows the temporal temperature trace from the Pt wire. The middle panel shows the temporal trace of optical intensity from the thermite reaction in Ar, with the designated ignition temperature (893 K). The top panel shows the temporal MS intensity of oxygen release from the decomposition of $K_2S_2O_8$, with the onset temperature at 626 K.

6.3.4. T-jump ignition temperature

Ignition temperatures of the nine oxysalts were determined from the optical emission profiles. For example as shown in Fig. 6.5, the ignition temperature of nano-Al/micro-$K_2S_2O_8$ in Ar was measured to be 893 K as the onset of optical increase. Given that this ignition temperature is ~270 K higher than the O_2 release temperature (Fig. 6.5), I previously speculated that the O_2 release is one of the prerequisites for ignition, while it does not determine the initiation of Al-$K_2S_2O_8$ reaction [50]. We raise an important question in this study as to whether O_2 release prior to ignition is necessary for the initiation of the other Al-oxysalt reactions.

To address this issue, I compared the O_2 release temperatures and ignition temperatures of all the nine nano-Al/micro-oxysalt thermites in Fig. 6.6. Fig. 6.6A shows that although Al-KNO_3, Al-$KClO_4$, Al-KIO_3, Al-$KClO_3$, Al-$KBrO_3$, Al-KIO_4, and Al-$K_2S_2O_8$ have different O_2 release temperatures, they all ignited around the same temperature in Ar, and nominally ~50 K below the melting point of Al. Furthermore, ignition appears to be insensitive to available gas phase oxygen since the ignition temperature in Ar and air appear to be similar. The dotted vertical line in the plot (Fig. 6.6A) corresponds to the melting point of aluminum, and it appears that most of the ignition temperatures are aligned vertically and parallel to the dotted line, and thus do not correlate with the O_2 release temperature. These results imply that the ignition of the Al-oxysalt thermites is dominated by the accelerated outward diffusion of Al when approaching its melting point. The generated O_2 concentration locally from the decomposition of oxysalts is much higher than that in air (see the following Section 6.3.5 for the detailed comparison of the O_2 concentrations in film and in air),

so that the effect of O_2 in air is minimal to the ignition temperature of reactive Al-oxysalt thermites (Fig. 6.6A). However, when ignited in vacuum, these thermites show strikingly increased and distinct ignition temperatures (Fig. 6.6B). Gaseous oxygen generated from the oxysalt will presumably have little time to interact with Al in vacuum (see the following Section 6.3.6 for the detailed estimation of the O_2 residence time in thermite film both in air and in vacuum). Therefore the delayed and thus higher temperature ignition in vacuum should be attributed to condensed phase transfer of oxygen.

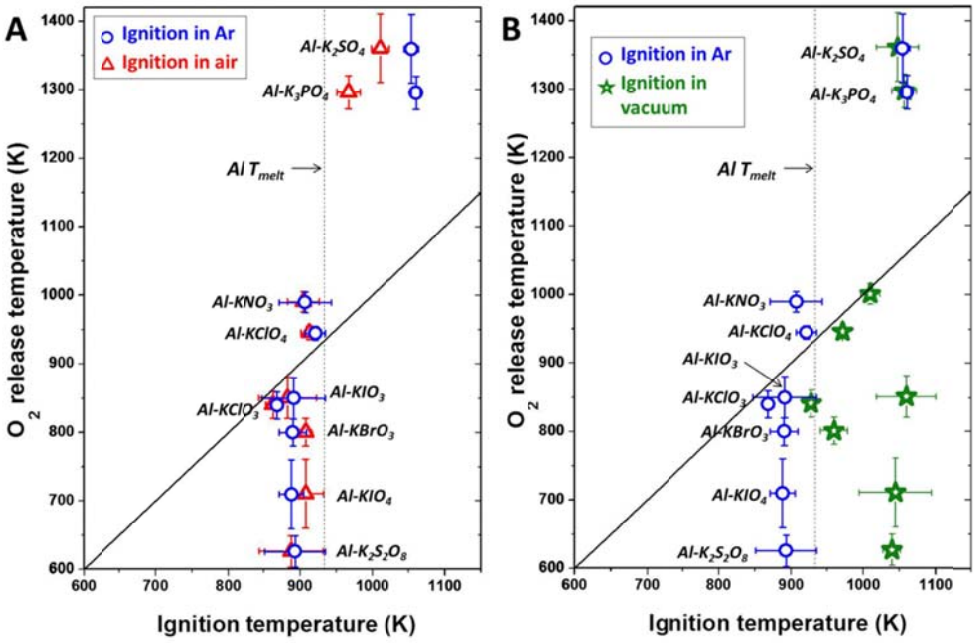

Figure 6.6. (A) Relationship between the oxygen release temperature in neat microscale oxysalt, and the ignition temperature of corresponding nano-Al-fueled thermite in Ar or in air. (B) Relationship between the oxygen release temperature in neat microscale oxysalt, and the ignition temperature of corresponding nano-Al-fueled thermite in Ar or in vacuum. Each temperature test was repeated at least twice. The diagonal solid line stands for a perfect correlation. The vertical dashed line indicates the melting temperature of Al (933 K).

The constant ignition temperature for these Al-oxysalt thermites at ~880 K corresponds to a critical phase change in the Al particle shell from amorphous (< 880 K) to γ-alumina [22]. Trunov et al reported that the density of γ-alumina is larger than amorphous alumina, thus the newly formed γ-alumina at ~880 K was not able to form a continuous dense layer outside the Al particle [22]. This partially covered shell facilitates the accelerated diffusion of Al, resulting in the increased oxidation rate of Al, which from the perspective of ignition, refers to the consistent ignition temperature for the reactive Al-oxysalt thermites at ~880 K.

The reaction behaviour of Al-K_2SO_4 and Al-K_3PO_4 thermites is clearly very different from the other seven thermites. Fig. 6.6A shows that their ignition temperatures in Ar are more than 100 K higher than the melting temperature of Al. In this case, Al is completely melted and most likely in intimate contact with the oxysalt. Considering that their O_2 release temperatures are even higher than their ignition temperatures, the ignition of Al-K_2SO_4 an Al-K_3PO_4 thermites presumably follows a condense phase route similar to the aforementioned case for the other thermites in vacuum (Fig. 6.6B). This postulated condense phase reaction mechanism for Al-K_2SO_4 and Al-K_3PO_4 thermites is further confirmed by their unchanged ignition temperatures in vacuum (Fig. 6.6B). However, when ignited in air, both Al-K_2SO_4 and Al-K_3PO_4 thermites show decreased ignition temperatures approaching the melting temperature of Al (Fig. 6.6A). This is consistent with these oxysalts acting almost as dead weight and the aluminum penetrating the alumina shell above its melting point to ignite with gaseous oxygen.

Table 6.4. Tabulated results of nine microscale oxysalts in Fig. 6.6 indicating their O_2 release temperatures, as well as ignition temperatures for corresponding aluminum-fueled thermites in Ar, in air and in vacuum, respectively. Each O_2 release temperature or ignition temperature was measured at least twice, and the average value is presented.

Microscale oxidizers	O_2 release temperatures (K)	Ignition temperatures in Ar (K)	Ignition temperatures in air (K)	Ignition temperatures in vacuum (K)
$K_2S_2O_8$	626 ± 23	893 ± 42	888 ± 44	1039 ± 12
K_2SO_4	1360 ± 50	1054 ± 10	1011 ± 12	1047 ± 29
KIO_4	710 ± 50	888 ± 17	908 ± 25	1044 ± 50
KIO_3	850 ± 30	891 ± 44	883 ± 40	1059 ± 41
$KClO_4$	945 ± 10	921 ± 14	913 ± 12	971 ± 5
$KClO_3$	840 ± 20	868 ± 8	863 ± 10	927 ± 6
$KBrO_3$	800 ± 20	890 ± 19	908 ± 8	959 ± 19
KNO_3	1000 ± 15	907 ± 31	905 ± 22	1009 ± 13
K_3PO_4	1296 ± 24	1060 ± 22	967 ± 16	1056 ± 17

We also conducted similar experiments by decreasing the dimension of oxysalts to nanometer scales so that the contact area between the fuel and oxidizer can be significantly increased. The motivation of this control experiment is to further evaluate my proposed reaction mechanism that includes reactive gaseous oxygen. Fig. 6.7 and Table 6.5 show a consistent correlation between ignition temperatures of the nano-Al/nano-oxysalt thermites in Ar, air and vacuum, similar to Fig. 6.6 for nano-Al/micro-oxysalt thermites. To understand the effect of the powder size of oxysalts, a typical comparison of the O_2 release temperature and the ignition temperature between nano-Al/nano-oxysalt and nano-Al/micro-oxysalt thermites in Ar was conducted in Fig. 6.8. Compared with the nano-Al/micro-oxysalt thermites, the nano-Al/micro-oxysalt thermites of Al-K_2SO_4 and Al-K_3PO_4 show more than 50 K reduction both in O_2 release and ignition temperatures. Since both thermites follow a condense phase reaction mechanism, it is reasonable to see the decrease in these

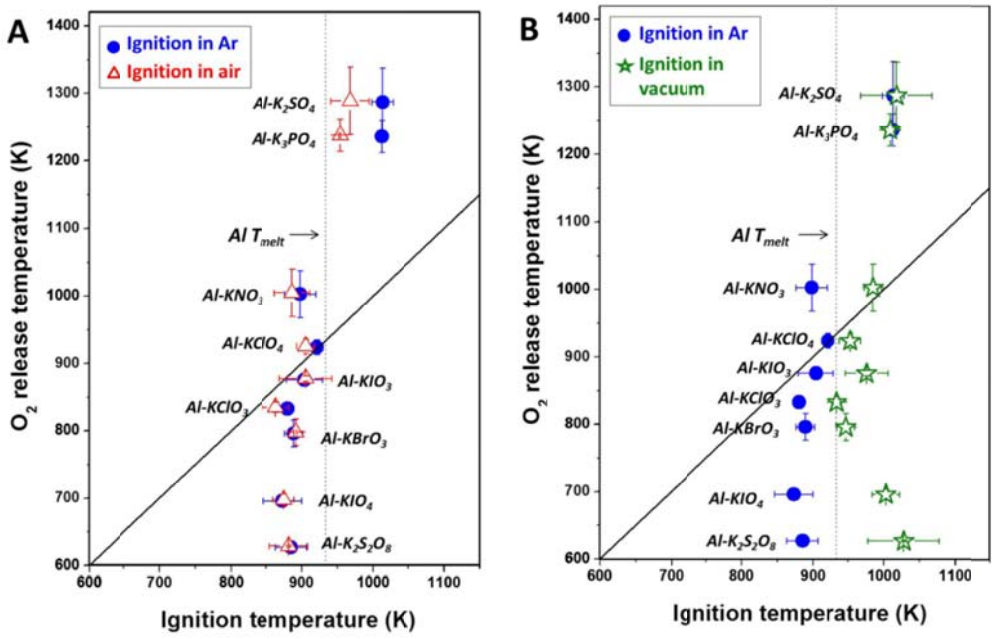

Figure 6.7. (A) Relationship between the oxygen release temperature in neat nanoscale oxysalt, and the ignition temperature of corresponding nano-Al/nano-oxysalt thermite in Ar or in air. (B) Relationship between the oxygen release temperature in neat nanoscale oxysalt, and the ignition temperature of corresponding nano-Al/nano-oxysalt thermite in Ar or in vacuum. Each temperature test was repeated at least twice. The diagonal solid line stands for a perfect correlation. The vertical dash line indicates the melting temperature of Al (933 K).

Table 6.5. Tabulated results of nine nanoscale oxysalts in Fig. 6.7 indicating their O_2 release temperatures, as well as ignition temperatures for corresponding aluminum-fueled nano-thermites in Ar, in air and in vacuum, respectively. Each O_2 release temperature or ignition temperature was measured at least twice, and the average value is presented.

Nanoscale oxidizers	O_2 release temperatures (K)	Ignition temperatures in Ar (K)	Ignition temperatures in air (K)	Ignition temperatures in vacuum (K)
$K_2S_2O_8$	627 ±1	885 ± 22	882 ± 27	1028 ± 50
K_2SO_4	1287 ± 50	1013 ± 15	968 ± 27	1018 ± 50
KIO_4	696 ± 8	873 ± 27	875 ± 15	1003 ± 19
KIO_3	876 ± 4	904 ± 25	906 ± 37	976 ± 30
$KClO_4$	924 ± 11	921 ± 9	906 ± 12	953 ± 15
$KClO_3$	833 ± 8	880 ± 5	864 ± 19	934 ± 5
$KBrO_3$	796 ± 20	889 ± 13	892 ± 2	947 ± 12
KNO_3	1003 ± 35	898 ± 22	887 ± 25	985 ± 12
K_3PO_4	1236 ± 24	1012 ± 50	954 ± 1	1009 ± 7

characteristic temperatures due to the increase of contact area between Al and oxysalt. In contrast, the ignition temperatures for the other seven thermites are independent of particle size, indicating that it is the reaction of Al and gaseous O_2 that contributes to the combustion initiation (Fig. 6.8).

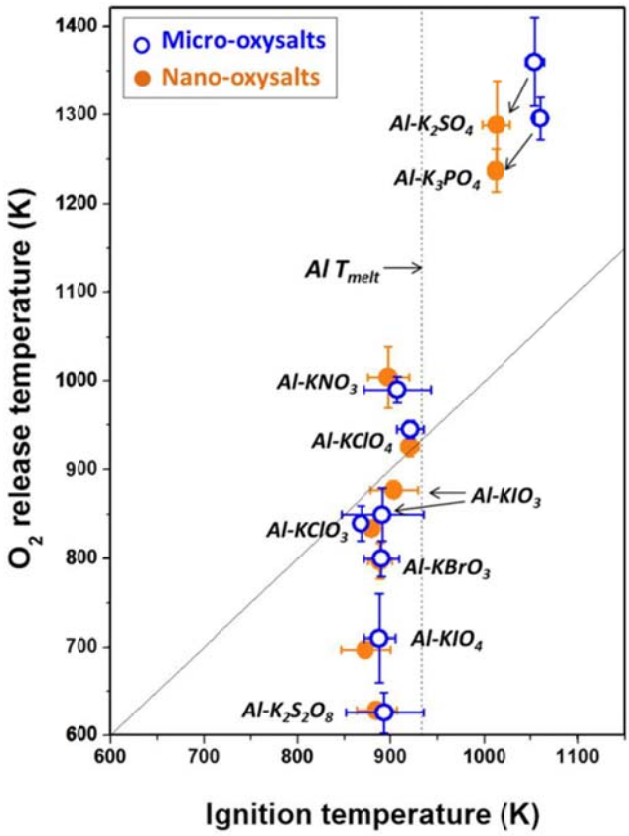

Figure 6.8. Effect of particle size: relationship between the oxygen release temperature in neat nanoscale and microscale oxysalts, and the ignition temperature of corresponding nano-Al-fueled thermite in Ar. The arrows designate the temperature shifts of both ignition temperatures and oxygen release temperatures for Al-K_2SO_4 and Al-K_3PO_4 thermites when the dimension of oxysalt drops from micrometer scale to nanometer scale.

Our proposed dual-phase reaction mechanism for reactive Al-oxysalts thermites, if correct, would provide a linear correlation between the ignition temperature and the relevant O_2 release temperature. However, since the Al fuel has a alumina shell that

limits the transport of Al and O, the thermite ignition is largely influenced by the accelerated Al diffusion, based on the fact that ignition occurs near the melting point of the metallic aluminum core (Fig. 6.6). The ignition temperatures of the seven reactive Al-oxysalt thermites were close to the aluminum melting point in both Ar and air (Fig. 6.6A and Fig. 6.7A) even though the corresponding oxysalts have different O_2 release temperatures. This indicates that the ignition was controlled by the accelerated outward diffusion of aluminum. However, this result provides no indication as to the nature of the reactive oxygen species that reacts with Al. The fact that in vacuum, where I expect little gas phase oxygen to play a role, the ignition temperature increases suggests that the initiating mechanism transitions from an oxygen gas reaction to a condensed phase oxygen exchange process.

To further explore this point I employ carbon as a fuel, because unlike Al, it has a very high melting temperature, thus no fuel mobility (> 3800 K), and since there is no oxide shell, the fuel is directly accessible to the oxidizer. Fig. 6.9 and Table 6.6 show that in contrast to Al, where ignition was confined to near the melting point of Al regardless of oxidizer species, the reactive nano-carbon/micro-oxysalt thermites (Al-KNO_3, Al-$KClO_4$, Al-KIO_3, Al-$KClO_3$, Al-$KBrO_3$, and Al-KIO_4) have a near perfect linear correlation between ignition and O_2 release temperatures both in Ar and in air. These reactive thermites are incombustible in vacuum, probably due to a lower reactivity of C than Al. These results clearly indicate that the reactive oxygen that leads to ignition with the surface bound carbon is from the released molecular oxygen, thus confirming the Al-O_2(g) reaction mechanism for the reactive oxysalt-containing thermites.

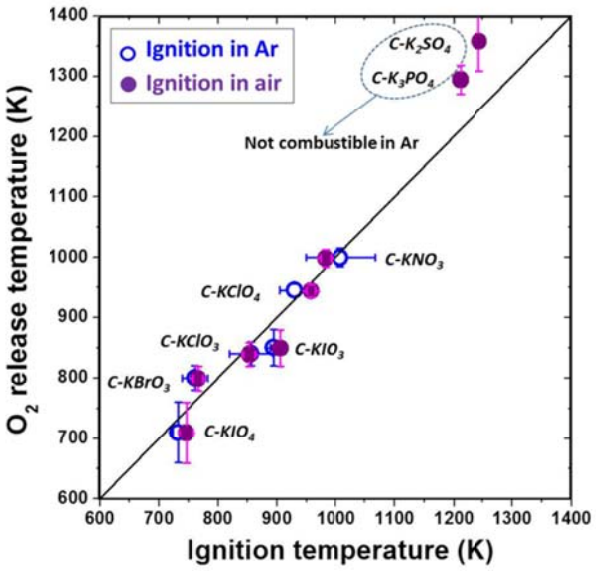

Figure 6.9. Relationship between the oxygen release temperature in neat microscale oxysalt, and the ignition temperature of corresponding nano-carbon-fueled thermite in Ar or in air. Each temperature test was repeated at least twice. The diagonal solid line stands for a perfect correlation. C-K_2SO_4 and C-K_3PO_4 thermites were found to be not combustible in Ar, and thus the relevant ignition temperatures were vacant in the diagram.

Table 6.6. Tabulated results of nine microscale oxysalts in Fig. 6.9 indicating their O_2 release temperatures, as well as ignition temperatures for corresponding carbon-fueled thermites in Ar, in air and in vacuum, respectively. Each O_2 release temperature or ignition temperature was measured at least twice, and the average value is presented.

Microscale oxidizers	O2 release temperatures (K)	Ignition temperatures in Ar (K)	Ignition temperatures in air (K)	Ignition temperatures in vacuum (K)
$K_2S_2O_8$	626 ± 23	Side reaction[a]	Side reaction[a]	Side reaction[a]
K_2SO_4	1360 ± 50	No reaction	1245 ± 50	No reaction
KIO_4	710 ± 50	732 ± 9	748 ± 12	No reaction
KIO_3	850 ± 30	894 ± 6	907 ± 50	No reaction
$KClO_4$	945 ± 10	929 ± 25	959 ± 7	No reaction
$KClO_3$	840 ± 20	856 ± 37	855 ± 10	No reaction
$KBrO_3$	800 ± 20	768 ± 22	768 ± 8	No reaction
KNO_3	1000 ± 15	1008 ± 50	984 ± 9	No reaction
K_3PO_4	1296 ± 24	No reaction	1213 ± 50	No reaction

Note: [a] $K_2S_2O_8$ is capable of oxidizing nano-C in the mixed suspension before ignition [60].

Two exceptions are C-K_2SO_4 and C-K_3PO_4, which are not combustible in Ar, while have higher ignition temperatures than their O_2 release temperatures in air. This result confirms my previous interpretation that the less reactive thermites undergo a condense phase reaction mechanism.

6.3.5. Estimation of the effect of O_2 in air to the ignition temperature of reactive Al-oxysalt thermites

For calculating the local O_2 concentration (C), I estimated that the mass ratio of oxygen in Al-oxysalt thermite is ~30% [50], and the packing density of the film is 20% [52]. Since most of the F/O reactants have similar mass densities (Al: 2.7 g/cm^3, $KClO_3$: 2.32 g/cm^3, KIO_3: 3.89 g/cm^3, K_2SO_4: 2.66 g/cm^3, etc.), I assume the average density of the loaded mass on wire is ~ 3 g/cm^3. Therefore, the O_2 concentration decomposed from the oxysalt can be calculated as C = 20% × (3 g/cm^3) × 30% / (32 g/mol) = 5626 mol/m^3.

On the other hand, the density of air is 1.3 kg/m^3, and the mass ratio of O_2 in air is ~21%. Thus the inherent oxygen concentration in air is C_{air} = (1.3kg/m^3) × 21% / (32 g/mol) = 8.5 mol/m^3. We can see that C is ~ 3 orders of magnitude larger than C_{air}. This result explains why the oxygen in air won't affect the ignition temperature.

6.3.6. Estimation of the O_2 residence time in thermite film

The diffusion coefficient, D for oxygen gas can be expressed by the Chapman–Enskog theory [59]:

$$D = \frac{1.86\times10^{-3}T^{1.5}}{P\sigma^2\Omega}\sqrt{1/M_1 + 1/M_2} \tag{6.10}$$

where M_1 and M_2 are the molar weights of O_2 and air, respectively, P is the external pressure, σ is the collision diameter, Ω is a temperature-dependent collision integral (usually equals to one). The diffusion coefficient of O_2 in 1 atm, r.t. air was documented as 0.176 cm^2/s [59]. Suppose the diffusion length for oxygen is L = 10 μm (the film thickness), the dwell time of O_2 in film in air is estimated as $t = L^2/D$ = 0.01ms. This time scale is close to the pressurization time scale of most reactive thermites (0.1ms - 1ms), indicating that the residence time of O_2 allows the ignition of Al in air or Ar.

However, when the experiment was conducted in vacuum (10^{-5} Pa), according to eq 6.10 the D value was increased by 10 orders of magnitude ($D' = 0.176\times10^{10}$ cm^2/s), resulting in a much shorter dwell time $t' = L^2/D' = 10^{-12}$ ms. This result evidently shows that the oxygen generated from the oxysalt will presumably have little time to interact with Al in vacuum.

6.3.7. Reaction mechanisms

Here I summarize the experimental results within a framework of some plausible mechanisms as illustrated in Fig. 6.10. In this study I consider mainly four characteristic temperatures. The ignition temperature (T_{ig}), the oxygen release temperature (T_{O2}), the phase change temperature for the alumina shell ($T_{\gamma\text{-}Al2O3}$, which is close to the melting temperature of aluminium, $T_{Al\text{-}melt}$), and the melting temperature of oxysalt ($T_{oxidizer\text{-}melt}$). The nine Al-oxysalt thermites can be generally divided into two groups. The first group includes Al-$K_2S_2O_8$, Al-KIO_4, Al-KIO_3, Al-$KClO_3$ and Al-$KBrO_3$ as they fall *below the diagonal* in Fig. 6.6A. These thermites

have $T_{O2} < T_{\gamma\text{-}Al2O3} = T_{ig} < T_{Al\text{-}melt}$, and minimal or lower $T_{oxidizer\text{-}melt}$. The ignition for these thermites is driven by the interaction of released O_2 from the oxysalt and the accelerated outwardly diffusing Al atoms when the temperature of the polymorphic phase change in alumina (~880 K, from amorphous to γ-Al_2O_3) is reached (which also approaches $T_{Al\text{-}melt}$ at ~930 K) [22]. This phase change at ~880 K features some degree of porosity in the alumina shell due to the increase of alumina density, leading to the enhancement of Al diffusion across the alumina shell, and therefore the initiation of thermite reaction. Two thermites including Al-KNO_3 and Al-$KClO_4$ have a transformed ignition type subordinate to the first group (Fig. 6.11), which ignite before oxygen is released. These are the thermites that are found *above the diagonal* in Fig. 6.6A. In this case, the oxysalt melts prior to ignition ($T_{oxidizer\text{-}melt} < T_{\gamma\text{-}Al2O3} = T_{ig} < T_{O2}$), thus the thermite must initially be ignited by the interaction of bound oxygen in the molten oxysalt and accelerated outwardly diffused Al at the temperature of polymorphic phase change in the alumina shell (~880 K, close by $T_{Al\text{-}melt}$). Once ignition commences, self-heating will generate gaseous oxygen which then will be the predominant reaction mechanism, as the in-vacuum experiments illustrate (Fig. 6.6B). The second group of thermites includes Al-K_2SO_4 and Al-K_3PO_4 that are *substantially above the diagonal* (Fig. 6.6A) and thus gas-phase generated oxygen cannot be important. The ignition temperatures for these less reactive thermites are higher than $T_{Al\text{-}melt}$, while lower than T_{O2} (Fig. 6.6A), suggesting that ignition is determined by the accelerated outward flow of oxygen from the melt oxysalt ($T_{Al\text{-}melt} < T_{oxidizer\text{-}melt} = T_{ig} < T_{O2}$). These results demonstrate that ignition of Al-oxysalt thermites requires both the availability of Al and oxygen at the reaction interface, and

is much related to the temperature of polymorphic phase change for alumina ($T_{\gamma\text{-}Al2O3}$). The first group of thermites has a lower temperature for oxygen availability (either T_{O2} or $T_{oxidizer\text{-}melt}$) than $T_{\gamma\text{-}Al2O3}$, thus ignition for these formulations is triggered by the accelerated diffusion of Al ($T_{ig} = T_{\gamma\text{-}Al2O3}$). Conversely, the other group of thermites has a higher temperature for oxygen availability (mainly $T_{oxidizer\text{-}melt}$) than $T_{\gamma\text{-}Al2O3}$, thus the limiting step in triggering is the accelerated diffusion of oxygen ($T_{ig} = T_{oxidizer\text{-}melt}$).

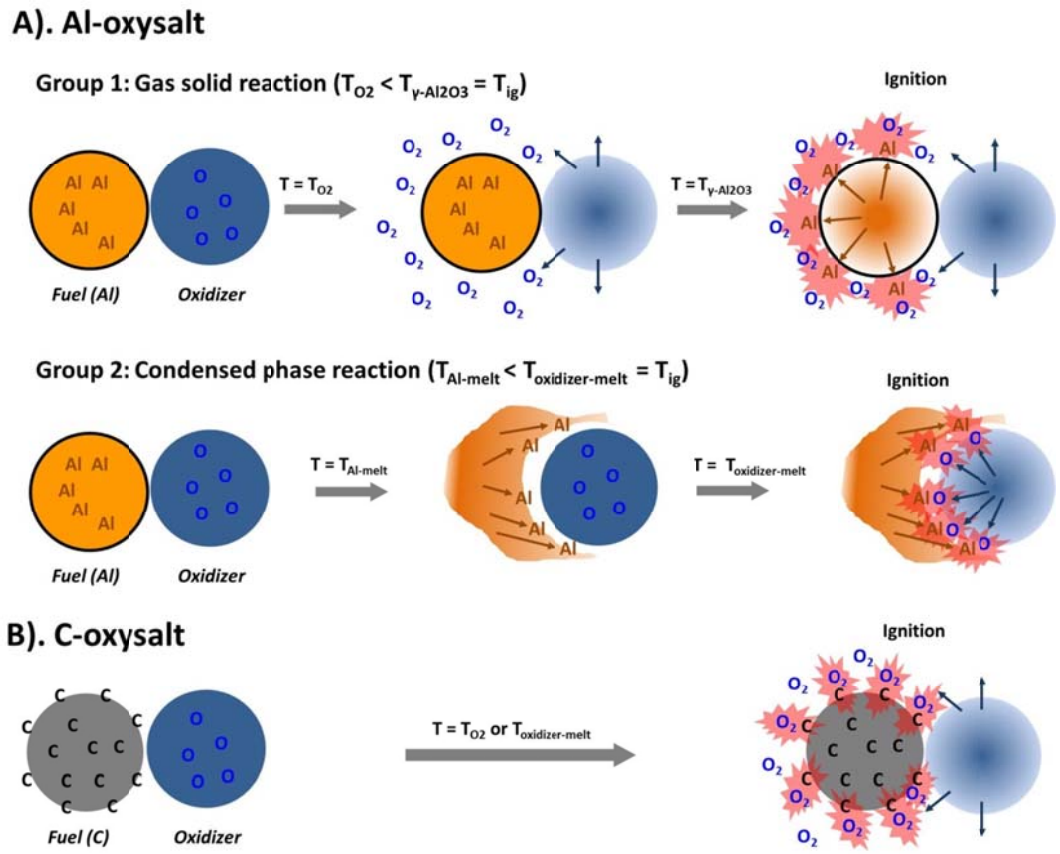

Figure 6.10. Ignition mechanisms for the Al-oxysalt thermites (A) and C-oxysalt thermites (B).

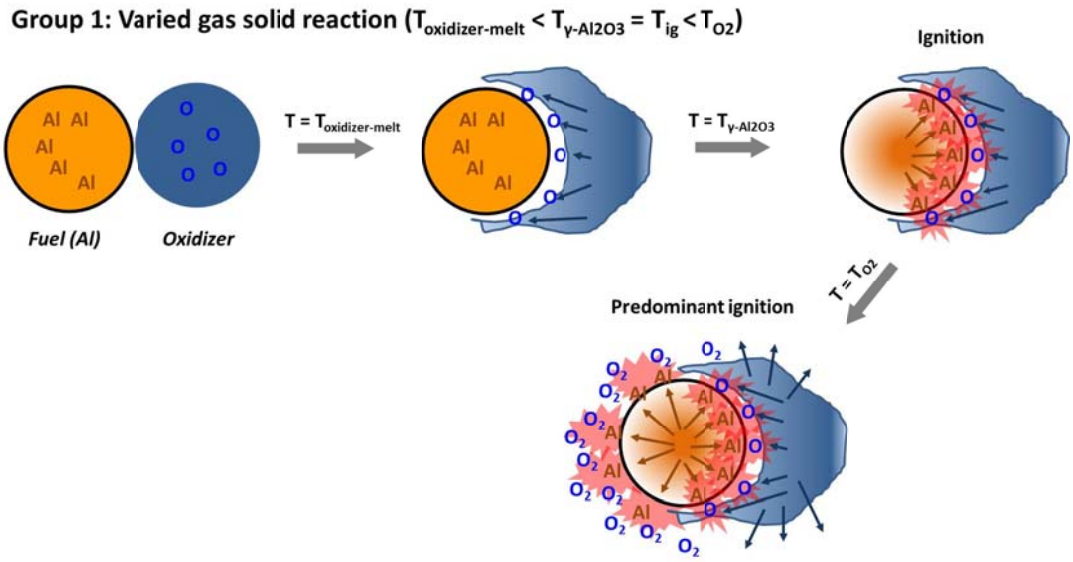

Figure 6.11. Ignition mechanism for Al-KNO_3 and Al-$KClO_4$.

For the ignition of nano-C with oxidizers, since carbon is solid and has no oxide shell at all the ignition temperatures, ignition is simply controlled by the availability of reactive oxygen from the oxidizers (decomposition or melting) (Fig. 6.10B). Thus, most of the ignition temperatures are linearly correlated to the relevant O_2 release temperature or melting temperature of oxidizers.

6.4. Conclusions

I implemented a study of the reaction mechanisms of oxysalt-containing thermites. Based on their combustion behavior, nine oxysalt-containing thermites were divided into two groups, with the reactive thermites (e.g., Al-$K_2S_2O_8$) showing ~10× higher maximum pressure, and ~10× shorter burn time than the less reactive thermites (e.g., Al-K_2SO_4). The difference in ignition temperature (T_{ig}) is attributed to the oxygen release temperature (T_{O2}), the temperature of polymorphic phase change for alumina

($T_{\gamma\text{-}Al2O3}$), and the melting temperature of oxysalt ($T_{oxidizer\text{-}melt}$). The basic results are: (1) T_{ig} of the reactive thermites in Ar and in air are similar to $T_{\gamma\text{-}Al2O3}$ (close to $T_{Al\text{-}melt}$), while the corresponding T_{ig} in vacuum are higher; (2) T_{ig} of the less reactive thermites in Ar and in vacuum are consistent, and much higher than $T_{Al\text{-}melt}$, although lower than T_{O2} and $T_{oxidizer\text{-}melt}$ of the corresponding oxysalts. These results indicate that the limiting initiation step of the reactive thermites is the capability of Al atoms to diffuse through the Al_2O_3 shell towards the reactive oxygen at the interface (gaseous or molten), whereas the limiting initiation step of the less reactive thermites is the decomposition or melting of oxysalts to deliver oxygen to the molten Al. Use of nano-carbon-fueled oxysalt thermites confirm that there are two reaction mechanisms for these oxysalt-containing thermites. In terms of the various ignition dependence of heterogeneous solid-gas reaction or condense state reaction, I proposed a general framework of ignition mechanisms for different oxysalt-containing thermites.

Chapter 7: Evaluating Free vs. Bound Oxygen on Ignition of Nano-aluminum Based Energetics Leads to a Critical Reaction Rate Criterion*

Overview

This study investigates the ignition of nano-aluminum (n-Al) and n-Al based energetic materials (nanothermites) at varying O_2 pressures (1-18 atm), aiming to differentiate the effects of free and bound oxygen on ignition and to assess if it is possible to identify a critical reaction condition for ignition independent of oxygen source. Ignition experiments were conducted by rapidly heating the samples on a fine Pt wire at a heating rate of ~10^5 °C s^{-1} to determine the ignition time and temperature. The ignition temperature of n-Al was found to reduce as the O_2 pressure increased, whereas the ignition temperatures of nanothermites (n-Al/Fe_2O_3, n-Al/Bi_2O_3, n-Al/K_2SO_4 and n-Al/$K_2S_2O_8$) had different sensitivities to O_2 pressure depending on the formulations. A phenomenological kinetic/transport model was evaluated to correlate the concentrations of oxygen both in condensed and gaseous phases, with the initiation rate of Al-O at ignition temperature. We found that a constant critical reaction rate (5×10^{-2} mol m^{-2} s^{-1}) for ignition exists which is independent to ignition temperature, heating rate and free vs. bound oxygen. Since for both the thermite and the free O_2 reaction the critical reaction rate for ignition is the same, the various

* The results presented in this chapter have been published in the following journal article: **W. Zhou**, J. B. DeLisio, X. Wang, G. C. Egan, M. R. Zachariah*. Evaluating Free vs. Bound Oxygen on Ignition of Nano-aluminum Based Energetics Leads to a Critical Reaction Rate Criterion. ***J. Appl. Phys.***, 2015, 118, 114303.

ignition temperatures are simply reflecting the conditions when the critical reaction rate for thermal runaway is achieved.

7.1. Introduction

Recent advances in large-scale manufacturing and processing of nanoparticles have motivated research on energetic materials with nanoscale features and structures [1-3]. Nano-aluminum (n-Al), due to its high energy density and superior reactivity, is one of the most widely studied nanomaterials for pyrotechnics, propellants, and explosives applications [4,5]. A variety of powdered n-Al explosives and aluminized nanocomposites (nanothermites) that contain oxidizers are being evaluated based on their rate and intensity of energy release [1-3], as well as their sensitivity and stability [6,7]. Compared to self-sustaining steady state combustion, reaction initiation (ignition) is difficult to study and control due to its very fast transient nature and its sensitivity to many parameters such as heating rate [8,9], particle size [10,11] and assembly [12,13] (influencing the contact area between fuel and oxidizer). For n-Al, ignition is further complicated by the thin (~2-5 nm) native oxide shell, alumina (Al_2O_3), that acts as a passivation layer at low temperatures [14,15].

In order for ignition to occur, a threshold must be surpassed where the mutual transfer of Al and O across the Al_2O_3 shell is rapid enough to induce a sufficiently higher energy release rate relative to energy loss to the surroundings. It is expected that oxygen anions and aluminum cations migrate radially inward and outward respectively by the concentration gradients [16]. In addition, the outward transport of Al cations is primarily driven by a built-in electrical field across the alumina shell, as

described by the Cabrera-Mott theory [17,18], as well as by the pressure-driven outward convection due to the volumetric expansion of Al core during heating [19,20]. Given these two additional mechanisms, and that the Al cations are smaller than the oxygen anions [16], the Al flux outwards should exceed that of oxygen inwards. This diffusion bias is prevailingly evidenced by several reports showing that hollow structures are formed during the oxidation of n-Al particles [21-23]. Therefore, the reaction interface is expected to be at the outer surface of the aluminum enriched alumina shell [16,21].

Ignition of n-Al in gaseous oxidizers and of aluminum-fueled nanothermites relies on the same fundamental global reaction between Al and O. The distinction is that for nanothermites, the reactive oxygen that participates in the ignition event comes from oxygen bound in the oxygen lattice sites of the solid oxidizers. Based on the availability of free gaseous oxygen in the ignition event, the ignition mechanisms can be divided into two categories: (1) the condensed phase Al-O reaction and (2) the Al-O_2(g) heterogeneous reaction. For many Al/metal oxide formulations (e.g., Al/Bi_2O_3 [24]), O_2 is released from oxidizers at a higher temperature than the corresponding ignition temperature, indicating that ignition is mainly triggered by the condensed phase reaction between Al and bound oxygen. In some other cases (e.g. Al/CuO [25]), oxygen release is prior too, or synchronized with ignition, suggesting that the predominant reactive oxygen that participates in the initiation reaction could be gaseous O_2. A recent study has investigated ignition temperatures of multiple oxysalt based thermites in various gaseous environments [26]. The results show that some reactive oxysalts, such as potassium periodate (KIO_4) [27] and potassium persulfate

($K_2S_2O_8$) [28], are more easily decomposed than traditional metal oxides, thus exhibiting very low O_2 release temperatures and ignition temperatures. In this case, it is believed that free gaseous O_2 plays the predominant role in triggering the ignition event [26-28]. Due to the reactive sintering of fuel and oxidizer at the initiation stage for many thermite formulations as observed from post-reaction products analysis [29,30] and in situ fast-heating electron microscopy [29,31,32], the two aforementioned ignition mechanisms may be actually coincident in a single ignition event. While many studies have supported these two main ignition mechanisms, they fail to explain when these different mechanisms exist, and under what conditions they prevail [28,33].

Previous studies have presented a muddled vision of the criteria that control the ignition of n-Al based energetic materials. The melting point of Al, or the decomposition temperature of oxidizer, have been presumed as the criterion for ignition [34,35]. However, some experimental results have also revealed that there is no correlation between these characteristic temperatures and ignition temperature [36]. These results suggest that the ignition phenomenon is not merely driven thermodynamically, but is also driven kinetically. Previous kinetic models have been proposed for the oxidation of n-Al in which power-law functions were adopted to describe the oxidation rate of Al [37-39]. Since these functions were developed to describe oxidation kinetics when a significant conversion from Al to Al_2O_3 had occurred, they are inappropriate for ignition kinetics, which feature a very small conversion ratio. Alternatively, zero-order Arrhenius models involving no concentration of reactants [40,41], and 1st order models which include oxygen

concentration as a parameter have been employed [42]. However, given that the concentration of Al at the reaction interface may also change with temperature [14,19, 22, 34-36, 43-45], an improved model containing both concentrations of Al and O needs to be evaluated. In addition, some consideration should be given which will shed light on the aspect of metal ignition when the source is free O_2 vs. bound oxygen.

In this Chapter, the ignition of n-Al based energetic materials was analyzed to explore the role of bound vs. free oxygen, and to assess if it is possible to identify a critical reaction condition for ignition independent of oxygen source. For these studies, I evaluate the ignition of n-Al and four aluminum based nanothermites (n-Al/Fe_2O_3, n-Al/Bi_2O_3, n-Al/K_2SO_4 and n-Al/$K_2S_2O_8$) in O_2. What distinguishes this particular work is that I simultaneously varied the O_2 concentration as a control variable through the initial pressure (1-18 atm). The experimental results were used in conjunction with a phenomenological kinetic/transport model to determine a critical condition for ignition and a global activation energy. When combined with the experimental results the model enables me to distinguish the role of free vs. bound oxygen on ignition. The result shows that the critical reaction condition for ignition is independent of oxygen source and heating rate.

7.2. Experimental section

7.2.1. Materials

N–Al particles (~50 nm) were obtained from Argonide Corporation. Bismuth oxide (Bi_2O_3) and iron oxide nanoparticles (Fe_2O_3) (~50 nm) were obtained from Sigma-Aldrich. Microscale potassium persulfate ($K_2S_2O_8$) and potassium sulfate (K_2SO_4)

powders were purchased from Fluka and Sigma Aldrich, respectively. Nanoscale potassium persulfate ($K_2S_2O_8$) and potassium sulfate (K_2SO_4) were prepared by spray drying of the $K_2S_2O_8$ water solution (0.02 mol L^{-1}) at 150 ˚C, and the K_2SO_4 water solution (0.02 mol L^{-1}) at 180 ˚C, respectively [26,28]. Nanothermites were prepared by sonicating the n-Al and nanoscale oxidizers stoichiometrically in hexane for 30 mins, followed by stirring overnight and desiccation in vacuum.

7.2.2. Temperature jump (T-jump) ignition measurements

The ignition tests were conducted by coating the hexane suspension of n-Al or aluminum-fueled nanothermites evenly onto a (76 μm diameter × 10 mm long) platinum (Pt) wire. The particle layer was found to have a length of ~ 8 mm and a thickness of 25 μm. In the case of ignition of n-Al, the mass of n-Al was estimated to be ~ 30 μg, assuming the sample pack density on wire is ~20% [25]. In the case of ignition of nanothermites, I controlled the same coating volume of samples on wire as that for n-Al, and the masses were around 30 μg – 75 μg depending on the formulations. After drying in air, the wire was resistively heated to ~1200 ˚C within 3 milliseconds (~4×10^5 ˚C s^{-1}) by a tunable voltage pulse generated by a home-built power source (Fig. 7.1). For any given voltage, the current passing through the wire was measured using a current probe (AM503, Tektronix). The transient voltage and current were simultaneously recorded into an oscilloscope (WR 606Zi, Teledyne-LeCroy). The transient temperature on the wire during the pulse time was measured according to the standard electrical resistance/temperature relationship for Pt (Callendar-Van Dusen equation [46]). The ignition time was determined using a high

speed camera (Vision Research Phantom v12.0) (Fig. 7.1) and identified as the onset time of an appreciable emission of light above the background signal from the wire. A new T-jump Pt wire was used for each experiment. Our previous analysis shows that for a particle layer up to ~30 μm in thickness, the difference in temperatures of particle layer and basement wire is not discernible [25]. This indicates that the temperature of nanopowders approximately matches the temperature on the wire prior to ignition.

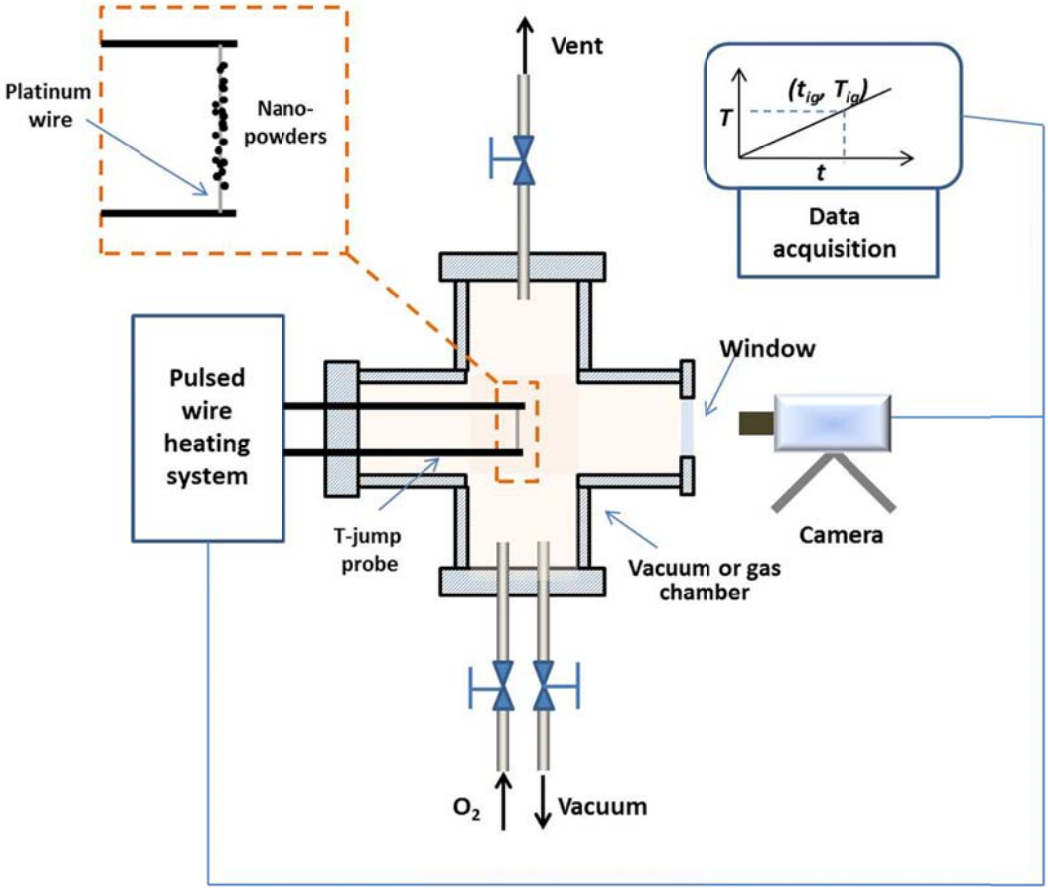

Figure 7.1. Schematic of the wire heating experiments.

To control the ignition of n-Al in different O_2 pressures, the T-jump probe was placed in a chamber that enabled ignition conditions to be varied from 10^{-10} atm up to

18 atm (Fig. 7.1). To control the ignition of n-Al at different heating rates, n-Al was heated to the same peak temperature of ~1200 ˚C but within different pulse times (2 ms, 4 ms, 8 ms, and 16 ms). A thinner Pt wire (radius = 12.7 μm) was also used in the ignition test of n-Al in O_2, to evaluate if the results were dependent on wire diameter. The mass loaded on the thinner wire was kept constant as ~ 20 μg.

7.3. Results and discussion

7.3.1. Ignition of n-Al in free oxygen

In order to evaluate the role of free O_2, the chamber was filled with the pure gas at pressures ranging from 10^{-10} atm to 18 atm. Fig. 7.2 shows that the ignition temperature decays with increasing O_2 pressure, and drops below the melting point of bulk Al at >7.4 atm. As the O_2 pressure further increases to over 15 atm, the ignition temperature asymptotically approaches a value of ~620 ˚C. This threshold implies that ignition at this point is limited by the mobility of Al migrating outwards, so that below a critical temperature, the surface concentration of Al is too low to support the ignition event. Considering that a smaller particle size is able to depress the ignition temperature of bulk Al [36], this critical temperature is probably correlated with the melting of n-Al. This strong dependence on O_2 pressure for ignition temperature represents a thermodynamic state (i.e. temperature) for rapid kinetics sufficient for run-away reaction.

7.3.2. Ignition of n-Al based thermites (i.e. bound oxygen)

In the previous example, O_2 was free and its concentration was systematically varied by changing the pressure. Next, bound oxygen was investigated through the ignition of four n-Al based thermites (n-Al/Fe_2O_3, n-Al/Bi_2O_3, n-Al/K_2SO_4 and n-Al/$K_2S_2O_8$). Fig. 7.3 shows that these nanothermites have a wide range of ignition temperatures in vacuum, with the highest ignition temperature for n-Al/Fe_2O_3 at 825 ˚C, and the lowest for n-Al/Bi_2O_3 at 590 ˚C. Since a low pressure environment will promote rapid extraction of any gaseous O_2 generated by the oxidizer away from the thermite mixture on the wire, the initiation reaction for these nanothermites in vacuum (~10^{-10} atm) should be predominantly controlled by the condensed phase reaction. Given that the ignition temperatures follow: n-Al/Fe_2O_3 > n-Al/K_2SO_4 ≈ n-Al/$K_2S_2O_8$ > n-Al/Bi_2O_3, and there is only a small difference in the oxygen densities of the four oxidizers, the different ignition temperatures in vacuum are more likely to be correlated to different activation energies of these four condensed phase Al-O reactions.

Increasing the O_2 pressure resulted in a variety of, mainly decreasing trends, that was dependent on the thermite system. The decaying dashed line represents a fit for pure n-Al from the data in Fig. 7.2. For the case of n-Al/Bi_2O_3, which already possesses a low ignition temperature, increasing the O_2 concentration has no discernible effect. This confirms previous work [33] that the initiation of the n-Al/Bi_2O_3 is controlled exclusively by a condensed phase reaction, with ignition occurring much earlier than the decomposition temperature of Bi_2O_3 (~1300 ˚C). This behavior has been explained by the fact that Bi_2O_3 has one of the highest known

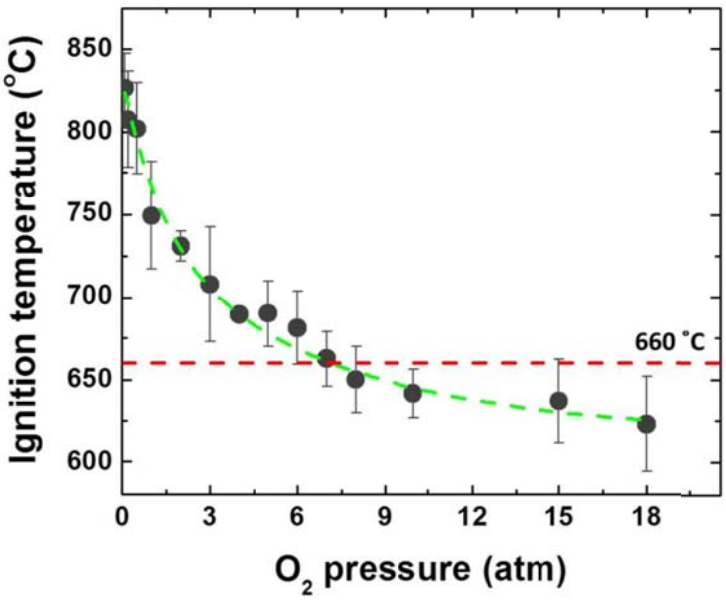

Figure 7.2. Ignition temperature of n-Al vs. external oxygen gas pressure. Each data point represents the average of at least three measurements. The error bars of ~10% are mainly from my temperature measurement which has a degree of inaccuracy of ± 25 ˚C.

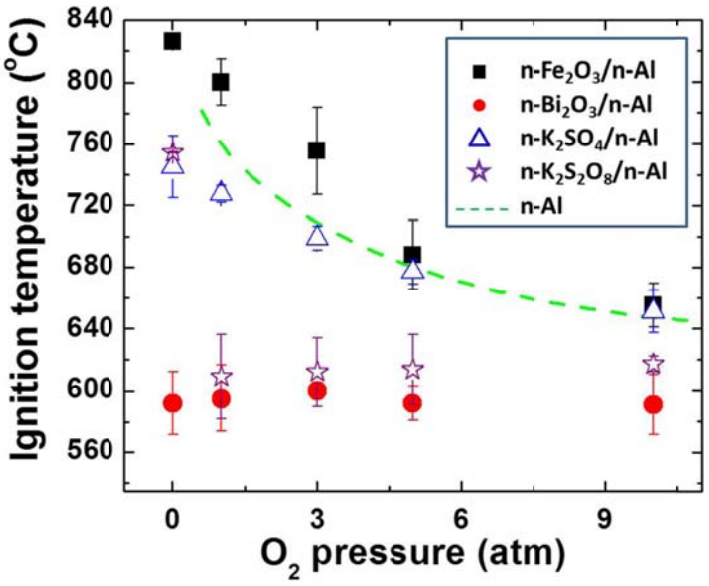

Figure 7.3. Ignition temperatures for four different n-Al based thermites (n-Al/Fe_2O_3, n-Al/Bi_2O_3, n-Al/K_2SO_4 and n-Al/$K_2S_2O_8$) as a function of external oxygen pressure. Each data point represents an average of at least two measurements. The decaying dashed line represents a fit for pure n-Al from the data in Fig. 7.2.

oxygen ion conductivities among typically used oxidizers [47], which would greatly enhance condensed phase transport of oxygen.

The opposite extreme to the Bi_2O_3 containing system would be one where gas phase O_2 is released from the oxidizer at a lower temperature than ignition [27]. One such system is n-Al/$K_2S_2O_8$, which shows a significant reduction of ignition temperature in O_2 (610 ˚C) when compared to that in vacuum (755 ˚C). If condensed phase reaction were important then I should expect no decrease in ignition temperature between vacuum and 1 atm. However the fact that increasing pressure of O_2 does not change the ignition temperature implies that O_2 release from n-Al/$K_2S_2O_8$ is controlling. Furthermore the fact that this reaction, has a lower ignition temperature than the neat n-Al in O_2, as represented by the decaying dashed line (Fig. 7.3), is consistent with the fact that the oxygen concentration in solid oxidizers (7×10^4 mol m^{-3}) is more than 2 orders of magnitude higher than that in gas (1- 100 mol m^{-3} when the O_2 pressure changes from 0.1 atm to 18 atm (Fig. 7.2)). Thus in the case of $K_2S_2O_8$ the bound oxygen is released at much higher concentration than the local O_2 pressures tested in this experiment [27,28].

For the other two investigated nano-thermite formulations, the ignition temperatures decrease as the O_2 pressure increases (Fig. 7.3). At O_2 pressures below 5 atm, the ignition temperatures of n-Al/Fe_2O_3 are higher than the corresponding ignition temperatures of n-Al, while the ignition temperatures of n-Al/K_2SO_4 are in contrast lower (Fig. 7.3). We have seen in Fig. 7.3 that the ignition points of n-Al/Fe_2O_3 and n-Al/K_2SO_4 in vacuum are above and below the dashed line, respectively, indicating that the reaction rate between Al and bound oxygen from

Fe_2O_3 is lower than that between Al and free O_2, while the reaction rate between Al and bound oxygen from K_2SO_4 is higher. If I consider the overall initiation reaction for these two nanothermites are comprised of two competitive reactions (Al reacting with gaseous oxygen and condensed phase oxygen), since the reaction rates follows: Al-O (from K_2SO_4) > Al-O_2 (g) > Al-O (from Fe_2O_3), one would expect to see that ignition temperatures follows: n-Al/Fe_2O_3 > n-Al > n-Al/K_2SO_4, consistent with my experimental results in the O_2 pressure range of 1-5 atm (Fig. 7.3). At O_2 pressures above 5 atm, their ignition temperatures asymptotically approach the corresponding ignition temperature of n-Al (Fig. 7.3). This indicates that once more gaseous oxygen is added, n-Al in the formulation initiates predominantly by a relatively more reactive Al-O_2 (g) mechanism, and the oxidizers gradually become dead weight in the system until after ignition.

7.3.3. Thermal transfer analysis and criterion for n-Al at ignition

The ignition results of n-Al and n-Al based nanothermites have suggested that ignition temperature is controlled by the local concentration of oxygen, either in the condensed phase as in the case of Bi_2O_3 or alternatively as an effective local O_2 concentration as in the case of $K_2S_2O_8$. A higher oxygen concentration (or lower activation energy) would lead to a larger reaction rate between Al and O, which as a result induces more heat generation at a given temperature. To evaluate these results more thoroughly, I will develop a relationship between a global reaction rate at the point of ignition (R_c), and the ignition temperature. We assume that n-Al has a radius r of ~25 nm and an alumina shell thickness d of ~4 nm, which is roughly consistent

with the n-Al employed in the experiments. Since only one size of n-Al was used in this study, the effect of contact area between Al and O was not considered. The energy balance for the n-Al coated Pt wire is as follows (also see Fig. 7.4(a)):

$$\dot{q}_a = \dot{q}_r + \dot{q}_{e,loss} + \dot{q}_{gain} + \dot{q}_{c,loss} + \dot{q}_{rad,loss} + \dot{q}_{r,evap} \tag{7.1}$$

where $\dot{q}_a$ is the net accumulated energy of the n-Al coated Pt wire, $\dot{q}_r$ is the generated energy from the Al-O reaction, $\dot{q}_{e,loss}$ is the energy loss from Al evaporation, $\dot{q}_{gain}$ is the energy gain from the resistive heating of the wire, $\dot{q}_{c,loss}$ is the conducted energy loss to the environment (mainly the electrodes that hold the wire), $\dot{q}_{rad,loss}$ is the heat loss by radiation, and $\dot{q}_{r,evap}$ is the heat generated from the reaction of O_2 and

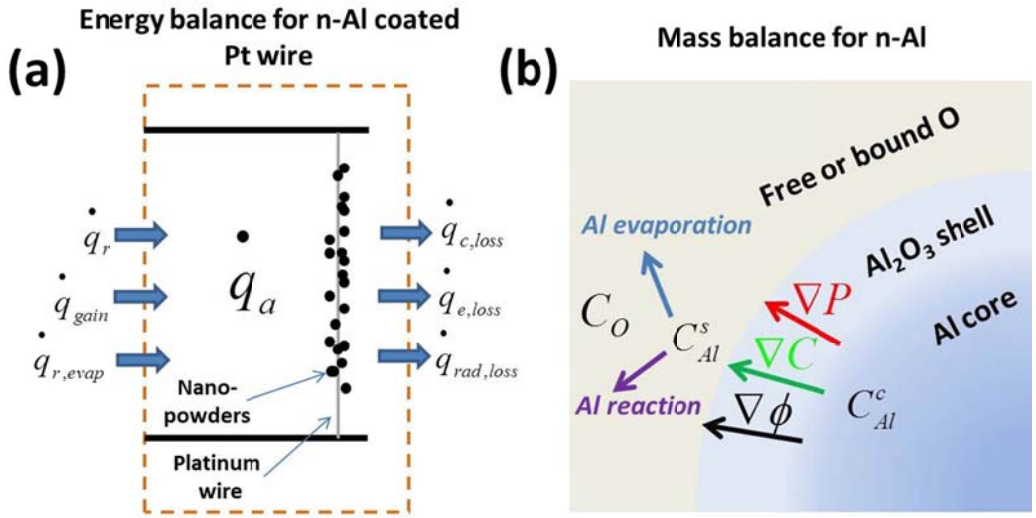

Figure 7.4. (a) The energy balance for the n-Al coated Pt wire. $\dot{\boldsymbol{q}}_{\boldsymbol{a}}$ is the net accumulated energy of the n-Al coated Pt wire, $\dot{\boldsymbol{q}}_{\boldsymbol{r}}$ is the generated energy from the Al-O reaction, $\dot{\boldsymbol{q}}_{\boldsymbol{e,loss}}$ is the energy loss from Al evaporation, $\dot{\boldsymbol{q}}_{\boldsymbol{gain}}$ is the energy gain from the resistive heating of the wire, $\dot{\boldsymbol{q}}_{\boldsymbol{c,loss}}$ is the conducted energy loss to the environment (mainly the electrodes that hold the wire), $\dot{\boldsymbol{q}}_{\boldsymbol{rad,loss}}$ is the heat loss by radiation, and $\dot{\boldsymbol{q}}_{\boldsymbol{r,evap}}$ is the heat generated from the reaction of O_2 and gaseous Al evaporated from the particle surface. (b) N-Al mass balance model at ignition. Al nanoparticles can be in direct contact with gaseous oxygen (oxygen concentration, $\boldsymbol{C^g_O}$) or solid oxidizer (oxygen concentration, $\boldsymbol{C^s_O}$). $\boldsymbol{C^c_{Al}}$ and $\boldsymbol{C^s_{Al}}$ are the Al concentrations in the core and on the particle surface, respectively. $\boldsymbol{\nabla C}$, $\boldsymbol{\nabla \Phi}$ and $\boldsymbol{\nabla P}$ are the Al concentration gradient, electrical potential gradient and pressure gradient across the alumina shell, respectively.

gaseous Al evaporated from the particle surface.

At the peak temperatures around the point of ignition, Al evaporation and thermal irradiation are not significant, the heat accumulation is mainly dominated by the resistive heating of the wire ($\dot{q}_{gain}$), the energy gain by reaction ($\dot{q}_r$), and the heat loss to the environment ($\dot{q}_{c,loss}$). Thus, eq 7.1 at peak temperatures around ignition point can be simplified as:

$$\dot{q}_a = \dot{q}_{gain} + \dot{q}_r + \dot{q}_{c,loss} \tag{7.2}$$

In eq 7.2, $\dot{q}_a$ and $\dot{q}_r$ can be expressed as follows:

$$\dot{q}_a = (n_{Al} Cp_{Al} + n_{Pt} Cp_{Pt}) \frac{dT}{dt} \tag{7.3}$$

$$\dot{q}_r = 4\pi r^2 R \Delta H_r N_{n-Al} \tag{7.4}$$

where n_{Al} and n_{Pt} are the molar amounts of Al and Pt, Cp_{Al} and Cp_{Pt} are the heat capacities of Al and Pt (Cp_{Pt} = 25.86 J mol^{-1} °C^{-1}) [48,49], ΔH_r is the heat of reaction per mole of Al (= 837.5 kJ mol^{-1}) [22], $N_{n\text{-}Al}$ is the number of n-Al particles loaded on the wire, and R is the reaction rate. Since $n_{Al} << n_{Pt}$ in my system, eq 7.3 can be simplified as $\dot{q}_a = n_{Pt} Cp_{Pt} dT/dt$. According to the dimension of the Pt wire (length = 1 cm, radius = 38.1 μm), as well as the density of Pt at the room temperature (= 21.45 g cm^{-3}), the molar amount of Pt (n_{Pt}) is calculated to be 5.1×10^{-6} mol. Considering that the mass loading on the wire is ~ 30 μg in the case of ignition of n-Al in O_2, $N_{n\text{-}Al}$ is calculated to be 1.9×10^{11}. For the ignition of nanothermites, $N_{n\text{-}Al}$ are distinct for different formations based on different total mass loading. In detail, $N_{n\text{-}Al}$ for n-Al/Fe_2O_3, n-Al/K_2SO_4, n-Al/$K_2S_2O_8$ and n-Al/Bi_2O_3 are 0.76×10^{11}, 0.32×10^{11}, $0.38\times10^{11}$and 0.48×10^{11}, respectively.

Using the T-Jump heating experiment, the temporal temperature history for n-Al particles, which is consistent with the temporal temperature history for the carrier Pt wire, was recorded during the 3 ms pulse time. For a 5 atm external pressure of O_2 a typical temperature-time curve for n-Al in the neighborhood of ignition temperature is shown in Fig. 7.5. The experimental temperature curve has a width of ~ 50 ˚C (as shown by the two dashed curves), demonstrating that the precision of the temperature measurement is ± 25 ˚C. It can be seen that the slope of temperature-time curve ($dT/dt|_{T<T_{ig}}$) for n-Al is close to constant, and equivalent to the slope of temperature-time curve on the bare wire ($dT/dt|_{wire}$) (without deposition of n-Al) below the ignition point (Fig. 7.5). This is consistent with the fact that prior to ignition, the heat accumulation is exclusively from the resistive heating of the wire ($\dot{q}_{gain}$) subtracted by the heat loss to the environment ($\dot{q}_{c,loss}$). So eq 7.2 prior to ignition can be expressed as:

$$\dot{q}_a\Big|_{T<T_{ig}} = \dot{q}_{gain} + \dot{q}_{c,loss} \tag{7.5}$$

At the point of ignition, a rapid excursion in the wire temperature (Fig. 7.5) occurs that leads to a higher slope of temperature-time curve ($dT/dt|_{T>T_{ig}}$). This result is indicative that the heat generated by reaction ($\dot{q}_r$) becomes significant. From the temperature-time curve for the bare Pt wire, I also know $\dot{q}_{gain}$ and $\dot{q}_{c.loss}$ are constants in the neighborhood of ignition point. In this regard, the energy balance at the point of ignition is:

$$\dot{q}_a\Big|_{T>T_{ig}} = \dot{q}_{gain} + \dot{q}_r + \dot{q}_{c,loss} \tag{7.6}$$

By combing eqs 7.5 and 7.6, I find that the reaction rate, R_c, at the ignition temperature can be taken as a function of the temperature gradient difference as:

$$R_c = \frac{n_{Pt} Cp_{Pt}}{4\pi r^2 \Delta H_r N_{n-Al}} \left(\frac{dT}{dt}\Big|_{T>T_{ig}} - \frac{dT}{dt}\Big|_{T<T_{ig}} \right) \tag{7.7}$$

It should be noted that the ignition point I chose in Fig. 7.5 is not the inflection point of the curve. This is to account for the uncertainty in the temperature measurement which as can be seen in the figure is ~ ± 25 ˚C. Ignition is defined as the point where the extrapolation of the ignition curve deviated by at least the uncertainty (25 ˚C) . In regard to eq 7.7, the value of $dT/dt|_{T>T_{ig}}$ is defined as the slope at this point, which can be approximated by the average slope of fitted wire within the temperature range of ± 50 ˚C of the ignition point. This definition of ignition point is different from that I utilized to measure the ignition temperatures of n-Al based energetic materials, which is determined by the onset of light emission from ignition [24-27]. However, since I found that these two defined ignition temperatures are usually very close (< 50 ˚C), I will use the current definition of ignition temperature for the following energy balance analysis.

In eq 7.7, the number of n-Al loaded on wire is an estimated value based on my calculation from an ideal geometry of the nanoparticle coating. The actual measurement of the mass gravimetrically confirms that the deposit of n-Al is ~ 30 ± 10 μg, which gives an uncertainty of 50% to the R_c value.

Eq 7.7 forms the basis of the following discussion to evaluating the ignition criteria.

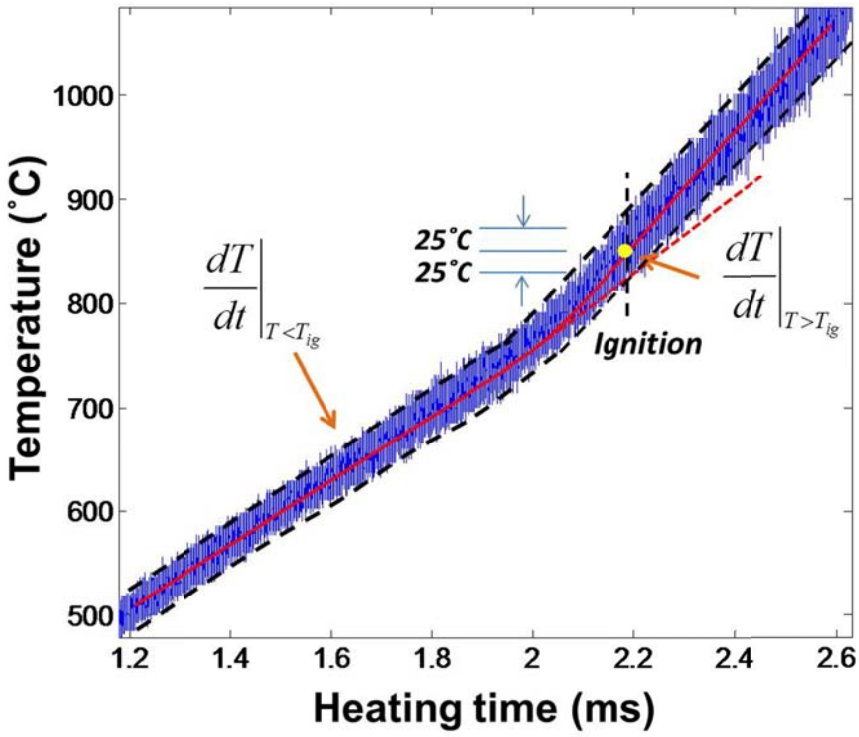

Figure 7.5. Experimental temporal temperature profile on n-Al particles. A fitted solid curve (red) was centered along the raw curve (blue). The width of the raw curve is 50 ˚C (as shown in between two dashed curves along the raw curve), demonstrating that the accuracy of the temperature measurement is ± 25 ˚C. The temperature gradients for n-Al before and after ignition, as well as the ignition point are labeled.

7.3.4. Critical reaction rate of n-Al with free and bound oxygen

Ignition is nominally the point when the exothermicity of a reaction exceeds the energy dissipation rate, which I can define as the critical reaction rate R_c. The question at hand is that given the similarity between the overall chemistry there is the critical reaction rate independent of the source of oxygen. In terms of my model (Fig. 7.5), by keeping constant all other external conditions that may influence the energy balance, such as the deposited mass on wire, the value of R_c is exclusively dependent on the temperature gradient difference before and after ignition (eq. 7.7). Evaluation of eq 7.7 from the measured temperature profiles of ignition experiments in different

O_2 pressures (Fig. 7.2) shows that the R_c for ignition is indeed a constant over a range of ignition temperatures, with an average value of 5×10^{-2} mol m^{-2} s^{-1} (Fig. 7.6(a)). This is further confirmed from another experiment using a thinner mass-loaded Pt wire (radius = 12.7 μm) which has a mass one ninth of that for the normal wire (radius = 38.1 μm). At 3 atm O_2 pressure, the difference of temperature slopes before and after ignition point increased by 9 folds when compared to that for normal wire. According to eq 7.7, these changes in temperature slope difference and Pt content result in a R_c (6.7×10^{-2} mol m^{-2} s^{-1}) that is similar to those (5×10^{-2} mol m^{-2} s^{-1}) obtained from my standard wire diameter experiments (see the star point in Fig. 7.6(a)). These results indicate that the role of O_2 is to enable achieving the critical reaction condition at a lower temperature for an increased concentration of O_2.

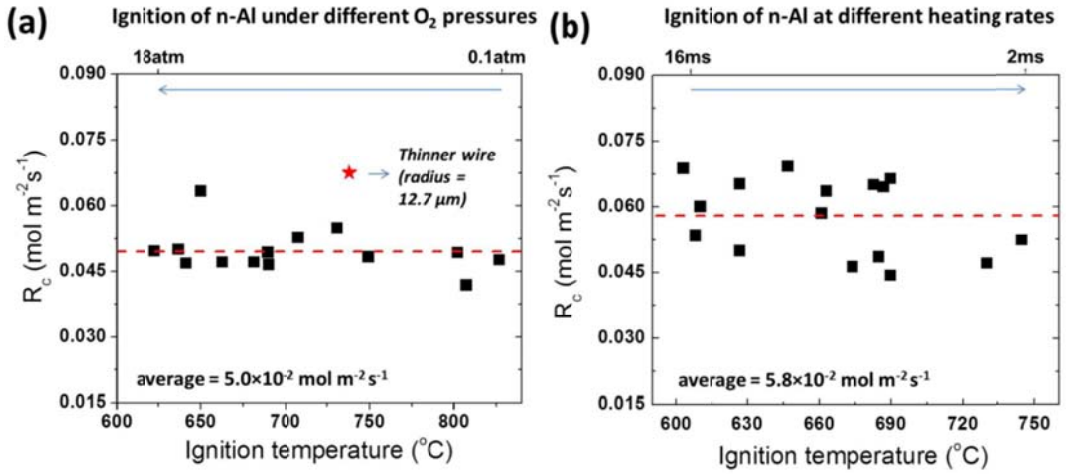

Figure 7.6. Critical reaction rate (R_c) evaluated from eq. 12 at ignition temperatures for n-Al under different O_2 pressures (0.1-18 atm) at a constant initial heating rate (~4×10^5 °C s^{-1}) (a), and under a constant O_2 pressure (3 atm) at different initial heating rates (~1×10^5- ~6×10^5 °C s^{-1}) (b). The star point in (a) represents the R_c of n-Al on a thinner Pt wire (radius = 12.7 μm), corresponding to an ignition temperature of 738 °C and external O_2 pressure of 3 atm.

We next explore if the critical reaction rate is dependent on the heating rate. The corresponding ignition experiments for pure n-Al were conducted at different initial

heating rates in 3 atm O_2 by using different pulse times (2 - 16 ms). Fig. 7.6(b) shows that over the range of heating rates from ~1×10^5 ˚C s^{-1} to ~6×10^5 ˚C s^{-1}, the ignition temperature of n-Al increases by 150 ˚C. However, the critical reaction rate remains constant at ~5.8×10^{-2} mol m^{-2} s^{-1}, which is similar to the value I obtained from ignition experiments when oxygen pressure was varied (Fig. 7.6(a)). The two experiments offer the same conclusion, namely that there exists a critical reaction rate that determines the initiation of reaction between Al and oxygen.

The critical reaction rate of Al with bound oxygen in the nano-thermites was also evaluated from the data in Fig. 7.3. In vacuum, the unavailability of gas presumably ensures that all nanothermite ignition follows a condensed phase mechanism (Fig. 7.3). Similarly to the aforementioned ignition of n-Al in O_2 (Fig. 7.2), the ignition reaction rate of each thermite formulation can be calculated according to eq 7.7 under the vacuum condition case. Since eq 7.7 is based on an energy balance that assumes nothing about where oxygen comes from, it is equally applicable to the measurement of the critical reaction rate for thermites. The $R_c's$ for the four thermite formulations were found to be similar (3.5×10^{-2} - 5.9×10^{-2} mol m^{-2} s^{-1}, see Table 7.1), which are also equivalent to the reaction rate of pure n-Al in O_2 (Fig. 7.6), and independent of ignition temperature. *Thus, a critical reaction rate for ignition, if it exists, should have a characteristic that it be constant and invariant of other factors such as ignition temperature, heating rate, and oxygen source.*

The key point however is to note that in both the thermite and the free O_2 reaction the critical reaction rate for ignition is the same, and the various ignition temperatures

are simply reflecting the conditions when the critical reaction rate for thermal runaway is achieved.

It may seem at first consideration odd, that both the free and bound oxygen case have essentially the same critical reaction rate. However when one considers these global reactions, they are actually very similar in both the free and bound oxygen cases. First, it must be considered that the same fuel particles are used in every case, so while the given reaction rate is normalized by surface area, the result is the same for both cases. Thus this critical reaction rate implies that, at ignition, the energy generation rate is the same for both free and bound oxygen systems. Second, the thermochemistry of the reaction of all the systems is quite similar, as it is dominated by the exothermic generation of Al_2O_3. If I consider a metric of the heat of reaction normalized by the heat capacity, which is a measure of how much the temperature of the energetic material will rise per unit of reaction, I find that all systems are within a factor of 2. Thus the result that the critical reaction rates for thermal runaway for both the free and bound oxygen cases are similar is perhaps not so surprising.

Table 7.1. Ignition temperatures in vacuum, interfacial concentrations of oxygen and aluminum at the ignition temperatures, the activation energies of the condensed phase Al-O reaction, as well as the condensed phase ignition reaction rates for n-Al/Fe_2O_3, n-Al/Bi_2O_3, n-Al/K_2SO_4 and n-Al/$K_2S_2O_8$.

Formulations	E_a^s (kJ/mol)	R_c' (mol/(m^2 s))
n-Al/Bi_2O_3	146[a]	4.1×10^{-2}
n-Al/K_2SO_4	167[a]	5.9×10^{-2}
n-Al/$K_2S_2O_8$	169[a]	4.9×10^{-2}
n-Al/Fe_2O_3	181[a]	3.5×10^{-2}
n-Al	134[b]	5.0×10^{-2}

Note: [a]activation energy of condensed phase reaction of Al and O(s); [b]activation energy of heterogeneous reaction of Al and O_2(g).

7.3.5. Arrhenius Parameters (free and bound) at ignition

One key takeaway from my results is that the various ignition temperatures are simply reflecting the conditions when the critical reaction rate for thermal runaway is achieved. While this ignition criterion is able to generally determine when ignition initiates, it does not provide me details about why different formulations show different ignition temperatures. We next explicitly investigate several vital factors (oxygen concentrations, activation energy, etc.) that contribute to the global reaction rate, aiming to systematically understand the control of ignition. From the results in Figs. 7.2 and 7.3, I have seen the critical roles of oxygen concentration and activation energy in controlling ignition temperature, though I did not evaluate these parameters in a quantitative manner. On the other hand, as the other reactant at ignition, the concentration of Al at the reaction interface also contributes to the reaction rate. As the temperature increases, Al will become increasingly mobile and migrate through the oxide shell driven by pressure, concentration gradient, and built-in electric fields [17-20]. The prevailing evidence shows that aluminum flux outward exceeds that of oxygen inwards, thus indicating that the Al-O reaction occurs at the outer surface of the aluminum enriched alumina shell [16,21]. Given that both concentrations of Al and O change with temperature, I can explore the above ignition criterion further by explicitly evaluating a rate law for R_c, expressed as:

$$R_c = k(C_{Al}^s)^m (C_O)^n \tag{7.8}$$

where

$$k = A\exp(-\frac{E_a}{RT}) \tag{7.9}$$

Here k is the reaction constant, C_O and C_{Al}^s are the concentrations of reactive oxygen

and aluminum at the reaction interface, m and n are positive indices of C_{Al}^{S} and C_O respectively, A is the pre-exponential factor, and E_a is the activation energy of the Al-O reaction. For the fast initiation of n-Al in O_2, both thermochemical calculations (using NASA CEA Code) and tests by T-jump time-of-flight mass spectrometry (TOF-MS) have demonstrated that the major intermediate product is Al_2O [50]. This implies that for the initial Al-O reaction, the production of Al_2O intermediates prevails. Therefore, the rate law is taken as $m = 1$, $n = 0.5$. If I further assume that the concentration of oxygen in the proximity of reaction interface is similar or at least scales with the external oxygen pressure ($C_{O2} = 0.5C_O$), the kinetic equation is:

$$R_c = A\exp(-\frac{E_a}{\bar{R}T})C_{Al}^{s}(2C_{O2})^{0.5} \tag{7.10}$$

where is $\bar{R}$ the universal gas constant.

To evaluate the activation energy (E_a), I employ the Flynn–Wall–Ozawa isoconversion method [51,52] as:

$$\ln\beta = const. - \frac{1.052E_a}{\bar{R}T} \tag{7.11}$$

To do this, the ignition temperature of n-Al at 1 atm O_2 was evaluated at different heating rates (β) from 7.5×10^4 °C s^{-1} to 6×10^5 °C s^{-1}. The slope of the Arrhenius plot of heating rate vs. ignition temperature shown in Fig. 7.7(a) yields an activation energy of 134 kJ mol^{-1}. Similar experiments at 3 atm O_2 yield a similar result of 137 kJ/mol (Fig. 7.8), indicating that it is independent of O_2 concentration. It should be noted that the activation energy measured here is smaller than most of the activation energies of Al oxidation previously reported [14], however, Jian et al [53] reported a similar result showing that the decomposition of metal oxides at high heating rates

(~10^5 °C s^{-1}) has lower activation energies than the values found at low heating rates. They attributed the decrease in activation energy to the mass-transfer constraints at higher heating rates.

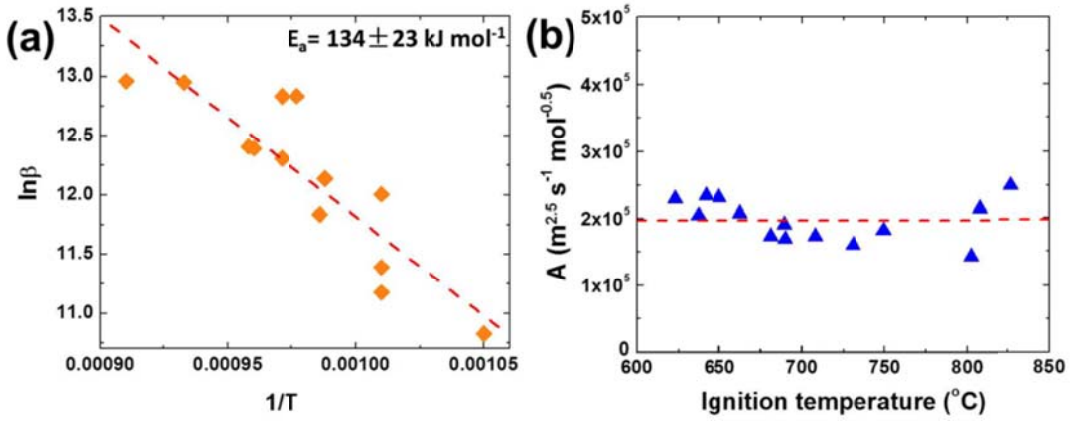

Figure 7.7. (a) Arrhenius plot of heating rate vs ignition temperature at 1 atm O_2. The temperature unit here is Kelvin. (b) Relationship of the pre-exponential factor (A) with respect to the ignition temperature of n-Al under different O_2 pressures.

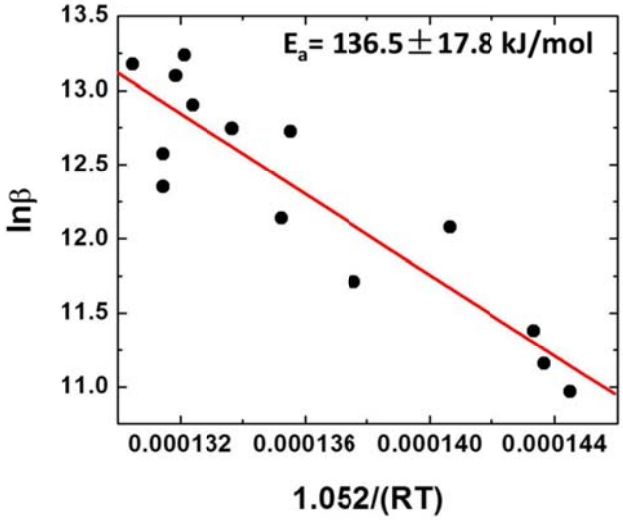

Figure 7.8. Arrhenius plot of heating rate vs. ignition temperature at 3 atm O_2. The temperature unit is in Kelvin.

In order to evaluate the pre-exponential factor A, it is necessary to estimate the surface aluminum concentration, C_{Al}^{S} which I do by a simple transport analysis. In

principal, the outward transport rate of Al should be equivalent to the sum of the reaction rate of Al with O at the particle surface, the evaporation rate of Al from the particle, as well as the accumulation rate of Al at the surface (Fig. 7.4(b)). Since my focus is on ignition where the reaction of Al and O becomes significant, the outwardly diffused Al is presumably consumed rapidly suggesting no accumulation of Al on the reaction interface. Therefore, the mass balance at the ignition temperature can be expressed as follows:

$$j_{Al}^{evap} + R_c = j_{Al}^{E} + j_{Al}^{P} \tag{7.12}$$

where j_{Al}^{evap} is the evaporation flux of Al escaped from the particle surface, j_{Al}^{E} is the diffusion fluxes of Al through the alumina shell driven by the built-in electrical field [17-20]. j_{Al}^{P} is the convection flux of Al through the alumina shell driven by the internal pressure [17-20]. Since the Al flux due to the concentration gradient was reported to be smaller than the other flux terms [19], I will neglect it in the following analysis.

In eq 7.12, the evaporation flux of Al (j_{Al}^{evap}) in the free molecular limit is expressed as:

$$j_{Al}^{evap} = \frac{P_d}{\sqrt{2\pi \overline{R} M_{Al} T}} \tag{7.13}$$

where M_{Al} is the molecular weight of Al, T is the particle temperature, and P_d is the equilibrium vapor pressure of Al over a particle. P_d can be deduced by the Kelvin equation [22,54]:

$$P_d = P_o \exp(\frac{2\sigma_{Al} M_{Al}}{r \overline{R} T \rho_{Al}}) \tag{7.14}$$

where P_o is the saturated vapor pressure of a flat Al surface (= exp(13.07-36373/T) atm) [22], σ_{Al} is the surface tension of Al (= 948-0.202T Dyne cm^{-1}) [22], and ρ_{Al} is the density of Al (= 2.7 g cm^{-3} at the room temperature, and 2.375 g cm^{-3} when melted) (Fig. 7.9(a)). The diffusion flux of Al driven by the electrostatic potential gradient is expressed in terms of the Nernst-Plank equation [3]:

$$j_{Al}^{E} = -\frac{zFDC_{Al}^{s}}{\overline{R}T} \nabla \phi = -\frac{zFDC_{Al}^{s}}{\overline{R}T} \frac{\Delta \phi}{d} \tag{7.15}$$

where D is the diffusion coefficient of Al (= 4.9×10^{-11}exp(-4240/T) m^2 s^{-1}) [22], $\Delta\Phi$ is the Mott potential (= -1.6 V for n-Al) [17,18], z is the valency of Al ions (= 3), and F is the molar charge of Al ions (= 96485 C mol^{-1}), C_{Al}^{s} is the surface concentration of Al on the outer alumina shell, d is the alumina shell thickness (= 4nm). Finally, the convection flux of Al driven by the internal pressure gradient is expressed as follows:

$$j_{Al}^{P} = -\frac{N_A D C_{Al}^{s} v_{Al}}{\overline{R}T} \nabla P \tag{7.16}$$

where N_A is Avogadros constant, and v_{Al} is the solubility of Al in alumina shell (= 0.02 nm^3) [19,22]. The relationship between pressure gradient and temperature has been previously simulated by Henz et al [19], and is plotted in Fig. 7.9(b).

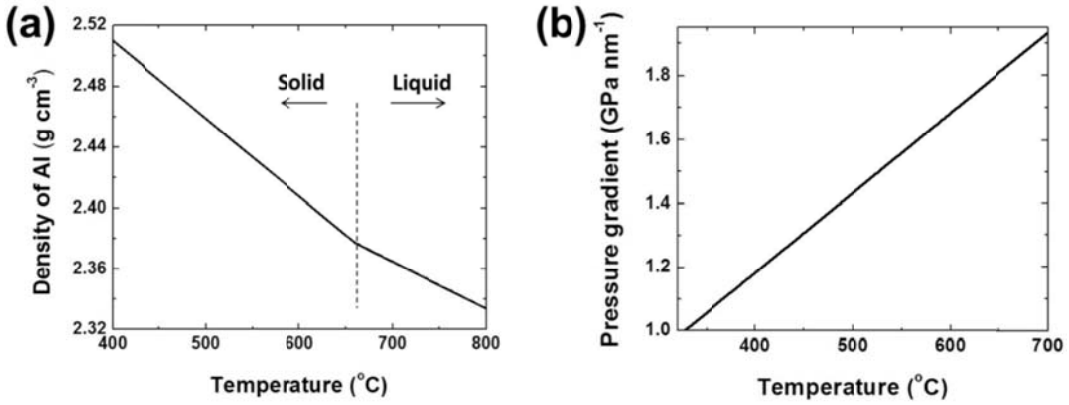

Figure 7.9. Estimation of the temperature-dependent density of Al core (a), and the pressure gradient across the alumina shell (b).

It should be noted that there are several approximations in my calculation of fluxes in eqs. 7.12 – 7.16. Firstly, since the Al evaporation actually occurs on the surface of alumina shell, the real values of P_o and σ_{Al} would be smaller. Thus, the flux of aluminum evaporation calculated from eqs 7.13 and 7.14 is actually larger than the real flux. Secondly, in the calculation of fluxes by the pressure and electrical field gradients in eqs 7.15 and 7.16, the effect of temperature on diffusion coefficient of Al in Al_2O_3 is subject to debate, which brings uncertainty to the final values of j_{Al}^{P} and j_{Al}^{E}. Finally, the value of Mott potential (-1.6V) I used in eq 7.15 is suitable for a very thin oxide shell [17]. For n-Al with a Al_2O_3 shell of 3-4 nm in thickness, the actual potential is smaller, which makes the actual j_{Al}^{E} smaller than what I calculated. Bearing these approximations in mind, eq 7.12 is still capable of presenting the relationship between the scales of R_c and C_{Al}^{S}.

Eq. 7.12 can be further simplified after comparing the dimensions of the three flux terms it contains. In terms of my results on ignition of n-Al in different O_2 pressures (Fig. 7.2), j_{Al}^{E} was ~1 order and ~6 orders of magnitude larger than j_{Al}^{P} and j_{Al}^{evap}

respectively (Fig. 7.10) within the ignition temperature range in Fig. 7.2. Therefore, eq 7.12 was simplified as $R_c = j_{Al}^E$, and can be extended by plugging in the expression of j_{Al}^E which is the electric field driven oxidation (see eq 7.15):

$$C_{Al}^S = \frac{\overline{RTd}}{zFD\Delta\phi} R_c \tag{7.17}$$

where D is the diffusion coefficient of Al (= $4.9\times10^{-11}\exp(-4240/T)$ m^2 s^{-1}) [22], $\Delta\Phi$ is the Mott potential (= -1.6 V for n-Al) [17,18], z is the valency of Al ions (= 3), and F is the molar charge of Al ions (= 96485 C mol^{-1}), C_{Al}^S is the surface concentration of Al on the outer alumina shell, and d is the alumina shell thickness (= 4nm). Given that R_c at different O_2 pressures was already measured, the above C_{Al}^S can be estimated using likely $\Delta\Phi$ and D, obtained from other studies.

Given that the values of E_a, C_{Al}^S and C_{O2} are known (Fig. 7.7(a) and Fig. 7.11), I can calculate the pre-exponential factor (A). This value is shown in Fig. 7.7(b) as a function of ignition temperature and appears to be a constant with the average value of 2×10^5 $m^{2.5}$ $mol^{-0.5}$ s^{-1} (Fig. 7.7(b)).

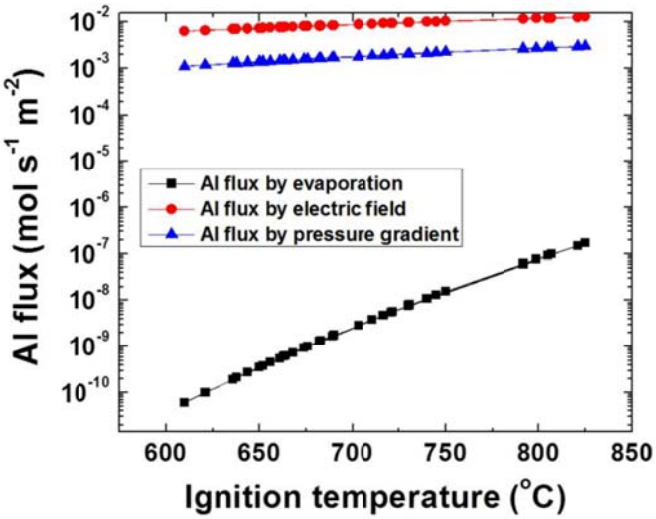

Figure 7.10. Relationships of ignition temperature and aluminum flux driven by evaporation, electric field, and pressure gradient, respectively.

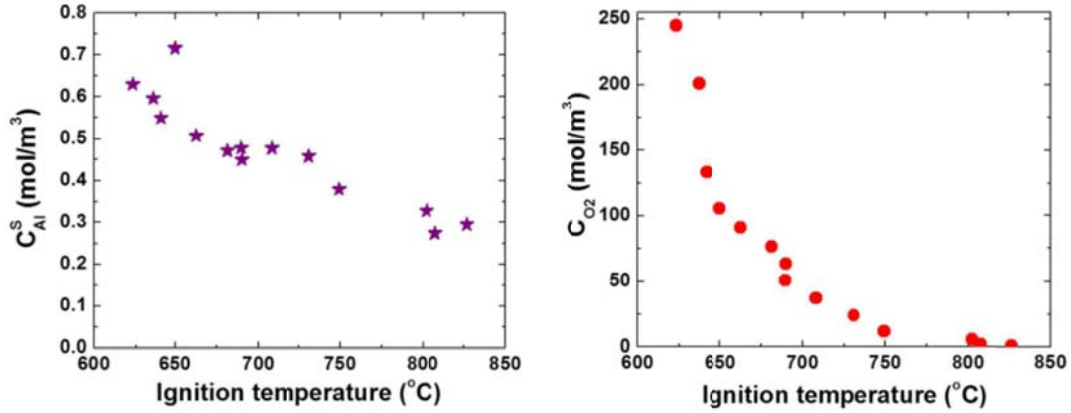

Figure 7.11. (a) Relationship between the calculated aluminum surface concentration ($\boldsymbol{C_{Al}^{s}}$) and the ignition temperature of n-Al under different O_2 pressures. (b) Relationship between the oxygen gas concentration ($\boldsymbol{C_{O2}}$) and the ignition temperature of n-Al under different O_2 pressures.

I now turn the attention to ignition in the presence of bound-oxygen. If I consider the ignition of nanothermites that undergo a condensed phase reaction as the reaction between the diffusing Al and bound oxygen from oxidizers, I can define the reaction rate in a similar manner:

$$R_c' = A' \exp\left(-\frac{E_a^s}{RT}\right) C_{Al}^s C_O^{s\,0.5} \tag{7.18}$$

Here R_c' is the condensed phase critical reaction rate, *A'* is the pre-exponential factor for the condensed phase reaction, E_a^s is the activation energy of condensed phase Al-O reaction, C_O^s is the interfacial concentration of reactive oxygen in the condensed phase. For a given thermite formulation, both reaction mechanisms in eqs 7.10 and 7.18 may exist. If I further assume the pre-exponential factors (*A* and *A'*) are similar in eq. 7.10 and 7.18 (= 2×10^5 $m^{2.5}$ $mol^{-0.5}$ s^{-1}), then I can use these equations to better understand the differences between the four nanothermites (Fig. 7.3).

All $R_c's$ for the four thermite formulations were discussed before as the same constant (~5×10^{-2} mol m^{-2} s^{-1}, see Table 7.1). The concentration of Al can be estimated in a similar way as for n-Al, while the concentration of bound O can be estimated based on the oxygen densities of these oxidizers. Results show that both the concentrations of Al and bound O are close to constant for these four nanothermites. In terms of eq 7.18, the E_a^s values of condensed phase Al-O reaction for these thermite formulations can be obtained. In all cases the thermites have larger activation energies than the direct reaction of n-Al with O_2 (Table 7.1). This is not surprising since O_2 is freely available, which must be thermally released from the oxidizers. The other activation energies of condensed phase Al-O reaction follow: E_a^s (n-Al/Bi_2O_3) < E_a^s (n-Al/K_2SO_4) ≈ E_a^s (n-Al/$K_2S_2O_8$) < E_a^s (n-Al/ Fe_2O_3). Since all R_c', A', C_{Al}^s, and C_O^s are constant for different nanothermites, the difference in activation energy is actually associated with the difference in ignition temperature for the four nanothermites in vacuum as: T (n-Al/Bi_2O_3) < T (n-Al/K_2SO_4) ≈ T (n-Al/$K_2S_2O_8$) < T (n-Al/ Fe_2O_3) (Fig. 7.3).

1. n-Al/Bi_2O_3 shows an invariant ignition temperature when O_2 pressure changes. This is because it has the lowest E_a^s among the four nanothermites, which is correlated to its high oxygen conductivity. Thus, even though this E_a^s is still larger than that for n-Al in O_2 (Table 7.1), a two orders of magnitude higher C_O^s than that for O_2 determines that the ignition is dominated by condensed phased reaction; i.e independent of O_2 pressure.

2. For n-Al/$K_2S_2O_8$, the ignition temperature in vacuum is much higher, correlating to a higher E_a^s. However, it shows a similar constant ignition temperature as n-Al/Bi_2O_3

when the O_2 pressure is above 1atm. In this case, the ignition mechanism is alternatively controlled by Al-O_2(g) reaction, and the reactant O_2 gas mostly from the decomposition of oxysalt which has a much higher oxygen concentration than that for the external O_2.

3. For n-Al/K_2SO_4 and n-Al/Fe_2O_3, ignition is controlled by condensed phase reaction when O_2 pressure is < 5atm. The fact that n-Al/ Fe_2O_3 shows a higher ignition temperature than n-Al/K_2SO_4 is consistent with the Arrhenius model that n-Al/ Fe_2O_3 has a higher E_a^s. When O_2 pressure is > 5atm, their ignition temperatures approach that for n-Al in O_2. In this case, the effect of increased O_2 concentration favoring the Al-O(g) reaction becomes dominant .

The reader is reminded that the activation energies and reaction rates deduced in this work are presumably only valid for ignition and should not be assumed to be applicable to the whole combustion event.

7.4. Conclusion

Ignition of nano-aluminum (n-Al) and n-Al based energetic materials (nanothermites) was examined in different O_2 pressures aiming to differentiate the effects of free and bound oxygen. Results show that the ignition temperature of n-Al decreased as the O_2 pressure increased, whereas the ignition temperatures of nanothermites have different sensitivities to O_2 pressure depending on the formulations. We found that a constant critical reaction rate (5×10^{-2} mol m^{-2} s^{-1}) for ignition exists which is independent to ignition temperature, heating rate and free vs. bound oxygen. The roles of oxygen concentration and activation energy of Al-O

reaction were demonstrated based on the ignition results, and were reflected more quantitatively in a kinetic model. This study suggests that the ignition of n-Al based energetic materials is controlled by a constant R_c, and fit a simple Arrhenius model, leading to different ignition temperatures for different formulations.

Chapter 8: Summary

8.1. Conclusions

The objective of this study was to explore effective approaches to neutralize bacterial spores. I explored new approaches based on rapid heating in addition to the generation of biocidal reaction products to neutralize spores.

In order to implement an accurate temperature measurement and control, a surface based heating method was used. In Chapter 2, I demonstrated the uniform attachment of bacterial spores electrophoretically onto fine wires in liquids and subsequently quantitatively detached back into suspension. It was found that by using a pulsed electroplating mode, the number of spores deposited onto the wire is linearly related to the number of pulse cycles employed. Typically, a uniform monolayer of Bs spores could be deposited by using 4 pulse cycles of 5V plus 30s. This method is also able to quantitatively measure the surface charge on spores along with the deposition rate.

Once a uniform monolayer of spores was immobilized on the wire, the spores were subjected to high temperatures (200 ˚C to 800 ˚C) at relatively high heating rates (~10^3 ˚C/s to ~10^5 ˚C/s). In Chapter 3, I reported that spore inactivation increased with temperature and fit a sigmoid response. I observed a critical peak temperature (T_c), which caused a 2-fold reduction in spore viability, of 382 ˚C and 199 ˚C for heating rates of ~10^4 ˚C/s and ~10^5 ˚C/s, respectively, indicating that a higher heating rate can potentiate the spore inactivation. The mechanism of spore inactivation was further investigated at two heating rates (~10^4 ˚C/s and ~10^5 ˚C/s). Viability reduction was mainly due to DNA damage at the heating rate of ~10^4 ˚C/s as mutant strains

defective for *sspA sspB* and *recA* were more sensitive to heat than the wide-type strains. At the higher heating rate (~10^5 ˚C/s), spore inactivation was correlated to the physical damage on the spore coat from ultrafast vapor pressurization inside the spores. This approach of pulse heating generates a temperature, time, and kill relationship for *Bacillus* spores at sub-second timescales.

In Chapter 4, I next investigated the synergism between rapid heating (~10^4 ˚C/s to ~10^5 ˚C/s) and chlorine gas exposure in the neutralization of *Bacillus* spores. Bt spores were heated in a gas chamber with defined concentrations of Cl_2 gas and relative humidity (RH). The critical peak temperature (T_c) of spores was decreased from 405 ˚C, when heated at ~10^4 ˚C/s in air, to 250 ˚C when heated at the same rate in 100 ppm Cl_2. Similarly, the T_c for Bt spores heated at the faster rate of ~10^5 ˚C/s was reduced from 230 ˚C, when heated in air, to 175˚C, when heated in 100 ppm Cl_2. The effect of Cl_2 was further examined by changing the RH of Cl_2 gas. The results show that highly humidified Cl_2 (RH = 100%) reduced the T_c by 170 ˚C and 70 ˚C at ~10^4 ˚C/s and ~10^5 ˚C/s, respectively, as compared to dry Cl_2 (RH = 0%). Energy dispersive spectrometric (EDS) results demonstrate that Cl_2 on the spore increased with elevated peak temperature, with the majority of the Cl located in the shed spore coat. SEM results show that at heating conditions of > 450 ˚C, ~10^5 ˚C/s with Cl_2, the spore coat detached from the underlying core. This study indicates that the major mechanism of spore neutralization by the synergism of Cl_2 and rapid heat is chlorine reacting with the spore surface.

For the rest of this study, I utilized the stress-kill databases that were achieved by evaluating the neutralization efficiencies of rapid heat and biocides to guide the

exploration of new biocidal energetic composites and probe their working mechanisms. In Chapter 5, nanoscale potassium persulfate ($K_2S_2O_8$), was evaluated as an alternative to other peroxy salts, such as periodates (KIO_4), in aluminum-fueled energetic nano-composite formulations. Results from constant-volume pressure cell experiments show that nano-Al/$K_2S_2O_8$ releases more gas and has a longer burn time than nano-Al/KIO_4. High speed imaging coupled with temperature jump (T-jump) ignition found the nano-Al/$K_2S_2O_8$ reaction to have an ignition temperature of 600 ˚C, which is comparable to nano-Al/KIO_4 and lower than nano-Al/K_2SO_4. Both experiments performed at slow (10 ˚C/min) and ultrafast heating rates (~10^5 ˚C/s) show that the low O_2 generation temperature of nano-$K_2S_2O_8$ contributes to its high reactivity in nano-thermite compositions. What is comparably important is that this thermite formulation can generate a considerable amount of SO_2 in addition to a comparable amount of O_2, rendering it a potential candidate for use in energetic biocidal applications.

The study for persulfate intrigued me to explore other strong oxysalts in regards to their performance in a thermite formulation. By evaluating the reaction mechanisms of these oxysalts containing thermites, I expected to better understand how to tune the reactivity of biocidal thermites for eventually obtaining the optimal spore neutralization formulations. In Chapter 6, nine aluminum-fueled oxysalt-containing thermites including $K_2S_2O_8$, K_2SO_4, KIO_4, KIO_3, $KClO_4$, $KClO_3$, $KBrO_3$, KNO_3 and K_3PO_4, were investigated. Results from combustion cell tests show that these thermites can be divided into two groups, with the reactive thermites (e.g. Al-$K_2S_2O_8$) generating ~10× higher pressure and ~10× shorter of burn time than the less reactive

thermites in the aforementioned list (e.g. Al-K_2SO_4). Experiments at both slow and fast heating rates demonstrate that these oxysalts have a wide range of oxygen release and melting temperatures. For the thermite reactions, ignition temperatures of the reactive thermites are consistent with the temperature of polymorphic phase change for alumina (close to the melting point of Al), indicating that the limiting initiation step of these thermites is the acceleration of outward diffusion flow of Al reacting with gas phase O_2 generated from the decomposition of oxysalts. In contrast, ignition temperatures of the two less reactive thermites are insensitive to pressure. They ignite at temperatures much higher than the melting point of Al, although lower than the decomposition temperature of the corresponding oxysalts, indicating a condensed phase reaction mechanism.

The above two main ignition mechanisms were re-evaluated in Chapter 7, aiming to further understand the roles of free and bound oxygen and their correlations to the idea of a critical reaction rate. In this case, ignition temperatures of n-Al and four Al-based nanothermites (n-Al/Fe_2O_3, n-Al/Bi_2O_3, n-Al/K_2SO_4 and n-Al/$K_2S_2O_8$) were investigated by varying the external oxygen pressure (0-18atm). The ignition temperature of n-Al was found to reduce as the O_2 pressure increased, whereas the ignition temperatures of nanothermites had different sensitivities to O_2 pressure depending on the formulations. A phenomenological kinetic/transport model was evaluated to correlate the concentrations of oxygen both in condensed and gaseous phases, with the initiation rate of Al-O at ignition temperature. A constant critical reaction rate (5×10^{-2} mol m^{-2} s^{-1}) for ignition was found that is independent of ignition temperature, heating rate and free vs. bound oxygen. Since for both the

thermite and the free O_2 reaction the critical reaction rate for ignition is the same, I concluded that the various ignition temperatures are simply reflecting the conditions when the critical reaction rate for thermal runaway is achieved.

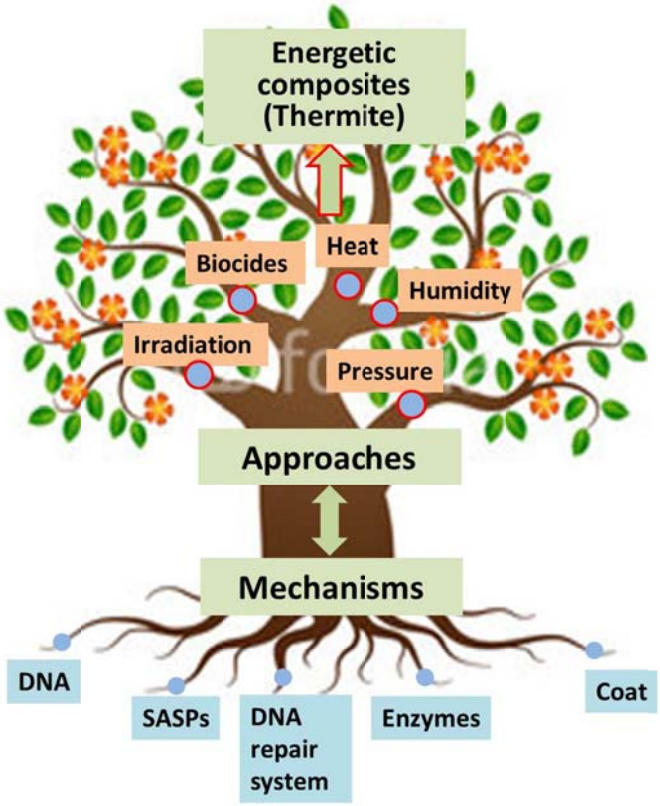

Figure 8.1. A tree schematic describing the correlations of spore neutralization mechanisms and neutralization approaches, as well as the guildance to explore the ideal energetic composites that enable to generate neutralization stresses for spores such as heat, biocides, pressure, etc.

8.2. Recommendations for future work

Future work derived from this study can be divided into two parts. The first part is to continue to evaluate the other possible stresses for spore neutralization. The effect of humidity has already been observed in part when I studied the synergistic effects of rapid heating and chlorine gas. However, its function is more related to the assistant effect for chlorine to produce HCl/HClO. In addition, I have also observed that

increment humidity alone enables an enhancement of the thermal neutralization of spores. In this experiment, the spore coated wire was treated in a similar way as that in Chapter 4, except that no Cl_2 gas was connected with the gas chamber (Fig. 4.1). Fig. 8.2 show that at both heating rates (~10^4 ˚C/s and ~10^5 ˚C/s), a higher relative humidity in air can decrease the critical peak temperature (T_c, which corresponds to 50% reduction in viability) for *Bs* spores. At ~10^4 ˚C/s, the critical peak temperature decreased from 386 ˚C in 0% RH air to 294 ˚C when heated at the same rate in 100% RH air. At ~10^5 ˚C/s, T_c decreased from 306 ˚C in 0% RH air to 127 ˚C when heated at the same rate in 100% RH air.

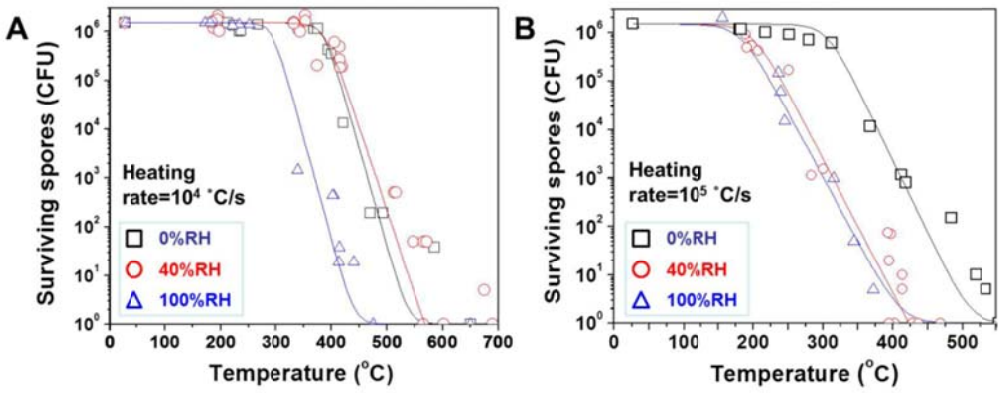

Figure 8.2. Survival curves of Bs spoes versus peak temperature and relative humidity for 2ms and 50ms heat pulses. The solid lines fit the results in a sigmoidal shape.

Viability tests for mutant Bs spores revealed that at ~10^4 ˚C/s, spores that lack coats (PS3228) have their viability significantly reduced (2 logs) when heated in 100% RH compared to that in 0% RH, indicating that the spore coat could be the primary target for humidity to cause viability reduction. Conversely, spores that lack SASPs (PS578) or DNA repair system (PS2318b) show a minor viability reduction when the relative humidity in air decreased from 100% RH to 0% RH. This converse trend

could be more due to the increased peak temperature from 300 ˚C to 400 ˚C that induced the viability reduction for PS578 and PS2318b spores, which is consistent with our previous results on the spore neutralization mechanism at this heating rate being from the DNA damage (see Chapter 3).

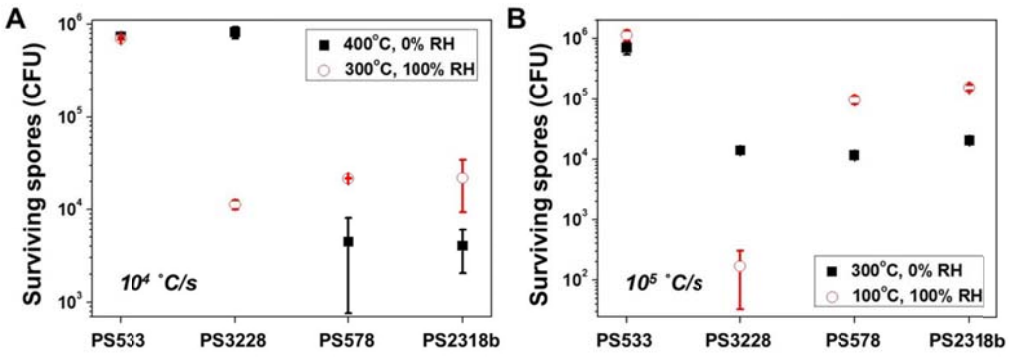

Figure 8.3. Survival counts of the wide-type strain (PS533) and three mutant strains (PS3328 (Δ*cotE*), PS578 (Δ*sspA* Δ*sspB*) and PS2318b (Δ*recA*)) of *Bs* spores at elevated peak temperatures in the 50 ms pulse heating (A) and in the 2 ms pulse heating (B). 0% RH and 100% RH were employed to affect the survivability of spores heated in air.

At ~10^5 ˚C/s, spores neutralization follows a different mechanism from that at ~10^4 ˚C/s. In this case, spore coat rupture due to the internal pressurization was supposed to be the predominant cause of spore neutralization. For the PS3228 spore strain, a similar viability reduction is observed when heated in humidity at both heating rates. A much larger 4 log viability reduction was induced even at lower temperatures (100 ˚C at ~10^5 ˚C/s versus 300 ˚C at ~10^4 ˚C/s). This is most likely because the main damage caused by humidity is on the spore coat, which is also attacked by the high pressurization. This dual effect of humidity and pressurization lead to the enhanced viability reduction.

The future work in this particular study is to carry out more experiments on the morphological and compositional analyses of the spores heated in hot air of varying

humidities in order to better understand the neutralization mechanisms by fast heat coupled with humidity.

The other part of my future research is to explore new biocidal energetic composites that have better energetic performance and biocide generation, based on the mechanism-approach correlations (Fig. 8.1). Examples include:

1. Iodine containing oxides and acids

Four iodine containing candidates, I_2O_5, I_4O_9, HIO_3, and HI_3O_8, are currently being tested. The major advantage of these species is their high content of biocidal iodine (> 50% by mass). The combustion cell results of the corresponding Al-based thermites are shown in Fig. 8.4. Generally, the two iodine oxides show more than 2 folds of maximum pressure or pressurization rate than the iodic acids, indicating that the oxides are better gas generators. In contrast, the two iodic acids performed better in heat generation, as their corresponding thermites show ~2 folds higher maximum optical emission than the iodine oxides containing thermites. Fig. 8.4D shows another interesting trend that a polyiodine structure, which can be either an oxide (I_4O_9) or an iodic acid (HI_3O_8), possesses a longer burning time than the common iodine oxide or iodic acid. Based on these combustion behaviors, I_4O_9 seems to offer the larger potential for biocidal applications because it features both high pressure generation and elongated energy release. In addition, it has the highest iodine content among these four formulations on a per mass basis.

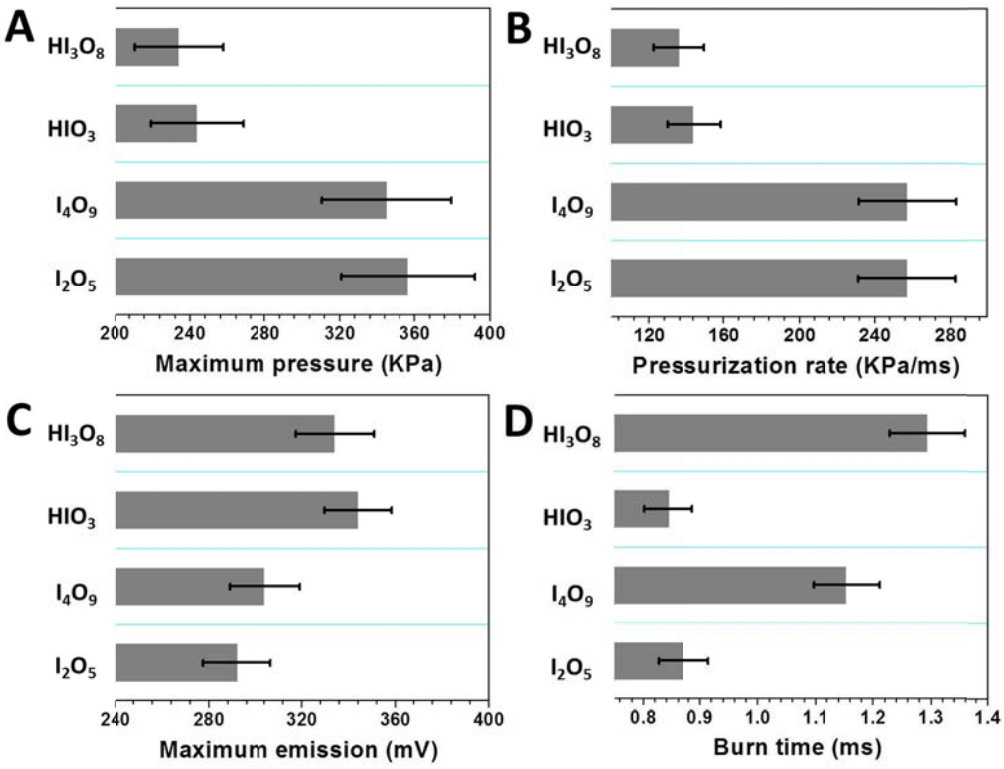

Figure 8.4. Temporal pressure (A), pressurization rate (B), light emission (C) and burn time (D) in the combustion cell tests of Al/I_2O_5, Al/I_4O_9, Al/HIO_3, and Al/HI_3O_8, respectively. Each experiment was repeatd at least twice.

I also investigated the ignition temperatures of these four thermites. Fig. 8.5 shows that most of these thermites generate oxygen at temperatures higher than the corresponding ignition temperatures, suggesting that the reaction mechanism for these formulations undergoes a condensed phase reaction. This is further confirmed by the fact that their ignition temperatures in Ar and in vacuum are similar, indicating that oxygen release plays a minor role in reaction initiation. On the other hand, all the iodine release temperatures for these thermites are lower than the corresponding ignition temperatures, suggesting that there is a pre-ignition reaction between iodine and aluminum. Previous studies on Al/I_2O_5 thermites by Pantoya et al [ref 47 in

Chapter 5] demonstrate that the pre-ignition effect of iodine is to form a bridge bond between iodine and alumina outside Al. This bonding at lower temperatures than the ignition temperature is beneficial in promoting the outward diffusion of aluminum through alumina shell at a later heating stage, thus improving the thermite reaction.

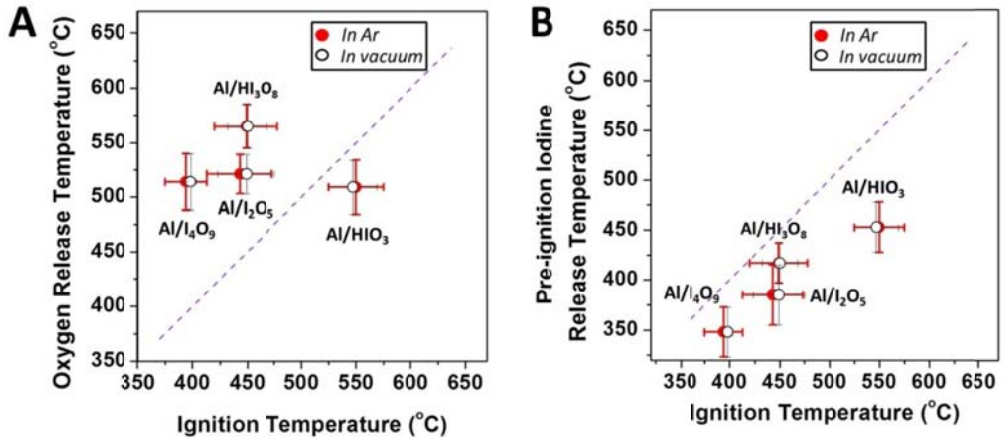

Figure 8.5. (A) Relationship between the oxygen release temperature in neat microscale iodine-containing oxidizers, and the ignition temperature of corresponding nano-Al-fueled thermite in Ar or in vacuum. (B) Relationship between the pre-ignition iodine release temperature in neat microscale iodine-containign oxysalt, and the ignition temperature of corresponding nano-Al-fueled thermite in Ar or in vacuum. Each temperature test was repeated at least twice. The diagonal dashed line stands for a perfect correlation.

2. Silver iodates including various Ag/I ratio in the formulations

Sullivan et al [ref 48 in Chapter 5] studied the thermite performance of Al/$AgIO_3$ and evaluated its potential use in biocidal applications. The initial aim to test this formulation is that $AgIO_3$ contains silver and iodine in its chemical structure, both of which are biocides effective for neutralizing spores. Unfortunately, their results show that although this thermite could generate high pressure and heat, it failed to release pure silver or iodine products due to the formation of AgI. Alternatively, I tried two other silver iodates, Ag_5IO_6 and AgI_3O_8, which are either rich in Ag or I. The purpose

is to eventually produce single silver from Al/Ag_5IO_6, and single iodine from Al/AgI_3O_8.

I first investigated their combustion performance. As a control, $Al/AgIO_3$ was also prepared together with two mixtures of $AgIO_3$ and Ag or I_2. The mass ratio of $AgIO_3$/Ag was kept consistent with that of Ag_5IO_6, while the mass ratio of $AgIO_3/I_2$ was controlled to be consistent with that of AgI_3O_8. Fig. 8.6 shows that compared with thermites mixed with additional Ag or I_2 particles, the formulations that involve Ag or I in the intrinsic molecular structures generated much higher peak pressures and pressurization rates. This is because the additive Ag or I_2 particles adversely diluted the original thermites and decreasd contact between fuel and oxidizer particles, leading to weaker reactivities (Fig. 8.6A and 8.6B). Among the three silver iodate formulations, AgI_3O_8 shows the best pressurization behavior upon ignition. A similar trend is observed for their optical emission results, with AgI_3O_8 corresponding to the generation of the highest light emission intensity and shortest burn time.

Results from the ignition tests demonstrate that Al/AgI_3O_8 shows the lowest ignition temperature in Ar (Fig. 8.7), while the other thermites ignited at temperatures of 100 ˚C higher on average. Fig. 8.7 indicates again that the chemically incorporated iodine (e.g. in the molecular structure) is beneficial for ignition of thermite, while the physically mixed iodine is unfavorable for ignition.

Compared to iodine, the silver component is relatively unfavorable for the ignition and combustion of thermites. The oxidation state of iodine in Ag_5IO_6 is +7 while in AgI_3O_8 it is +5, indicating that Ag_5IO_6 should have a higher oxidation capability. However, as seen in Fig. 8.6C, the maximum optical emission from Al/Ag_5IO_6 is just

half that of Al/AgI_3O_8. In addition, the ignition temperature of Al/Ag_5IO_6 is much higher than that of Al/AgI_3O_8 (Fig. 8.7). These results seem to conclude that the molecular design for biocidal energetic materials in the future should avoid considering a silver release approach.

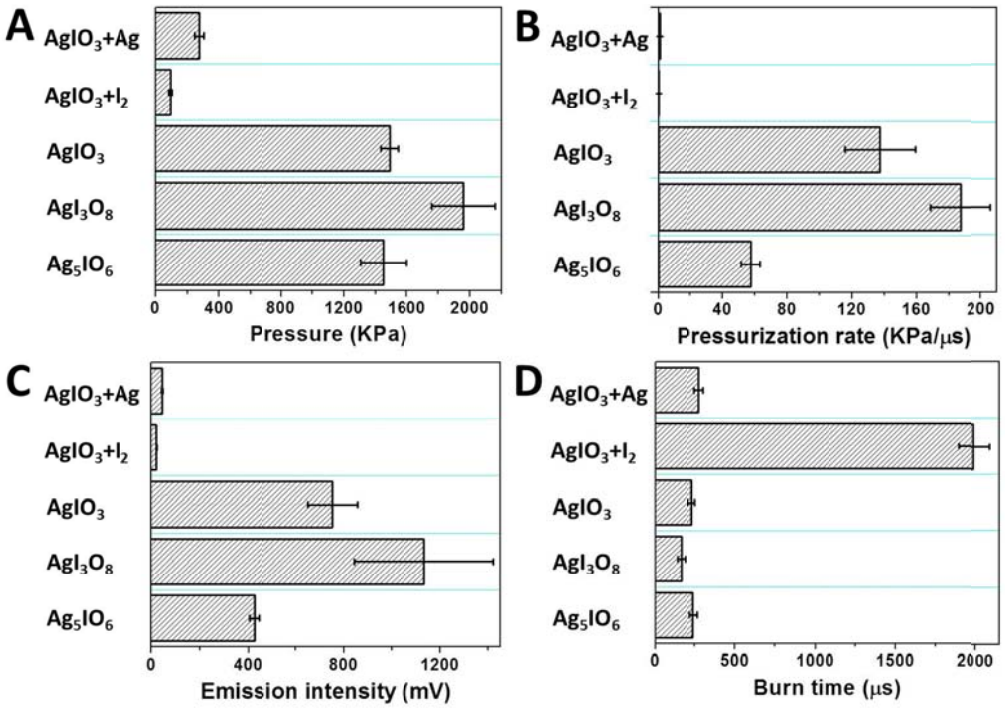

Figure 8.6. Temporal pressure (A), pressurization rate (B), light emission (C) and burn time (D) in the combustion cell tests of $Al/AgIO_3$, Al/AgI_3O_8, Al/Ag_5IO_6, $Al/AgIO_3/Ag$, and $Al/AgIO_3/I_2$, respectively. Each experiment was repeatd at least twice.

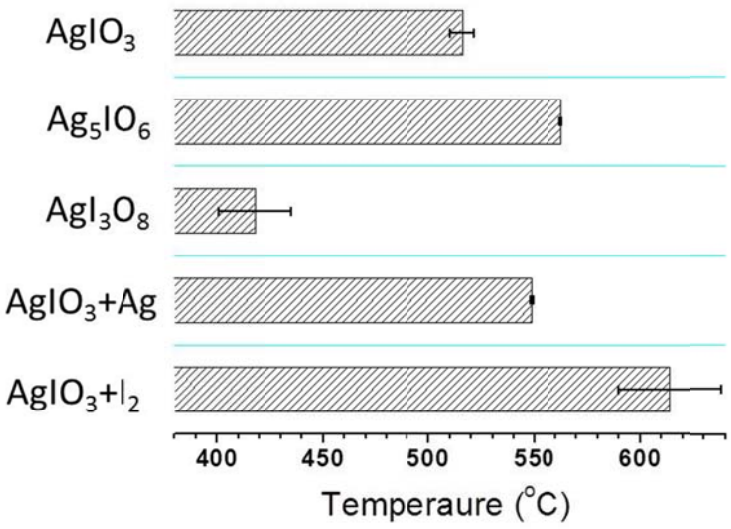

Figure 8.7. List of ignition temperatures of $Al/AgIO_3$, Al/AgI_3O_8, Al/Ag_5IO_6, $Al/AgIO_3/Ag$, and $Al/AgIO_3/I_2$ in Ar.

3. Non-metal oxides

Researchers have assessed many metal oxides as oxidizers in thermite formulations. From an energy density standpoint, an overall view of the heat of reaction for most Al-fueled thermites is presented in Fig. 8.8. We can see that the three non-metal oxides that are highlighted in red feature the highest heat of reaction in their Al-fueled thermites. The mass based heat of formation for Al/I_2O_5, Al/P_4O_{10}, Al/SeO_2 are -6.2kJ/g, -8.7kJ/g and -6.9kJ/g, respectively, which are am average of two folds higher than the most commonly studied thermites that involve metal oxides (e.g. -4.1kJ/g for Al/CuO and -2.1kJ/g for Al/Bi_2O_3).

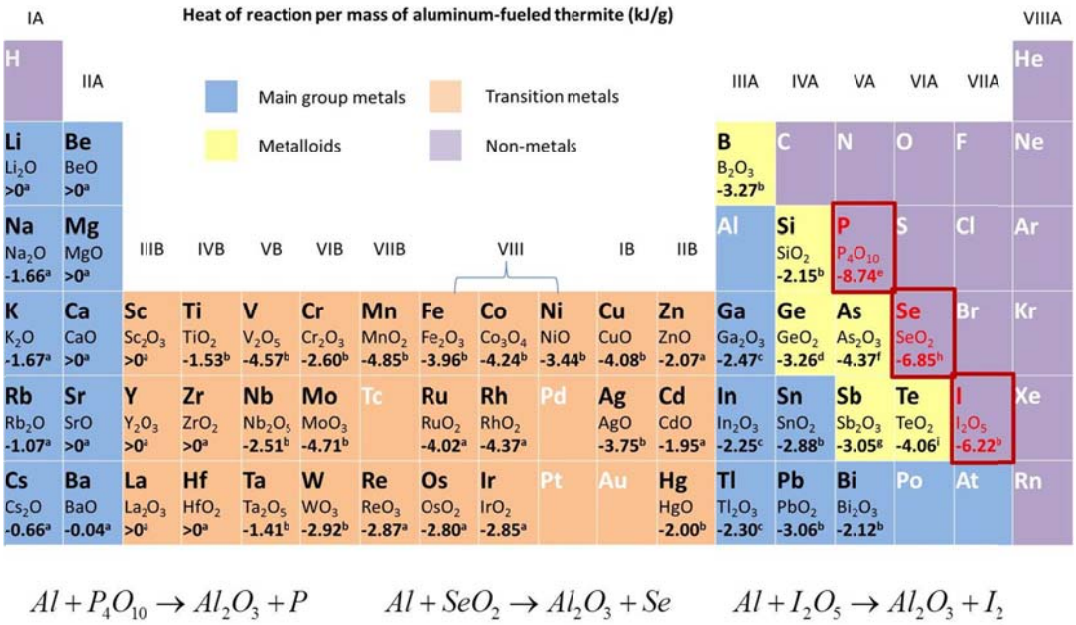

$$Al + P_4O_{10} \rightarrow Al_2O_3 + P \qquad Al + SeO_2 \rightarrow Al_2O_3 + Se \qquad Al + I_2O_5 \rightarrow Al_2O_3 + I_2$$

Figure 8.8. Element periodic table showing the standard heat of reaction per mass of aluminum-based thermites. The bottom three reaction equations highlight the formulations that generate the highest heat of reaction.

These calculations led me to test the combustion and ignition performance of these three thermites involving non-metal oxides. The combustion cell tests (Fig. 8.9A and 8.9B) show that the maximum peak pressures and pressurization rates for Al/I_2O_5 and Al/SeO_2 are comparable with that for Al/Bi_2O_3, and are much higher than the other metal oxide containing thermites. The optical emission results also demonstrate that the peak light emission from Al/I_2O_5 and Al/SeO_2 are more than 2 folds higher, and they have the shortest burn time. Al/P_4O_{10}, which possesses the largest heat of formation (Fig. 8.8), to my surprise, shows a mild pressurization rate and very poor optical emission (Fig. 8.9). This weakened reactivity of Al/P_4O_{10} can be attributed to the extremely high hygroscopicity of P_4O_{10} that introduces a large amount of water, which is unfavorable for the thermite reaction.

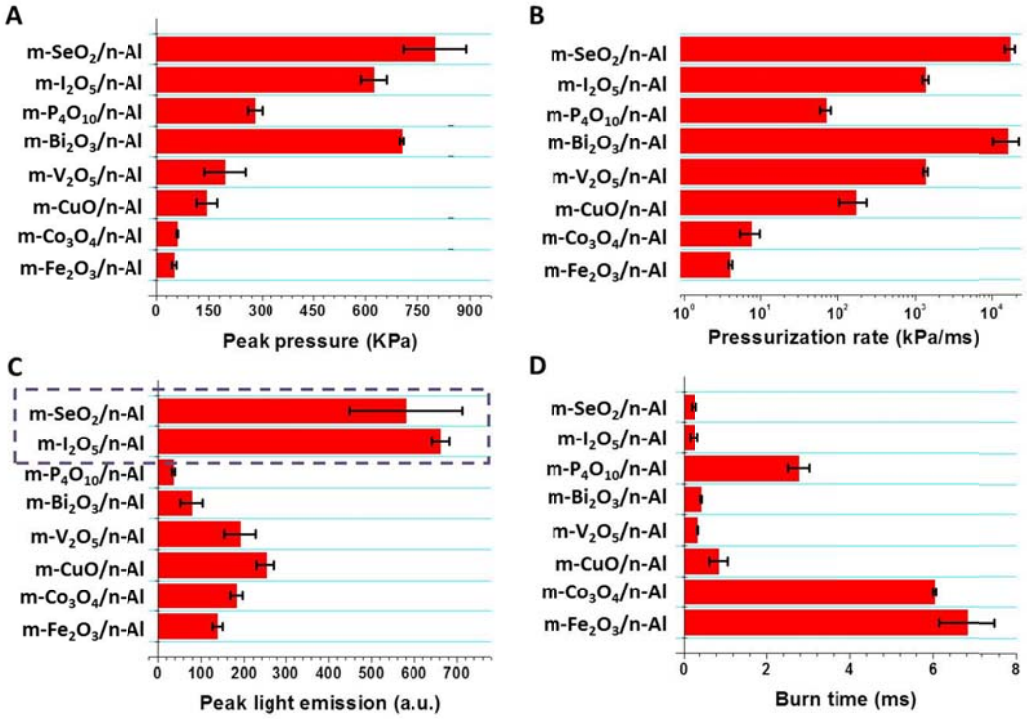

Figure 8.9. Temporal pressure (A), pressurization rate (B), light emission (C) and burn time (D) in the combustion cell tests of Al/I_2O_5, Al/P_4O_{10}, Al/SeO_2, and other five Al-based thermites, respectively. Each experiment was repeatd at least twice.

The ignition tests (Fig. 8.10) demonstrate that the oxygen release temperature for P_4O_{10} is ~250 ˚C lower than the ignition temperatures of Al/P_4O_{10}. This indicates that the ignition of Al/P_4O_{10} is controlled by the condensed phase reaction, which is further validated by the result that its ignition temperatures in Ar or in vacuum are similar. In comparison, the ignition temperature of Al/SeO_2 in Ar is also consistent with that in vacuum. However, no oxygen release was found by heating SeO_2. Instead, the sublimation of the entire SeO_2 molecule was observed at a temperature (~200 ˚C, data from TG measurement) lower than the ignition temperature of Al/SeO_2. Future work needs to be conducted to better understand the ignition mechanism of Al/SeO_2,

which may be completely different from the solid-gas and the condensed phase reaction mechanisms.

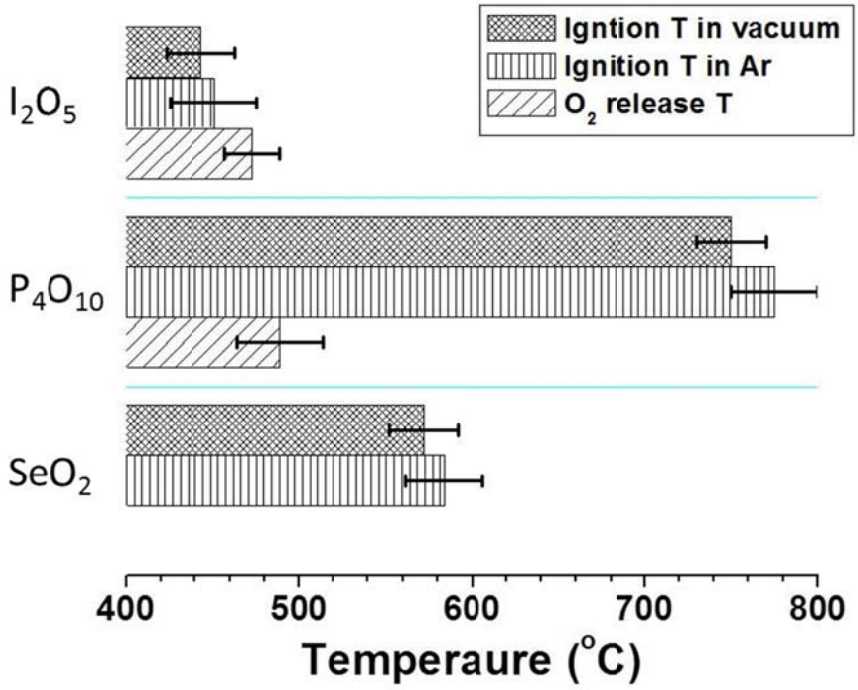

Figure 8.10. Relationship between the oxygen release temperature in neat microscale oxidizers, and the ignition temperature of corresponding nano-Al-fueled thermite in Ar and in vacuum. Each experiment was repeatd at least twice.

Appendix 1: Journal paper list

Papers published and submitted:

1. **W. Zhou**, S. K. Watt, D-H. Tsai, V. T. Lee*, M. R. Zachariah*. Quantitative Attachment and Detachment of Bacterial Spores from Fine Wires through Continuous and Pulsed DC Electrophoretic Deposition. ***J. Phys. Chem. B***, 2013, 117, 1738-1745.

2. **W. Zhou**, M. W. Orr, G. Jian, S. K. Watt, V. T. Lee*, M.R. Zachariah*. Inactivation of Bacterial Spores Subjected to Sub-Second Thermal Stress. ***Chem. Eng. J.***, 2015, 279, 578-588.

3. **W. Zhou**, M. W. Orr, V. T. Lee*, M. R. Zachariah*. Synergistic Effects of Ultrafast Heating and Chlorine Gas on the Inactivation of Bacterial Spores. ***Chem. Eng. Sci.***, 2015, *Submitted*.

4. **W. Zhou**, J. B. DeLisio, X. Li, L. Liu, M. R. Zachariah*. Persulfate Salt as an Oxidizer for Biocidal Energetic Nano-thermites. ***J. Mater. Chem. A***, 2015, 3, 11838–11846. (*Elected as "2015 Journal of Materials Chemistry A Hot Papers")*

5. **W. Zhou**, J. B. DeLisio, X. Wang, M. R. Zachariah*. Reaction Mechanisms of Energetic Composites Containing Potassium Oxysalts as Oxidizers. ***Combust. Flame***, 2015, *Submitted*.

6. **W. Zhou**, J. B. DeLisio, X. Wang, G. C. Egan, M. R. Zachariah*. Evaluating Free vs. Bound Oxygen on Ignition of Nano-aluminum Based Energetics Leads to a Critical Reaction Rate Criterion. ***J. Appl. Phys.***, 2015, 118, 114303.

7. H. Wang, J. B. DeLisio, G. Jian, **W. Zhou**, M. R. Zachariah*. Electrospray Formation and Combustion Characteristics of Iodine-Containing Al/CuO Nanothermite Microparticles. ***Combust. Flame***, 2015, 162, 2823-2829.

8. H. Wang, G. Jian, **W. Zhou**, J. B. DeLisio, V. T. Lee, M. R. Zachariah*. Metal Iodate-based Energetic Composites and Their Combustion and Biocidal Performance. ***ACS Appl. Mater. Interfaces***, 2015, 7, 17363-17370.

9. X. Li, P. Guerieri, **W. Zhou**, C. Huang, M. R. Zachariah*. Direct Deposit Laminate Nanocomposites with Enhanced Propellant Properties. ***ACS Appl. Mater. Interfaces***, 2015, 7, 9103-9109.

10. X. Hu, J. B. DeLisio, X. Li, **W. Zhou**, M. R. Zachariah*. Direct Deposit of Highly Reactive $Bi(IO_3)_3$ - Polyvinylidene Fluoride Biocidal Energetic Composite. ***Adv. Eng. Mater.***, 2015, *Submitted*.

11. X. Wang, **W. Zhou**, G. C. Egan, M. R. Zachariah*. Oxygen-ion Conductivity as a Metric for Ignition. ***J. Appl. Phys***., 2015, *Submitted*.

Appendix 2: Conference talk and poster list

1. **W. Zhou**, S. K. Watt, D-H. Tsai, V. T. Lee*, M. R. Zachariah*. Morphological Changes to Surface Attached Bacterial Spores Subjected to Sub-second Thermal Stress. ResearchFest 2013 (Poster and Short Presentation), University of Maryland, College Park, July 16, 2013;

2. **W. Zhou**, S. K. Watt, D-H. Tsai, V. T. Lee*, M. R. Zachariah*. Morphological Changes to Surface Attached Bacterial Spores Subjected to Sub-second Thermal Stress. ASM Biodefense and Emerging Diseases Research Meeting (Poster), Washington D.C., Jan 27, 2014.

3. **W. Zhou**, S. K. Watt, D-H. Tsai, V. T. Lee*, M. R. Zachariah*. Inactivation of Bacterial Spores Subjected to Sub-Second, High-Temperature Thermal Stress: Mimicking an Energetic material. Defense Threat Reduction Agency Annual Project Meeting (Poster), Virginia, July 30, 2014;

4. H. Wang, G. Jian, **W. Zhou**, J. B. DeLisio, V. T Lee, M. R. Zachariah*. Electrospray Formed Metal Iodate-based Energetic Composites and their Application as Biocidal Agents. Defense Threat Reduction Agency Annual Project Meeting (Poster), Virginia, July 30, 2014;

5. **W. Zhou**, S. K. Watt, D-H. Tsai, V. T. Lee*, M. R. Zachariah*. Inactivation of Bacterial Spores Subjected to Sub-Second, High-Temperature Thermal Stress: Mimicking an Energetic material. 2014 AIChE Annual Meeting (Presentation), Atlanta, Georgia, Nov 18, 2014.

6. H. Wang, G. Jian, **W. Zhou**, J. B. DeLisio, V. T Lee, M. R. Zachariah*. Electrospray Formed Metal Iodate-based Energetic Composites and their Application as Biocidal Agents. 2014 AIChE Annual Meeting (Poster), Atlanta, Georgia, Nov 18, 2014.

References

Chapter 1:

[1] A.D. Russell. The destruction of bacterial spores. Academic Press Inc., London, 1982.

[2] P. Setlow. J. Appl. Microbiol. 2006, 101, 514-525.

[3] M.J. Leggett, G. McDonnell, S.P. Denyer, P. Setlow, J.-Y. Maillard. J. Appl. Microbiol. 2012, 113, 485-498.

[4] R.J. Cano, M.K. Borucki. Science. 1995, 268, 1060-1064.

[5] P.T. McKenney, A. Driks, P. Eichenberger. Nat. Rev. Microbiol. 2013, 11, 33-44.

[6] A. Driks. Microbiol. Mol. Biol. Rev. 1999, 63, 1-20.

[7] A.O. Henriques, J. Moran. Annu. Rev. Microbiol. 2007, 61, 555-588.

[8] M. Plomp, A.M. Carroll, P. Setlow, A.J. Malkin. PLOS One. 2014, 9, e108560.

[9] W.L. Nicholson, N. Munakata, G. Horneck, H.J. Melosh, P. Setlow. Microbiol. Mol. Biol. Rev. 2000, 64, 548-572.

[10] W.H. Coleman, D. Chen, Y. Li, A.E. Cowan, P. Setlow. J. Bacteriology. 2007, 189, 8458-8466.

[11] W.H. Coleman, P. Zhang, Y.-q. Li, P. Setlow. Lett. Appl. Microbiol. 2010, 50, 507-514.

[12] W.H. Coleman, P. Setlow. J. Appl. Microbiol. 2009, 106, 1600-1607.

[13] C.A. Loshon, P.C. Genest, B. Setlow, P. Setlow. J. Appl. Microbiol. 1999, 87, 8-14.

[14] R. Tennen, B. Setlow, K.L. Davis, C.A. Loshon, P. Setlow. J Appl. Microbiol. 2000, 89, 330-338.

[15] C.A. Loshon, E. Melly, B. Setlow, P. Setlow. J. Appl. Microbiol. 2001, 91, 1051-1058.

[16] P.J. Riesenman, W.L. Nicholson. Appl. Environ. Microbiol. 2000, 66, 620-666.

[17] P. Setlow. Trends Microbiol. 2007, 15, 172-180.

[18] S.D. Gates, A.D. McCartt, P. Lappas, J.B. Jeffries, R.K. Hanson, L.A. Hokama, K.E. Mortelmans. J. Appl. Microbiol. 2010, 109, 1591-1598.

[19] S.D. Gates, A.D. McCartt, J.B. Jeffries, R.K. Hanson, L.A. Hokama, K.E. Mortelmans. J. Appl. Microbiol. 2011, 111, 925-931.

[20] S.A. Grinshpun, A. Adhikari, C. Li, T. Reponen, M. Yermakov, M. Schoenitz, E. Dreizin, M. Trunov, S. Mohan. J. Aerosol Sci. 2010, 41, 352-363.

[21] S.A. Grinshpun, C. Li, A. Adhikari, M. Yermakov, T. Reponen, M. Schoenitz, E. Dreizin, V. Hoffmann, M. Trunov. Aerosol Air Qual. Res. 2010, 10, 414-424.

[22] E. Johansson, A. Adhikari, T. Reponen, M. Yermakov, S.A. Grinshpun. Aerosol Sci. Technol. 2011, 45, 376-381.

[23] J.H. Jung, J.E. Lee, S.S. Kim. Sci. Total Environ. 2009, 407, 4723-4730.

[24] Y.H. Lee, B.U. Lee. J. Microbiol. Biotechnol. 2006, 16, 1684-1689.

[25] O. Hofmann, K. Murray, A. Wilkinson, T. Coxc, A. Manz. Lab Chip. 2005, 5, 374-377.

[26] A.G. Li, Y. Xing, L.W. Burggraf. Langmuir. 2013, 29, 8343−8354.

[27] Y. Xing, A. Li, D.L. Felker, L.W. Burggraf. Appl. Environ. Microbiol. 2014, 80, 1739-1749.

[28] S.A. Grinshpun, A. Adhikari, M. Yermakov, T. Reponen, E. Dreizin, M. Schoenitz, V. Hoffmann, S. Zhang. Environ. Sci. Technol. 2012, 46, 7334-7341.

[29] C. Rossi, K. Zhang, D. Esteve, P. Alphonse, P. Tailhades, C. Vahlas. J. Microelectromech. Syst. 2007, 16, 919-931.

[30] R.A. Yetter, G.A. Risha, S.F. Son. Proc. Combust. Inst. 2009, 32, 1819-1838.

[31] E.L. Dreizin. Prog. Energy Combust. Sci. 2009, 35, 141-167.

[32] N.H. Yen, L.Y. Wang. Propellants Explos. Pyrotech. 2012, 37, 143-155.

[33] J.P. Agrawal. High Energy Materials: Propellants, Explosives and Pyrotechnics. Wiley-VCH, 2010.

[34] R.A. Schaefer, S.M. Nicolich. Development and Evaluation of New High Blast Explosives, Insenstive Munitions & Energetic Materials Technical Symposium, (IMEMTS 2004), San Francisco, CA, 2004.

[35] S.H. Fischer, M.C. Grubelich. Survey of Combustible Metals, Thermites, and Intermetallics for Pyrotechnic Applications, SAN95-2248C, 32nd AIAA/ASME/SAF/ASEE Joint Propulsion Conference, Lake Buena Vista, FL, 1996.

[36] R. Thiruvengadathan, A. Bezmelnitsyn, S. Apperson, C. Staley, P. Redner, W. Balas, S. Nicolich, D. Kapoor, K. Gangopadhyay, S. Gangopadhyay. Combust. Flame. 2011, 158, 964-978.

[37] W.K. Lewis, B.A. Harruff, J.R. Gord, A.T. Rosenberger, T.M. Sexton, E.A. Guliants, C.E. Bunker. J. Phys. Chem. C. 2011, 115, 70-77.

[38] S. Umbrajkar, M.A. Trunov, M.Schoenitz, E.L. Dreizin. Propellants Explos. Pyrotech. 2007, 32, 32-41.

[39] R.W. Armstrong, B. Bschung, D.W. Booth, M. Samirant. Nano Lett. 2003, 3, 253-255.

[40] A.N. Pivkina, Y.V. Frolov, D.A. Ivanov. Combust. Explos. Shock Waves. 2007, 43, 51-55.

[41] X. Kang, J. Zhang, Q. Zhang, K. Du, Y. Tang. J. Therm. Anal. Calorim. 2012, 109, 1333-1340.

[42] C. Wu, K. Sullivan, S. Chowdhury, G. Jian, L. Zhou, M. R. Zachariah. Adv. Funct. Mater. 2012, 22, 78-85.

[43] W. Zhou, J.B. DeLisio, X. Li, L. Liu, M.R. Zachariah. J. Mater. Chem. A. 2015, 3, 11838.

[44] G. Jian, J. Feng, R. J. Jacob, G. C. Egan, M. R. Zachariah. Angew. Chem. Int. Ed. 2013, 52, 1-5.

[45] C.E. Aumann, G.L. Skofronick, J.A. Martin. J. Vac. Sci. Technol. B. Microelectron. Process. Phenom. 1995, 13, 1178-1183.

[46] M.E. Brown, S.J. Taylor, M.J. Tribelhorn. Propellants Explos. Pyrotech. 1998, 23, 320-327.

[47] S. Bhattacharya, Y. Gao, S. Apperson, S. Subramaniam, R. Shende, S. Gangopadhyay, E. Talantsev. J. Energ. Mater. 2006, 24, 1-15.

[48] A.E. Gash, T.M. Tillotson, J.H. Satcher, Jr., J.F. Poco, L.W. Hrubesh, R.L. Simpson. Chem. Mater. 2001, 13, 999-1007.

[49] T.M. Tillotson, A.E. Gash, R.L. Simpson, L.W. Hrubesh, J.H. Satcher, Jr., J.F. Poco.

J. Non-Cryst. Solids. 2001, 285, 338-345.

[50] A. Prakash, A.V. McCormick, M.R. Zachariah. Chem. Mater.2004, 16, 1466-1471.

[51] M. Petrantoni, C. Rossi, L. Salvagnac, V. Conedera, A. Esteve, C, Tenailleau, P. Alphonse, Y.J. Chabal. J. Appl. Phys. 2010, 108, 084323.

[52] K.J. Blobaum, M.E. Reiss, J.M.P. Lawrence, T.P. Weihs. J. Appl. Phys. 2003, 94, 2915-2922.

[53] K. Zhang, C. Rossi, G.A.A. Rodriguez, C. Tenailleau, P. Alphonse. Appl. Phys. Lett. 2007, 91, 113117.

[54] D. Xu, Y. Yang, H. Cheng, Y.Y. Li, K. Zhang. Combust. Flame. 2012, 159, 2202-2209.

[55] X. Zhou, D. Xu, Q. Zhang, J. Lu, K. Zhang. ACS Appl. Mater. Interfaces. 2013, 5, 7641-7646.

[56] S.M. Umbrajkar, M. Schoenitz, E.L. Dreizin. Thermochim. Acta. 2006, 451, 34-43.

[57] S.H. Kim, M.R. Zachariah. Adv. Mater. 2004, 16, 1821-1825.

[58] J.M. Slocik, C.A. Crouse, J.E. Spowart, R.R. Naik. Nano Lett. 2013, 13, 2535-2540.

[59] F. Severac, P. Alphonse, A. Esteve, A. Bancaud, C. Rossi. Adv. Funct. Mater. 2012, 22, 323-329.

[60] L. Meda, G. Marra, L. Galfetti, S. Inchingalo, F. Severini, L.T.D. Luca. Compos. Sci. Technol. 2005, 65, 769.

[61] L. Galfetti, L.T.D. Luca, F. Severini, L. Meda, G. Marra, M. Marchetti, M. Regi, S. Bellucci. J. Phys.: Condens. Matter. 2006, 18, S1991.

[62] I.G. Loscertales, A. Barrero, I. Guerrero, R. Cortijo, M. Marquez, A.M. Ganan-Calvo. Science. 2002, 295, 1695-1698.

[63] S. Yan, G. Jian, M.R. Zachariah. ACS Appl. Mater. Interfaces. 2012, 4, 6432-6435.

[64] R. Li, H. Xu, H. Hu, G. Yang, J. Wang, J. Shen. J. Energ. Mater. 2014, 32, 50-59.

[65] H. Wang, G. Jian, S. Yan, J.B. DeLisio, C. Huang, M.R. Zachariah. ACS Appl. Mater. Interfaces. 2013, 5, 6797-6801.

[66] H. Wang, G. Jian, G.C. Egan, M.R. Zachariah. Combust. Flame. 2014, 161, 2203-2208.

[67] C. Huang, G. Jian, J.B. DeLisio, H. Wang, M.R. Zachariah. Adv. Eng. Mater. 2015, 17, 95-101.

[68] X. Li, P. Guerieri, W. Zhou, C. Huang, M.R. Zachariah. ACS Appl. Mater. Interfaces. 2015, 7, 9103-9109.

[69] http://homeoint.org/seror/clarkgun/index.htm

[70] B-D. Lee, R. Thiruvengadathan, S. Puttaswamy, B.M. Smith, K. Gangopadhyay, S. Gangopadhyay, S. Sengupta. BMC Biotechnol. 2013, 13, 30.

[71] O. Mulamba, E.M. Hunt, M.L. Pantoya. Biotechnol. Bioproc. Eng. 2013, 18, 918-925.

[72] S. Zhang, M. Schoenitz, E.L. Dreizin. J. Phys. Chem. Solids. 2010, 71, 1213-1220.

[73] S. Zhang, M. Schoenitz, E.L. Dreizin. J. Phys. Chem. C. 2010, 114, 19653-19659.

[74] S. Zhang, C. Badiola, M. Schoenitz, E.L. Dreizin. Combust. Flame. 2012, 159, 1980-1986.

[75] K.S. Martirosyan, L. Wang, D. Luss. Chem. Phys. Lett. 2009, 483, 107-110.

[76] B.R. Clark, M.L. Pantoya. Phys. Chem. Chem. Phys. 2010, 12, 12653-12657.

[77] C. Farley, M. Pantoya. J. Therm. Anal. Calorim. 2010, 102, 609-613.

[78] C.W. Farley, M.L. Pantoya, M. Losada, S. Chaudhuri. J. Chem. Phys. 2013, 139, 074701.

[79] J. Feng, G. Jian, Q. Liu, M.R. Zachariah. ACS Appl. Mater. Interfaces. 2013, 5, 8875-8880.

[80] O. Mulamba, M. Pantoya. J. Nanopart. Res. 2014, 16, 2310.

[81] R. Russell, S. Bless, M. Pantoya. J. Energ. Mater. 2011, 29, 175-192.

[82] K.T. Sullivan, C. Wu, N.W. Piekiel, K. Gaskell, M.R. Zachariah. Combust. Flame. 2013, 160, 438-446.

[83] F. Solymosi. Fourth International Conference on Thermal Analysis, Vol. 1. Budapest, 1975.

[84] K.T. Sullivan, N.W. Piekiel, S. Chowdhury, C. Wu, M.R. Zachariah, C.E. Johnson. Combust. Sci. Technol. 2011, 183, 285-302.

[85] K.J. Rao, S. Paria. RSC Advances. 2013, 3, 10471.

[86] L. Palou, C.H. Crisosto, D. Garner, L.M. Basinal, J.L. Smilanick, J.P. Zoffoli. Am. J. Enol. Vitic. 2002, 53, 110-115.

[87] V.C. Papadimitriou, R.W. Portmann, D.W. Fahey, J. Muhle, R.F. Weiss, J.B. Burkholder. J. Phys. Chem. A. 2008, 112, 12657-12666.

[88] D.B. Hamal, J.A. Haggstrom, G.L. Marchin, M.A. Ikenberry, K. Hohn, K.J. Klabunde. Langmuir. 2010, 26, 2805-2810.

[89] S.M. Tichapondwa, W.W. Focke, O.D. Fabbro, C. Kelly. Propellants Explos. Pyrotech. 2015, 40, 518-525.

[90] M. Comet, G. Vidick, F. Schnell, Y. Suma, B. Baps, D. Spitzer. Angew. Chem. Int. Ed. 2015, 54, 1-6.

[91] S.R. Choudhury, M. Ghosh, A. Mandal, D. Chakravorty, M. Pal, S. Pradhan, A. Goswami. Appl. Microbiol. Biotechnol. 2011, 90, 733-743.

[92] J. Sun, M.L. Pantoya, S.L. Simon. Thermochim. Acta. 2006, 444, 117.

[93] D. Spitzer, M. Comet, C. Baras, V. Pichot, N. Piazzon. J. Phys. Chem. Solids. 2010, 71, 100.

[94] J. Bouillarda, A. Vignes, O. Dufaud, L. Perrinb, D. Thomas. J. Hazardous Mater. 2010, 181, 873-880.

[95] B. Siegert, M. Comet, D. Spitzer. Nanoscale. 2011, 3, 3534-3544.

[96] M.A. Trunov, M. Schoenitz, E.L. Dreizin. Combust. Theory Modell. 2006, 10, 603.

[97] D.A. Firmansyah, K. Sullivan, K-S. Lee, Y.H. Kim, R. Zahaf, M.R. Zachariah, D. Lee, J. Phys. Chem. C. 2012, 116, 404.

[98] C. Snehaunshu, K. Sullivan, N. Piekiel, L. Zhou, M.R. Zachariah. J. Phys. Chem. C. 2010, 114, 9191.

[99] L.P.H. Jeurgens, W.G. Sloof, F.D. Tichelaar, E.J. Mittemeijer. J. Appl. Phys. 2002, 92, 1649.

[100] A. Ermoline, E.L. Dreizin. Chem. Phys. Lett. 2011, 505, 47.

[101] B. J. Henz, T. Hawa, M.R. Zachariah. J. Appl. Phys. 2010, 107, 024901.

[102] V.I. Levitas, B.W. Asay, S.F. Son, M.L. Pantoya. J. Appl. Phys. 2007, 101, 083524.

[103] S. Zhang, E.L. Dreizin. J. Phys. Chem. C. 2013, 117, 14025.

[104] A. Rai, K. Park, L. Zhou, M.R. Zachariah. Combust. Theory Modell. 2006, 10, 843.

[105] R. Nakamura, D. Tokozakura, H. Nakajima, J.G. Lee, H. Mori. J. Appl. Phys. 2007, 101, 074303.

[106] N.W. Piekiel, L. Zhou, K.T. Sullivan, S. Chowdhury, G.C. Egan, M.R. Zachariah. Combust. Sci. Technol. 2014, 186, 1209-1224.

[107] L. Zhou, N. Piekiel, S. Chowdhury, M.R. Zachariah. J. Phys. Chem. C. 2010, 114, 14269.

[108] K.T. Sullivan, N.W. Piekiel, S. Chowdhury, S.T. Kelly, T.C. Hufnagel, K. Fezzaa, M.R. Zachariah. Combust. Flame. 2012, 159, 2.

[109] R.J. Jacob, G. Jian, P.M. Guerieri, M.R. Zachariah. Combust. Flame. 2015, 162, 258-264.

[110] K.T. Sullivan, W-A. Chiou, R. Fiore, M.R. Zachariah. Appl. Phys. Lett. 2010, 97, 133104.

[111] G.C. Egan, K.T. Sullivan, T. LaGrange, B.W. Reed, M.R. Zachariah. J. Appl. Phys. 2014, 115, 084903.

[112] V.I. Levitas, B.W. Asay, S.F. Son, M. Pantoya. Appl. Phys. Lett. 2006, 89, 071909.

[113] V.I. Levitas, M.L. Pantoya, B. Dikici. Appl. Phys. Lett. 2008, 92, 011921.

Chapter 2:

[1] G.W. Christopher, T.J. Cieslak, J.A. Pavlin, E.M. Eitzen. J. Am. Med. Assoc. 1997, 278, 412-417.

[2] R.M. Altas. Annu. Rev. Microbiol. 2002, 56, 167-185.

[3] S.A. Grinshpun, A. Adhikari, C. Li, T. Reponen, M. Yermakov, M. Schoenitz, E. Dreizin, M. Trunov, S. Mohan. J. Aero. Sci. 2010, 41, 352-363.

[4] S.D. Gates, A.D. McCartt, J.B. Jeffries, R.K. Hanson, L.A. Hokama, K.E. Mortelmans. J. Appl. Microbiol. 2011, 111, 925-931.

[5] G. McDonnell, A.D. Russell. Clin. Microbiol. Rev. 1999, 12, 147-179.

[6] N.R. Reddy, R.C. Tetzloff, H.M. Solomon, J.W. Larkin. Innov. Food Sci. Emerg. 2006, 7, 169-175.

[7] N. Staack, L. Ahrne, E. Borch, D. Knorr. J. Food Eng. 2008, 89, 319-324.

[8] M.K. Boudam, M. Moisan. J. Phys. D: Appl. Phys. 2010, 43, 295202.

[9] W.L. Nicholson, N. Munakata, G. Horneck, H.J. Melosh, P. Setlow. Microbiol. Mol. Biol. Rev. 2000, 64, 548-572.

[10] P. Setlow. J. Appl. Microbiol. 2006, 101, 514-525.

[11] P. Setlow. Trends Microbiol. 2007, 15, 172-180.

[12) S.D. Gates, A.D. McCartt, P. Lappas, J.B. Jeffries, R.K. Hanson, L.A. Hokama, K.E. Mortelmans. J. Appl. Microbiol.. 2010, 109, 1591-1598.

[13) A.D. McCartt, S.D. Gates, R.K. Hanson, L.M. Joubert, T.L. Buhr. Z. Phys. Chem. 2011, 225, 1367-1377.

[14] S.A. Grinshpun, C. Li, C.; Adhikari, A.; Yermakov, M.; Reponen, T.; Schoenitz, M.; Dreizin, E.; Hoffmann, V.; Trunov, M. Aerosol Air Quality Res. 2010, 10, 414-424.

[15] L. Zhou, N. Piekiel, S. Chowdhury, M.R. Zachariah. Rapid Commun. Mass Sp. 2009, 23, 194-202.

[16] M.B. Miller, B.L. Bassler. Annu. Rev. Microbiol. 2001, 55, 165-199.

[17] J.G. Mitchell, K. Kogure. FEMS Microbiol. Ecol. 2006, 55, 3-16.

[18] G. Reguera. Trends Microbiol. 2011, 19, 105-113.

[19] K. Colville, N.Tompkins, A.D. Rutenberg, M.H. Jericho. Langmuir. 2010, 26, 2639-2644.

[20] B. Fang, S. Gon, M-H. Park, K-N. Kumar, V.M. Rotello, K. Nusslein, M.M. Santore. Langmuir. 2012, 28, 7803-7810.

[21] A. Wakeham, R. Kennedy, A. McCartney. J. Aero. Sci. 2004, 35, 835-850.

[22] B.H. Lapizco-Encinas, M. Rito-Palomares. Electrophoresis. 2007, 28, 4521-4538.

[23] M. Urdaneta, E. Smela. J. Micromech. Microeng. 2008, 18, 015001.

[24] G.H. Markx, P.A. Dyda, R. Pethig. J. Biotechnol. 1996, 51, 175-180.

[25] H.A. Pohl, I. Hawk. Science. 1966, 152, 647-649.
[26] L. Benguigui, I.J. Lin. J. Electrostat. 1988, 21, 205-213.
[27] Y. Huang, R. Pethig. Meas. Sci. Technol. 1991, 2, 1142-1146.
[28] Y. Kazoe, M. Yoda. Langmuir. 2011, 27, 11481-11488.
[29] H.W. Douglas. Trans. Faraday Soc. 1955, 51, 146-152.
[30] M.A. Resnick, R.D. Tippetts, R.K. Mortimer. Science. 1967, 158, 803-804.
[31] B.H. Lapizco-Encinas, R.V. Davalos, B.A. Simmons, E.B. Cummings, Y. Fintschenko. J. Microbiol.Meth. 2005, 62, 317-326.
[32] N. Gadish, J. Voldman. Anal. Chem. 2006, 78, 7870-7876.
[33] M. Koklu, S. Park, S.D. Pillai, A. Beskok. Biomicrofluidics. 2010, 4, 034107.
[34] G. Chen, A. Driks, K. Tawfiq, M. Mallozzi, S. Patil. Colloid Surf. B. 2010, 76, 512-518.
[35] R.B. Seale, P.J. Bremer, S.H. Flint, A.J. McQuillan. J. Appl. Microbiol. 2010, 109, 1339-1348.
[36] A.T. Poortinga, H.J. Busscher. Biotechnol. Bioeng. 2000, 67, 117-120.
[37] B. Neirinck, L. Van Mellaert, J. Fransaer, O. Van der Biest, J. Anne, J. Vleugels. Electrochem. Commun. 2009, 11, 1842-1845.
[38] S. Novak, U. Maver, S. Peternel, P. Venturini, M. Bele, M. Gaberscek. Colloid Surface A. 2009, 340, 155-160.
[39] M. Ammam, J. Fransaer. Electrochim. Acta. 2010, 55, 3206-3212.
[40] P-C. Hsu, S-K. Seol, T-N. Lo, C-J. Liu, C-L. Wang, C-S. Lin, Y. Hwu, C.H. Chen, L-W. Chang, J.H. Je, G. Margaritondo. J. Electrochem. Soc. 2008, 155, D400-D407.
[41] V.S.J. Craig. Soft Matter. 2011, 7, 40-48.
[42] G. Tauveron, C. Slomianny, C. Henry, C. Faille. Int. J. Food Microbiol. 2006, 110, 254-262.
[43] M. Mercier-Bonin, A. Dehouche, J. Morchain, P. Schmitz. Int. J. Food Microbiol. 2011, 146, 182-191.
[44] L.M. Granhag, J.A. Finlay, P.R. Jonsson, J.A. Callow, M.E. Callow. Biofouling. 2004, 20, 117-122.

[45] C.K. Bower, J. McGuire, M.A. Daeschel. Trends Food Sci. Technol. 1996, 7, 152-157.

[46] A. Andersson, U. Ronner. Biofouling. 1998, 13, 51-67.

[47] M. Amman, J. Fransaer. Biosens. Bioelectron. 2009, 25, 191-197.

[48] B. Neirinck, J. Fransaer, O. Van der Biest, J. Vleugels. Electrochem. Commun. 2009, 11, 57-60.

[49] L. Besra, T. Uchikoshi, T.S. Suzuki, Y. Sakka. J. Am. Ceram. Soc. 2008, 91, 3154-3159.

[50] L. Besra, T. Uchikoshi, T.S. Suzuki, Y. Sakka. Euro. Ceram. Soc. 2009, 29, 1837-1845.

[51] A.T. Poortinga, R. Bos, W. Norde, H.J. Busscher. Surf. Sci. Rep. 2002, 47, 1-32.

[52] E. Chung, S. Yiacoumi, I. Lee, C. Tsouris. Environ. Sci. Technol. 2010, 44, 6209-6214.

[53] O.R. Walton. KONA Powder Particle Journal. 2008, 26, 129-141.

[54] S.K. Srivastava, A. Gencoglu, A.R. Minerick. Anal. Bioanal. Chem. 2011, 399, 301-321.

[55] M. Carrera, R.O. Zandomeni, J. Fitzgibbon, J-L. Sagripanti. J. Appl. Microbiol. 2007, 102, 303-312.

[56] W.D. Ristenpart, I.A. Aksay, D.A. Saville. Langmuir. 2007, 23, 4071-4080.

[57] W.D. Ristenpart, I.A. Aksay, D.A. Saville. J. Fluid Mech. 2007, 575, 83-109.

[58] P. Atkins. Physical Chemistry, 6th ed.; W. H. Freeman and Company: New York, 1997.

[59] J. Burgos, J.A. Ordonez, F. Sala. Appl. Microbiol. 1972, 24, 497-498.

[60] J.A. Ordonez, J. Burgos. Appl. Environ. Microbiol. 1976, 32, 183-184.

[61] R. Pagan, S. Esplugas, M.M. Gongora-Nieto, G.V. Barbosa-Canovas, B.G. Swanson. Food Sci. Teachnol. Int. 1998, 4, 33-44.

[62] S. Spilimbergo, F. Dehghani, A. Bertucco, N.R. Foster. Biotechnol. Bioeng. 2003, 82, 118-125.

[63] P.C. Hiemenz, R. Rajagopalan. Principles of Colloid and Surface Chemistry, 3rd ed.; Taylor & Francis Group: Boca Raton, 1997.

[64] D-H. Tsai, L.F. Pease III, R.A. Zangmeister, M.J. Tarlov, M.R. Zachariah. Langmuir. 2009, 25, 140-146.

[65] H.W. Douglas. Trans. Faraday Soc. 1959, 55, 850-856.

[66] M. Bohmer. Langmuir. 1996, 12, 5747-5750.

[67] H.C. Hamaker. Trans.Faraday Soc. 1940, 36, 279-87.

[68] P. Sarkar, P.S. Nicholson. J. Am. Ceram. Soc. 1996, 79, 1987-2002.

Chapter 3:

[1] G.W. Gould. J. Appl. Microbiol. 2006, 101, 507-513.

[2] W.L. Nicholson, N. Munakata, G. Horneck, H.J. Melosh, P. Setlow. Microbiol. Mol. Biol. Rev. 2000, 64, 548-572.

[3] P. Setlow. J. Appl. Microbiol. 2006, 101, 514-525.

[4] E. Nadasi, T. Varjas, I. Prantner, V. Virag, I. Ember. Gene Ther. Mol. Biol. 2007, 11, 315-320.

[5] Y. Gilbert, C. Duchaine. Can. J. Civ. Eng. 2009, 36, 1873-1886.

[6] V. Kummer, W.R. Thiel. Int. J. Hyg. Environ –Health. 2008, 211, 299-307.

[7] T.L. Buhr, A.A. Young, Z.A. Minter, C.M. Wells, D.C. McPherson, C.L. Hooban, C.A. Johnson, E.J. Prokop, J.R. Crigler. J. Appl. Microbiol. 2012, 113, 1037-1051.

[8] W.H. Coleman, D. Chen, Y-Q. Li, A.E. Cowan, P. Setlow P. J. Bacteriol. 2007, 189, 8458-8466.

[9] R. Conesa, P.M. Periago, A. Esnoz, A. Lopez, A. Palop. Eur. Food Res. Technol. 2003, 217, 319-324.

[10] O. Couvert, S. Gaillard, N. Savy, P. Mafart, I. Leguerinel. Int. J. Food Microbiol. 2005,101, 73-81.

[11] J. Iciek, A. Papiewska, M. Molska. J. Food Eng. 2006, 77, 406-410.

[12] J-H. Mah, D-H. Kang, J. Tang. J. Food Prot. 2008, 71, 953-958.

[13] T.J. Montville, R. Dengrove, T. de Siano, M. Bonnet, W. Schaffner. J. Food Prot. 2005, 68, 2362-2366.

[14] N.E.M. Mustafa, U. Keller, U. Malkus, D. Harmsen, R. Reichelt, A.A. Hussein, S.M. El-Sanousi. Curr. Res. Bacteriol. 2010, 3, 214-226.

[15] J.S. Novak, V.K. Juneja, B.A. McClane. Int. J. Food Microbiol. 2003, 86, 239-247.

[16] F.T. Tabit, E. Buys. Int. J. Food Microbiol. 2010, 140, 207-213.

[17] S.D. Gates, A.D. McCartt, P. Lappas, J.B. Jeffries, R.K. Hanson, L.A. Hokama, K.E. Mortelmans. J. Appl. Microbiol. 2010, 109, 1591-1598.

[18] S.D. Gates, A.D. McCartt, J.B. Jeffries, R.K. Hanson, L.A. Hokama, K.E. Mortelmans. J. Appl. Microbiol. 2011, 111, 925-931.

[19] S.A. Grinshpun, A. Adhikari, C. Li, T. Reponen, M. Yermakov, M. Schoenitz, E. Dreizin, M. Trunov, S. Mohan. J. Aerosol Sci. 2010, 41, 352-363.

[20] S.A. Grinshpun, C. Li, A. Adhikari, M. Yermakov, T. Reponen, M. Schoenitz, E. Dreizin, V. Hoffmann, M. Trunov. Aerosol Air Qual. Res. 2010, 10, 414-424.

[21] S.A. Grinshpun, A. Adhikari, M. Yermakov, T. Reponen, E. Dreizin, M. Schoenitz, V. Hoffmann, S. Zhang. Environ. Sci. Technol. 2012, 46, 7334-7341.

[22] E. Johansson, A. Adhikari, T. Reponen, M. Yermakov, S.A. Grinshpun. Aerosol Sci. Technol. 2011, 45, 376-381.

[23] J.H. Jung, J.E. Lee, S.S. Kim. Sci. Total Environ. 2009, 407, 4723-4730.

[24] Y.H. Lee, B.U. Lee. J. Microbiol. Biotechnol. 2006, 16, 1684-1689.

[25] A.D. McCartt, S.D. Gates, J.B. Jeffries, R.K. Hanson, L.M. Joubert, T.L. Buhr. Z. Phys. Chem. 2011, 225, 1367-1377.

[26] N. Piekiel, M.R. Zachariah. J. Phys. Chem. A. 2012, 116, 1519-1526.

[27] K.T. Sullivan, N.W. Piekiel, S. Chowdhury, C. Wu, M.R. Zachariah, C.E. Johnson. Combust. Sci. Technol. 2011, 183, 285-302.

[28] C. Wu, K. Sullivan, S. Chowdhury, G. Jian, L. Zhou, M.R. Zachariah. Adv. Funct. Mater. 2012, 22, 78-85.

[29] G. Young, N. Piekiel, S. Chowdhury, M.R. Zachariah. Combust. Sci. Technol. 2010, 182, 1341-1359.

[30] L. Zhou, N. Piekiel, S. Chowdhury, M.R. Zachariah. Rapid Commun. Mass Sepctrom. 2009, 23, 194-202.

[31] L. Zhou, N. Piekiel, S. Chowdhury, M.R. Zachariah. J. Phys. Chem. C. 2010, 114, 14269-14275.

[32] J.M. Mason, P. Setlow. J. Bacteriology. 1986, 167, 174-178.

[33] W.L. Nicholson, B. Setlow, P. Setlow. J. Bacteriology. 1990,172, 6900-6906.

[34] P. Setlow, I will survive: protecting and repairing spore DNA, J. Bacteriology. 1992,174, 2737-2741.

[35] B. Setlow, P. Setlow. Appl. Environ. Microbiol. 1995, 61, 2787-2790.

[36] B. Setlow, P. Setlow. J. Bacteriology. 1996, 178, 3486-3495.

[37] W.H. Coleman, P. Setlow. J. Appl. Microbiol. 2009, 106, 1600-1607.

[38] P. Zhang, L. Kong, P. Setlow, Y-Q. Li. Appl. Envrion. Microbiol. 2010, 76, 1796-1805.

[39] D.L. Popham, J. Helin, C.E. Costello, P. Setlow. J. Bacteriology. 1996, 178, 6451-6458.

[40] H Fairhead, B. Setlow, P. Setlow. J. Bacteriology. 1993, 175, 1367-1374.

[41] B. Setlow, S. Atluri, R. Kitchel, K. Koziol-Dube, P. Setlow. J. Bacteriology. 2006, 188, 3740-3747.

[42] B. Setlow, E. Melly, P. Setlow. J. Bacteriology. 2001, 183, 4894-4899.

[43] S. Nakashio, P. Gerhardt. J. Bacteriology. 1985, 162, 571-578.

[44] P. Gerhardt, R.E. Marquis. Spore thermoresistance mechanisms, In: Regulation of Procaryotic Development cd, American Society for Microbiology, DC, 1986, pp. 43-63.

[45] S. Kozuka, K. Tochikubo. J. Gen. Microbiol. 1991, 137, 607-613.

[46] P. Zhang, L. Kong, G. Wang, P. Setlow, Y.Q. Li. Appl. Environ.Microbiol. 2011, 77, 4754-4769.

[47] E. Melly, A.E. Cowan, P. Setlow. J. Appl. Microbiol. 2002, 93, 316-325.

[48] S.B. Young, P. Setlow. J. Appl. Microbiol. 2003, 95, 54-67.

[49] S.B. Young, P. Setlow. J. Appl. Microbiol. 2004, 96, 1133-1142.

[50] B. Setlow, S. Parish, P. Zhang, Y.Q. Li, W.C. Neely, P. Setlow. J. Appl. Microbiol. 2013, 116, 805-814.

[51] W. Zhou, S.K. Watt, D-H. Tsai, V.T. Lee, M.R. Zachariah. J. Phys. Chem. B. 2013, 117, 1738-1745.

[52] P.R.N. Childs. Practical Temperature Measurement, Butterworth Heinemann, London, UK, 2001.

[53] X. Zhang, H. Xie, M. Fujii, K. Takahashi, T. Ikuta, H. Ago, H. Abe, T. Shimizu. Int. J. Heat Mass Transfer. 2006, 49, 3879-3883.

[54] R. Kumar, N. Sahoo, V. Kulkarni. Int. J. Heat Mass Transfer. 2012, 55, 2707-2713.

[55] S. Middleman. An introduction to mass and heat transfer. John Wiley & Sons, Inc., Hoboken, NJ, 1998.

[56] T.C. Beaman, P. Gerhardt. Appl. Environ. Microbiol. 1986, 52, 1242-1246.

[57] J.N. Junior, P.R. de Massaguer. J. Food Proc. Eng. 2007, 30, 625-639.

[58] B. Setlow, K.A. McGinnis, K. Ragkousi, P. Setlow. J. Bacteriology. 2000, 182, 6906-6912.

[59] M. Paidhungat, K. Ragkousi, P. Setlow. J. Bacteriology. 2001, 183, 4886-4893.

[60] A. Driks, S. Roels, B. Beall, C.P. Moran Jr., R. Losick. Genes Dev. 1994, 8, 234-244.

[61] P. Setlow. Ann. Rev. Microbiol. 1988, 42, 319-38.

[62] R. Kumar, S. Saurav, E.V. Titov, D.A. Levin, R.F. Long, W.C. Neely, P. Setlow. Int. J. Heat Mass Transfer. 2011,54, 755-765.

[63] Y. Xing, A. Li, D.L. Felker, L.W. Burggraf. Appl. Environ. Microbiol. 2014, 80, 1739-1749.

[64] M. Peleg, M.B. Cole. Crit. Rev. Food Sci. Nutr. 1998, 38, 353-380.

[65] A. Driks. Microbiol. Mol. Biol. Rev. 1999, 63, 1-20.

[66] H. Takamatsu, K. Watabe. Cell Mol. Life Sci. 2002, 59, 434-444.

[67] S. Ghosh, B. Setlow, P.G. Wahome, A.E. Cowan, M. Plomp, A.J. Malkin, P. Setlow. J. Bacteriol. 2008, 190, 6741-6748.

[68] T.C. Beaman, P. Gerhardt. Appl. Environ. Microbiol. 1986, 52, 1242-1246.

[69] S.I. Sandler, Chemical, biochemical, and engineering thermodynamics, John Wiley & Sons, Inc., Hoboken, NJ, 2006.

[70] A.G. Li, Y. Xing, L.W. Burggraf. Langmuir. 2013, 29, 8343-8354.

[71] E.P. Black, P. Setlow, A.D. Hocking, C.M. Stewart, A.L. Kelly, D.G. Hoover. Compr. Rev. Food Sci. Food Saf. 2007, 6, 103-119.

[72] H-W Huang, H-M Lung, B.B. Yang, C-Y Wang. Food Control. 2014, 40, 250-259.

[73] Z. Zhang, B. Jiang, X. Liao, J. Yi, X. Hu, Y. Zhang. Int J Food Microbiol. 2012, 160, 99-104.

Chapter 4:

[1] E. Nadasi, T. Varjas, I. Prantner, V. Virag, I. Ember. Gene Ther. Mol. Biol. 11 (2007) 315-320.

[2] Y. Gilbert, C. Duchaine. Can. J. Civ. Eng. 36 (2009) 1873-1886.

[3] V. Kummer, W.R. Thiel. Int. J. Hyg. Environ –Health. 211 (2008) 299-307.

[4] G.W. Gould. J. Appl. Microbiol. 101 (2006) 507-513.

[5] W.L. Nicholson, N. Munakata, G. Horneck, H.J. Melosh, P. Setlow. Microbiol. Mol. Biol. Rev. 64 (2000) 548-572.

[6] P. Setlow. J. Appl. Microbiol. 101 (2006) 514-525.

[7] R. Conesa, P.M. Periago, A. Esnoz, A. Lopez, A. Palop. Eur. Food Res. Technol. 217 (2003) 319-324.

[8] O. Couvert, S. Gaillard, N. Savy, P. Mafart, I. Leguerinel. Int. J. Food Microbiol. 101 (2005) 73-81.

[9] W.H. Coleman, D. Chen, Y-Q. Li, A.E. Cowan, P. Setlow. J. Bacteriol. 189 (2007) 8458-8466.

[10] S.D. Gates, A.D. McCartt, P. Lappas, J.B. Jeffries, R.K. Hanson, L.A. Hokama, K.E. Mortelmans. J. Appl. Microbiol. 109 (2010) 1591-1598.

[11] S.D. Gates, A.D. McCartt, J.B. Jeffries, R.K. Hanson, L.A. Hokama, K.E. Mortelmans. J. Appl. Microbiol. 111 (2011) 925-931.

[12] S.A. Grinshpun, A. Adhikari, C. Li, T. Reponen, M. Yermakov, M. Schoenitz, E. Dreizin, M. Trunov, S. Mohan. J. Aerosol Sci. 41 (2010) 352-363.

[13] S.A. Grinshpun, C. Li, A. Adhikari, M. Yermakov, T. Reponen, M. Schoenitz, E. Dreizin, V. Hoffmann, M. Trunov. Aerosol Air Qual. Res. 10 (2010) 414-424.

[14] E. Johansson, A. Adhikari, T. Reponen, M. Yermakov, S.A. Grinshpun. Aerosol Sci. Technol. 45 (2011) 376-381.

[15] J.H. Jung, J.E. Lee, S.S. Kim. Sci. Total Environ. 407 (2009) 4723-4730.

[16] Y.H. Lee, B.U. Lee. J. Microbiol. Biotechnol. 16 (2006) 1684-1689.

[17] B-D. Lee, R. Thiruvengadathan, S. Puttaswamy, B.M. Smith, K. Gangopadhyay, S. Gangopadhyay, S. Sengupta. BMC Biotechnol. 13 (2013) 30.
[18] P.R.N. Childs. Practical Temperature Measurement, Butterworth Heinemann, London, UK, 2001.
[19] W. Zhou, M.W. Orr, G. Jian, S.K. Watt, V.T. Lee, M.R. Zachariah. Chem. Eng. J. 279 (2015) 578-588.
[20] G. McDonnell, A.D. Russell. Clin. Microbiol. Rev. 12 (1999) 147-179.
[21] A. Fraise. J. Hosp. Infect. 77 (2011) 210-212.
[22] M.M. Coombs, J.F. Danielli. Nature. 183 (1959) 1257-1258.
[23] M. Deborde, U. von Gunten. Water Res. 42 (2008) 13-51.
[24] G.A. DeQueiroz, D.F. Day. Lett. Appl. Microbiol. 46 (2008) 176-180.
[25] S.B. Young, P. Setlow. Appl. Environ. Microbiol. 95 (2003) 54-67.
[26] L.J. Rose, E.W. Rice, B. Jensen, R. Murga, A. Peterson, R.M. Donlan, M.J. Arduino. Appl. Environ. Microbiol. 71 (2005) 566-568.
[27] A.R. Brazis, J.E. Leslie, P.W. Kabler, R.L. Woodward. Appl. Microbiol. 6 (1958) 338-342.
[28] E.W. Rice, N.J. Adcock, M. Sivaganesan, L.J. Rose. Appl. Environ. Microbiol. 71 (2005) 5587-5589.
[29] G.M. Fair, J.C. Morris, S.L. Chang. J. New Engl. Water Works Assoc. 61 (1947) 285-301.
[30] A.A. Hosni, W.T. Shane, J.G. Szabo, P.L. Bishop. Can. J. Civ. Eng. 36 (2009) 732-737.
[31] J. Szabo, S. Minamyer. Environ. Int. 72 (2014) 124-128.
[32] A.C. Kreske, J-H. Ryu, C.A. Pettigrew, L.R. Beuchat. J. Food Prot. 69 (2006) 2621-2634.
[33] L.V. Venczel, M. Arrowood, M. Hurd, M.D. SoBsey. Appl. Environ. Microbiol. 63 (1997) 1598-1601.
[34] C.H. Johnson, M.M. Marshall, L.A. DeMaria, J.M. Moffet, D.G. Korich. Appl. Environ. Microbiol. 69 (2003) 1325-1326.
[35] H. Son, M. Cho, H. Chung, S. Choi, J. Yoon. J. Ind. Eng. Chem. 10 (2004) 705-709.

[36] J. Perez, S. Springthorpe, S.A. Sattar. Am. J. Infect. Control. 33 (2005) 320-325.
[37] D.E. John, C.N. Haas, N. Nwachuku, C.P. Gerba. Water Res. 39 (2005) 2369-2375.
[38] R.M.S. Thorn, G.M. Robinson, D.M. Reynolds. Antimicrob. Agents Chemother. 57 (2013) 2216-2225.
[39] http://emergency.cdc.gov/agent/chlorine/basics/facts.asp
[40]http://www.accessdata.fda.gov/scripts/cdrh/cfdocs/cfCFR/CFRSearch.cfm?CFRPart=173
[41]http://www.accessdata.fda.gov/scripts/cdrh/cfdocs/cfcfr/CFRSearch.cfm?CFRPart=178
[42] S. Xu, T.P. Labuza, F. Diez-Gonzalez. Appl. Environ. Microbiol. 74 (2008) 3336-3341.
[43] J-L. Sagripanti, M. Carrera, J. Insalaco, M. Ziemski, J. Rogers, R. Zandomeni. J. Appl. Microbiol. 102 (2007) 11-21.
[44] W. Zhou, S.K. Watt, D-H. Tsai, V.T. Lee, M.R. Zachariah. J. Phys. Chem. B. 117 (2013) 1738-1745.
[45] J.N. Junior, P.R. de Massaguer. J. Food Proc. Eng. 30 (2007) 625-639.
[46] http://www.grc.nasa.gov/WWW/CEAWeb/ceaHome.htm
[47] L.R. Wyatt, W.M. Waites. J. Gen. Microbiol. 89 (1975) 337-344.
[48] B. Setlow, C.A. Loshon, P.C. Genest, A.E. Cowan, C. Setlow, P. Setlow. J. Appl. Microbiol. 92 (2002) 362-375.
[49] M. Cho, J-H. Kim, J. Yoon. Water Res. 40 (2006) 2911-2920.

Chapter 5:

[1] R.A. Yetter, G.A. Risha, S.F. Son. Proc. Combust. Inst. 2009, 32, 1819-1838.
[2] E.L. Dreizin. Prog. Energy Combust. Sci. 2009, 35, 141-167.
[3] N.H. Yen, L.Y. Wang. Propellants, Explos., Pyrotech. 2012, 37, 143-155.
[4] C. Rossi. Propellants, Explos., Pyrotech. 2014, 39, 323-327.

[5] S. Apperson, R. V. Shende, S. Subramanian, D. Tappmeyer, S. Gangopadhyay, Z. Chen, K. Gangopadhyay, P. Redner, S. Nicholich, D. Kapoor. Appl. Phys. Lett. 2007, 91, 243109.

[6] D.K. Kim, J.H. Bae, M.K. Kang, H.J. Kim. Curr. Appl. Phys. 2011, 11, 1067-1070.

[7] J. Wang, A. Hu, J. Persic, J.Z. Wen, Y.N. Zhou. J. Phys. Chem. Solids. 2011, 72, 620-625.

[8] J. Mei, R. D. Halldearn, P. Xiao. Scr. Mater. 1999, 41, 541-548.

[9] T.M. Tillotson, A.E. Gash, R.L. Simpson, L.W. Hrubesh, J.H. Satcher Jr., J.F. Poco. J. Non-Cryst. Solids. 2001, 285, 338-345.

[10] L. Menon, S. Patibandla, K. Bhargava Ram, S.I. Shkuratov, D. Aurongzeb, M. Holtz, J. Berg, J. Yun, H. Temkin. Appl. Phys. Lett. 2004, 84, 4735-4737.

[11] J.A. Puszynski, C.J. Bulian, J.J. Swiathiewiz. J. Propul. Power. 2007, 23, 698-706.

[12] K.S. Martirosyan, L. Wang, A. Vicent, D. Luss. Nanotechnology. 2009, 20, 405609.

[13] R. Thiruvengadathan, A. Bezmelnitsyn, S. Apperson, C. Staley, P. Redner, W. Balas, S. Nicolich, D. Kapoor, K. Gangopadhyay, S. Gangopadhyay. Combust. Flame. 2011, 158, 964-978.

[14] W.K. Lewis, B.A. Harruff, J.R. Gord, A.T. Rosenberger, T.M. Sexton, E.A. Guliants, C.E. Bunker. J. Phys. Chem. C. 2011, 115, 70-77.

[15] S. Umbrajkar, M.A. Trunov, M. Schoenitz, E.L. Dreizin. Propellants, Explos., Pyrotech. 2007, 32, 32-41.

[16] M.A. Machado, D.A. Rodriguez, Y. Aly, M. Schoenitz, E.L. Dreizin, E. Shafirovich. Combust. Flame. 2014, 161, 2708-2716.

[17] R.W. Armstrong, B. Bschung, D. W. Booth, M. Samirant. Nano Lett. 2003, 3, 253-255.

[18] A.N. Pivkina, Y.V. Frolov, D.A. Ivanov. Combust. Explos. Shock Waves. 2007, 43, 51-55.

[19] X. Kang, J. Zhang, Q. Zhang, K. Du, Y. Tang. J. Therm. Anal. Calorim. 2012, 109, 1333-1340.

[20] C. Wu, K. Sullivan, S. Chowdhury, G. Jian, L. Zhou, M.R. Zachariah. Adv. Funct. Mater. 2012, 22, 78-85.
[21] C.R. Becker, S. Apperson, C.J. Morris, S. Gangopadhyay, L.J. Currano, W.A. Churaman, C.R. Stoldt. Nano Lett. 2011, 11, 803-807.
[22] J.C. Poret, A.P. Shaw, C.M. Csernica, K.D. Oyler, J.A. Vanatta, G. Chen. ACS Sustainable Chem. Eng. 2013, 1, 1333-1338.
[23] Y.R. Luo. Comprehensive Handbook of Chemical Bond Energies. CRC Press, Boca Raton, FL, 2007.
[24] B.D. Darwent. Bond Dissociation Energies in Simple Molecules. Nat. Stand. Ref. Data Ser., Nat. Bur. Stand. (U.S.A.), 1970, 31, pp. 1-52.
[25] G. Jian, J. Feng, R. J. Jacob, G.C. Egan, M.R. Zachariah. Angew. Chem. Int. Ed. 2013, 52, 1-5.
[26] J.A. Conkling, C.J. Mocella. Chemistry of Pyrotechnics: Basic Principles and Theory, 2nd ed. CRC Press-Taylor & Francis Group, Boca Raton, 2010, pp. 69-70.
[27] R.T. Sanderson. Chemical Bonds and Bond Energy. Academic Press, New York, 1971.
[28] I.M. Kolthoff, I.K. Miller. J. Am. Chem. Soc. 1951, 73, 3055-3059.
[29] K-C. Huang, R.A. Couttenye, G.E. Hoag. Chemosphere. 2002, 49, 413-420.
[30] R.H. Waldemer, P.G. Tratnyek, R.L. Johnson, J.T. Nurmi. Environ. Sci. Technol. 2007, 41, 1010-1015.
[31] A. Tsitonaki, B. Petri, M. Crimi, H. MosbÆk, R.L. Siegrist, P.L. Bjerg. Crit. Rev. Environ. Sci. Technol. 2010, 40, 55-91.
[32] F.A. Cotton, G. Wilkinson. Advance Iorganic Chemistry, 3rd ed. John Wiley & Sons, New York, 1972.
[33] E. Nadasi, T. Varjas, I. Prantner, V. Virag, I. Ember. Gene Ther. Mol. Biol. 2007, 11, 315-320.
[34] Y. Gilbert, C. Duchaine, Can. J. Civ. Eng., 2009, 36, 1873-1886.
[35] W.L. Nicholson, N. Munakata, G. Horneck, H.J. Melosh, P. Setlow. Microbiol. Mol. Biol. Rev. 2000, 64, 548-572.
[36] P. Setlow. J. Appl. Microbiol. 2006, 101, 514-525.

[37] S. Zhang, M. Schoenitz, E.L. Dreizin. J. Phys. Chem. Solids. 2010, 71, 1213-1220.

[38] S. Zhang, M. Schoenitz, E.L. Dreizin. J. Phys. Chem. C. 2010, 114, 19653-19659.

[39] S. Zhang, C. Badiola, M. Schoenitz, E.L. Dreizin. Combust. Flame. 2012, 159, 1980-1986.

[40] R. Russell, S. Bless, M. Pantoya. J. Energ. Mater. 2011, 29, 175-192.

[41] K.T. Sullivan, C. Wu, N.W. Piekiel, K. Gaskell, M.R. Zachariah. Combust. Flame. 2013, 160, 438-446.

[42] K.S. Martirosyan, L. Wang, D. Luss. Chem. Phys. Lett. 2009, 483, 107-110.

[43] B.R. Clark, M.L. Pantoya, Phys. Chem. Chem. Phys. 2010, 12, 12653-12657.

[44] C. Farley, M. Pantoya. J. Therm. Anal. Calorim. 2010, 102, 609-613.

[45] C.W. Farley, M.L. Pantoya, M. Losada, S. Chaudhuri. J. Chem. Phys. 2013, 139, 074701.

[46] J. Feng, G. Jian, Q. Liu, M. R. Zachariah. ACS Appl. Mater. Interfaces. 2013, 5, 8875-8880.

[47] O. Mulamba, M. Pantoya. J. Nanopart. Res. 2014, 16, 2310.

[48] K.T. Sullivan, N.W. Piekiel, S. Chowdhury, C. Wu, M.R. Zachariah, C.E. Johnson. Combust. Sci. Technol. 2011, 183, 285-302.

[49] K.J. Rao, S. Paria. RSC Advances. 2013, 3, 10471.

[50] L. Palou, C.H. Crisosto, D. Garner, L.M. Basinal, J.L. Smilanick, J.P. Zoffoli. Am. J. Enol. Vitic. 2002, 53, 110-115.

[51] V.C. Papadimitriou, R.W. Portmann, D.W. Fahey, J. Muhle, R.F. Weiss, J.B. Burkholder. J. Phys. Chem. A. 2008, 112, 12657-12666.

[52] D.B. Hamal, J.A. Haggstrom, G.L. Marchin, M.A. Ikenberry, K. Hohn, K.J. Klabunde. Langmuir. 2010, 26, 2805-2810.

[53] S.R. Choudhury, M. Ghosh, A. Mandal, D. Chakravorty, M. Pal, S. Pradhan, A. Goswami. Appl. Microbiol. Biotechnol. 2011, 90, 733-743.

[54] G.L. Cohen, G. Atkinson. Inorg. Chem. 1964, 3, 1741-1743.

[55] C. Liang, C. J. Bruell, M. C. Marley, K. L. Sperry. Chemosphere. 2004, 55, 1213-1223.

[56] S-Y. Oh, H-W. Kim, J-M. Park, H-S. Park, C. Yoon. J. Hazard. Mater. 2009, 168, 346-351.
[57] O.S. Furman, A.L. Teel, R.J. Watts. Environ. Sci. Technol. 2010, 44, 6423-6428.
[58] L. Zhou, N. Piekiel, S. Chowdhury, M.R. Zachariah. Rapid Commun. Mass Spectrom. 2009, 23, 194-202.
[59] E. de Hoffmann, V. Stroobant. Mass Spectrometry: Principles and Applications, 3rd ed. John Wiley & Sons, West Sussex, England, 2007, pp. 17.
[60] NIST webbook, http://webbook.nist.gov/chemistry/form-ser.html.
[61] K.H. Stern. High Temperature Properties and Thermal Decomposition of Inorganic Salts with Oxyanions. CRC Press, Boca Raton, FL, 2007, pp. 66.
[62] http://www.grc.nasa.gov/WWW/CEAWeb/.
[63] N.W. Piekiel, G.C. Egan, K.T. Sullivan, M.R. Zachariah. J. Phys. Chem. C. 2012, 116, 24496-24502.
[64] N.W. Piekiel, L. Zhou, K.T. Sullivan, S. Chowdhury, G.C. Egan, M.R. Zachariah. Combust. Sci. Technol. 2014, 186, 1209-1224.

Chapter 6:

[1] H. Goldschmidt. Iron Age. 1908, 82, 232.
[2] E.L. Dreizin. Prog. Energ. Combust. Sci. 2009, 35, 141-167.
[3] R.A. Yetter, G.A. Risha, S.F. Son. Proc. Combust. Inst. 2009, 32, 1819-1838.
[4] D.G. Piercey, T.M. Klapoetke. Centr. Euro. J. Energ. Mater. 2010, 7, 115-129.
[5] X. Zhou, M. Torabi, J. Lu, R. Shen, K. Zhang. ACS Appl. Mater. Interfaces. 2014, 6, 3058-3074.
[6] Y. Li, J. Yao, Y. Liu. Surf. Coat. Technol. 2003, 172, 57-64.
[7] E.B. Motlagh, J.V. Khaki, M.H. Sabzevar. Mater. Chem. Phys. 2012, 133, 757-763.
[8] P. Lynch, H. Krier, N. Glumac. Proc. Combust. Instit. 2009, 32, 1887-1893.
[9] J.C. Poret, A.P. Shaw, C.M. Csernica, K.D. Oyler, J.A. Vanatta, G. Chen. ACS Sustainable Chem. Eng. 2013, 1, 1333-1338.

[10] K. Jayaraman, K.V. Anand, S.R. Chakravarthy, R.Sarathi. Combust. Flame. 2009, 156, 1662-1673.

[11] J. Bouillard, A. Vignes, O. Dufaud, L. Perrin, D. Thomas. J. Hazard. Mater. 2010, 181, 873-880.

[12] B. Siegert, M. Comet, D.Spitzer. Nanoscale. 2011, 3, 3534-3544.

[13] L. Menon, S. Patibandla, K. Bhargava Ram, S.I. Shkuratov, D. Aurongzeb, M. Holtz, J. Berg, J. Yun, H. Temkin. Appl. Phys. Lett. 2004, 84, 4735-4737.

[14] C.E. Aumann, G.L. Skofronick, J.A. Martin. J. Vac. Sci. Technol. B. 1995, 13, 1178-1183.

[15] A.N. Pivkina, Y.V. Frolov, D.A. Ivanov. Combust. Exp. Shock Waves. 2007, 43, 51-55.

[16] A.B. Morgan, J. Douglas Wolf, E.A. Guliants, K.A. Shiral Fernando, W.K. Lewis. Thermochim. Acta. 2009, 488, 1-9.

[17] Y. Li, R.K. Kalia, A. Nakano, P. Vashishta. J. Appl. Phys. 2013, 114, 134312.

[18] K. Zhang, C. Rossi, P. Alphonse, C. Tenailleau, S. Cayez, J-Y. Chane-Ching. Appl. Phys. A. 2009, 94, 957-962.

[19] F. Severac, P. Alphonse, A. Esteve, A. Bancaud, C. Rossi. Adv. Funct. Mater. 2012, 22, 323-329.

[20] J.Y. Ahn, W.D. Kim, K. Cho, D. Lee, S.H. Kim. Powder Technol. 2011, 211, 65-71.

[21] J.J. Granier, M.L. Pantoya. Combust. Flame. 2004, 138, 373-383.

[22] M.A. Trunov, M. Schoenitz, E.L. Dreizin, Combust. Theory Modelling. 2006, 10, 603-623.

[23] A. Rai, K. Park, L. Zhou, M.R. Zachariah. Combust. Theory Modelling. 2006, 10, 843-859.

[24] M. Schoenitz, B. Patel, O. Agboh, E.L. Dreizin. Thermochim. Acta. 2010, 507-508, 115-122.

[25] S. Chowdhury, K. Sullivan, N. Piekiel, L. Zhou, M.R. Zachariah. J. Phys. Chem. C. 2010, 114, 9191-9195.

[26] V.I. Levitas, B.W. Asay, S.F. Son, M. Pantoya. Appl. Phys. Lett. 2006, 89, 071909.

[27] V.I. Levitas, B.W. Asay, S.F. Son, M. Pantoya. J. Appl. Phys. 2007, 101, 083524.
[28] V.I. Levitas, M. Pantoya, B. Dikici. Appl. Phys. Lett. 2008, 92, 011921.
[29] M.L. Pantoya, J.J. Granier. Propellants Explo. Pyrotech. 2005, 30, 53-62.
[30] G. Jian, S. Chowdhury, K. Sullivan, M.R. Zachariah. Combust. Flame. 2013, 160, 432-437.
[31] K. Sullivan, M.R. Zachariah. J. Propul. Power. 2010, 26, 467-472.
[32] S.W. Dean, M.L. Pantoya, A.E. Gash, S.C. Stacy, L.J. Hope-Weeks. J. Heat Transfer. 2010, 132, 111201.
[33] J.Z. Wen, S. Ringuette, G. Bohlouli-Zanjani, A. Hu, N.H. Nguyen, J. Persic, C.F. Petre, Y.N. Zhou. Nanoscale Res. Lett. 2013, 8, 184.
[34] K.T. Sullivan, W.A. Chiou, R. Fiore, M.R. Zachariah. Appl. Phys. Lett. 2010, 97, 133104.
[35] K.T. Sullivan, N.W. Piekiel, C. Wu, S. Chowdhury, S.T. Kelly, T.C. Hufnagel, K. Fezzaa, M.R. Zachariah. Combust. Flame. 2012, 159, 2-15.
[36] N.W. Piekiel, G.C. Egan, K.T. Sullivan, M.R. Zachariah. J. Phys. Chem. C. 2012, 116, 24496-24502.
[37] N.W. Piekiel, L. Zhou, K.T. Sullivan, S. Chowdhury, G.C. Egan, M.R. Zachariah. Combust. Sci. Technol. 2014, 186, 1209-1224.
[38] R. Thiruvengadathan, A. Bezmelnitsyn, S. Apperson, C. Staley, P. Redner, W. Balas, S. Nicolich, D. Kapoor, K. Gangopadhyay, S. Gangopadhyay. Combust. Flame. 2011, 158, 964-978.
[39] W.K. Lewis, B.A. Harruff, J.R. Gord, A.T. Rosenberger, T.M. Sexton, E.A. Guliants, C.E. Bunker. J. Phys. Chem. C. 2011, 115, 70-77.
[40] S. Umbrajkar, M.A. Trunov, M. Schoenitz, E.L. Dreizin. Propul. Explo. Pyrotech. 2007, 32, 32-41.
[41] M.A. Machado, D.A. Rodriguez, Y. Aly, M. Schoenitz, E.L. Dreizin, E. Shafirovich. Combust. Flame. 2014, 161, 2708-2716.
[42] R.W. Armstrong, B. Bschung, D.W. Booth, M. Samirant. Nano Lett. 2003, 3, 253-255.
[43] A.N. Pivkina, Y.V. Frolov, D.A. Ivanov. Combust. Exp. Shock Waves. 2007, 43, 51-55.

[44] C. Wu, K. Sullivan, S. Chowdhury, G. Jian, L. Zhou, M.R. Zachariah. Adv. Funct. Mater. 2012, 22, 78-85.

[45] K.T. Sullivan, N.W. Piekiel, S. Chowdhury, C. Wu, M.R. Zachariah, C.E. Johnson. Combust. Sci. Technol. 2011, 183, 285-302.

[46] C.R. Becker, S. Apperson, C.J. Morris, S. Gangopadhyay, L.J. Currano, W.A. Churaman, C.R. Stoldt. Nano Lett. 2011, 11, 803-807.

[47] G. Jian, J. Feng, R.J. Jacob, G.C. Egan, M.R. Zachariah. Angew. Chem. Int. Ed. 2013, 52, 9743-9746.

[48] A. Prakash, A.V. McCormick, M.R. Zachariah. Nano Lett. 2005, 5, 1357-1360.

[49] A. Prakash, A.V. McCormick, M.R. Zachariah. Adv. Mater. 2005, 17, 900-903.

[50] W. Zhou, J.B. Delisio, X. Li, L. Liu, M.R. Zachariah. J. Mater. Chem. A. 2015, 3, 11838-11846.

[51] P.R.N. Childs. Practical Temperature Measurement, Butterworth Heinemann, London, U.K., 2001.

[52] L. Zhou, N. Piekiel, S. Chowdhury, M.R. Zachariah. J. Phys. Chem. C. 2010, 114, 14269-14275.

[53] K is an intermediate product due to its high chemical activity. The final products in eqs 6.7 and 6.8 can be K_2S. The final products in eqs 6.1 and 6.9 are unknown.

[54] http://webbook.nist.gov/chemistry/form-ser.html

[55] W.M. Haynes. WCRC Handbook of Chemistry and Physics, 92nd Edition, Boca Raton, FL, 2011.

[56] K.H. Stern. High Temperature Properties and Thermal Decomposition of Inorganic Salts with Oxyanions, CRC Press, Boca Raton, FL. 2007, p. 66.

[57] K.H. Stern. High Temperature Properties and Thermal Decomposition of Inorganic Salts with Oxyanions, CRC Press, Boca Raton, FL. 2007, p. 148.

[58] M.E. Hagerman, V.L. Kozhevnikov, K.R. Poeppelmeier. Chem. Mater. 1993, 5, 1211-1215.

[59] E.L. Cussler. Diffusion: Mass Transfer in Fluid Systems, 2nd Edition, New York, Cambridge University Press, 1997.

[60] P. Liu, T. Wang. Appl. Phys. A. 2009, 97, 771.

Chapter 7:

[1] C. Rossi, K. Zhang, D. Esteve, P. Alphonse, P. Tailhades and C. Vahlas. J. Microelectromech. Syst. 2007, 16, 919.

[2] R.A. Yetter, G.A. Risha, S.F. Son. Proc. Combust. Inst. 2009, 32, 1819.

[3] D.G. Piercey, T.M. Klapotke. Centr. Euro. J. Energ. Mater. 2010, 7, 115.

[4] E.L. Dreizin. Prog. Energ. Combust. Sci. 2009, 35, 141.

[5] N.H. Yen, L.Y. Wang. Propellants Explos. Pyrotech. 2012, 37, 143.

[6] B. Siegert, M. Comet, D. Spitzer. Nanoscale. 2011, 3, 3534.

[7] A. Vignes, F. Munoz, J. Bouillard, O. Dufaud, L. Perrin, A. Laurent, D. Thomas. Process Saf. Environ. 2012, 90, 304.

[8] E.M. Hunt, M.L. Pantoya. J. Appl. Phys.. 2005, 98, 034909.

[9] M. Schoenitz, B. Patel, O. Agboh, E.L. Dreizin. Thermochim. Acta. 2010, 507-508, 115.

[10] J. Sun, M.L. Pantoya,S.L. Simon. Thermochim. Acta. 2006, 444, 117.

[11] D. Spitzer, M. Comet, C. Baras, V. Pichot, N. Piazzon. J. Phys. Chem. Solids. 2010, 71, 100.

[12] F. Severac, P. Alphonse, A. Esteve, A. Bancaud, C. Rossi. Adv. Funct. Mater. 2012, 22, 323.

[13] H. Wang, G. Jian, G.C. Egan, M.R. Zachariah. Combust. Flame. 2014, 161, 2203.

[14] M.A. Trunov, M. Schoenitz, E.L. Dreizin. Combust. Theory Modell. 2006, 10, 603.

[15] D.A. Firmansyah, K. Sullivan, K-S. Lee, Y.H. Kim, R. Zahaf, M.R. Zachariah, D. Lee. J. Phys. Chem. C. 2012, 116, 404.

[16] C. Snehaunshu, K. Sullivan, N. Piekiel, L. Zhou, M.R. Zachariah. J. Phys. Chem. C. 2010, 114, 9191.

[17] L.P.H. Jeurgens, W.G. Sloof, F.D. Tichelaar, E.J. Mittemeijer. J. Appl. Phys. 2002, 92, 1649.

[18] A. Ermoline, E.L. Dreizin. Chem. Phys. Lett. 2011, 505, 47.

[19] B.J. Henz, T. Hawa, M.R. Zachariah. J. Appl. Phys. 2010, 107, 024901.

[20] V.I. Levitas, B.W. Asay, S.F. Son, M.L. Pantoya. J. Appl. Phys. 2007, 101, 083524.

[21] S. Zhang, E.L. Dreizin. J. Phys. Chem. C. 2013, 117, 14025.

[22] A. Rai, K. Park, L. Zhou, M.R. Zachariah. Combust. Theory Modell. 2006, 10, 843.

[23] R. Nakamura, D. Tokozakura, H. Nakajima, J.G. Lee, H. Mori. J. Appl. Phys. 2007, 101, 074303.

[24] N.W. Piekiel, L. Zhou, K.T. Sullivan, S. Chowdhury, G.C. Egan, M.R. Zachariah. Combust. Sci. Technol. 2014, 186, 1209.

[25] L. Zhou, N. Piekiel, S. Chowdhury, M.R. Zachariah. J. Phys. Chem. C. 2010, 114, 14269.

[26] G. Jian, J. Feng, R. J. Jacob, G.C. Egan, M.R. Zachariah. Angew. Chem. Int. Ed. 2013, 52, 9743.

[27] W. Zhou, J.B. DeLisio, X. Li, L. Liu, M.R. Zachariah. J. Mater. Chem. A. 2015, 3, 11838.

[28] W. Zhou, J.B. DeLisio, X. Wang, M.R. Zachariah. "Reaction mechanisms of energetic composites containing potassium oxysalts as oxidizers," Submitted.

[29] K.T. Sullivan, N.W. Piekiel, S. Chowdhury, S.T. Kelly, T.C. Hufnagel, K. Fezzaa, M.R. Zachariah. Combust. Flame. 2012, 159, 2.

[30] R.J. Jacob, G. Jian, P.M. Guerieri, M.R. Zachariah. Combust. Flame. 2015, 162, 258.

[31] K.T. Sullivan, W-A. Chiou, R. Fiore, M.R. Zachariah. Appl. Phys. Lett. 2010, 97, 133104.

[32] G.C. Egan, K.T. Sullivan, T. LaGrange, B.W. Reed, M.R. Zachariah. J. Appl. Phys. 2014, 115, 084903.

[33] G. Jian, S. Chowdhury, K. Sullivan, M.R. Zachariah, Combust. Flame. 2013, 160, 432.

[34] A. Rai, D. Lee, K. Park, M.R. Zachariah. J. Phys. Chem. B. 2004, 108, 14793.

[35] J. Sivan, Y. Haas, D. Grinstein, S. Kochav, G. Yegudayev, L. Kalontarov. Combust. Flame. 2015, 162, 516.

[36] M.A. Trunov, S.M. Umbrajkar, M. Schoenitz, J.T. Mang, E.L. Dreizin. J. Phys. Chem. B. 2006, 110, 13094.

[37] K. Park, D. Lee, A. Rai, D. Mukherjee, M.R. Zachariah. J. Phys. Chem. B. 2005, 109, 7290.

[38] M. Schoenitz, S. Umbrajkar, E.L. Dreizin. J. Prop. Power. 2007, 23, 683.

[39] L. Zhou, A. Rai, N. Piekiel, X. Ma, M.R. Zachariah. J. Phys. Chem. C. 2008, 112, 16209.

[40] S. Mohan, M. A. Trunov, E.L. Dreizin. J. Heat Transfer. 2008, 130, 104505.

[41] T.S. Ward, M.A. Trunov, M. Schoenitz, E.L. Dreizin. Int. J. Heat Mass Transfer. 2006, 49, 4943.

[42] M.A. Trunov, M. Schoenitz, E.L. Dreizin. Propell. Explo. Pyrotech. 2005, 30, 36.

[43] S. Alavi, J.W. Mintmire, D.L. Thompson. J. Phys. Chem. B. 2005, 109, 209.

[44] C. Lanthony, J.M. Ducere, M.D. Rouhani, A. Hemeryck, A. Esteve, C. Rossi. J. Chem. Phys. 2012, 137, 094707.

[45] A. Ermoline, D. Yildiz, E.L. Dreizin. Combust. Flame. 2013, 160, 2982.

[46] W. Zhou, M.W. Orr, G. Jian, S.K. Watt, V.T. Lee, M.R. Zachariah. Chem. Eng. J. 2015, 279, 578.

[47] E.D. Wachsman, S. Boyapati, M.J. Kaufman, N. Jiang. Solid-state Ionic Devices: Proceedings of the International Symposium (Pennington, New Jersey, 1999), Vol. 1, pp. 42.

[48]http://webbook.nist.gov/cgi/cbook.cgi?ID=C7429905&Units=SI&Mask=2#Thermo-Condensed.

[49] N. Cabrera, N.F. Mott. Rep. Prog. Phys. 1948, 12, 163.

[50] G. Jian, N.W. Piekiel, M.R. Zachariah. J. Phys. Chem. C. 2012, 116, 26881.

[51] H. Flynn, L.A. Wall. J. Res. Natl. Bur. Stand. 1966, 70, 487.

[52] T. Ozawa. Thermochim. Acta. 1992, 203, 159.

[53] G. Jian, L. Zhou, N.W. Piekiel, M.R. Zachariah. ChemPhysChem. 2014, 15, 1666.

[54] D. Mukherjee, C.G. Sonwane, M.R. Zachariah. J. Chem. Phys. 2003, 119, 3391.